Electronic Theses and Dissertations

1973

Electronic spectra of erbium+(3) and praseodymium+(3) ions in calcium fluoride crystals.

V. P. Bhola
University of Windsor

Recommended Citation

Bhola, V. P., "Electronic spectra of erbium+(3) and praseodymium+(3) ions in calcium fluoride crystals." (1973). *Electronic Theses and Dissertations.* Paper 1910.

ELECTRONIC SPECTRA OF Er^{+3} AND Pr^{+3} IONS

IN CaF_2 CRYSTALS

by

V. P. Bhola

A Thesis
Submitted to the Faculty of Graduate Studies through
the Department of Physics in Partial Fulfillment
of the Requirements for the Degree
of Doctor of Philosophy at
the University of Windsor

Windsor, Ontario

1973

ABSTRACT

The optical absorption spectrum of CaF_2Er^{+3} (1%) at LNT has been studied in the spectral region 6600 cm^{-1} to 65400 cm^{-1}. $4f^{11} - 4f^{11}$ and interconfiguration transitions $4f^{11} \rightarrow 4f^{10}5d$ have been observed. The Er^{+3} ion levels $^2F_{7/2}$ and $^2F_{5/2}$ at 54795 cm^{-1} and 63091 cm^{-1}, respectively, have also been observed. The positions of a number of energy levels above 31000 cm^{-1} have been established.

The optical absorption spectrum of CaF_2Pr^{+3} (1%) at LNT has been studied in the spectral range 4250 cm^{-1} to 50000 cm^{-1}. The positions of the energy levels $^3P_2$, $^1I_6$, $^3P_1$ and $^3P_0$ have been established to be 22526 cm^{-1}, 21481 cm^{-1}, 21306 cm^{-1} and 20777 cm^{-1}, respectively. It is suggested that energy levels $^3P_1$ and $^1I_6$ are brought into close proximity in the CaF_2 matrix. Also the presence of a mixture of site symmetries for the rare earth ions in CaF_2 has been established. The two symmetries manifest themselves in the thermoluminescence spectra, while usually one symmetry manifests itself in the luminescence emission spectra.

Employing luminescence excitation techniques, the excitation spectrum of CaF_2Er^{+3} (0.1%) has been studied in the spectral range 18200 cm^{-1} to 50000 cm^{-1}. The results are in agreement with the absorption spectrum as expected, indicating that both spectra are essentially of similar

origin. The excitation spectrum of CaF_2Pr^{+3} in the spectral region 23800 cm^{-1} to 50000 cm^{-1} has been carried out. A tentative scheme of transitions between energy levels has also been constructed, assuming a mixture of cubic and tetragonal symmetries as mentioned above.

Impurity concentration dependent bands at 2620 Å, 2740 Å, 3530 Å, 3660 Å and 3950 Å have been observed and tentatively identified. An attempt has been made to construct an energy level scheme assuming a cubic site symmetry in the case of CaF_2Pr^{+3}. Under the influence of cubic site symmetry, the splitting of the ground state has, in this case, been found to be approximately 200 cm^{-1}. The position of $^3P_2$ has been established to be at 22800 cm^{-1}. This one level does not manifest itself at the same position in the absorption spectrum of CaF_2Pr^{+3}.

iv

ACKNOWLEDGEMENTS

TABLE OF CONTENTS

viii

LIST OF FIGURES

x

LIST OF TABLES

Chapter 1 INTRODUCTION

1.1 General Remarks

The rare-earth atoms have a common feature of $4f^N$-shell with N = 1 for cerium and increasing regularly to N = 14 for lutecium. The spectra of these elements differ largely among themselves as each element has its own characteristic spectra both in the case of free atoms and ions and in the case of ions in solution and in crystals. Extensive studies on their spectral properties have been carried out in the past. These studies not only reveal the electronic structure of rare-earth atoms but also have opened up a new way for the study of the nature of solids.

It is known that the $4f^N$ configuration of rare-earth ions is well shielded by the electrons in the 5s and 5p shells. As the number of electrons in the 4f shell increases from cerium to lutecium, the effective nuclear charge also increases and, due to increased effective nuclear charge, the electrons in the 4f shell are attracted towards the nucleus, thus producing Lanthanide Contraction (0). Due to Lanthanide Contraction, the ionic radii decrease as the atomic number is increased.

In a crystal the 4f electrons interact weakly with their surroundings. As a result of the interaction with the crystal field, some degree of degeneracy of the

1

free ions is removed and also some forbidden transitions become possible. Meanwhile, the essential structure of the free ion configuration is still preserved. During transitions between energy levels of rare-earth ions corresponding to the well shielded inner 4f shell, different characteristic spectra with a clearly discrete structure are obtained. This structure is closely related to the internal structure of the medium in which the ion is embedded. As a result, the investigation of rare-earth ions introduced into the crystal can serve as a sensitive probe.

1.2 CaF_2 Structure

The main object of the present study is to investigate the crystal field spectra of Pr^{+3} and Er^{+3} in the visible and UV spectral regions. The CaF_2 crystal is one of the most suitable hosts that can be used for studying the rare-earth ions in crystals. It is transparent from 1250 Å to 90,000 Å and can artificially be doped with rare-earth elements. CaF_2 crystals doped with tripositive rare-earth ions of different concentrations are available from the commercial manufacturers.

Calcium fluoride belongs to the O_h space group and its lattice structure is face-centred cubic, with a basis of one divalent calcium ion at (000) and 16 F^- ions at $(\pm1/4,\pm1/4,\pm1/4)$ and $(\pm3/4,\pm3/4,\pm3/4)$ as shown in Fig. 1.1(a). This may be regarded as a cubic lattice of fluorine ions in which every other body centre position is occupied

a) UNDOPED

b) COMPENSATION BY INTERSTITIAL FLUORIDE

c) COMPENSATION BY SUBSTITUTIONAL O^{2-}
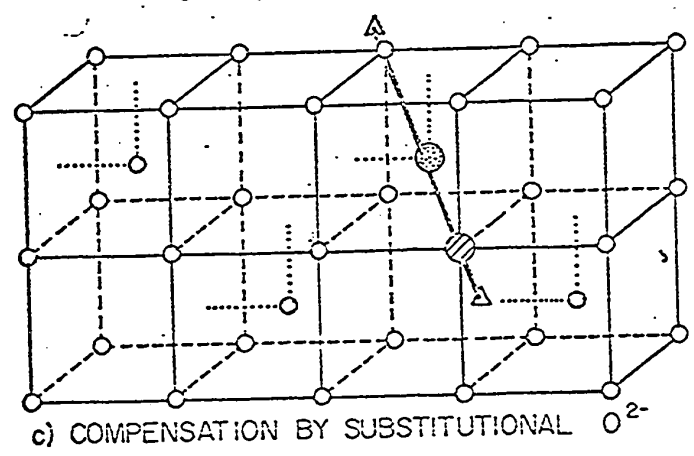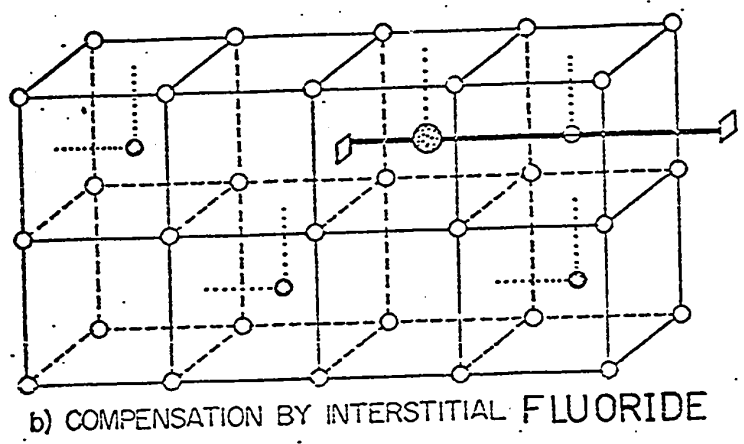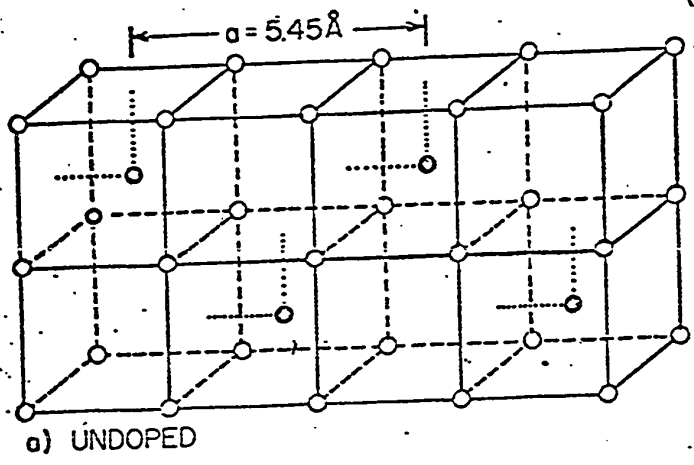
○ F^- ⊛ RE^{3+}
◉ Ca^{2+} ◍ O^{2-}

Fig. 1.1 Calcium fluoride lattice

by a divalent calcium ion. When the rare-earth trifluoride
is added to CaF_2 melt, the tripositive ion replaces the
divalent calcium ion, thus introducing an extra positive
charge in the lattice. To preserve the charge neutrality,
there must be an additional negative charge to compensate
for the extra positive one. The symmetry about the rare-
earth ion depends upon the various factors, among which
the most important ones are the initial growing conditions,
heat treatment given to the crystal, and type and amount
of impurities, as all these affect the position of the
charge compensator.

The charge compensation may be achieved by an
interstetial F^- ion in one of the empty cubes adjacent to
the rare-earth ion. The symmetry about the rare-earth
ion then reduces from cubic to tetragonal (C_{4v}), and the
four-fold rotational axis C_4 will be in the [100]
direction, as shown in Fig. 1.1(b). Using EPR techniques,
Weber and Bierig (1) have observed this type of symmetry
for Sm^{+3}, Er^{+3} and Yb^{+3} ions. Low (2) and various other
investigators (3-6) have reported similar results for the
other ions of the Lanthanide series. On the basis of this
model, Stepanov and Feofilov (7) have explained the results
of their optical spectra of Lanthanides in an oxygen-free
crystal of CaF_2 (Type II).

Charge compensation can also be furnished by
introducing an O^{-2} ion into the lattice of the CaF_2 matrix.
The O^{-2} ion replaces one of the F^- ions surrounding the

Re^{+3} ion from the eight corners of the cube and results in trigonal symmetry (C_{3v}), Fig. 1.1(c). Due to an extra negative charge carried by O^{-2}, the three fold axis (C_3) will point along the [111] direction. Forrester and Hempstead (8) have observed this type of symmetry for Tb^{+3}. Low and Rosenberger (9) have detected the presence of trigonal symmetry after introducing the O^{-2} ion into the crystal lattice of CaF_2Tb^{+3}. They heated the crystal up to 1200°C in air for several hours. Vinokurov et al (10) and Makovsky (11) have reported similar results for Gd^{+3}. Sierro (12), McLaughlan and Newman (13) have presented another kind of trigonal symmetry in which the charge compensation has been achieved by an OH^- ion instead of an O^{-2} ion. When the charge compensator is located several lattice spacings away from the rare-earth ion, the symmetry about the rare earth ion may be considered to be cubic. Evidence of such compensation has been found in the cases of Nd^{+3} (14), Gd^{+3} (15,16), Ce^{+3} (17), Dy^{+3} (18,19), and Yb^{+3} (20,21).

D. Marsh (41) has presented the calculations for Tm^{+2} trigonal centres formed by substituting an H^- ion for an F^- ion in a nearest neighbour position relative to a substitutional Tm^{+2} ion in alkaline earth fluoride lattices.

Charge mobility has been studied by Friedman and Low (23). Many investigators (25-29) have found that the divalent ions produced by ionizing the trivalent ions are mainly under the cubic symmetry. Merritt and co-workers

(30) found Pr^{+2} in cubic sites after electrolysis.

From the spectral distribution of thermoluminescent glow peaks at 155, 206 and 333°K and the room temperature phosphorescence, Schlesinger and Whippey (24) have suggested that as the relative intensities of the various emission lines change from peak to peak, it gives an indication that the compensator associated with an Ho^{+3} ion becomes mobile at about room temperature. The authors (39,40) have also pointed out that in the case of CaF_2Gd^{+3}, rare-earth ions in sites other than cubic are mainly responsible for the emission below RT. In the case of CaF_2Ho^{+3}, from excitation, emission and thermoluminescence spectra of the as received crystal and the heat treated crystal, Pai (22) has claimed that the symmetry surrounding the Ho^{+3} ion in the as received crystal is predominantly cubic.

Rare-earth ions may be found at different sites in the same crystal. Examples of such symmetries for different rare-earth ions have been reported by many investigators (31-33). All the three types of symmetries have been observed for Sm^{+3} and Dy^{+3} (34,35). From thermoluminescence spectra of CaF_2Dy^{+3}, Schlesinger and Kwan (38) have shown that sites of different symmetries are responsible for thermoluminescence emission, even at temperatures close to that of liquid nitrogen. Recently, by employing absorption, luminescence and thermoluminescence techniques, Schlesinger and Nara (36,37) have shown the existence of two different sites for CaF_2Sm^{+3} and CaF_2Dy^{+3} crystals.

The authors have also calculated the crystal field parameters for each site and have assigned an irreducible representation to each stark split level. They have also identified vibronic lines in CaF_2Dy^{+3} (42).

1.3 Survey of CaF_2Pr^{+3} and CaF_2Er^{+3}

A comprehensive review of the spectra of the rare-earth elements both in the gaseous state and that in some host crystals has been made by El'Yashevich (43). An extensive study of the spectra of rare-earth ions in different host lattices has been carried out by Dieke et. al. (44). These authors have given references dealing with the subject dating as far back as 1906. Both theoretical and experimental values of energy levels of tripositive rare-earth ions in aqueous solution have been reported by Carnall et al (45). Hence, in this section, only the literature for Pr^{+3} and Er^{+3} in the matrix of CaF_2 will be surveyed.

(a) $\underline{CaF_2Pr^{+3}}$

The tripositive ion of Proseodymium has the electronic structure $(Xe)4f^2$ where (Xe) stands for the xenon configuration; $1s^2 2s^2 2p^6 3s^2 3p^6 3d^{10} 4s^2 4p^6 4d^{10} 5s^2 5p^6$. The ground state of Pr^{+3} is $^3H_4$. The luminescence spectrum of CaF_2Pr^{+3} was first reported by Stepanov and Feofilov (46). These authors have observed two types of spectra depending upon oxidizing and reduction conditions during growth of the crystal. In the second type of CaF_2Pr^{+3}, they observed

two strongest emissions, one in the blue green region and another in the red region. In type I, they were unable to see the emission from the blue green region. McClure and Kiss (47) have studied the divalent rare-earth ions produced by γ-irradiation of trivalent ions in the CaF_2 crystal.

By employing x-ray as the exciting source, luminescence spectrum studies of CaF_2Pr^{+3} were carried out by many investigators (48,49,50). From luminescence experiments, Low (49,50) has identified the position of the $^1S_0$ level at 46300 cm^{-1}. Later on, Loh (51) claimed this level to be at 47200 cm^{-1} in the absorption spectrum of CaF_2Pr^{+3}. Merz and Pershan (52) have studied the thermoluminescence spectrum of CaF_2Pr^{+3}. These authors have reported that the excitation is only due to cubic sites, but the presence of another symmetry around the Pr^{+3} ion in the lattice of CaF_2 is possible. Recently, Hargreaves (61) has grown the crystal of CaF_2Pr^{+3} (1 %) under high vacuum conditions, with adequate F^- ions present during the growth. He carried out the absorption measurements with a McPherson Model 218 scanning monochromator. From his absorption measurements, he has calculated the crystal field parameters, Slater integrals and spin-orbit constant. The author has also established new positions for ^3P and ^1I multiplets.

Employing EPR techniques, Weber and Bierig (1) have carried out an extensive research work on the tripositive rare-earth ions. These authors have reported that the lowest stark split component of the ground state of Pr^{+3} is either

Γ_1 or Γ_5, depending upon the ratio of the crystal field parameters. U. Ranon (53) and LLW (54) have suggested that the lowest component of stark split level of the ground state under cubic symmetry is Γ_5. Later on, by using EPR methods, McLaughlan (55) has observed the Pr^{+3} ion in the CaF_2 matrix at the trigonal site. From the high field Zeeman effect, Masui (56) has found Pr^{+3} ions at trigonal sites.

From infrared quantum counter experiments, Esterowitz and Noonan (57) have suggested an energy level scheme for CaF_2Pr^{+3} (1 %) at RT. Loh (58-60) has measured at RT and at LNT the UV absorption spectra of the Pr^{+3} ion in CaF_2, SrF_2 and BaF_2 crystals. He has concluded that:

1. Due to strong action of the crystal field, the ground state of the $4f^{n-1}5d$ configuration is lowered, thus the energy of the $4f \rightarrow 5d$ transition in the crystal environment is lowered by 18000 cm^{-1} as compared to that of the free ion $4f \rightarrow 5d$ transition.

2. At LNT because of increasing crystal field strength in the contracted lattice, the $4f \rightarrow 5d$ bands sharpen and shift ~ 200 cm^{-1} towards the lower wavenumber.

3. Interconfiguration transitions take place for
(a) $4f^2 \rightarrow 4f5d$ between 4400 and 6900 cm^{-1}.
(b)   a possible $4f^2 \rightarrow 4f6s$ at 7600 cm^{-1}.
(c)   a charge transfer $F^-(2p^6) \rightarrow Pr^{+3}(6s)$ near 80000 cm^{-1}.

The author has also pointed out that the crystal field is dominant in the higher configurations 5d and 6s

due to the presence of electrons in the 5d and 6s shells which are not shielded from the outside as in the case of the $4f^N$ configuration.

(b) $\underline{CaF_2Er^{+3}}$

The triply ionized erbium ion has the electronic structure $(Xe)4f^{11}$ and its ground state is $^4I_{15/2}$. The fluorescence of triply ionized erbium in fluorites was reported by various authors (62-64). Fluorescence experiments were also carried out by Stepanov and Feofilov (7) and they observed the green and red emissions in type II and only the green emission in type I. They attributed this difference to the presence of different charge compensators in CaF_2Er^{+3}. A survey of the spectra of divalent rare-earth ions in cubic crystals has been published by Kiss and McClure (47). Using γ-rays, these authors obtained divalent ions from the trivalent ions in CaF_2 crystals. They have shown that at higher energies the structure of the $4f^N$ configuration is destroyed by the broad band due to $4f^N \rightarrow 4f^{N-1}5d$ transitions. The x-ray luminescence spectrum of CaF_2Er^{+3} from 2800 Å to 10,000 Å at $300°K$ and $77°K$ has been described in reference (48).

Pollack (65) has photographed the absorption and emission spectra of CaF_2Er^{+3} (0.1 %) at $4°K$, $77°K$ and $300°K$. He has analysed his results by making a comparison with the spectrum of $ErCl_3$. He has reported 23 distinct groups extending from 1.5μ to 2300 Å and a continuous absorption whose edge starts around 1700 Å. The resolution of all of

these groups is poor and agreement of the levels above
36500 cm^{-1} is not very good. The detailed structure of the
groups and classification of individual lines according
to certain symmetry surrounding the Er^{+3} ion in the CaF$_2$
crystal is lacking. Rector et al (66) have studied the
Zeeman splittings of the fluorescence of erbium in CaF$_2$
and found that the emission from tetragonal site dominated
the optical spectra. These authors did not classify the
crystal-field split energy levels according to different
site symmetries.

A great deal of research work on the EPR experiment
has been carried out under the supervision of W. Low at the
Hebrew University of Jerusalem. Many investigators (1,7,32,67-69)
have reported different types of spectra due to the presence
of the Er^{+3} ion at various site symmetries in the CaF$_2$
crystal, and they have calculated the values of g. Under
cubic symmetry, the lowest level of the crystal field
split component of the ground state of the Er^{+3} ion in the
CaF$_2$ crystal is Γ_7. This has been supported experimentally
and theoretically by different authors (1,53,54).

Merz and Pershan (52) have carried out thermolumin-
escence experiments in which they claim that above RT
emission is due to the presence of Er^{+3} ions at tetragonal
sites. From cathodoluminescence experiments, cubic centres
of the Er^{+3} ion in various crystals of fluorite types have
been studied by Aizenberg et al (70).

Visible absorption spectrum of CaF$_2$Er^{+3} at liquid

oxygen temperatures has been carried out by Narasimhm et al (71). They have reported some new lines in E group (19104 to 18612 cm^{-1}), F group (19390 to 19180 cm^{-1}), K group (26187 to 25878 cm^{-1}) and L group (26278 to 26197 cm^{-1}). Concentration series and selective excitation methods have been employed by Voron'ko (74) to study the presence of various sites of the Er^{+3} ion in cubic crystals of the fluorite type. From absorption and luminescence spectra of the Er^{+3} ion in fluorite type crystals, Smirnov et al (72,73), Stolov et al (75) have constructed the stark levels of $^4S_{3/2}$ and $^4I_{15/2}$ under the trigonal symmetry.

Theoretical calculations of energy levels and transition schemes have been given by Judd and Loydon (76.) and by Wybourne (77).

1.4 Aim of the Present Study

The present investigation is an attempt to study the spectroscopic properties of CaF_2Pr^{+3} and CaF_2Er^{+3} systems in general, and special considerations will be given to the following:

1. Absorption spectra in the spectral region of 1250 Å to 2000 Å by using electric discharge through different gases.

2. Luminescence excitation spectra in the spectral region of 2000 Å to 4500 Å in the case of CaF_2Pr^{+3} and that of CaF_2Er^{+3} from 2000 Å to 5500 Å.

3. To identify the lines due to different symmetries surrounding the rare-earth ions.

Chapter 2   THEORY

2.1 Introductory Remarks

The theory of atomic spectra has been treated by
Slater (1) and by Condon and Shortley (2). Racah (3-6)
has extended the work of Condon and Shortley by developing
the theory of tensor operator which is a powerful tool in
dealing with the complex spectra such as that of rare earth
atoms. Using group theory and quantum mechanics (7,8,9),
crystal field theory has been developed by many other
authors (10-17).

The theory usually starts with a system which is
sufficiently simplified by omitting all types of inter-
actions other than the central field, so that the energy
levels of the system are obtained without much complica-
tions. Each additional interaction is then taken into
account successively as a perturbation to the simplified
system.   In the central-field approximation, all
states of a given configuration will have the same energy.
The degeneracy for a N-4f electron system is $\binom{14}{N}$. Some
of the degeneracy will be removed by considering the
electrostatic interaction and spin-orbit interaction. If
the ion is placed in a crystal field, degeneracy will
further be removed. Finally, by applying an external
magnetic field (Zeeman effect) all the degeneracy may be

completely removed.

2.2 Classification of the States

Classification of states usually can be done by using three quantum numbers, namely L, S and J. However, for the f^N configuration, in certain cases there are some states having the same quantum number of L and S but with different energies. In order to distinguish those states having the same L and S values, additional quantum numbers other than L and S are needed.

Under certain symmetry operations, the wavefunctions of a state in the f^N configuration usual.y undergo a linear transformation. The irreducible representation of the symmetry operation, to which the function belongs, can serve as an additional quantum number. Furthermore, the properties of the symmetry group can be used to simplify the calculation of the matrix elements of the tensor operators, corresponding to a certain interaction. Based on this principle, Racah (6) has classified the states of f^N configuration by introducing the quantum numbers $W = (w_1, w_2, w_3)$ and $U = (U_1, U_2)$ such that $2 \geq w_1 \geq w_2 \geq w_3 \geq 0$ and $2 \geq U_1 \geq U_2 \geq 0$. Using these quantum numbers, the states of the f^N configuration may be further specified by writing the basis states as $| f^N \tau WUSL \rangle$ in which τ is a label to distinguish the remaining unseparated states.

According to the Pauli equivalence theorem, the classification of the states of the f^{14-N} configuration is

identical to those of the f^N configuration, and hence we
have to enumerate the systems for $N \leq 7$ only. The class-
ification of the states for the f^2 and f^{11} configurations
are given in Table 2.1.

2.3 Fractional Parentage

In a configuration, when three or more equivalent
electrons are present, the number of multiplets becomes
very large. For calculating the wavefunctions, an extremely
large number of determinantal functions must be written
down. Moreover, in this method there is no simple
connection between the wavefunctions of ℓ^{N-1} and ℓ^N
systems. In order to overcome these problems, the concept
of fractional parentage (4-6,10,18) has been introduced.
This is a powerful tool for constructing the antisymmetrised
wavefunction for ℓ^N provided the wavefunctions of ℓ^{N-1} are
known.

With this method, the eigenfunction of the f^N
configuration can be expressed as

$$\psi(f^N \alpha LS) = \sum_{\alpha'L'S'} \psi(f^{N-1}\alpha'L'S') . \bar{\Phi}(\ell sm\ell ms) x$$

$$\langle f^{N-1}\alpha'L'S' \mid f^N \alpha LS \rangle$$

where the summation extends over all the states $\psi(f^{N-1}\alpha'L'S')$
of the complete set of the f^{N-1} configuration. α is a
quantum number other than L and S. $\bar{\Phi}(\ell_s m\ell ms)$ is the
eigenfunction of the Nth electron which can be defined
as

TABLE 2.1

Classification of the States

of the f^2 and f^{11} Configurations

N	v*	W	U	SL
2	2	(110)	(10)	^3F
2	2	(110)	(11)	$^3P\,^3H$
2	2	(200)	(20)	$^1D\,^1G\,^1I$
2	0	(000)	(00)	^1S
3	3	(111)	(00)	^4S
3	3	(111)	(10)	^4F
3	3	(111)	(20)	$^4D\,^4G\,^4I$
3	3	(210)	(11)	$^2P\,^2H$
3	3	(210)	(20)	$^2D\,^2G\,^2I$
3	3	(210)	(21)	$^2D\,^2F\,^2G\,^2H\,^2K\,^2L$
3	1	(100)	(10)	^2F

* v is the seniority number.

$$\Phi(\ell s \ m\ell \ ms) = \frac{1}{r} R_{n\ell}(r) \ Y_{\ell}^{m\ell} \ (\theta \ \Phi). \quad \sigma(ms)$$

and $\qquad \langle f^{N-1}\alpha'L'S' \mid f^{N}\alpha LS \rangle$

is the coefficient of fractional parentage (C.F.P.). The coefficient of fractional parentage describes how the state $\psi(f^{N}\alpha LS)$ is built from its parent state $\psi(f^{N-1}\alpha'L'S')$ and the coefficients can be used for the simplification of the matrix elements. For the f^{N} configuration C.F.P. have been calculated and tabulated by Nielson and Koster (19).

2.4 Calculation of Energy Levels

The system may be described by the non-relativistic Hamiltonian

$$H = H_{o} + H_{1} + H_{2} + H_{3}$$

$$= \sum_{i=1}^{N} [- \frac{h^2}{2m} \nabla_i^2 + U(ri)] + \sum_{i>j}^{N} \frac{e^2}{r_{ij}}$$

$$+ \sum_{i=1}^{N} \xi i \ \ell i.si + \sum_{kqi} B_q^k (C_q^{(k)})_i \qquad (2.4.1)$$

in which the weak interactions such as spin-spin, orbit-orbit, spin-other orbit, electron nuclear magnetic moment interaction and the configuration interaction are neglected. The first term H_o in (2.4.1) describes the independent motion of each electron under the influence of field produced by the nucleus plus fifty-four electrons of the xenon structure.

The rest of the terms, H_1, H_2 and H_3 are the

perturbations arising from the electrostatic interaction, spin-orbit interaction and crystal-field, respectively. As far as the energy level structure is concerned, the first term H_c contributes a common energy shift to all the levels in a given configuration, therefore, practically only the perturbation Hamiltonians are significant. For calculating the matrix elements of the perturbed Hamiltonian, one needs a complete set of basis states in some well-defined coupling scheme. However, in some cases, none of the well-defined coupling schemes will closely fit the real physical situation. The matrix elements of the Hamiltonian are therefore first calculated in terms of the basis states of a well-defined coupling scheme and then transformed to the actual coupling scheme at a later stage. For free ion energy levels, evaluation of the matrix elements of the Hamiltonian H_1 and H_2 are essential. The detailed procedures are given in the following sub-sections (a) and (b). Evaluation of the crystal field Hamiltonian H_3 will be discussed in sub-section (c).

(a) Electrostatic Interaction

Matrix elements of the second term H_1 in equation (2.4.1) for the configuration f^N can be expressed in terms of tensor operator (2,6) and that the energy

$$E_1 = \langle \tau SLJM_J \mid \sum_{i>j}^{N} \frac{e^2}{r_{ij}} \mid \tau'S'L'J'M'_J \rangle$$

$$= \sum_k e^2 \langle \tau SL \mid \sum_{i>j} \frac{r^k_<}{r^{k+1}_>} (C_i^{(k)} \cdot C_j^{(k)}) \mid \tau'SL \rangle \qquad (2.4.2.)$$

where r_{ij} is the distance between the two electrons, $r_<$ and $r_>$ is the distance to the nearest and farthest electron from the nucleus. The tensor operator $c_q^{(k)}$ is defined as

$$c_q^{(k)} = \left(\frac{4\pi}{2k+1}\right)^{1/2} Y_{kq}(\theta \Phi)$$

where Y_{kq} are the spherical harmonics.

The matrix elements so obtained are diagonal in L and S and are independent of J and M_J, as the Hamiltonian due to electrostatic interaction commutes with the operators L^2, S^2, J and M_J. The matrix elements can be further reduced in terms of Slater integrals F^K such that

$$E_1 = \sum_{k=0}^{3} e_k E^k \qquad (2.4.3.)$$

where e_k are the matrices arising from the angular parts of the operators and are tabulated by Racah (6), and E^K are defined

$$E^0 = F_0 - 10 F_2 - 33 F_4 - 286 F_6$$

$$E^1 = \frac{70 F_2 - 231 F_4 - 2002 F_6}{9}$$

$$E^2 = \frac{F_2 - 3 F_4 - 7 F_6}{9}$$

$$E^3 = \frac{5 F_2 - 6 F_4 - 91 F_6}{3}$$

where

$$F_k = \frac{F^k}{D_k} = \frac{e^2}{D_k} \int_0^\infty \int_0^\infty \frac{r_<^k}{r_>^{k+1}} R_{n\ell}^2(r_1) R_{n\ell}^2(r_2) d\tau_1 \cdot d\tau_2$$

and D_K are given in reference (2).

Assuming radial hydrogenic wavefunctions, the R.H.S. of equation (2.4.3) then can be written in terms of a single parameter F_2 such that $E_1 = (\text{constant})\, F_2$. The parameter F_2 can be determined from experimental results. Slater radial integrals have been determined by Freeman and Watson (23). A complete tabulation of the electrostatic energy matrices for the f^N configuration has been made available by Nielson and Koster (19).

(b) Spin-Orbit Interaction

Using the tensor operator method of Racah (4), the J dependent matrix elements of spin-orbit interaction H_2 for the f^N configuration may be expressed as

$$E_2 = \langle f^N \alpha SLJM_J | \xi_{n\ell} \sum_{i=1}^{N} (s_i \cdot \ell_i) | f^N \alpha' S' L' JM_J \rangle$$

$$= \xi_{n\ell} (-1)^{J+L+S'} \begin{Bmatrix} L & L' & 1 \\ S' & S & J \end{Bmatrix} \times$$

$$\langle f^N \alpha SL | \sum_{i=1}^{N} (s_i \cdot \ell_i) | f^N \alpha' S' L' \rangle \qquad (2.4.4)$$

where $\xi_{n\ell}$ is the spin-orbit integral which is constant for a given configuration and is defined as

$$\xi_{n\ell} = \int_{0}^{\infty} R_{n\ell}^2 (r)\, \xi(r)\, dr \qquad \text{where}$$

$$\xi(r) = \frac{\hbar^2}{2m^2 c^2 r_i} \frac{dU(r_i)}{dr_i}$$

where $U(r_i)$ is the average potential experienced by the ith electron.

The spin-orbit Hamiltonian commutes with J^2 and M_J but not with L^2 and S^2, hence its matrix elements are

diagonal in J. In the equation (2.4.4) { } is the 6-j symbol and are given in Ref. (20). Using equations (2-74, 2-35 and 2-49) of Ref. (15), the second term of the equation (2.4.4) can be simplified

$$\langle f^N \alpha SL | \sum_{i=1}^{N} (s_i \cdot \ell_i) | f^N \alpha'S'L' \rangle$$

$$= [\ell(\ell+1)(2\ell+1)]^{1/2} \times \langle f^N \alpha SL \| V^{(11)} \| f^N \alpha'S'L' \rangle$$

and values of $\langle f^N \alpha SL \| V^{(11)} \| f^N \alpha'S'L' \rangle$

are tabulated in Ref. (19).

Several authors (21,22) have calculated the matrix elements of spin-orbit interactions for f^3 and f^4 configurations. The matrix elements for the $\ell^{4\ell+2-N}$ configuration are of the same magnitude but of opposite sign to that of ℓ^N configuration.

(c) Crystal Field

A free atom or ion possesses spherical symmetry and each J level is (2J + 1) fold degenerate. On placing the ion in the crystal, the spherical symmetry is destroyed. The degree up to which the (2J + 1) fold degeneracy of the free ion is removed, will depend upon the symmetry surrounding the ion in the crystalline matrix. For the rare earth ions, the effect of the crystal field is usually smaller than that of the Coulomb and spin-orbit interaction of the electrons, hence it may be evaluated by applying perturbation theory.

Assuming point charge model, the static crystalline

electric potential can be expanded in terms of tensor
operators as:

$$V = \sum_{kq} B_q^k \sum_{i=1}^{N} (C_q^{(k)})_i \qquad (2.4.5)$$

where the summation over k extends in principle from 0 to
∞ and that over q from -k to +k, i is the summation over
the number of electrons in the f-shell and B_q^k are parameters
which can be determined experimentally by finding the best
fit between the experimental and theoretical results. The
tensor operator $C_q^{(k)}$ is related to the spherical harmonics
$Y_{kq}(\theta\Phi)$ by the expression

$$C_q^{(k)} = \left(\frac{4\pi}{2k+1}\right)^{1/2} Y_{kq}(\theta\Phi) \qquad (2.4.6)$$

From equation (2.4.5), it appears that an infinite number
of terms should be considered in the series expansion;
however, for the f^N configuration, no more than fifteen
terms are necessary for evaluation, since the matrix
elements of V will be non-zero only if the following
conditions are satisfied:

K ≤ 6 (Triangle condition for spherical harmonic
integrals.)

K should be even (Parity condition)

m" - m' + q = 0 (otherwise the integral over Φ
part will be zero.)

Once the appropriate form of the crystal field
potential is decided, then the construction of the crystal
field energy matrix can be performed. Under octrahedral,

tetragonal and trigonal symmetries, the crystal field
potentials are

(a) $V_{(O_h)} = \sum_{i=1}^{N} B_o^4 [C_o^{(4)} + \left(\frac{5}{14}\right)^{1/2} \left(C_4^{(4)} + C_{-4}^{(4)}\right)] +$

$$B_o^6 [C_o^{(6)} - (\frac{7}{2})^{1/2} (C_4^{(6)} + C_{-4}^{(6)})]_i$$

where $B_4^4 = (\frac{5}{14})^{1/2} B_o^4$ and $B_4^6 = -(\frac{7}{2})^{1/2} B_o^6$.

(b) $V(C_{4v}) = \sum_{i=1}^{N} [B_o^2 C_o^{(2)} + B_o^4 C_o^{(4)} + B_4^4 (C_4^{(4)} + C_{-4}^{(4)})$

$$+ B^6 C_o^{(6)} + B_4^6 (C_4^{(6)} + C_{-4}^{(6)})]_i$$

(c) $V(C_{3v}) = \sum_{i=1}^{N} [B_o^2 C_o^{(2)} + B_o^4 C_o^{(4)} + B_3^4 (C_{-3}^{(4)} - C_3^{(4)})$

$$+ B_o^6 C_o^{(6)} + B_3^6 (C_{-3}^{(6)} - C_3^{(6)})$$

$$+ B_6^6 (C_{-6}^{(6)} + C_6^{(6)})]_i$$

From the above expressions, one can notice that only two
B_q^k parameters are to be determined in the case of O_h
symmetry, five for C_{4v} and six for C_{3v} symmetry.

From group theory considerations, one can infer

the number of components into which a "free ion" energy level under the crystalline environment of definite symmetry will split. The crystal field split levels may be designated by the appropriate irreducible representations. Under O_h, C_{4v} and C_{3v} symmetries, the number of levels and the combinations of irreducible representation for Pr^{+3} and Er^{+3} ions are given in Tables 2.2 to 2.7, respectively.

The crystal field energy matrices can be calculated in terms of a basis $|\alpha SLJ^\delta \Gamma_r\rangle$ involving the irreducible representation $^\delta \Gamma_r$ of the point groups. The irreducible representation or the crystal quantum number $\mu = |q|$ can be used as good quantum numbers as the $\alpha SLJJ_z$ scheme can usually no longer adequately specify the states.

By employing the tensor operator techniques (10,15,24-28) the matrix elements of the crystalline potential V for the f^N configuration can be expressed as

$$\langle f^N \alpha SLJJ_z \,|v|\, f^N \alpha' SL'J'J_z' \rangle$$

$$= \sum_{k,q} B_q^k \langle f^N \alpha SLJJ_z \,|\, \sum_{i=1}^{N} (C_q^{(k)})_i \,|\, f^N \alpha' S\, L'J'J_z'\rangle$$

$$= \sum_{k,q} B_q^k \langle f^N \alpha SLJJ_z \,|\, C_q^{(k)}(1) + C_q^{(k)}(2) + \ldots + C_q^{(k)}(N) \,|\, f^N \alpha' S\, L'\, J'J_z'\rangle \times$$

$$\langle f\|C^{(k)}\|f\rangle$$

$$= \sum_{k,q} B_q^k \langle f^N \alpha SLJJ_z \,|U_q^{(k)}|\, f^N \alpha' SL'J'J_z'\rangle \times \langle f\|C^{(k)}\|f\rangle \qquad (2.4.7)$$

TABLE 2.2

Splitting of Levels of Pr^{+3} Under O_h Symmetry

J	2J + 1	Irreducible Representations	No. of Levels
0	1	$^1\Gamma_1$	1
1	3	$^3\Gamma_4$	1
2	5	$^2\Gamma_3 + {}^3\Gamma_5$	2
3	7	$^1\Gamma_2 + {}^3\Gamma_4 + {}^3\Gamma_5$	3
4	9	$^1\Gamma_1 + {}^2\Gamma_3 + {}^3\Gamma_4 + {}^3\Gamma_5$	4
5	11	$^2\Gamma_3 + 2{}^3\Gamma_4 + {}^3\Gamma_5$	4
6	13	$^1\Gamma_1 + {}^1\Gamma_2 + {}^2\Gamma_3 + {}^3\Gamma_4 + 2{}^3\Gamma_5$	6

TABLE 2.3

Splitting of Levels of Pr^{+3} Under C_{4v} Symmetry

J	2J + 1	Irreducible Representations	No. of Levels
0	1	$^1\Gamma_1$	1
1	3	$^1\Gamma_2 + {}^2\Gamma_5$	2
2	5	$^1\Gamma_1 + {}^1\Gamma_3 + {}^1\Gamma_4 + {}^2\Gamma_5$	4
3	7	$^1\Gamma_2 + {}^1\Gamma_3 + {}^1\Gamma_4 + 2{}^2\Gamma_5$	5
4	9	$2{}^1\Gamma_1 + {}^1\Gamma_2 + {}^1\Gamma_3 + {}^1\Gamma_4 + 2{}^2\Gamma_5$	7
5	11	$^1\Gamma_1 + 2{}^1\Gamma_2 + {}^1\Gamma_3 + {}^1\Gamma_4 + 3{}^2\Gamma_5$	8
6	13	$2{}^1\Gamma_1 + {}^1\Gamma_2 + 2{}^1\Gamma_3 + 2{}^1\Gamma_4 + 3{}^2\Gamma_5$	10

TABLE 2.4

Splitting of Levels of Pr^{+3} Under C_{3v} Symmetry

J	2J + 1	Irreducible Representations	No. of Levels
0	1	$^1\Gamma_1$	1
1	3	$^1\Gamma_2 + {}^2\Gamma_3$	2
2	5	$^1\Gamma_1 + 2{}^2\Gamma_3$	3
3	7	$^1\Gamma_1 + 2{}^1\Gamma_2 + 2{}^2\Gamma_3$	5
4	9	$2{}^1\Gamma_1 + {}^1\Gamma_2 + 3{}^2\Gamma_3$	6
5	11	$^1\Gamma_1 + 2{}^1\Gamma_2 + 4{}^2\Gamma_3$	7
6	13	$3{}^1\Gamma_1 + 2{}^1\Gamma_2 + 4{}^2\Gamma_3$	9

TABLE 2.5

Splitting of Energy Levels of the Er^{+3} Ion

Under O_h Symmetry

J	$2J + 1$	Irreducible Representations	No. of Levels
1/2	2	$^2\Gamma_6$	1
3/2	4	$^4\Gamma_8$	1
5/2	6	$^2\Gamma_7 + {}^4\Gamma_8$	2
7/2	8	$^2\Gamma_6 + {}^2\Gamma_7 + {}^4\Gamma_8$	3
9/2	10	$^2\Gamma_6 + 2{}^4\Gamma_8$	3
11/2	12	$^2\Gamma_6 + {}^2\Gamma_7 + 2{}^4\Gamma_8$	4
13/2	14	$^2\Gamma_6 + 2{}^2\Gamma_7 + 2{}^4\Gamma_8$	5
15/2	16	$^2\Gamma_6 + {}^2\Gamma_7 + 3{}^4\Gamma_8$	5

TABLE 2.6

Splitting of Energy Levels of the Er^{+3} Ion

Under C_{4v} Symmetry

J	2J + 1	Irreducible Representations	No. of Levels
1/2	2	$^2\Gamma_6$	1
3/2	4	$^2\Gamma_6 + {}^2\Gamma_7$	2
5/2	6	$^2\Gamma_6 + 2{}^2\Gamma_7$	3
7/2	8	$2{}^2\Gamma_6 + 2{}^2\Gamma_7$	4
9/2	10	$3{}^2\Gamma_6 + 2{}^2\Gamma_7$	5
11/2	12	$3{}^2\Gamma_6 + 3{}^2\Gamma_7$	6
13/2	14	$3{}^2\Gamma_6 + 4{}^2\Gamma_7$	7
15/2	16	$4{}^2\Gamma_6 + 4{}^2\Gamma_7$	8

TABLE 2.7

Splitting of Energy Levels of the Er^{+3} Ion

Under C_{3v} Symmetry

J	2J + 1	Irreducible Representations	No. of Levels
1/2	2	$^2\Gamma_4$	1
3/2	4	$(^1\Gamma_5 + {}^1\Gamma_6) + {}^2\Gamma_4$	2
5/2	6	$(^1\Gamma_5 + {}^1\Gamma_6) + 2{}^2\Gamma_4$	3
7/2	8	$(^1\Gamma_5 + {}^1\Gamma_6) + 3{}^2\Gamma_4$	4
9/2	10	$2(^1\Gamma_5 + {}^1\Gamma_6) + 3{}^2\Gamma_4$	5
11/2	12	$2(^1\Gamma_5 + {}^1\Gamma_6) + 4{}^2\Gamma_4$	6
13/2	14	$2(^1\Gamma_5 + {}^1\Gamma_6) + 5{}^2\Gamma_4$	7
15/2	16	$3(^1\Gamma_5 + {}^1\Gamma_6) + 5{}^2\Gamma_4$	8

where $U_q^{(k)}$ is the sum of N single particle tensor operators. The operators $C_q^{(k)}(1) \ldots C_q^{(k)}(N)$ are the unit tensor operators defined as $C_q^{(k)} = \left(\frac{4\pi}{2k+1}\right)^{1/2} Y_{kq}(\theta\Phi)$ and each of them operates respectively on the corresponding electron orbital. The quantity

$$\langle \ell \| C^{(k)} \| \ell \rangle = (-1)^{\ell} [(2\ell + 1)(2\ell' + 1)]^{1/2} \begin{pmatrix} \ell & k & \ell' \\ o & o & o \end{pmatrix} \quad (2.4.8)$$

or

$$\langle 3 \| C^{(k)} \| 3 \rangle = (-1)^3 [7 \times 7]^{1/2} \begin{pmatrix} 3 & k & 3 \\ o & o & o \end{pmatrix}$$

Since the matrix elements of the tensor operators are diagonal in the spin and by using Wigner-Eckert theorem, equation (2.4.7) can be further simplified as

$$\langle f^N \alpha S L J J_z | U_q^{(k)} | f^N \alpha' S L' J' J_z' \rangle = (-1)^{J-J_z} \begin{pmatrix} J & K & J' \\ -J_z & q & J_z' \end{pmatrix} \times$$

$$\langle f^N \alpha S L J \| U^{(k)} \| f^N \alpha' S L' J' \rangle \quad (2.4.9)$$

where

$$\langle f^N \alpha S L J \| U^{(k)} \| f^N \alpha' S L' J' \rangle = (-1)^{S+L+J'+K} [(2J+1)(2J'+1)]^{1/2} \times \begin{Bmatrix} J & J' & K \\ L' & L & S \end{Bmatrix}$$

$$\langle f^N \alpha S L \| U^{(k)} \| f^N \alpha' S L \rangle \quad (2.4.10)$$

The doubly reduced matrix elements of $U^{(k)}$ have been tabulated by Nielson and Koster (19) or they can be calculated by using the coefficients of fractional-

parentage (e.g. equation 2-92 of reference (15) can be used).

The values of 3-j ( ) and 6-j $\{ \}$ symbols are also made available by Rotenberg et al (20). As all the quantities in the above equations are known, except B_q^k's which are treated as parameters to be determined experimentally, hence one can calculate the matrix elements of the crystal field potential V.

Margolis (29) has diagonalized the complete crystal field energy matrices for $4f^2$ configuration including the effects of intermediate coupling and the crystal field mixing of the free ion levels. In order to get better agreement between the experimental and theoretical results, recently Carnall et al (30) have made calculations including configuration interaction for LaF_3Er^{+3} and $ErCl_3 \cdot 6H_2O$.

2.5 Intensity and Transition Selection Rules for Rare Earth Ions in Crystals

Intensity of a spectral line emitted from a state $|\alpha J J_z \rangle$ to state $| \alpha'J'J_z' \rangle$ depends upon (1) the transition probability $T(\alpha J J_z, \alpha'J'J_z')$, (2) $\bar{\nu}$ the wavenumber of the transition, and (3) the number of atoms $N(\alpha J J_z)$ in the state $| \alpha J J_z \rangle$.

i.e. $I(\alpha J J_z, \alpha'J'J_z') = N(\alpha J J_z) hc\bar{\nu} T(\alpha J J_z; \alpha'J'J_z')$.

The total transition probability between two states is determined by the following three probabilities:

$$T_{Dipole} = \frac{64\pi^4}{3h}\, \bar{\nu}^3 \; | \; \langle \alpha J J_z | P | \alpha' J' J'_z \rangle |^2$$

$$T_{Mag} = \frac{64\pi^4}{3h}\, \bar{\nu}^3 \; | \; \langle \alpha J J_z | M | \alpha' J' J'_z \rangle |^2$$

$$T_{Quad} = \frac{32\pi^6}{5h}\, \bar{\nu}^5 \; | \; \langle \alpha J J_z | Q | \alpha' J' J'_z \rangle |^2$$

where P, M and Q are the electric dipole, magnetic dipole and electric quadrupole moments operators, respectively. h is Planck's constant and $\bar{\nu}$ is the wavenumber, corresponding to the transition.

Within the same configuration, for a free ion the electric dipole transitions are parity forbidden, so the transitions are made possible through the magnetic dipole and electric quadrupole. However, when the rare earth ion is placed into the composition of a crystal lattice, the electric dipole transition within f^N configuration becomes allowed through the mixing of states of opposite parity (31,32).Recent studies have indicated that for rare earth ions in crystal, electric dipole type transitions are predominant. Van Vleck (31) and Hoogschagen et al (32) have found that the intensity of quadrupole emission is less than the intensity of magnetic dipole emission, while the intensity of electric dipole emission is noticeably greater than the previous two. Hence, in the present work, only the electric dipole transition will be considered for the Pr^{+3} and Er^{+3} in the matrices of CaF_2. Carnall

et al (34), Rahman (35) have treated the optical emission intensity for Er^{+3} ion in different host lattices. The transition probability can also be written in terms of the oscillator strength $f(\alpha J, \alpha' J')$;

$$T(\alpha J J_z, \alpha' J' J_z') = \frac{8\pi^2 e^2 \bar{\nu}^2}{mc^3} f(\alpha J, \alpha' J')$$

where

$$f(\alpha J, \alpha' J') = \frac{8\pi^2 mc}{3e^2 h\lambda} \frac{S(\alpha J; \alpha' J')}{2J + 1}$$

λ is the wavelength in A° and $S(\alpha J, \alpha' J')$ is the line-strength. For electric dipole transitions, the line strength has been given (15) as

$$S^{1/2}(\alpha J; \alpha' J') = (-1)^{J+L'+S+1} [(2J+1)(2J'+1)]^{1/2} \times \begin{Bmatrix} J & 1 & J' \\ L' & S & L \end{Bmatrix} \times$$

$$[-e\langle \alpha SL \| \sum_i r_i C_i^{(1)} \| \alpha' SL' \rangle]$$

As pointed out previously, for a free ion, electric dipole transitions within the same configuration are parity forbidden, and thus any explanation of the observed spectra of inter configuration of crystals must concern itself with noncentro-symmetric interactions. Oflet et al (33) have derived selection rules which can be applied to crystal spectra. These rules are as follows:

$$\Delta\ell = \pm 1, \quad \Delta S = 0, \quad \Delta L \leq 2\ell \; ; \quad \Delta J \leq 6$$

The first selection rule means that the f^N configuration can interact only with $4f^{N-1}5d$ or $4f^{N-1}5g$ configuration. In case of strong spin-orbit interaction, the second and

third selection rules may break down and for practical

purposes only the fourth selection rule holds.

Since the stark-split components of the crystal

spectra are also labelled by the crystal quantum number

or by irreducible representation of a symmetry group,

additional selection rules other than the ones given above

are needed for the analysis of crystal spectra. It is

known that the transition between two states is allowed

if the direct product $\Gamma_i \times \Gamma_o \times \Gamma_f$ contains the identity

representation $\cdot \Gamma_1$. Here Γ_o is the representation to

which the particular transformation operator belongs,

Γ_i and Γ_f are the initial and final states, respectively.

The allowed transitions for Pr^{+3} and Er^{+3} in some

symmetries are given in Tables 2.8 to 2.13.

2.6 Configuration Interaction

For a given configuration, the energy levels

obtained by the diagonalization of the combined electro-

static and spin-orbit interactions, usually deviate

considerably from the observed energy levels(22,36-40). This

difference is attributed to the configuration interaction.

The configuration interaction has been divided into two

types: (a) strong configuration interaction, and (b) weak

configuration interaction depending upon the strength of

the Coulomb field between the perturbed and perturbing

configurations. For strong configuration interaction,

all the electrostatic interactions within and between the

TABLE 2.8

Electric Dipole Transition and Polarization
for Er^{+3} Under O_h Symmetry

	Γ_6	Γ_7	Γ_8
Γ_6	a	f	a
Γ_7	f	a	a
Γ_8	a	a	a

TABLE 2.9

Electric Dipole Transition and Polarization
for Er^{+3} Under C_{3v} Symmetry

	Γ_4	$(\Gamma_5 + \Gamma_6)$
Γ_4	a π σ	a σ
$(\Gamma_5 + \Gamma_6)$	a σ	f π

a   Allowed Transition
f   Forbidden Transition
π, σ Respective Polarization

TABLE 2.10

Electric Dipole Transition and Polarization

for Er^{+3} Under C_{4v} Symmetry

	Γ_6	Γ_7
Γ_6	$a\ \begin{matrix}\pi\\\sigma\end{matrix}$	$a\ \sigma$
Γ_7	$a\ \sigma$	$a\ \begin{matrix}\pi\\\sigma\end{matrix}$

TABLE 2.11

Electric Dipole Transition and Polarization

For Pr^{+3} Under O_h Symmetry

	Γ_1	Γ_2	Γ_3	Γ_4	Γ_5
Γ_1	f	f	f	a	f
Γ_2	f	f	f	f	a
Γ_3	f	f	f	a	a
Γ_4	a	f	a	a	a
Γ_5	f	a	a	a	a

TABLE 2.12

Electric Dipole Transition and Polarization

For Pr^{+3} Under C_{3v} Symmetry

	Γ_1	Γ_2	Γ_3
Γ_1	a^{π}	f	a^{σ}
Γ_2	f	a^{π}	a^{σ}
Γ_3	a^{σ}	a^{σ}	a^{π}_{σ}

TABLE 2.13

Electric Dipole Transition and Polarization

For Pr^{+3} Under C_{4v} Symmetry

	Γ_1	Γ_2	Γ_3	Γ_4	Γ_5
Γ_1	a^{π}	f	f	f	a^{σ}
Γ_2	f	a^{π}	f	f	a^{σ}
Γ_3	f	f	a^{π}	f	a^{σ}
Γ_4	f	f	f	a^{π}	a^{σ}
Γ_5	a^{σ}	a^{σ}	a^{σ}	a^{σ}	a^{π}

connected configurations are taken into account, but the effect of weak configuration interaction can be considered by modifying the energy matrices of the principal electron configuration. The resultant eigenvectors obtained by diagonalization can be expressed in terms of linear combination of the states of the connected configurations.

In the case of free ion, configuration interaction occurs between the configurations of the same parity. Crystal field couples configurations of both parities and it introduces an additional configuration mixing. Using the second order perturbation, Wybourne and Rajnak (41) have calculated the correction factor which is to be added to each electrostatic matrix element; i.e.

$$\Delta C(\alpha LS; \alpha'LS) = \sum_k P^k \langle f^N \alpha LS | \sum_{i>j}^N (U_i^{(k)} \cdot U_j^{(k)}) | f^N \alpha'LS \rangle$$

where P^k are the parameters depending on the radial integrals and the excitation energy. For even values of k the effect has been included in the Slater radial integrals, but for odd k's the correction factor is modified as

$$\delta(\alpha LS; \alpha'LS) [\alpha L(L + 1) + \beta G(G_2) + \gamma G(R_7)]$$

where α, β and γ are linear combinations of radial integrals and are treated as adjustable parameters which can be determined from the experimental results. $G(G_2)$ and $G(R_7)$ are the eigenvalues of Casimir's operators (10) for the groups G_2 and R_7, which are used to classify the states

of the f^N configuration.

   Eisentein (42-44) has shown that a single set of crystal field parameters is not sufficient for calculating the crystal field levels for the whole spectrum. The discrepancy is due to the configuration interaction as the crystal field parameters do change due to the configuration interaction (45). The influence of configuration interaction is taken into account by replacing each matrix element of the crystal field potential

$$\langle f^N \alpha SLJJ_z | B_q^k C_q^{(k)} | f^N \alpha'SL'J'J_z' \rangle$$

by

$$(1 + \Delta c) \langle f^N \alpha SLJJ_z | B_q^k C_q^{(k)} | f^N \alpha'SL'J'J_z' \rangle$$

where Δc is the correction factor due to configuration interaction. The correction factor consists of two parts, one part corresponds to the configuration mixing purely by the crystal field and the second part corresponds to an electrostatically correlated crystal field interaction. Both these parts have been defined in equations (6) and (7) of reference (46). Recently, W. T. Carnall et al (33) have considered the effect of configuration interaction in the case of LaF_3Er^{+3} and $ErCl_36H_2O$ and have improved the agreement between the experimental and theoretical results.

Chapter 3   EXPERIMENTAL

3.1   Excitation Spectra of CaF_2Er^{+3} and CaF_2Pr^{+3}

The crystals used in the present work were obtained from the Harshaw Chemical Company and from Optovac Inc. The exciting light from a 1000 watt xenon lamp, Oriel Model C-60-50, was focussed on the entrance slit of a 1 meter McPherson 225 monochromator (for a detailed description, see section 4.1). The light source has a continuum from 2000 $\overset{o}{A}$ to 6000 $\overset{o}{A}$ as shown in Fig. 3.1.

TYPICAL RELATIVE EMISSION
SPECTRUM FROM XENON LAMPS

WAVELENGTH (Angstroms)
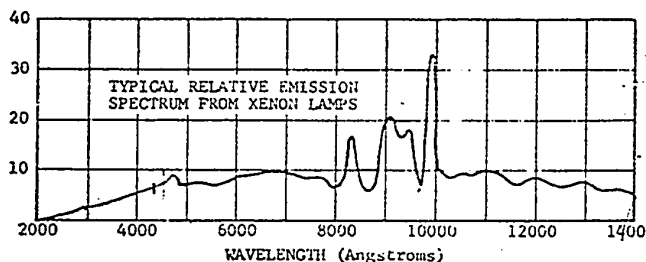
Fig. 3.1   Xenon continuum from 2000
           to 6000 .

A crystal 12 x 8 x 2 mm was placed in the crystal
holder of a custom built Andonian vacuum cryostat fitted
with a copper-constant thermocouple for recording the
temperature of the crystal. The light coming out from the
exit slit of the monochromator was focussed on the large
face of the crystal facing the monochromator. The other
face (12 x 8 mm) of the crystal was facing the entrance
slit of the home made grating spectrograph with a low f-
number about 2.5 and of medium resolution; i.e., better
than 0.5 Å in the first order. The entrance slit of the
spectrograph was always kept at 0.3 mm. A photomultiplier
tube, type 9514S, supplied by the McPherson Company, was
fixed on the exit slit of the spectrograph. The photo-
current from the photomultiplier was fed to a Keithley
410 micro-microammeter, the output of which was recorded
by a strip chart recorder model 7128A supplied by Hewlett-
Packard. The experimental set-up is shown in Fig. 3.2.

The home-made spectrograph was set for the green
spectral region for CaF_2Er^{+3} (0.1 %). The excitation
spectrum in the range 2000 Å to 5500 Å was recorded at
room and at liquid nitrogen temperatures. The experiment
was performed with crystals obtained from Optov Inc. and
Harshaw Chemical Co.   The results were identical in both
cases except that the intensity of some of the components
were strong in one sample and weak in the other sample (Fig. 3.15,
3.18,3.20,3.21). One energy level, $^4D_{5/2}$ at 2600 Å, was
absent in the sample obtained from Optov Inc. A complete
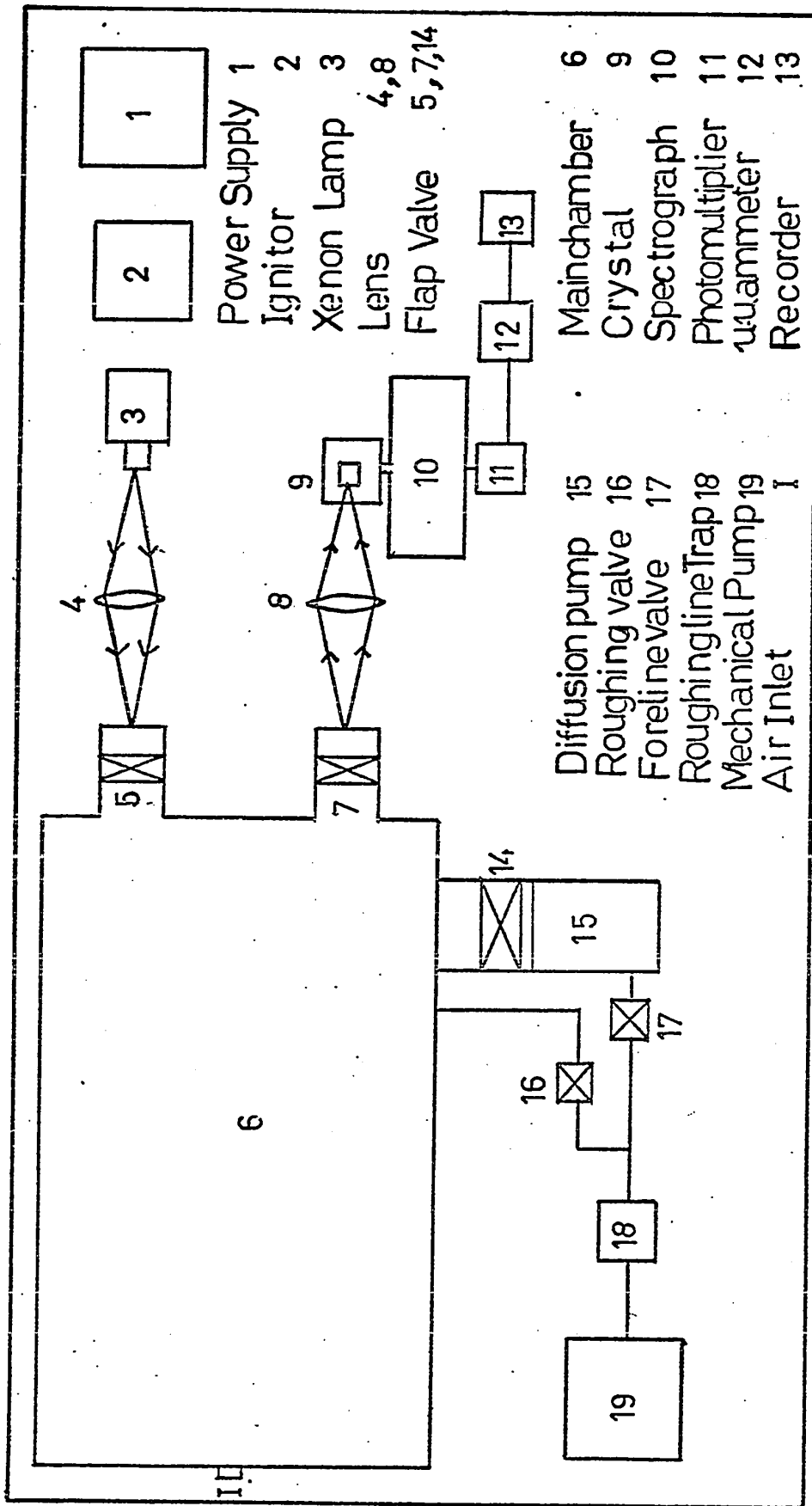
Fig. 3.2 Experimental set-up for excitation spectrum.

Power Supply 1
Ignitor 2
Xenon Lamp 3
Lens 4,8
Flap Valve 5,7,14

Mainchamber 6
Crystal 9
Spectrograph 10
Photomultiplier 11
μμammeter 12
Recorder 13

Diffusion pump 15
Roughing valve 16
Foreline valve 17
Roughling Trap 18
Mechanical Pump 19
Air Inlet I

43

excitation spectrum of CaF_2Er^{+3} (0.1 %) from 3000 Å to

5500 Å at LNT is shown in Fig. 3.3, and its SLJ assignments

are in accordance with reference (1). The results for

individual groups, at RT and at LNT, are shown in figs. 3.4

to 3.19 . Peaks are numbered for future use and their

energy has been expressed in cm^{-1} in Table 3.2.A summary

of these figures, along with their experimental conditions,

is presented in Table 3.1.

For recording the excitation spectrum of CaF_2Pr^{+3}

(0.1 %), the home-made spectrograph was set for the blue

green spectral region. The complete excitation spectrum

of CaF_2Pr^{+3} from 3400 Å to 4500 Å at LNT is shown in Fig.

3.23. The SLJ assignments are made in accordance with

energy levels in aqueous solution (2). The results for

individual groups at LNT and RT are shown in Figs. 3.24 to

3.28. The experiment was repeated with different

concentrations of the Pr^{+3} ion in the CaF_2 crystal and

we found that the intensity decreased with increasing

concentration of the Pr^{+3} ion. Peaks are numbered for

future use and their energies have been expressed in cm^{-1}

in Table 3.4.A summary of these figures, along with their

experimental conditions, is presented in Table 3.3.

3.2 Emission Spectra of CaF_2Er^{+3} and CaF_2Pr^{+3}

For photographing the emission spectra of CaF_2Er^{+3}

and CaF_2Pr^{+3}, the experimental set-up was the same as shown

in Fig. 3.2, except that the photomultiplier was replaced
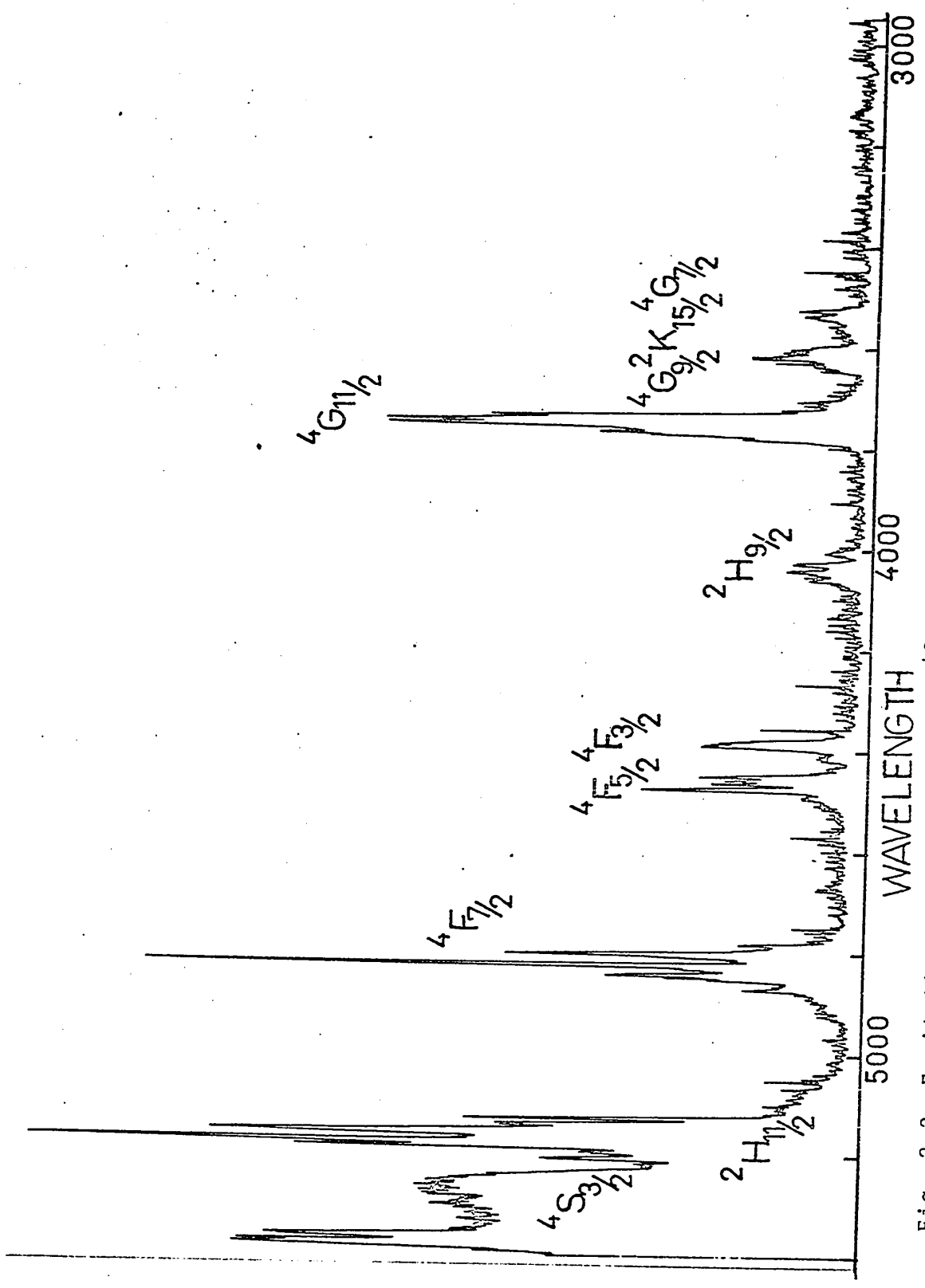
Fig. 3.3 Excitation spectrum of CaF_2 Er^{+3} at LNT from 3000 Å to 5400 Å.

TABLE 3.1

Summary of the Figures Regarding the Excitation Spectrum of CaF_2Er^{+3}

Fig. No.	Crystal	Temperature	Spectral Range
3.4	As-received crystal (Optovac)	RT	5250 Å to 5500 Å
3.5	"	"	5100 Å to 5250 Å
3.6	"	"	4800 Å to 4900 Å
3.7	"	"	4350 Å to 4600 Å
3.8	"	"	4000 Å to 4150 Å
3.9	"	"	3720 Å to 3820 Å
3.10	"	"	3450 Å to 3700 Å
3.11	"	"	2200 Å to 3200 Å
3.12	"	LNT	5250 Å to 5500 Å
3.13	"	"	5100 Å to 5250 Å
3.14	"	"	4800 Å to 4900 Å
3.15	"	"	4350 Å to 4550 Å
3.16	"	"	4000 Å to 4100 Å
3.17	"	"	3720 Å to 3820 Å
3.18	"	"	3450 Å to 3650 Å
3.19	"	"	2200 Å to 3200 Å
3.20	As-received crystal (Harshaw)	"	4350 Å to 4550 Å
3.21	"	"	3500 Å to 3650 Å
3.22	"	"	2200 Å to 3200 Å
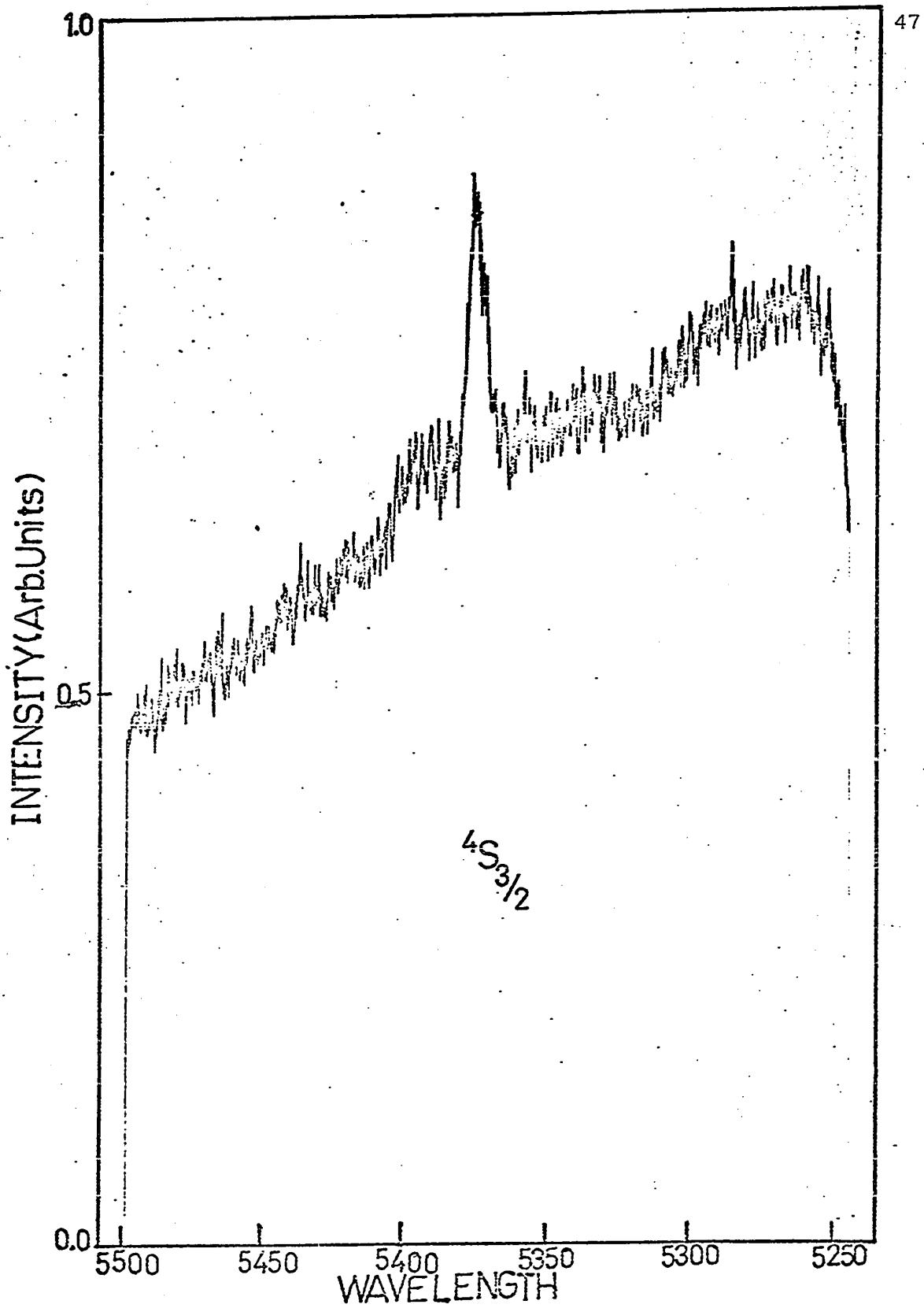
Fig. 3.4 Excitation spectrum of CaF_2Er^{+3} at RT from 5250 Å to 5500 Å.
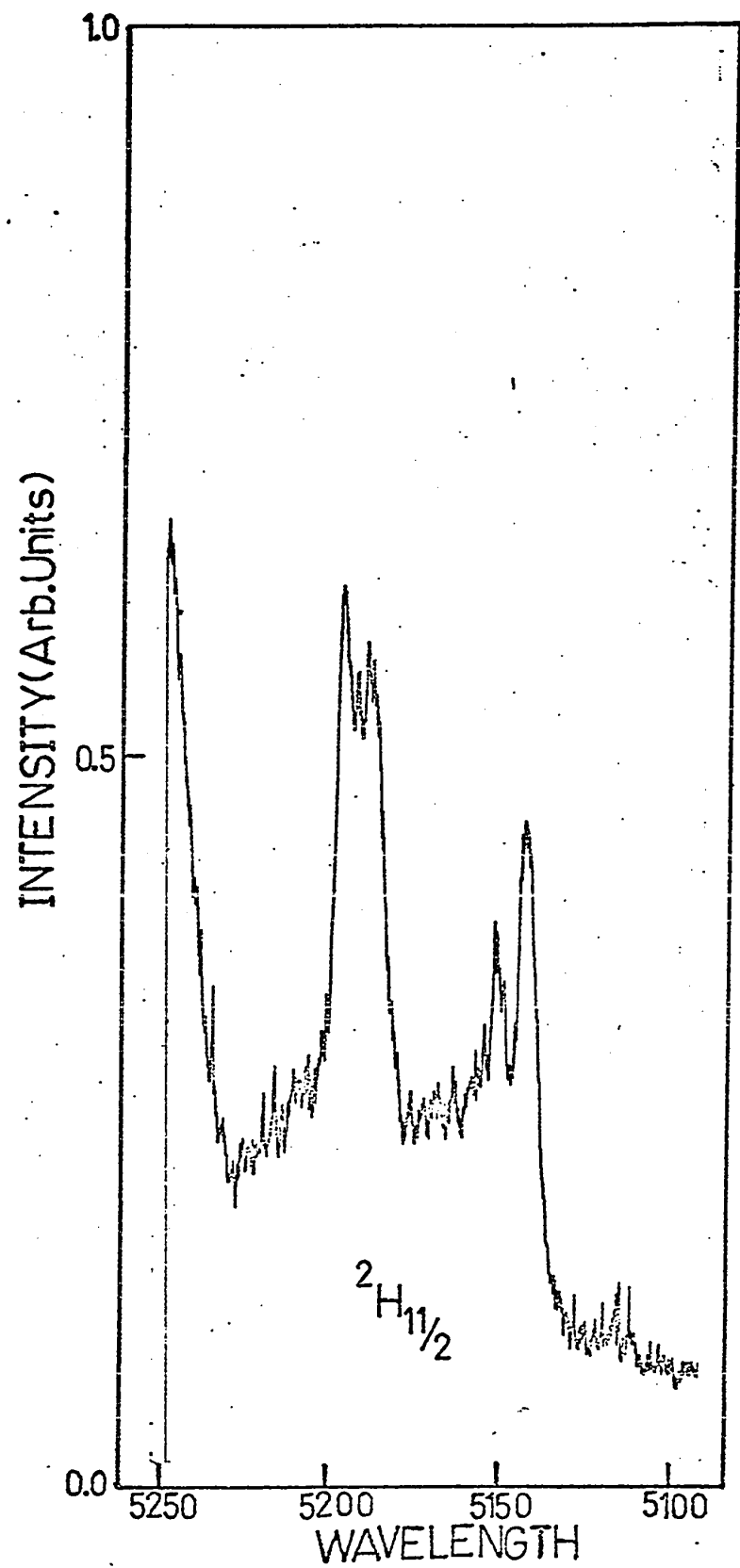
Fig. 3.5 Excitation spectrum of CaF_2Er^{+3} at RT from 5100 Å to 5250 Å.
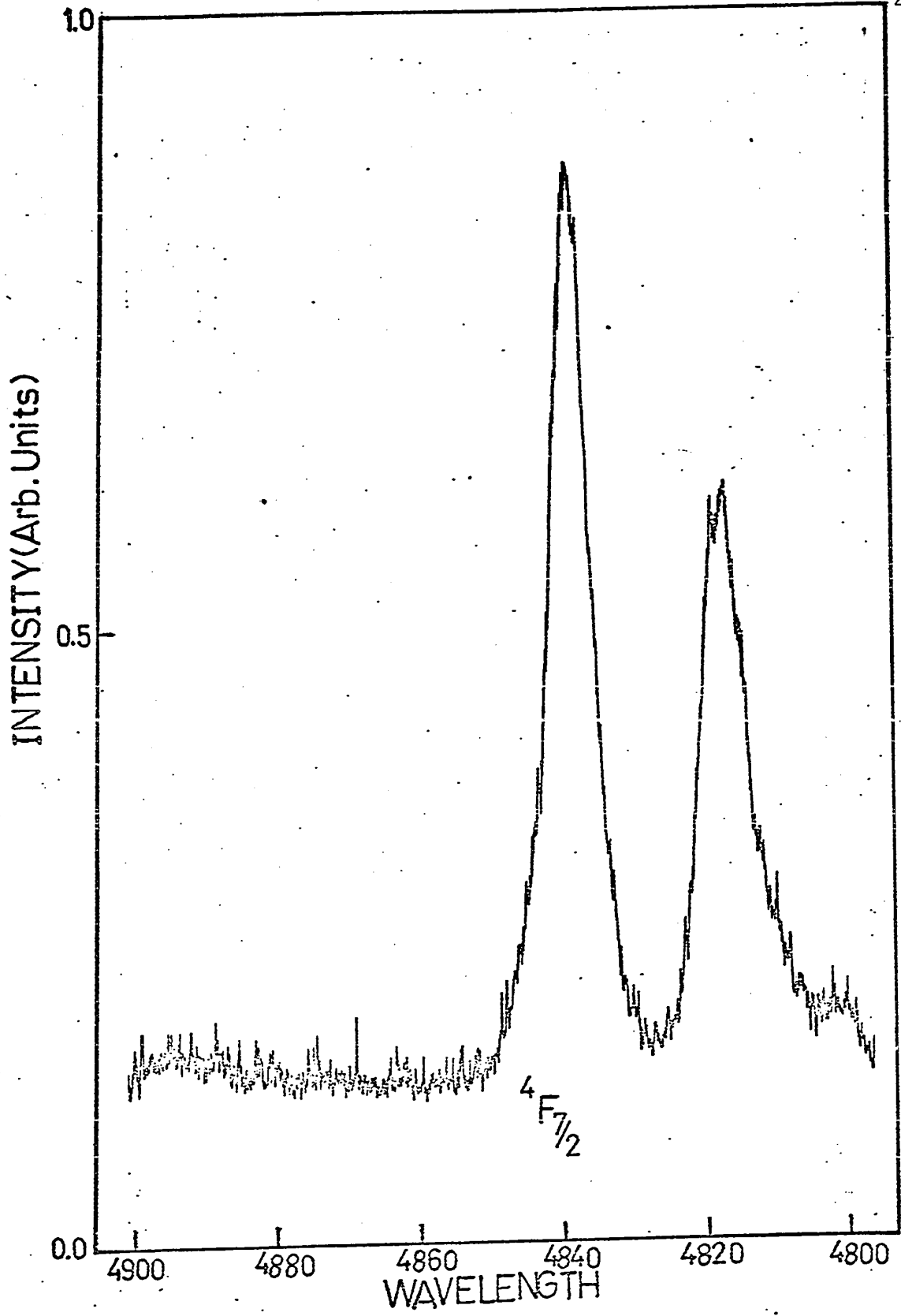
Fig. 3.6 Excitation spectrum of CaF_2Er^{+3} at RT from 4800 Å to 4900 Å.
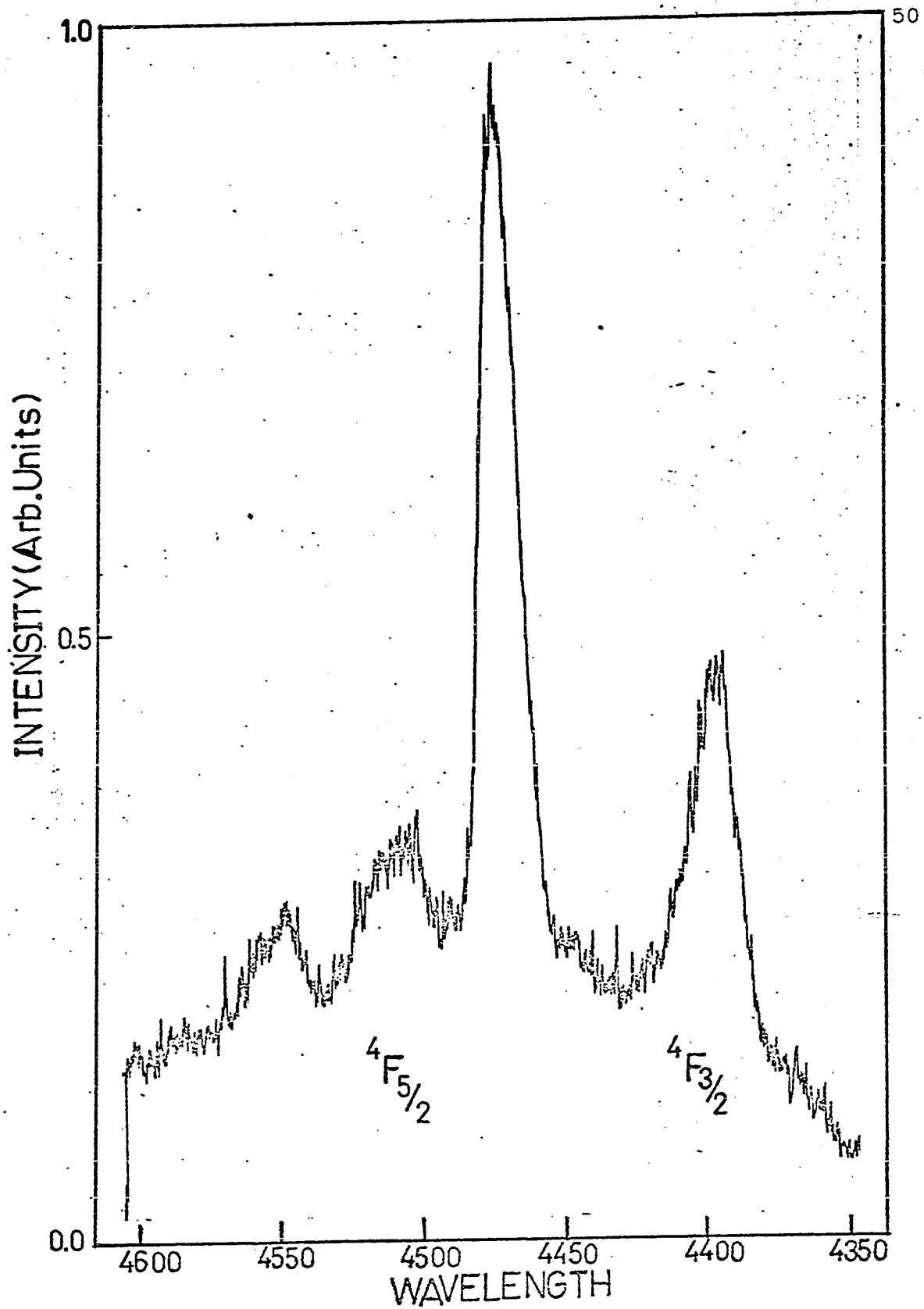
Fig. 3.7 Excitation spectrum of CaF_2Er^{+3} at RT from 4350 Å
to 4600 Å.
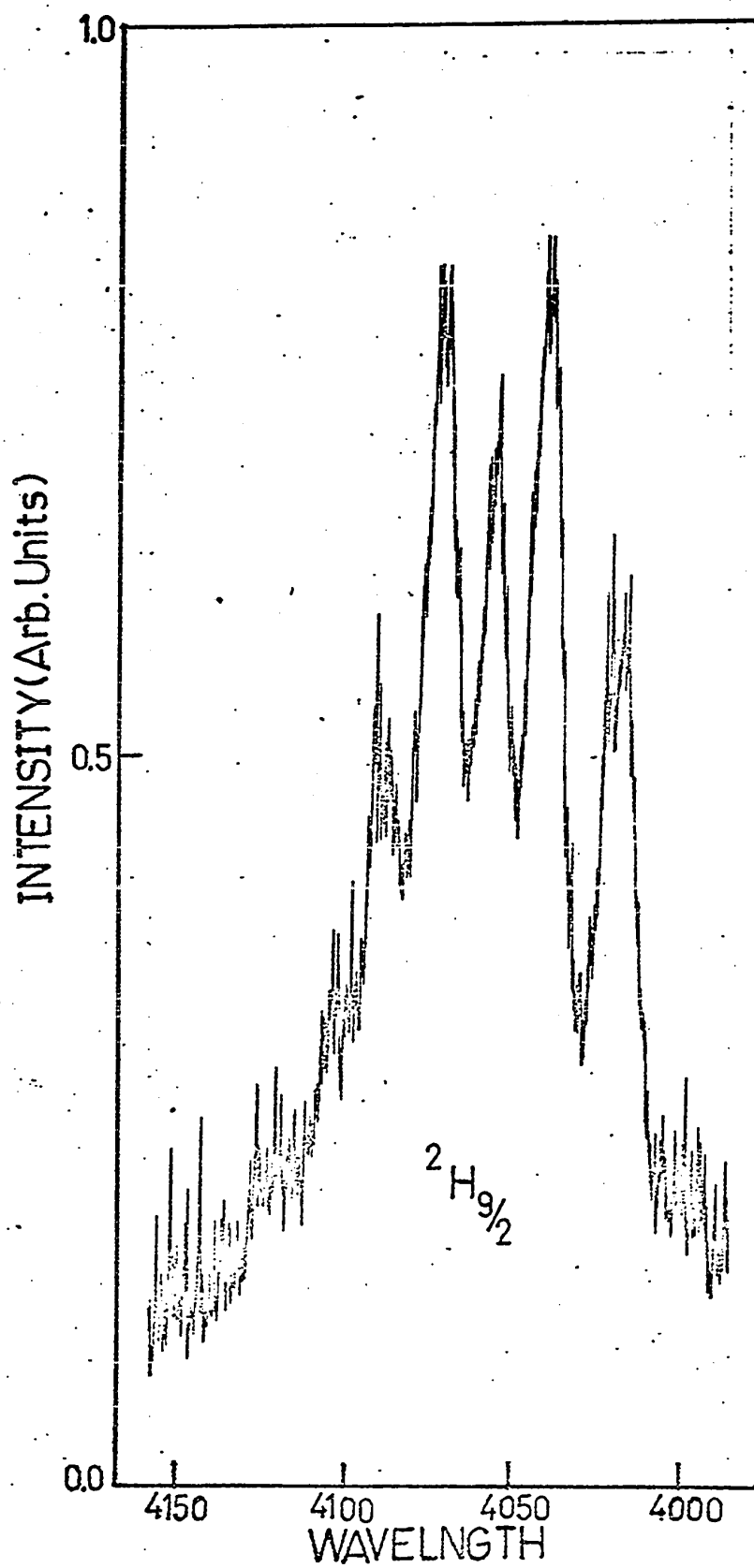
Fig. 3.8 Excitation spectrum of CaF_2Er^{+3} at RT from 4000 Å to 4150 Å.
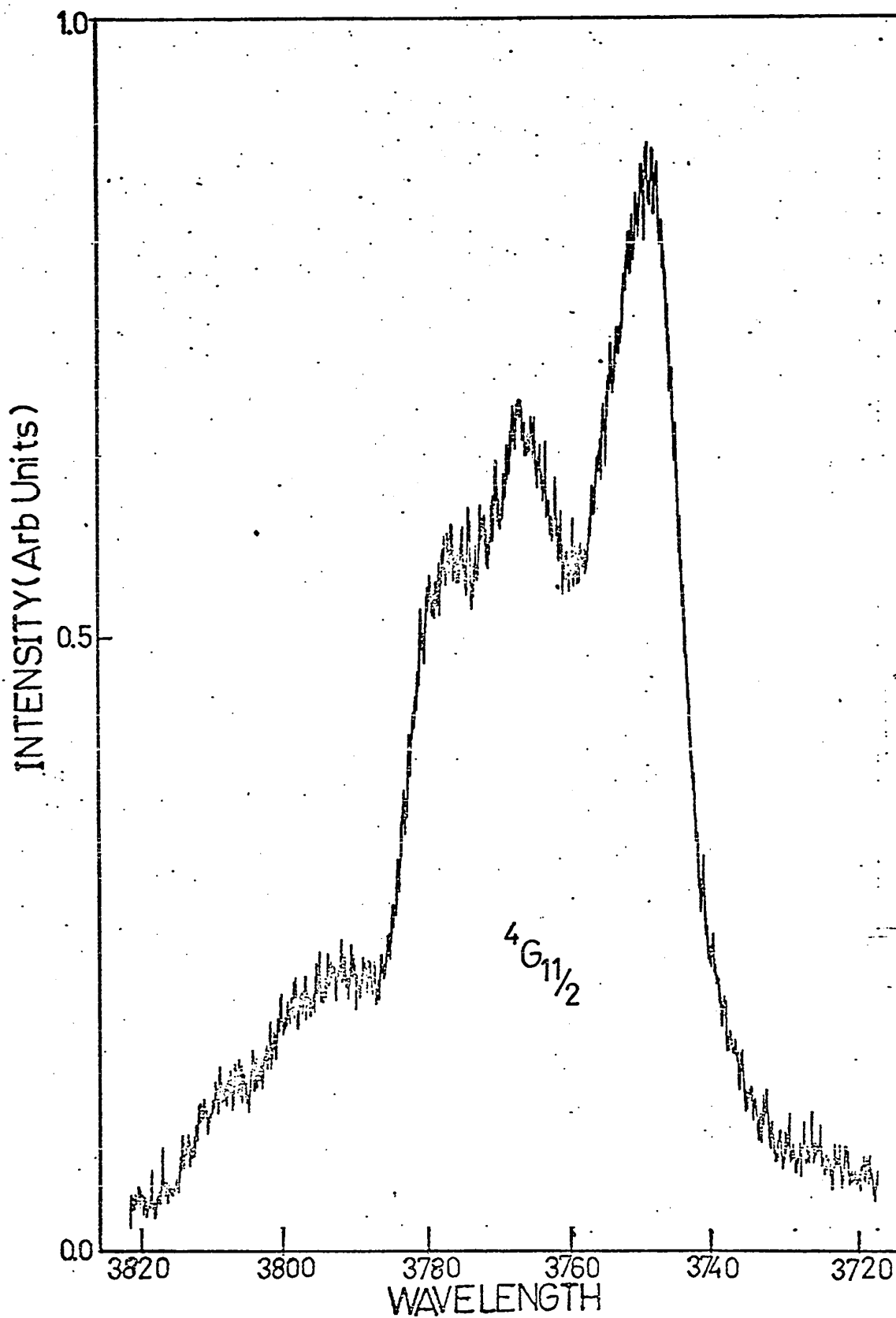
Fig. 3.9 Excitation spectrum of CaF_2Er^{+3} at RT from 3720 Å to 3820 Å.
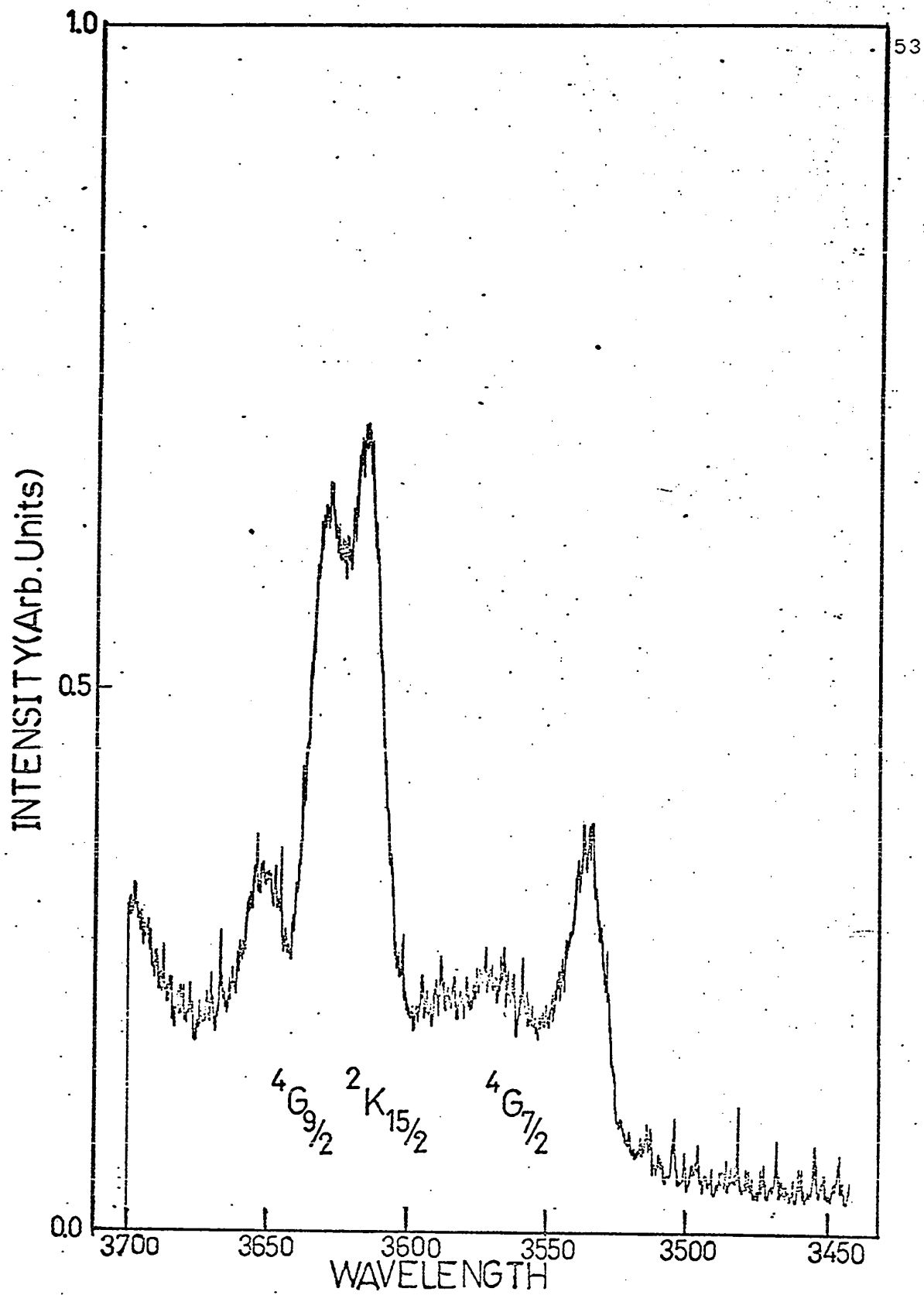
Fig. 3.10   Excitation spectrum of CaF_2Er^{+3} at RT from 3450 Å to 3700 Å.
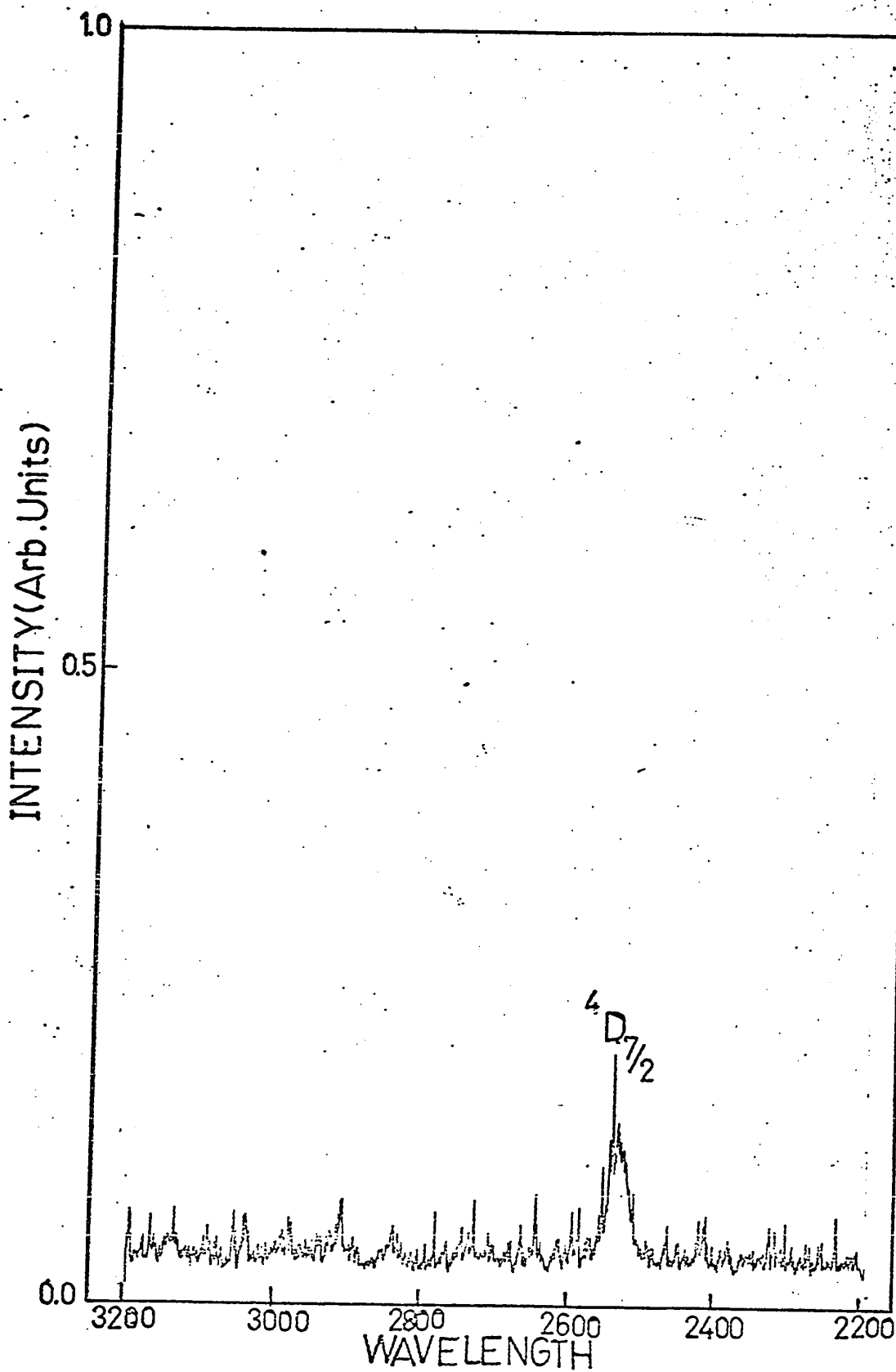
Fig. 3.11 Excitation spectrum of CaF_2Er^{+3} at RT from 2200 Å to 3200 Å.
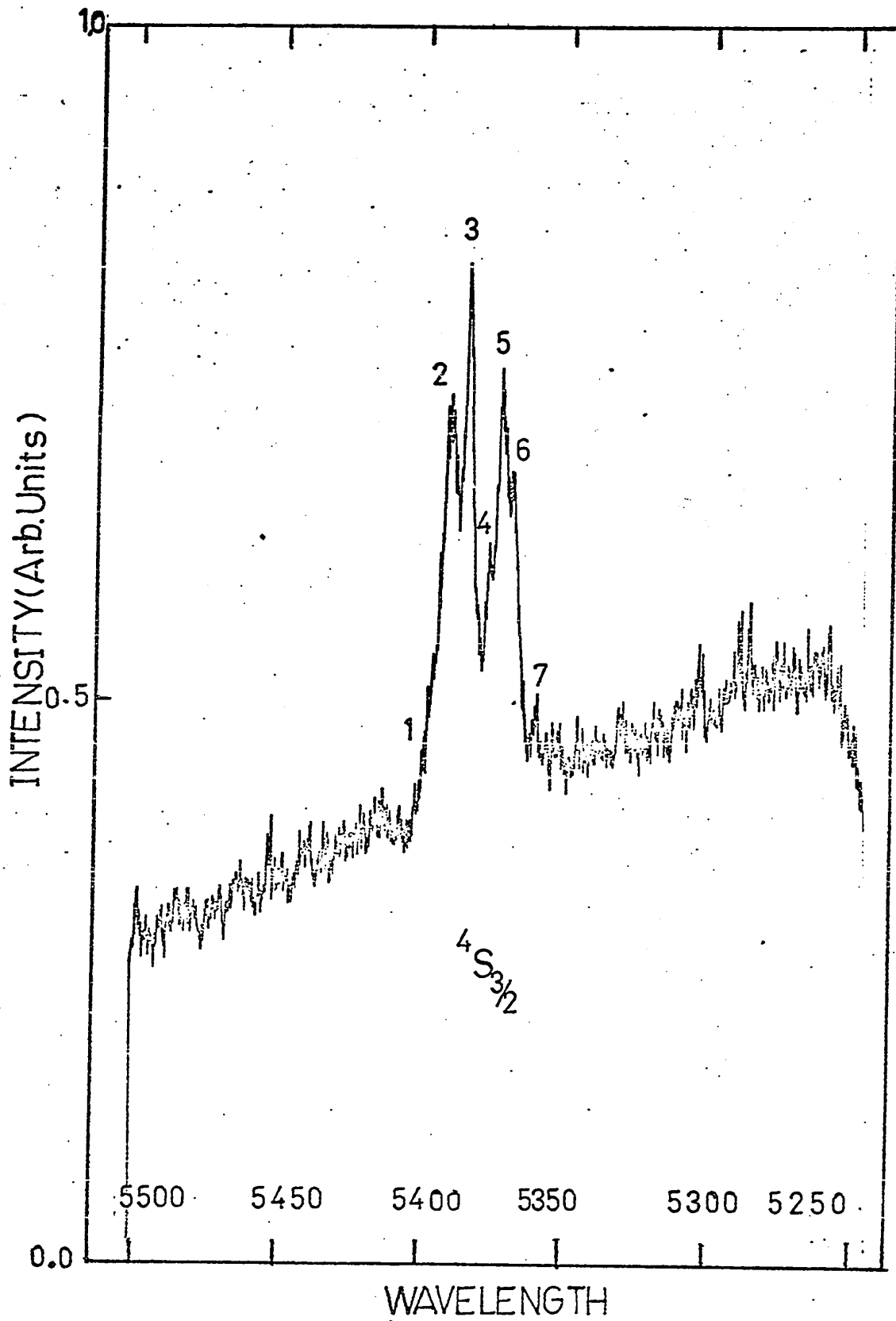
Fig. 3.12 Excitation spectrum of CaF_2Er^{+3} at LNT from 5250 Å to 5500 Å.
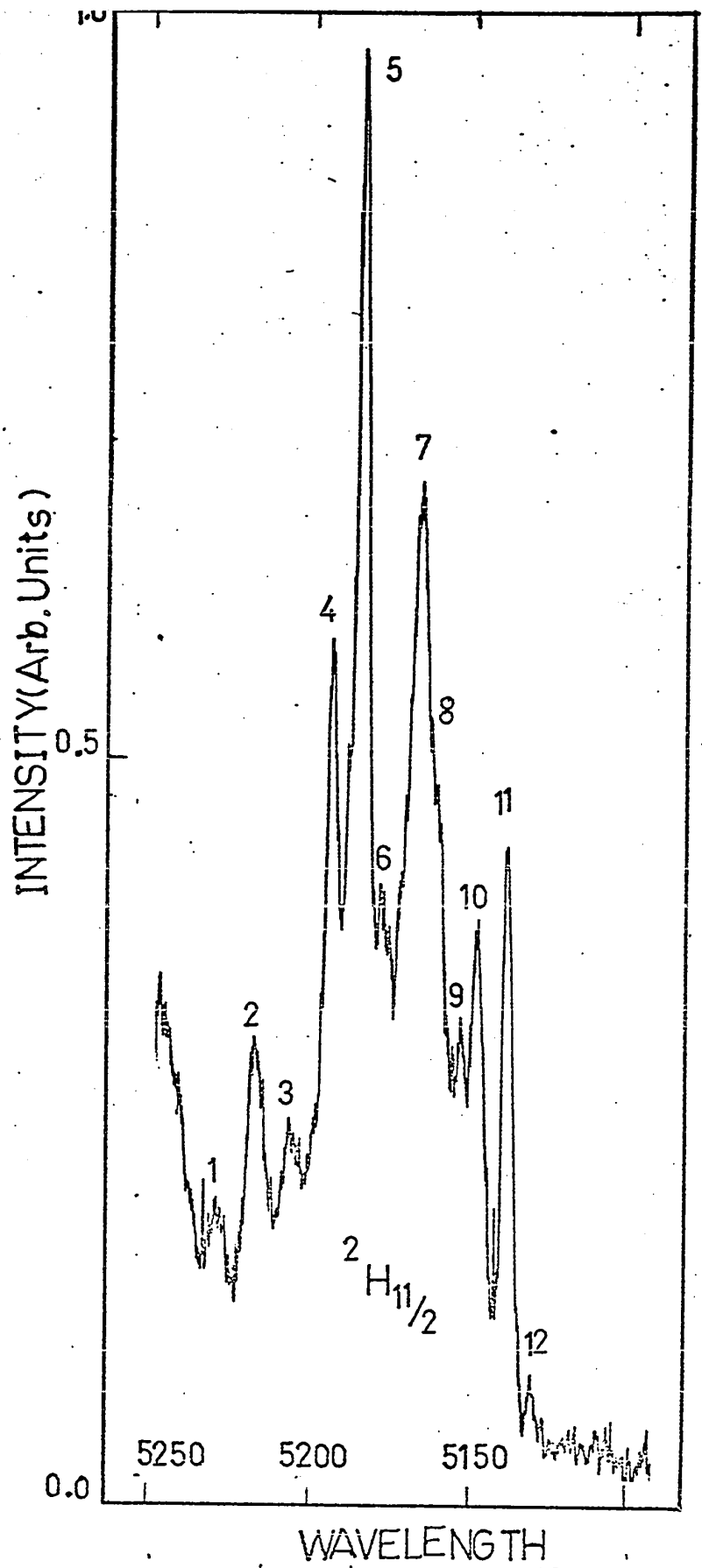
Fig. 3.13 Excitation spectrum of CaF_2Er^{+3} at LNT from 5100 Å to 5250 Å.
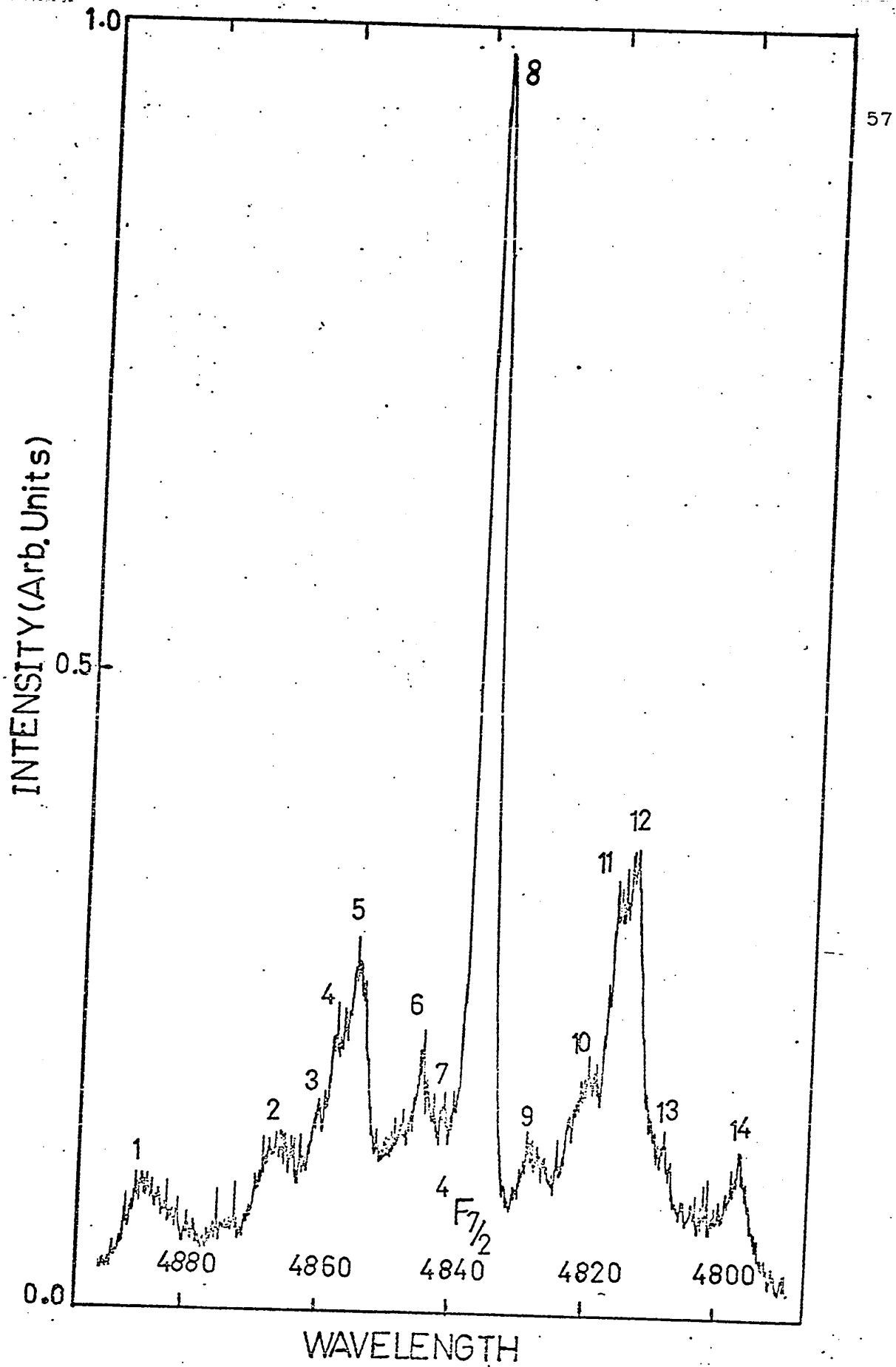
Fig. 3.14   Excitation spectrum of CaF_2Er^{+3} at LNT from 4800Å to 4900 Å
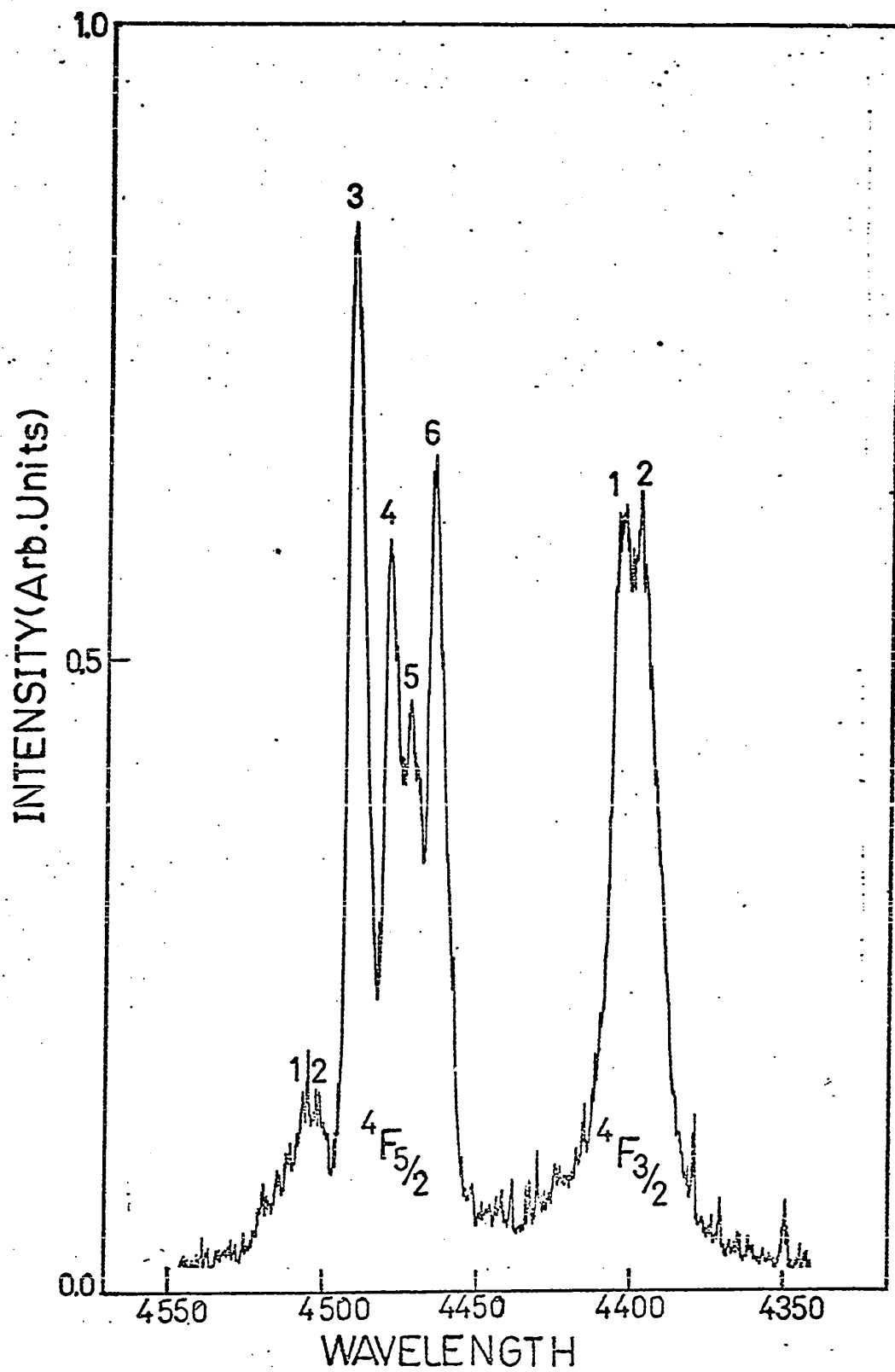
Fig. 3.15 · Excitation spectrum of CaF_2Er^{+3} at LNT from 4350 Å to 4550 Å.
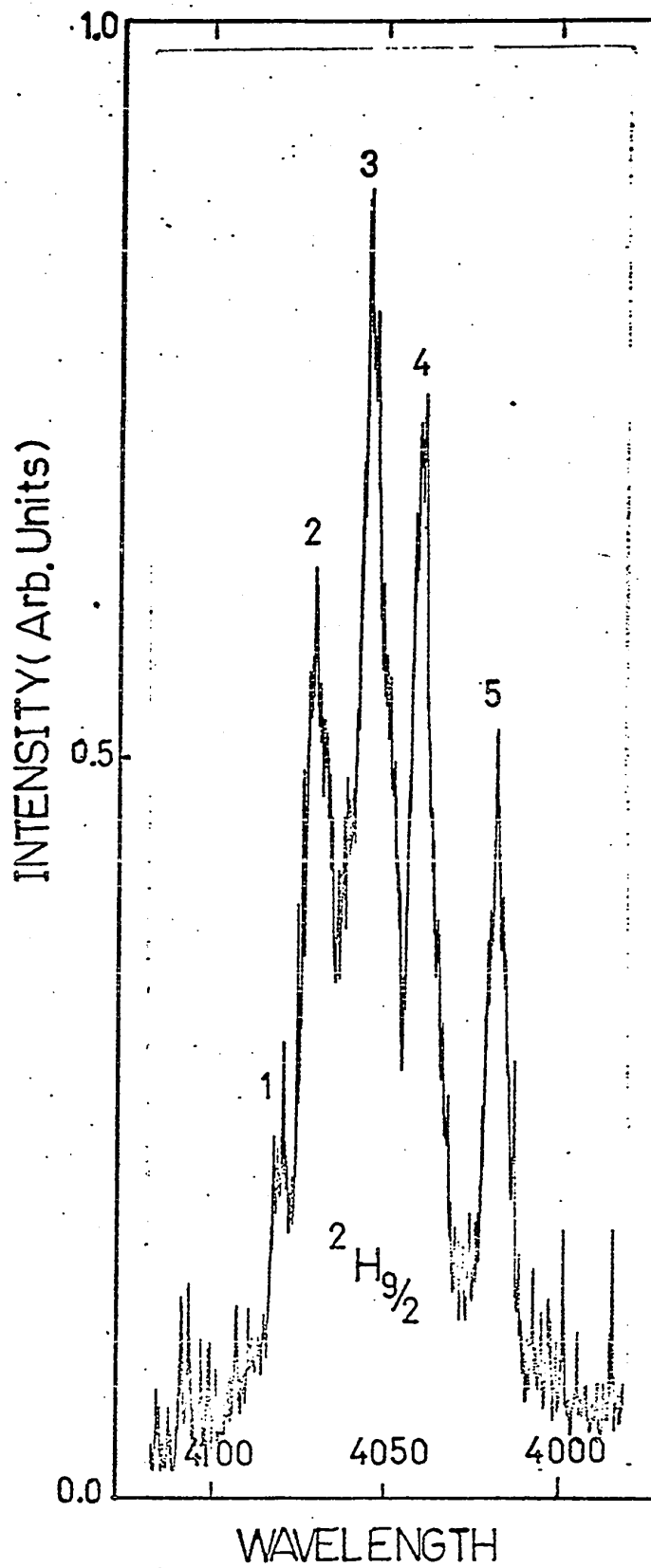
Fig. 3.16 Excitation spectrum of $CaF_2 Er^{+3}$ at LNT from 4000 Å to 4100 Å.
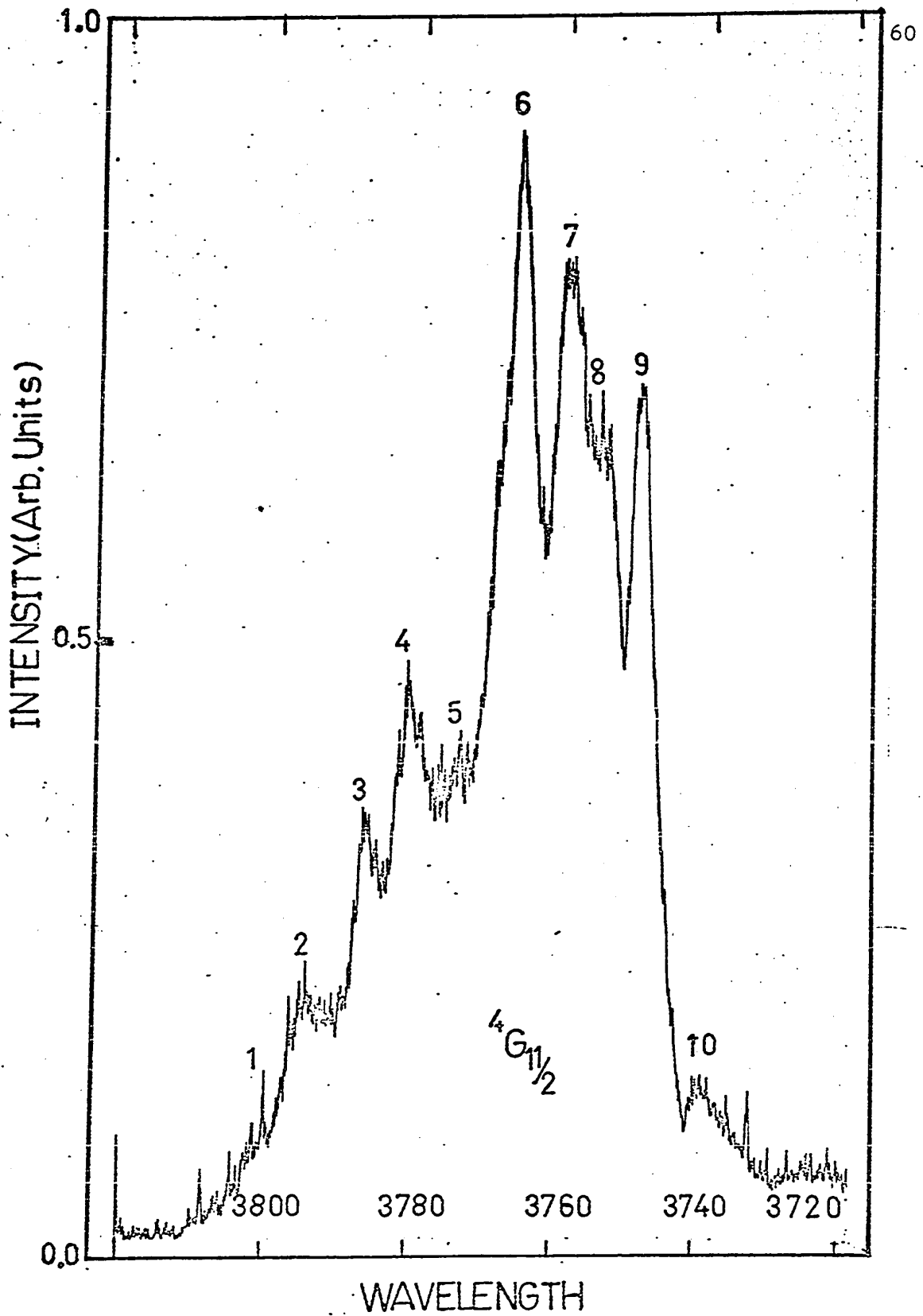
Fig. 3.17 Excitation spectrum of CaF_2Er^{+3} at LNT from 3720 Å to 3820 Å.
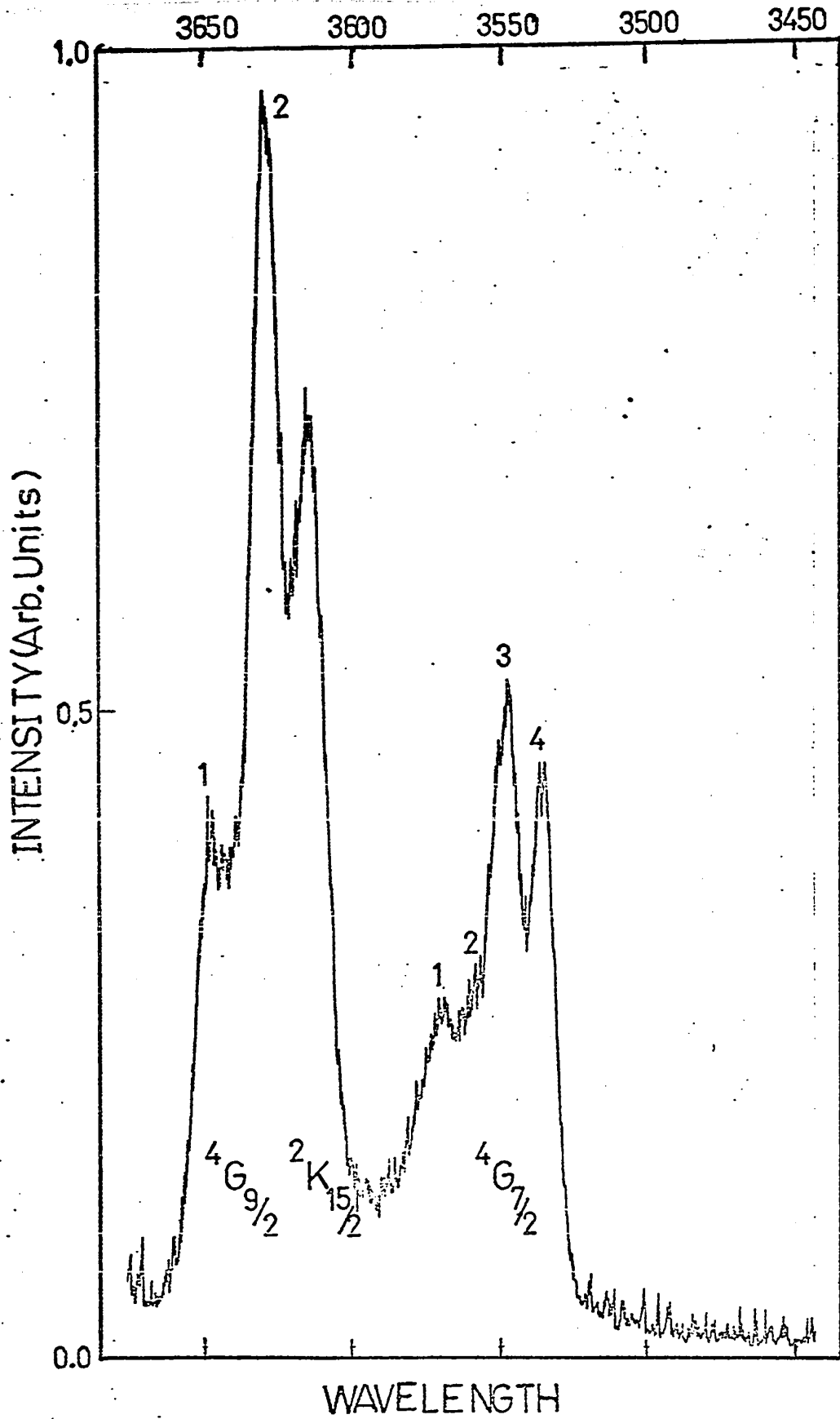
Fig. 3.18 Excitation spectrum of CaF_2Er^{+3} at LNT from 3450 Å to 3650 Å.
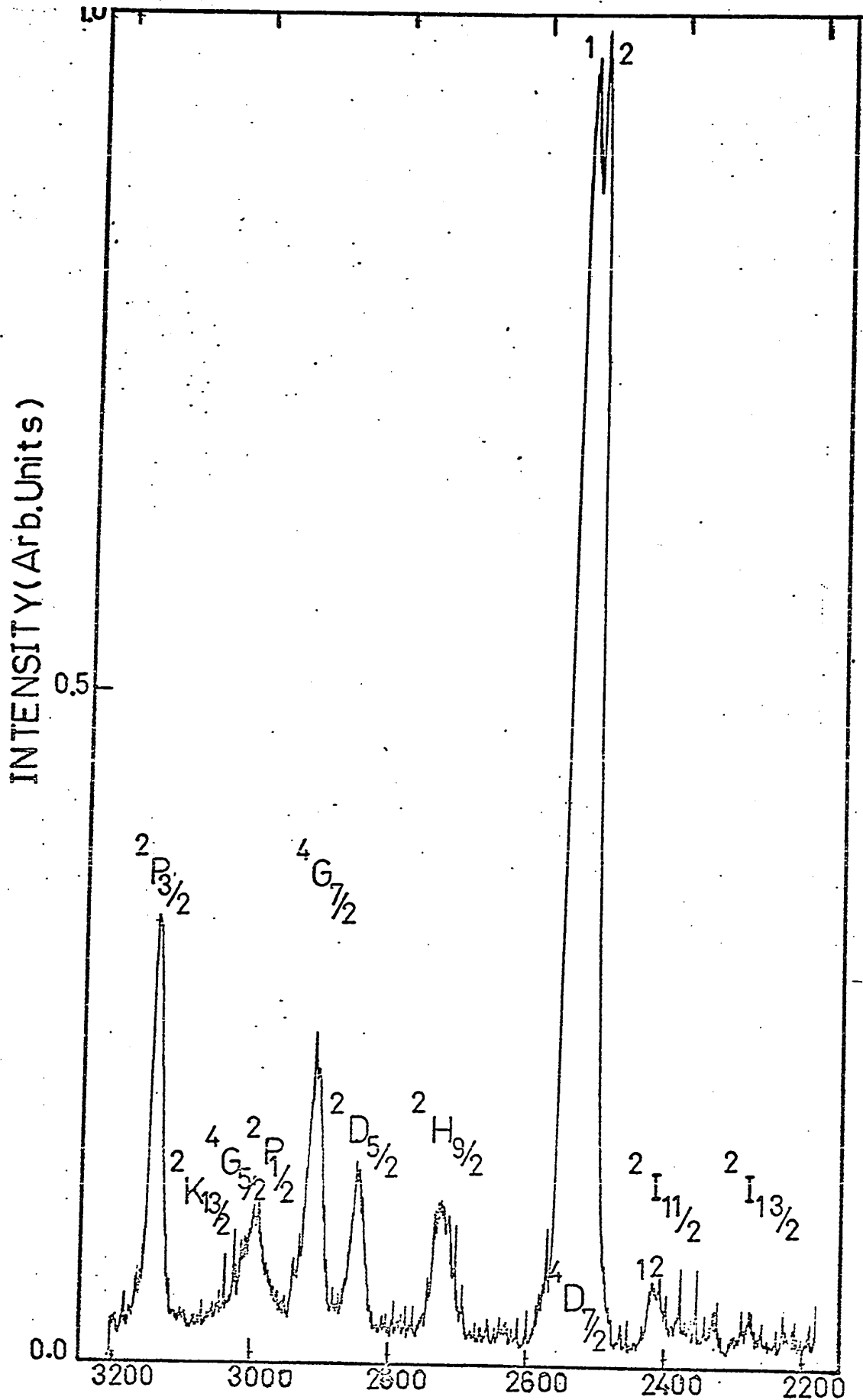
Fig. 3.19 Excitation spectrum of $CaF_2 Er^{+3}$ at LNT from 2200Å to 3200 Å.
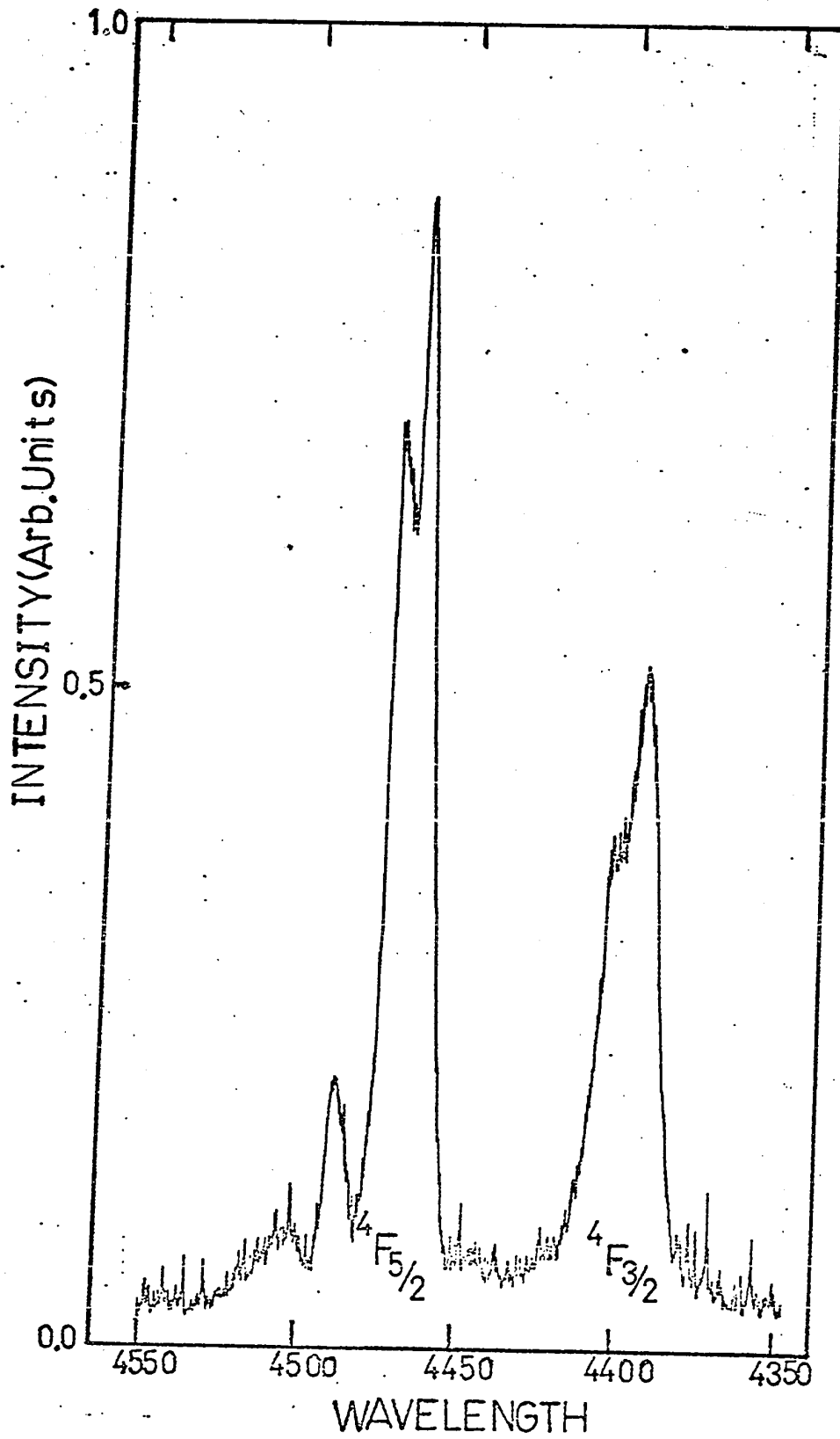
Fig. 3.20 Excitation spectrum of CaF_2Er^{+3} (Harshaw) at LNT from 4350 Å to 4550 Å.
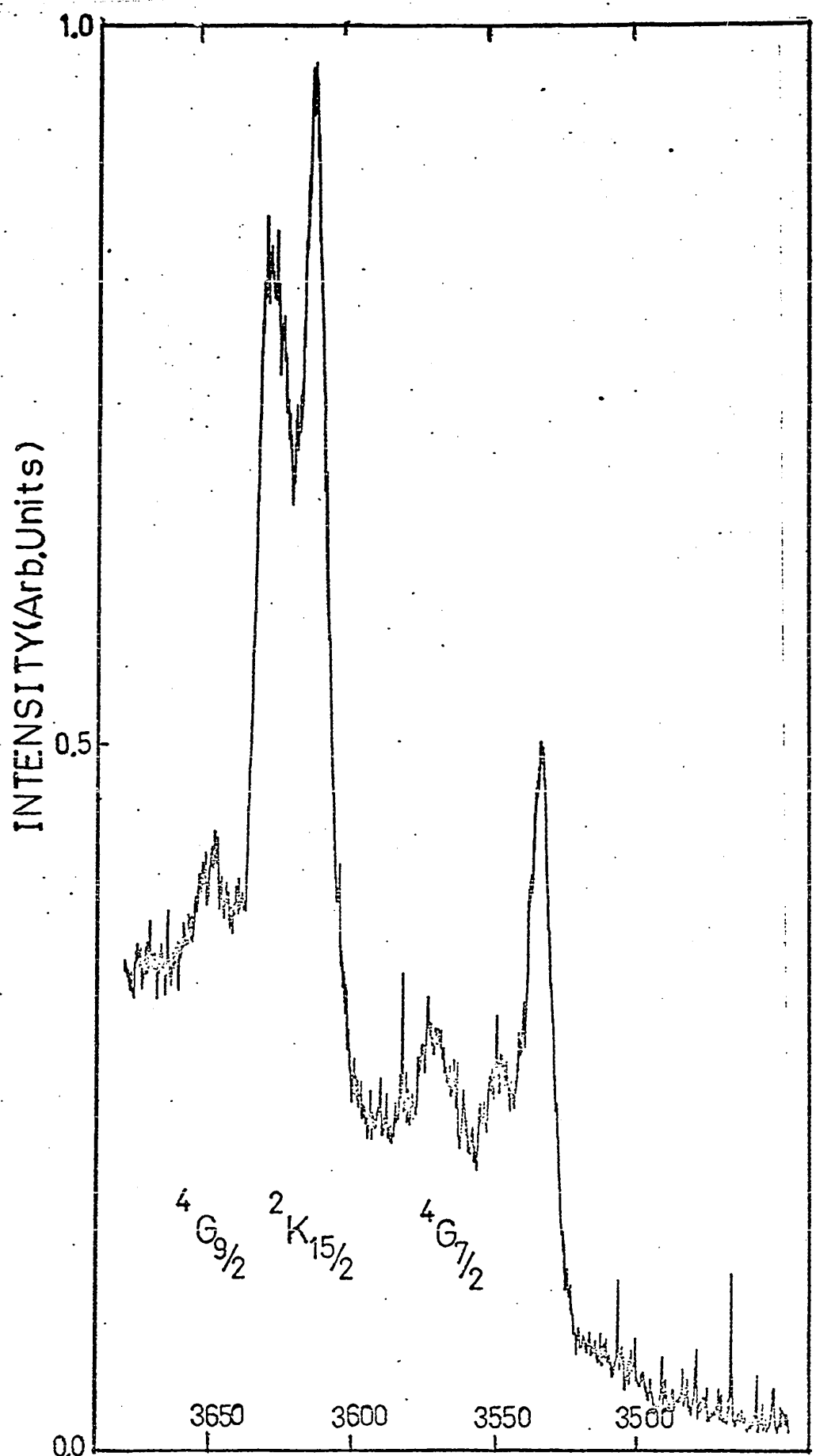
Fig. 3.21   Excitation spectrum of CaF_2Er^{+3} (Harshaw) at
            LNT from 3500 Å to 3650 Å.
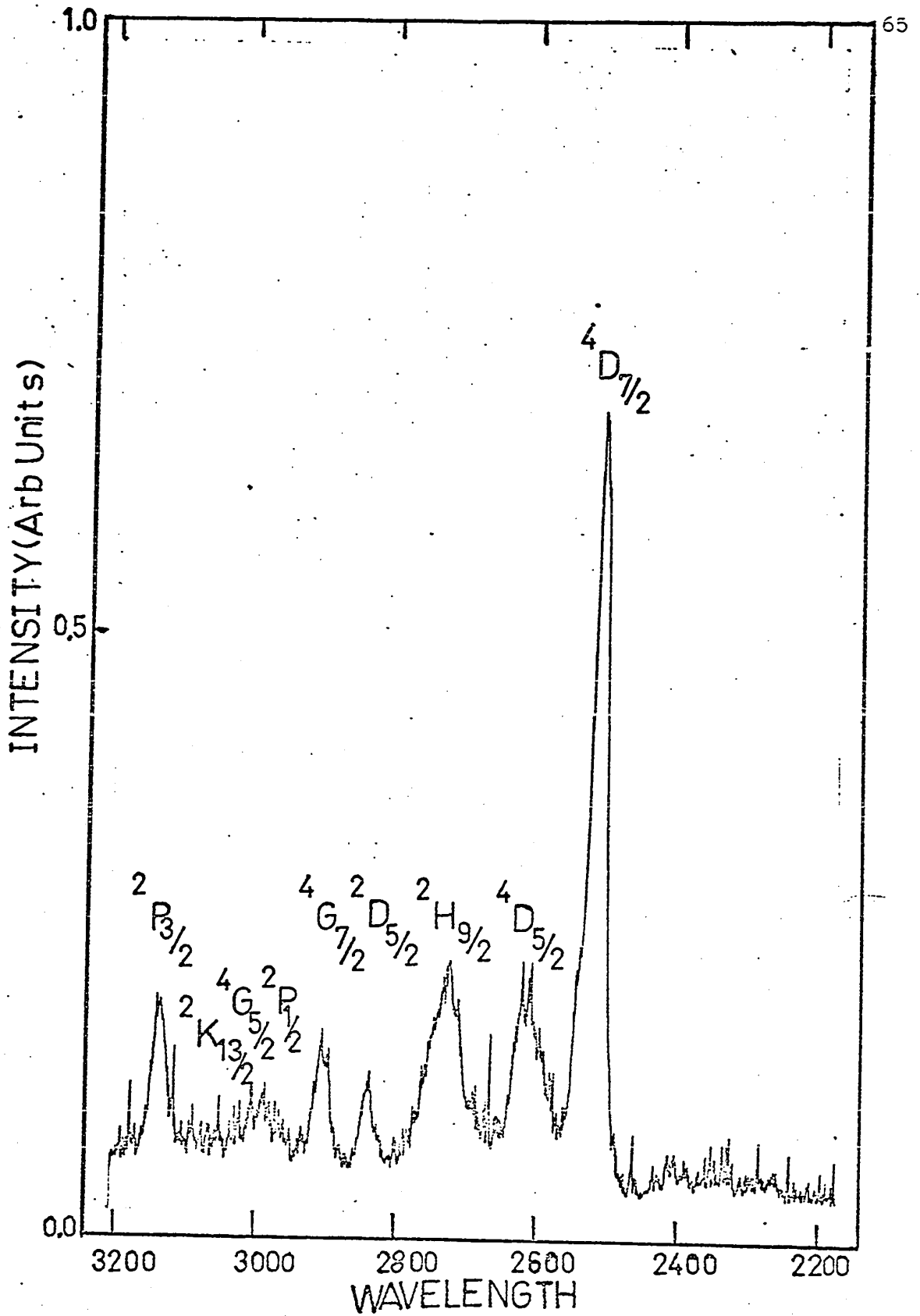
Fig. 3.22   Excitation spectrum of CaF_2Er^{+3} (Harshaw) at LNT from 2200 Å to 3200 Å.

TABLE 3.2

Luminescence Excitation Spectrum of CaF$_2$Er^{+3} at 77°K

SLJ Assignment	Excitation Peaks Energy (cm^{-1})	Wavelength λ (Å)	Peak No.	Centroid (cm^{-1})	Differences between Expt. and Calc. Energy Values (cm^{-1}) Ref. (1)
$^4S_{3/2}$	18518	5400	1		
	18539	5394	2		
	18560	5388	3		
	18587	5380	4	18570	124
	18601	5376	5		
	18622	5370	6		
	18649	5362	7		
$^2H_{11/2}$	19120	5230	1		
	19164	5218	2		
	19201	5208	3		
	19257	5193	4		
	19286	5185	5		
	19324	5175	6	19322	66
	19350	5168	7		
	19380	5160	8		
	19410	5152	9		
	19425	5148	10		
	19463	5138	11		
	19485	5132	12		
$^4F_{7/2}$	20462	4887	1		
	20551	4866	2		
	20572	4861	3		
	20585	4858	4		
	20597	4855	5		
	20640	4845	6	20680	84

Table 3.2 (continued)

SLJ Assignment	Excitation Peaks Energy (cm⁻¹)	Wavelength λ (Å)	Peak No.	Centroid (cm⁻¹)	Differences between Expt. and Calc. Energy Values (cm⁻¹) Ref. (1)
$^4F_{7/2}$	20653	4842	7		
	20678	4836	8		
	20708	4829	9		
	20747	4820	10		
	20764	4816	11		
	20773	4814	12		
	20799	4808	13		
	20846	4797	14		
$^4F_{5/2}$	22173	4510	1		
	22198	4505	2		
	22282	4488	3		
	22336	4477	4	22326	95
	22371	4470	5		
	22411	4462	6		
$^4F_{3/2}$	22717	4402	1		
	22753	4395	2	22735	218
$^2H_{9/2}$	24510	4080	1		
	24570	4070	2		
	24667	4054	3	24695	107
	24752	4040	4		
	24900	4016	5		
$^4G_{11/2}$	26316	3800	1		
	26357	3794	2		
	26420	3785	3		
	26462	3779	4		
	26504	3773	5	26569	90

Table 3.2 (continued)

SLJ Assignment	Excitation Peaks Energy (cm⁻¹)	Wavelength λ (Å)	Peak No.	Centroid (cm⁻¹)	Differences between Expt. and Calc. Energy Values (cm⁻¹) Ref. (1)
$^4G_{11/2}$	26567	3764	6		
	26617	3757	7		
	26652	3752	8		
	26688	3747	9		
	26745	3739	10		
$^4G_{9/2}$	27420	3647	1	27500	108
	27533	3632	2		
$^2K_{15/2}$	27662	3615		27662	-106
$^4G_{7/2}$	28011	3570	1	28166	205
	28114	3557	2		
	28193	3547	3		
	28265	3538	4		
$^2P_{3/2}$	31847	3140		31847	239
$^2K_{13/2}$	33111	3020		33111	99
$^4G_{5/2}$	33333	3000		33333	106
$^2P_{1/2}$	33557	2980		33557	182
$^4G_{7/2}$	34305	2915		34305	334
$^2D_{5/2}$	35088	2850		35088	215
$^2H_{9/2}$	36697	2725		36697	150

Table 3.2 (continued)

SLJ Assignment	Excitation Peaks Energy (cm^{-1})	Wavelength λ (Å)	Peak No.	Centroid (cm^{-1})	Differences between Expt. and Calc. Energy Values Ref. (1) (cm^{-1})
$^4D_{5/2}$	38759	2580		38759	179
$^4D_{7/2}$	39216	2550	1	39370	93
	39525	2530	2		
$^2I_{11/2}$	41322	2420	1	41414	365
	41493	2410	2		
$^2I_{13/2}$	43859	2280		43859	203
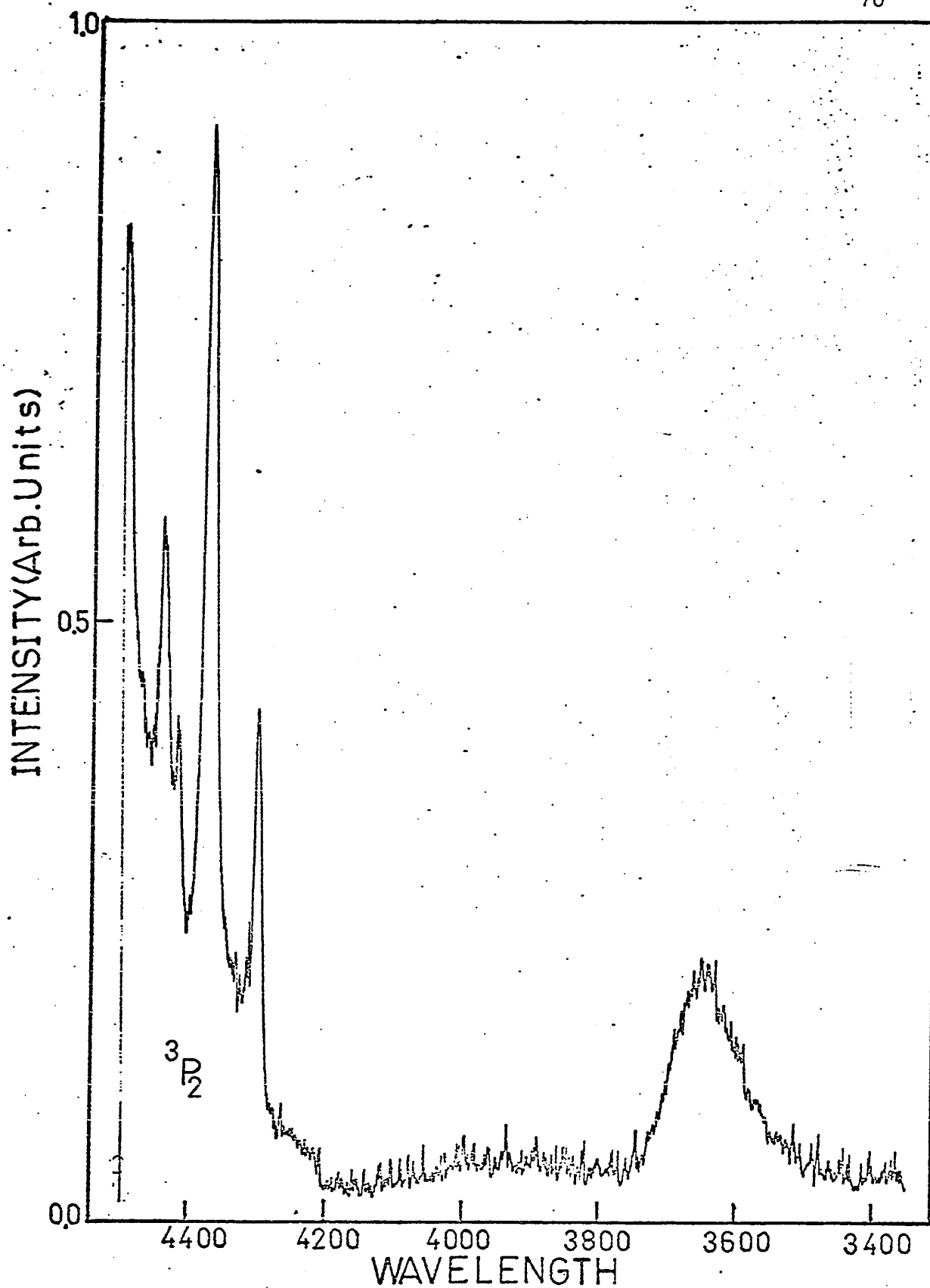
Fig. 3.23 Excitation spectrum of CaF_2Pr^{+3} at LNT from 3400 Å to 4500 Å.

TABLE 3.3

Summary of the Figures Regarding the Excitation

Spectrum of CaF_2Pr^{+3}

Fig. No.	Crystal	Temperature	Spectral Range
3.24	As-received	RT	4200 Å to 4500 Å
3.25	" "	"	3200 Å to 4200 Å
3.26	" , "	LNT	4200 Å to 4500 Å
3.27	" "	"	3200 Å to 4200 Å
3.28	" "	"	2200 Å to 3200 Å
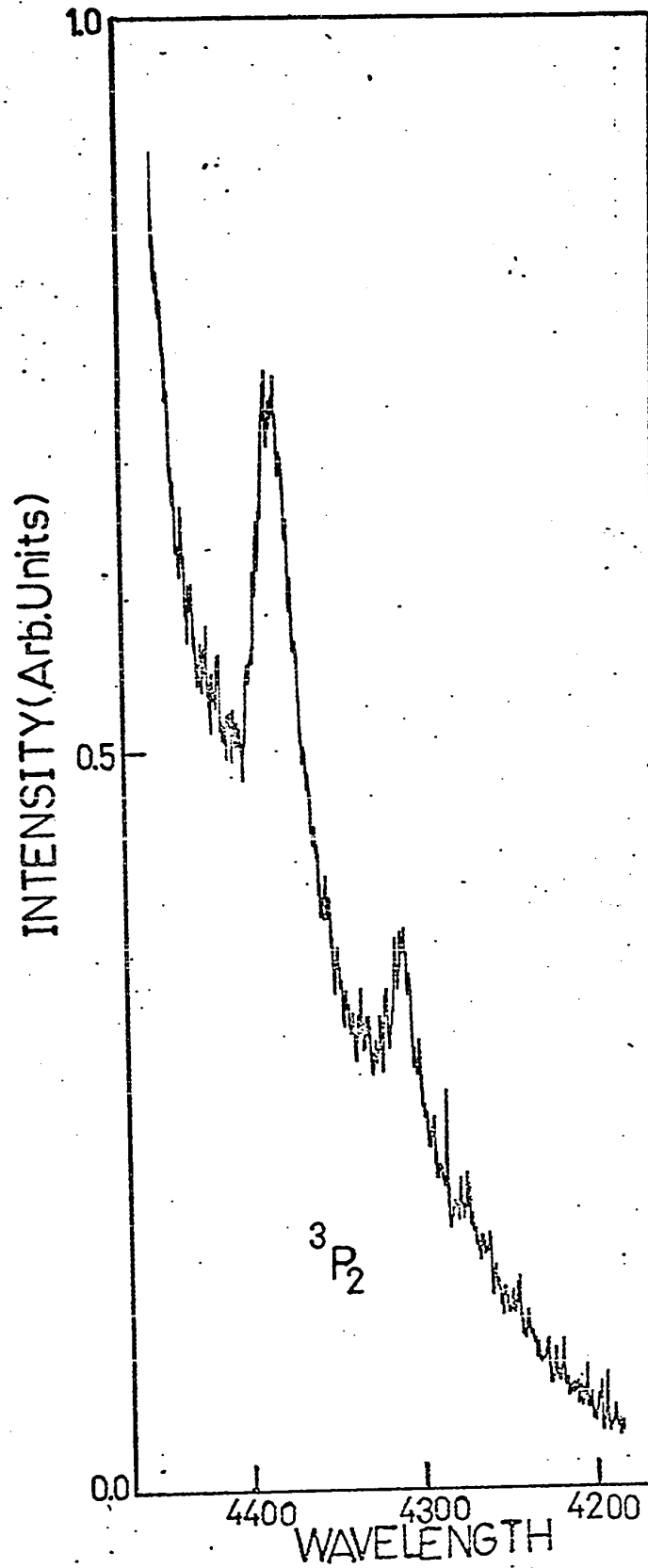
Fig. 3.24 Excitation spectrum of CaF_2Pr^{+3} at RT from 4200 Å to 4500 Å.
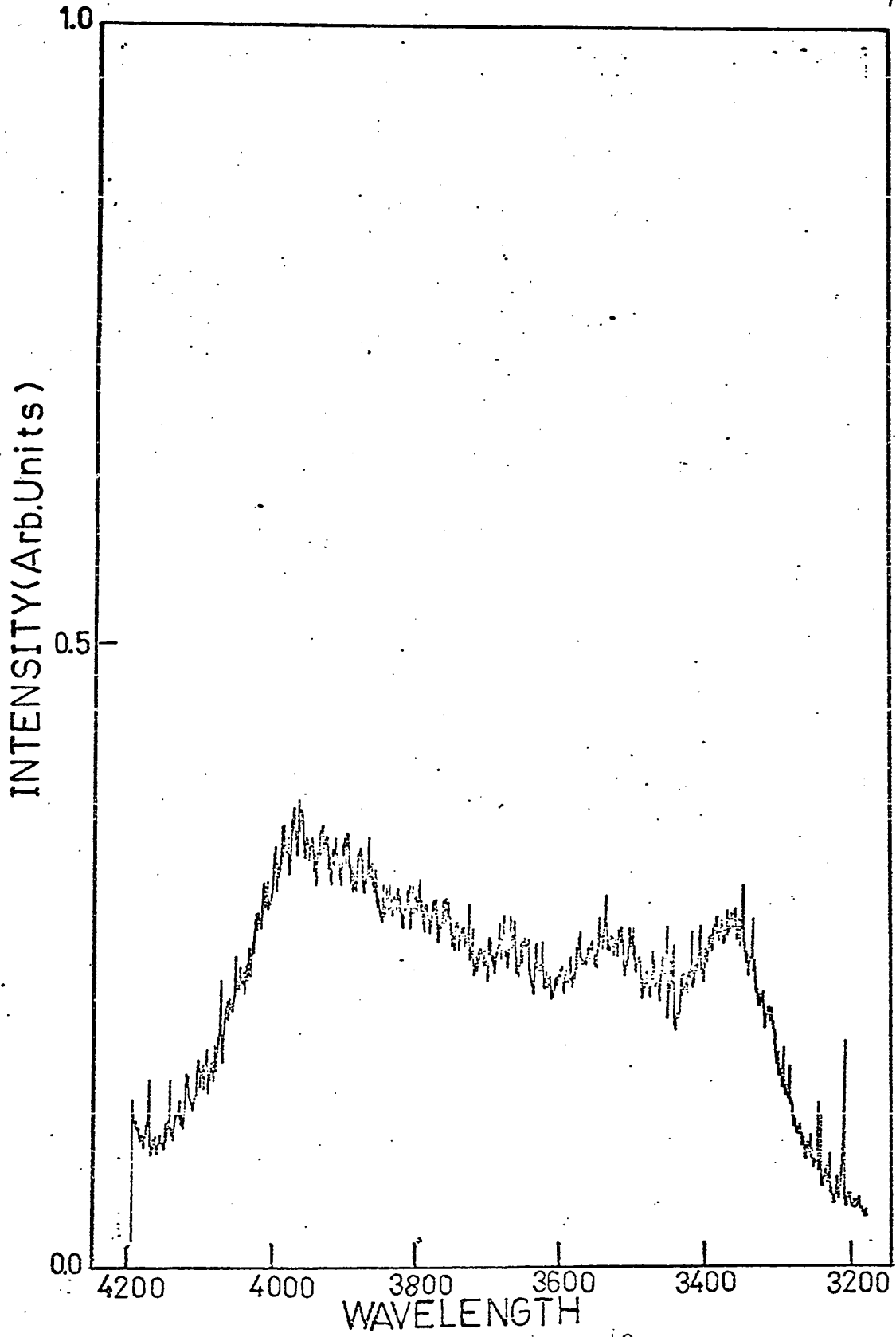
Fig. 3.25 Excitation spectrum of CaF_2Pr^{+3} at RT from 3200 Å to 4200 Å.
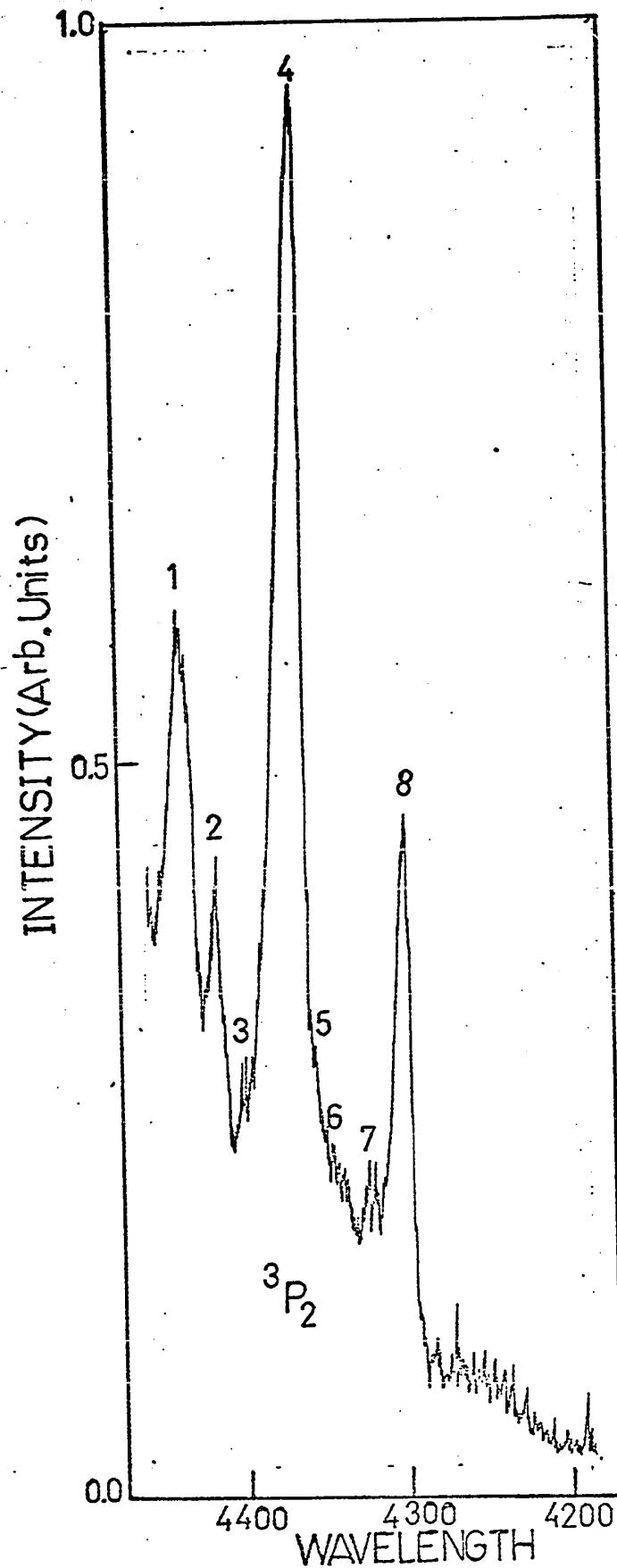
Fig. 3.26 Excitation spectrum of CaF_2Pr^{+3} at LNT from 4200 Å to 4500 Å.
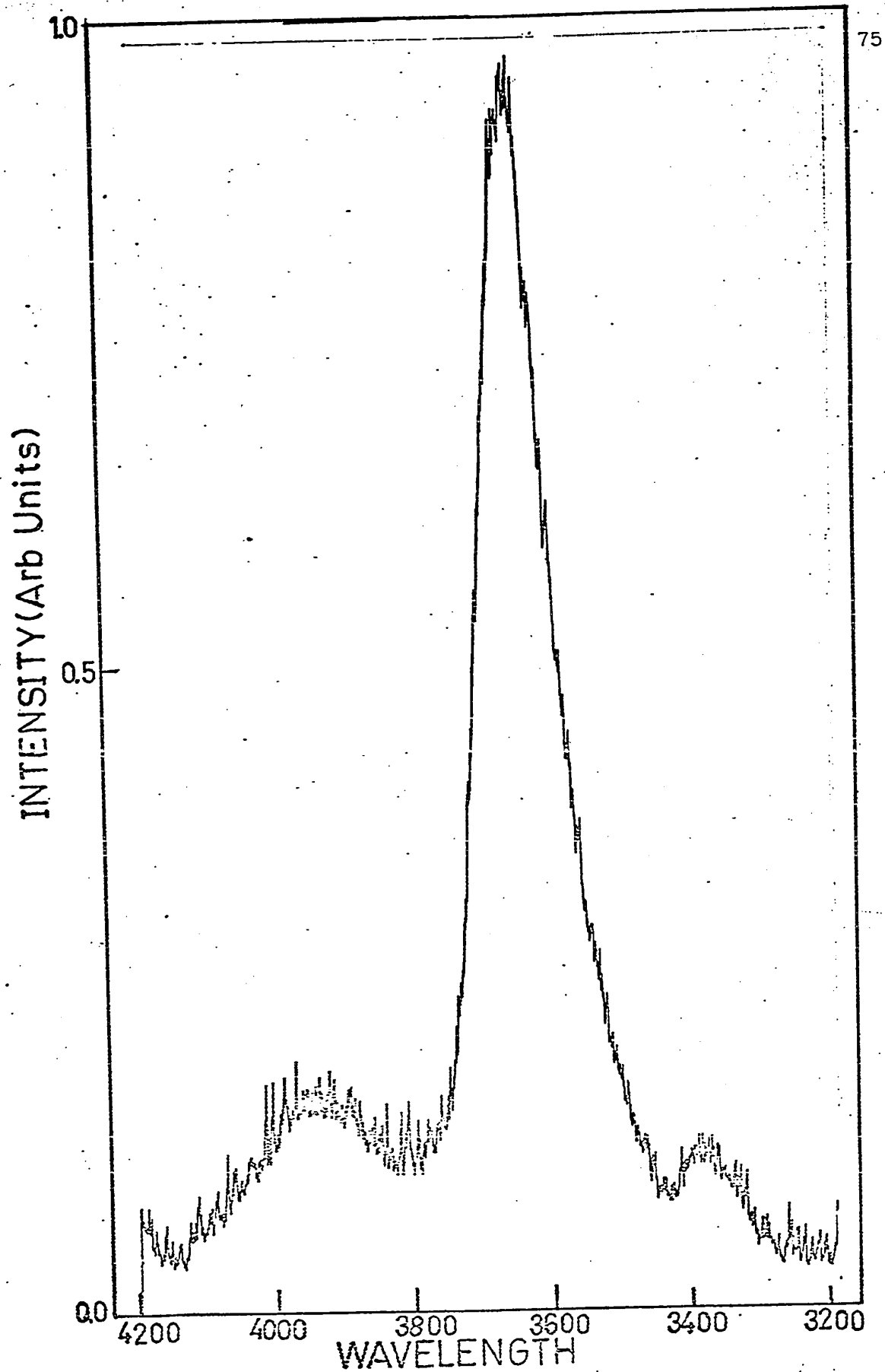
Fig. 3.27 Excitation spectrum of $CaF_2 Pr^{+3}$ at LNT from 3200 Å to 4200 Å.
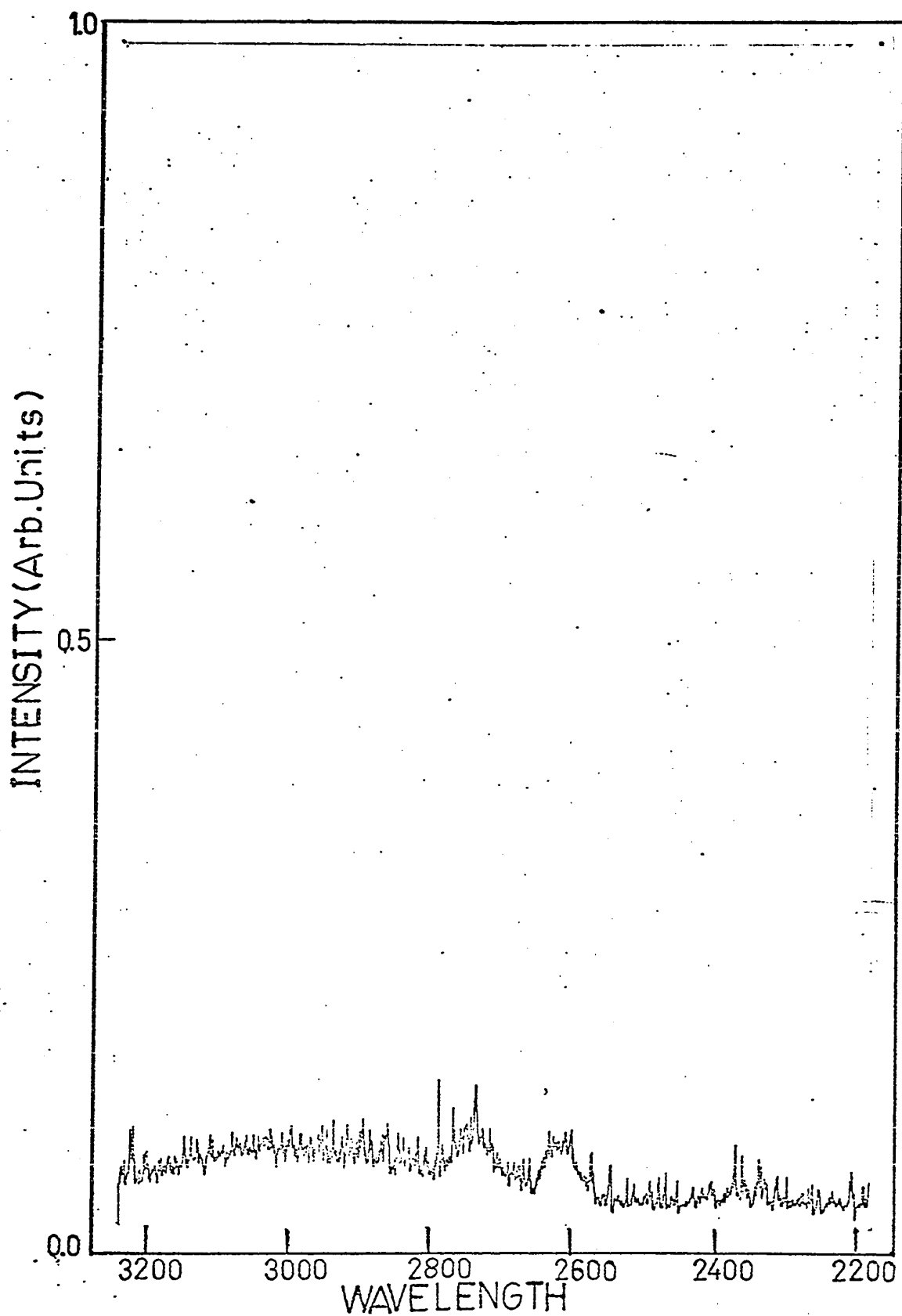
Fig. 3.28   Excitation spectrum of CaF_2Pr^{+3} at LNT from 2200 Å to 3200 Å.

TABLE 3.4

Luminescence Excitation Spectrum of CaF_2Pr^{+3} at LNT

SLJ Assignment	Excitation Peaks Energy (cm^{-1})	Wavelength λ (Å)	Peak No.	Centroid (cm^{-1})	Differences Between Expt. and Calc. Energy Values (cm^{-1})
	22497	4445	1		
	22599	4425	2		
	22696	4406	3		
$^3P_2$	22831	4380	4	22795	
	22946	4358	5		
	22988	4350	6		
	23084	4332	7		
	23212	4308	8		
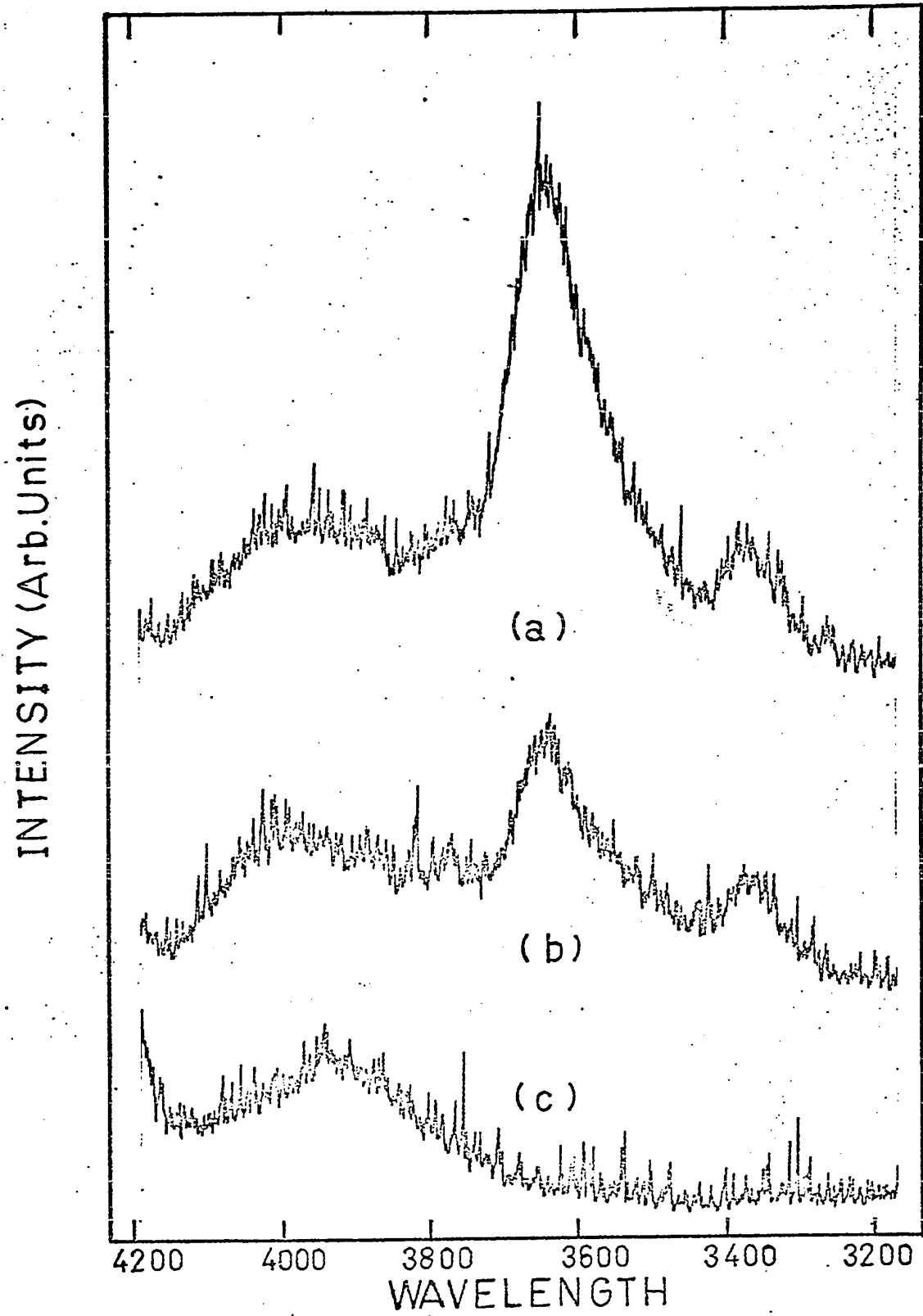
Fig. 3.29   Impurity concentration dependent bands of CaF_2Pr^{+3}.
            (a) 0.05% (b) 0.5% (c) 1%

by a home-made camera loaded with a 3-x Kodak film.
Different exciting wavelengths from the excitation spectrum
were selected for exciting the crystal. The time of
exposure varied from one-half hour to two hours. Standard
wavelengths from the Hg lamp were superimposed on the film
for calibrating the emission spectra.

The microdensitameter traces of emission spectrum
of CaF_2Er^{+3} in the green and that of CaF_2Pr^{+3} in the blue
green are shown in Figs. 3.30 to 3.40. The emission spectrum
of x-irradiated crystals was also photographed in each
case and the results obtained were identical to the ones
observed before. Figs. 3.34 & 3.38 show that the intensities
of the lines 5444 Å and 5393 Å in the case of CaF_2Er^{+3} was
decreased, but for CaF_2Pr^{+3}, the intensity of the lines
4850 Å and 4826 Å was increased by exciting the crystals
with different exciting wavelengths. The peaks have been
numbered for future use and their energies are expressed
in cm^{-1} in Tables 3.7 & 3.8, respectively. A summary of the
figures, along with their experimental conditions, is
tabulated in Tables 3.5 & 3.6, respectively.

3.3 Thermoluminescent Spectra of CaF_2Er^{+3} and CaF_2Pr^{+3}

Crystals were placed in the crystal holder of an
Andonian vacuum cryostat. They were fitted with a copper-
constantan thermocouple for measuring the temperature. The
holder was also fitted with a heater of nichrome-resistance
wire for heating the crystal. The crystal was first cooled

TABLE 3.5

Summary of the Figures Regarding the Emission Spectrum of CaF_2Er^{+3}

Fig. No.	Crystal	Temperature	Exciting Light	Spectral Range
3.30	As-received	RT	3750 Å	5350 Å to 5550 Å
3.31	"	LNT	3750 Å	5350 Å to 5550 Å
3.32	"	"	3760 Å	5350 Å to 5550 Å
3.33	"	"	4810 Å	5350 Å to 5550 Å
3.34	"	"	3785 Å	535C Å to 5550 Å
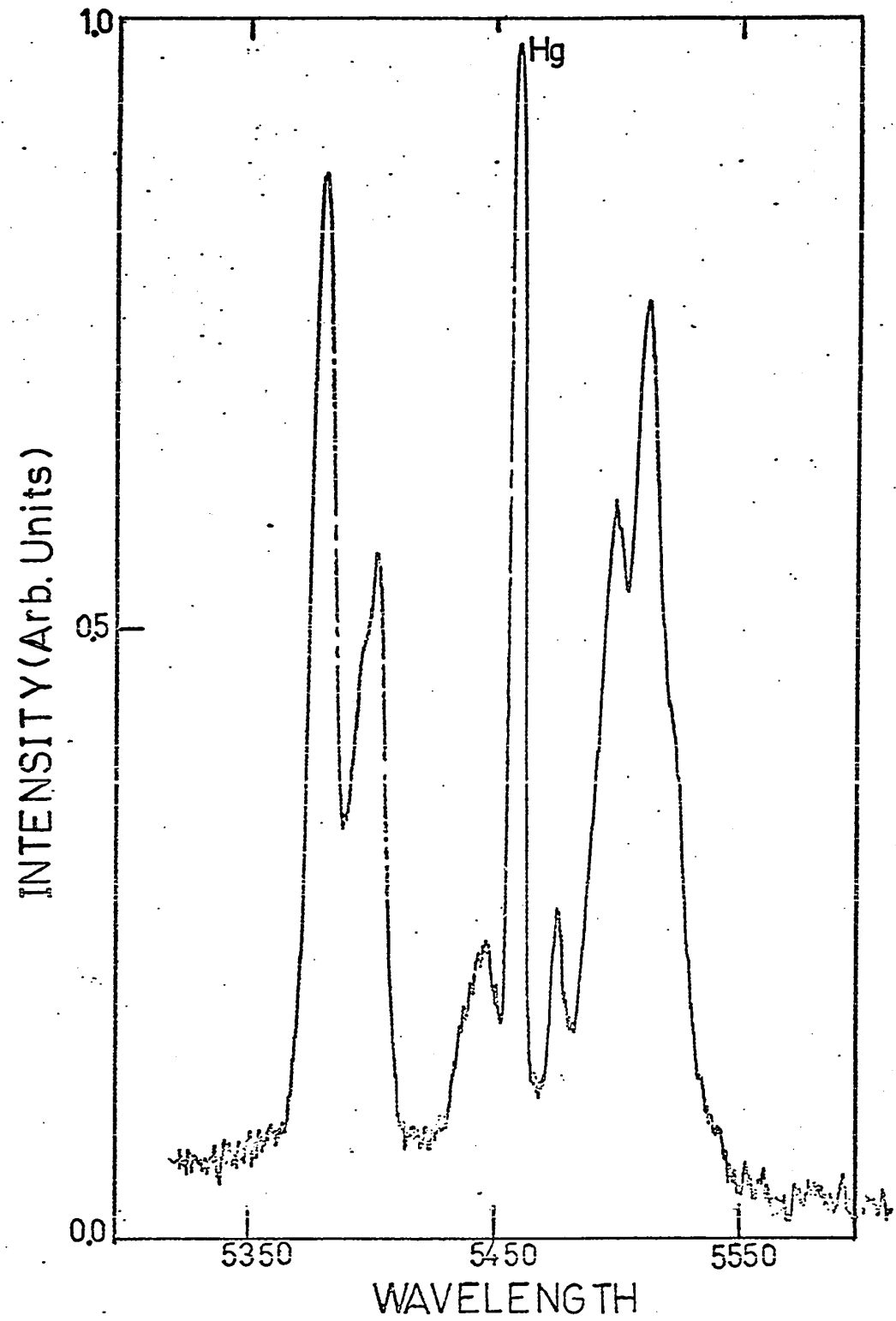
Fig. 3.30 Emission spectrum of CaF$_2$Er^{+3} at RT from 5350 Å to 5500 Å excited with 3750 Å.
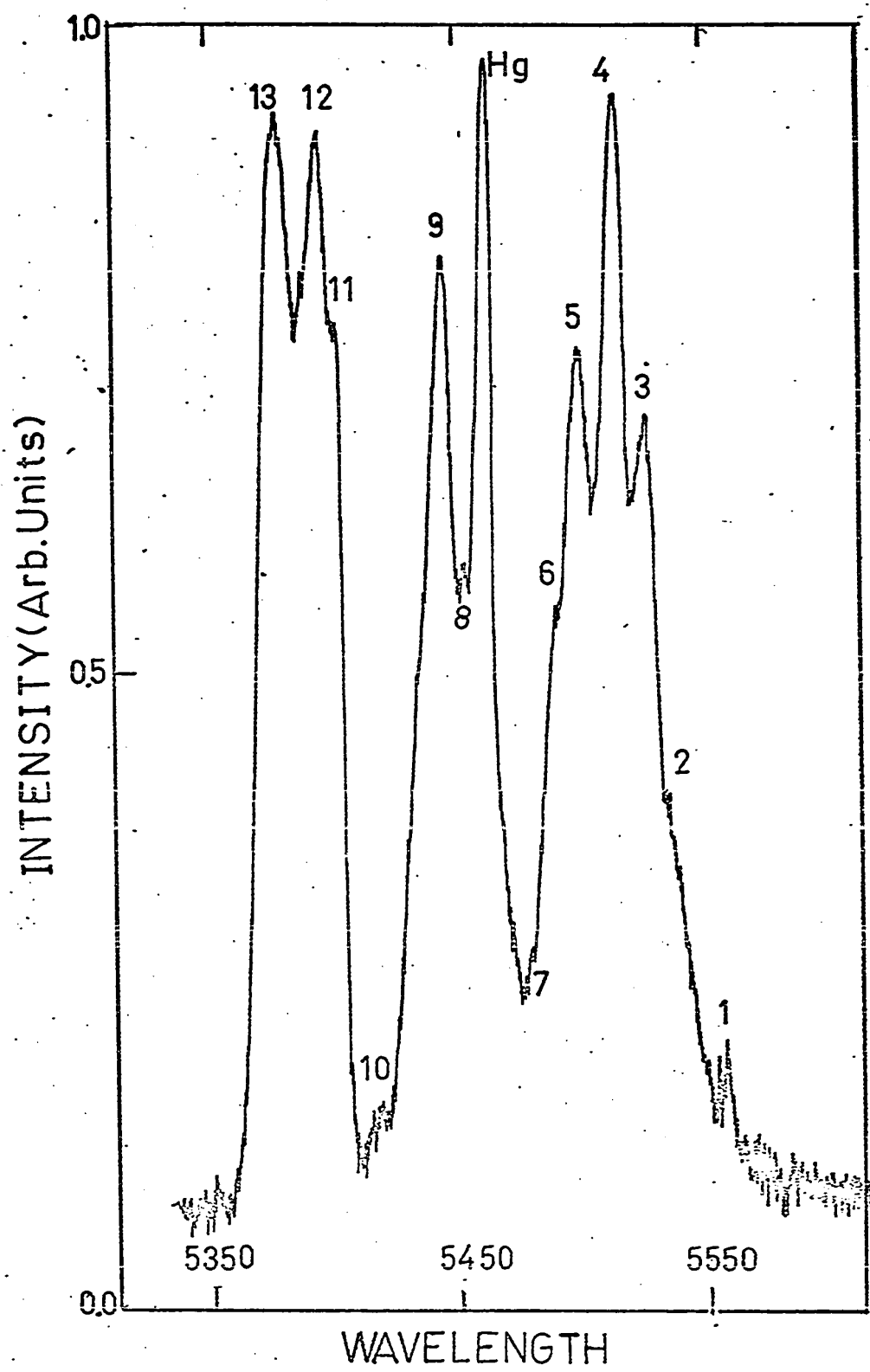
Fig. 3.31. Emission spectrum of CaF_2Er^{+3} at LNT from 5350 Å to 5550 Å excited with 3750 Å.
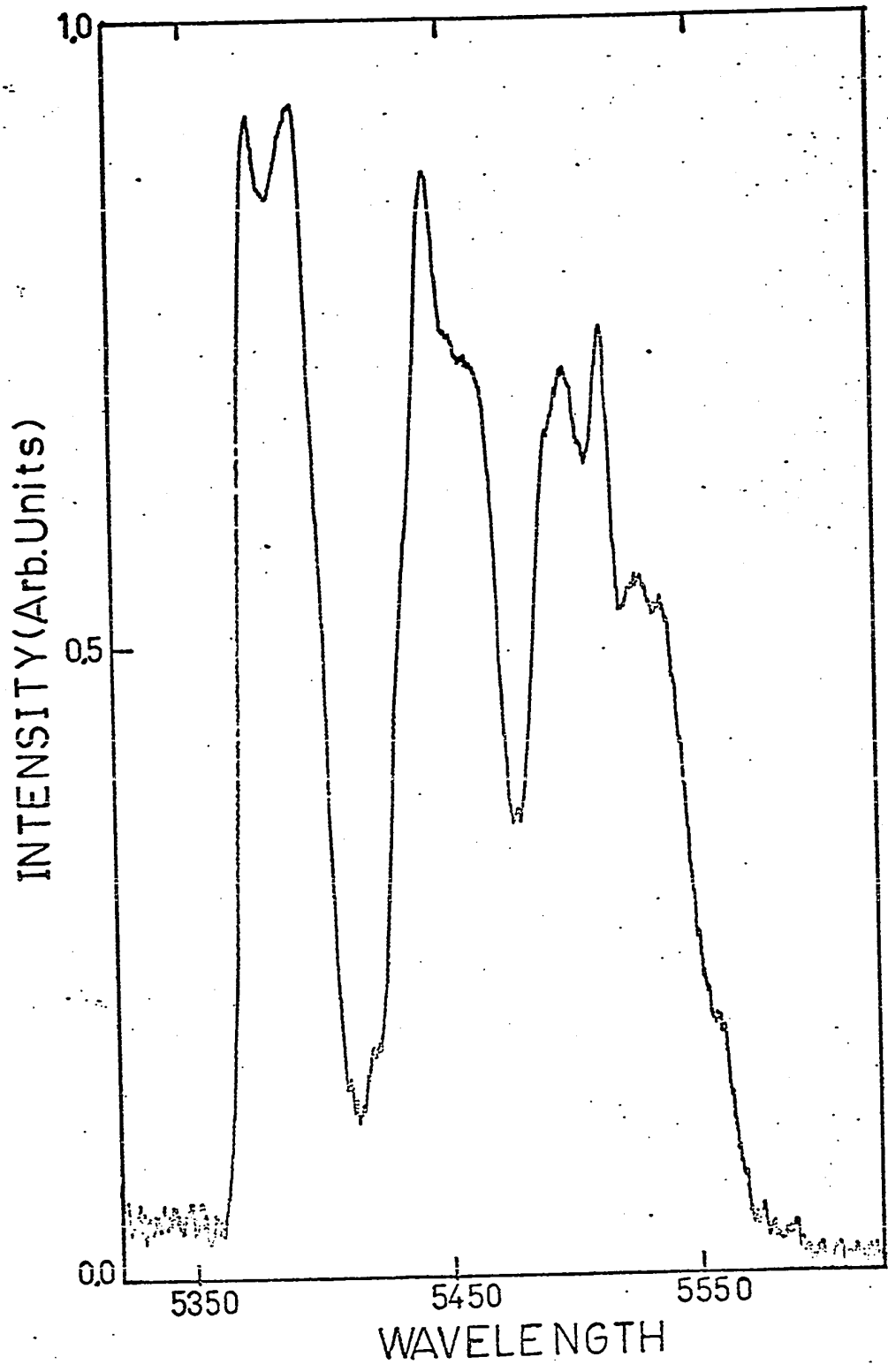
Fig. 3.32. Emission spectrum of CaF_2Er^{+3} at LNT from 5350 Å to 5550 Å excited with 3760 Å.
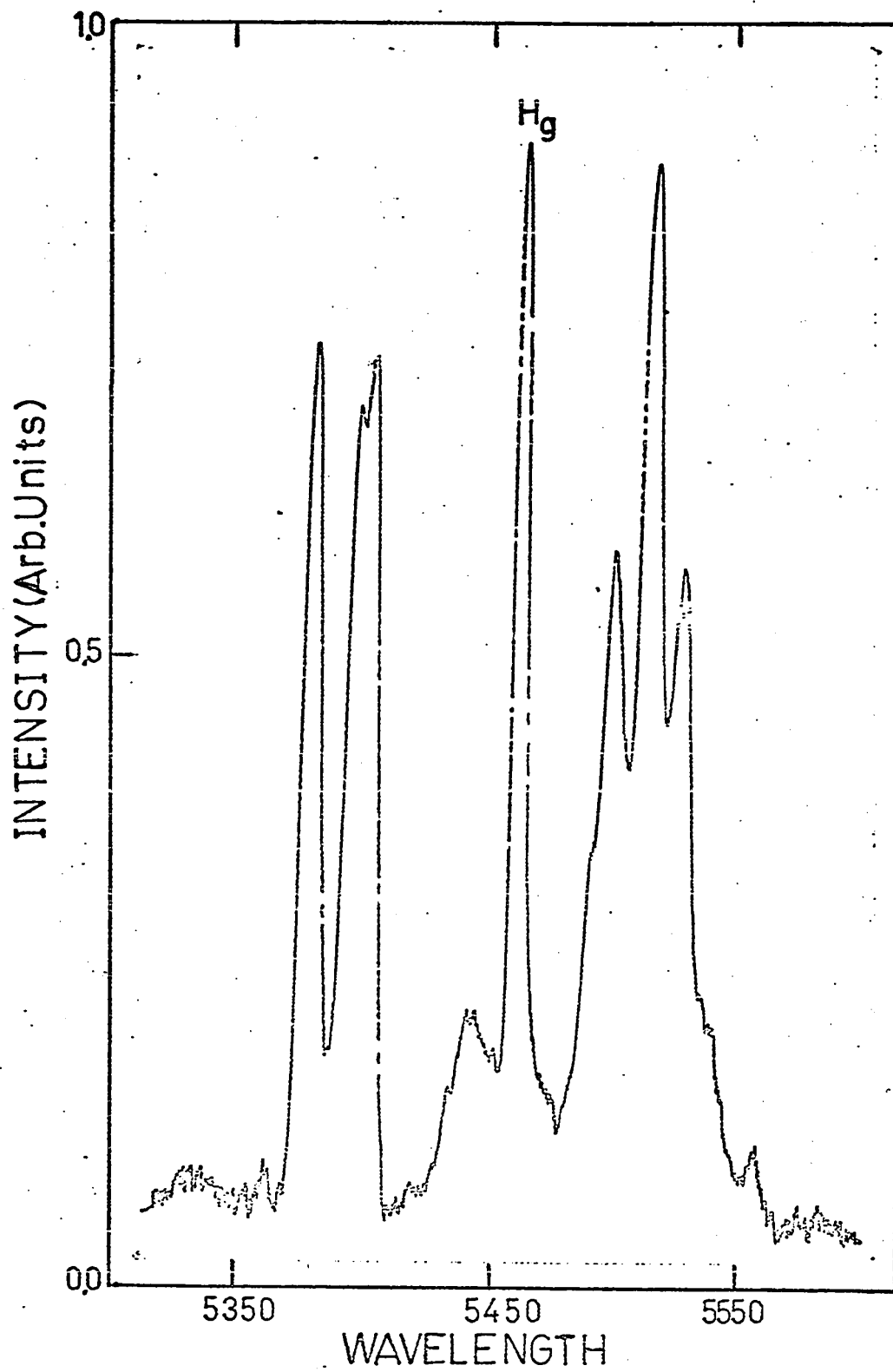
Fig. 3.33 Emission spectrum of CaF_2Er^{+3} at LNT from 5350 Å to 5550 Å excited with 4810 Å.
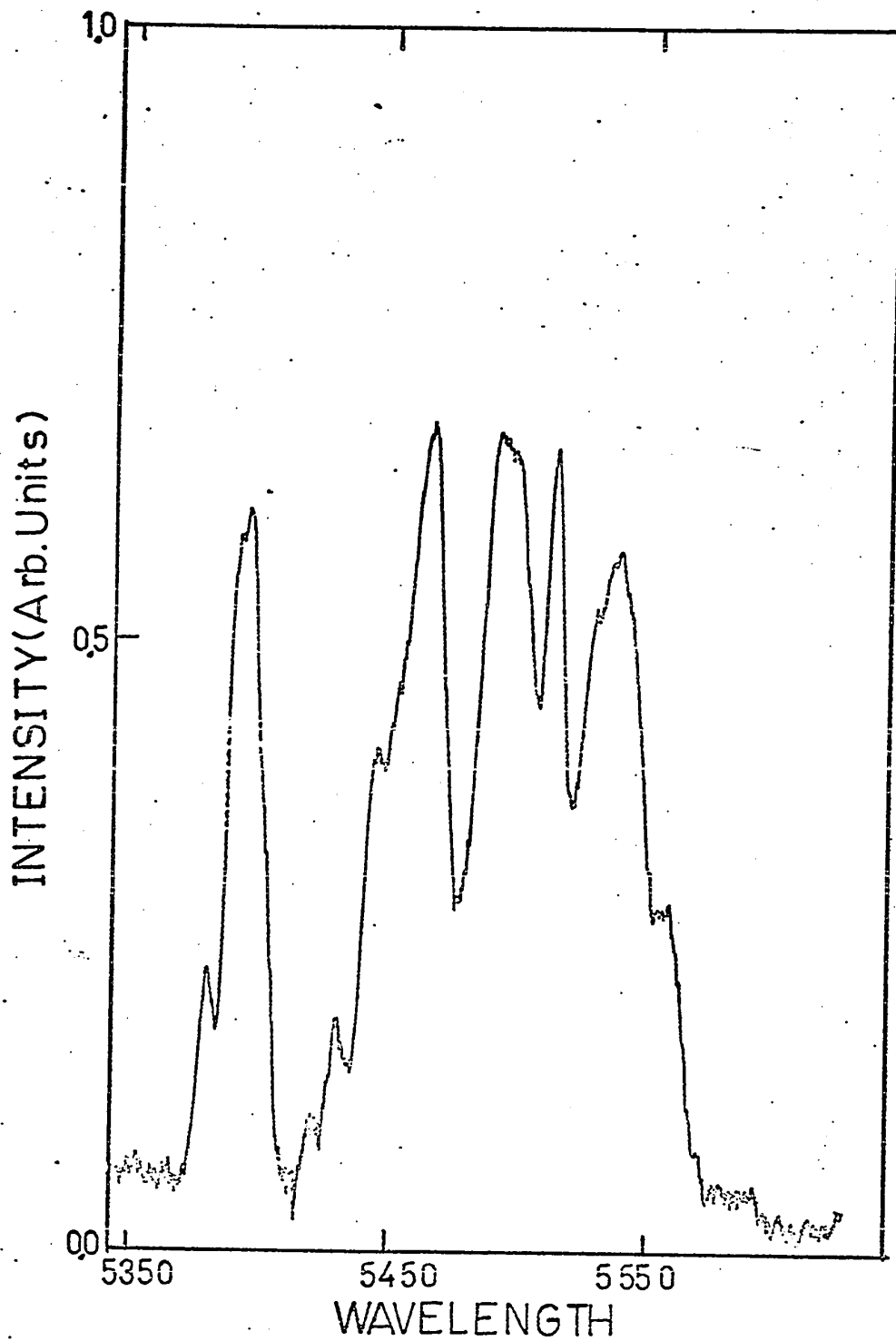
Fig. 3.34 . Emission spectrum of CaF_2Er^{+3} at LNT from 5350 Å to 5550 Å excited with 3785 Å.

TABLE 3.6

Emission Spectrum of CaF_2Er^{+3} at 77°K

Transition	Emission Peak Energy (cm⁻¹)	Wavelength λ (Å)	Peak No.	Centroid (cm⁻¹)	Differences between Expt. and Calc. Energy Values (cm⁻¹)
	17976	5563	1		
	18059	5538	2		
	18084	5530	3		
	18135	5514	4		
	18181	5500	5		
	18212	5491	6		
$^4S_{3/2} \rightarrow {}^4I_{15/2}$	18272	5473	7		
	18342	5452	8		
	18372	5443	9		
	18450	5420	10		
	18516	5400.6	11		
	18543	5393	12		
	18608	5374	13		
	18308	5462			
	18423	5428			

TABLE 3.7

Summary of the Figures Regarding the Emission Spectrum of CaF_2Pr^{+3}

Fig. No.	Crystal	Temperature	Exciting Light	Spectral Range
3.35	As-received	RT	4382 Å	4750 Å to 4950 Å
3.36	"	LNT	4382 Å	4750 Å to 4950 Å
3.37	"	"	4448 Å	4750 Å to 4950 Å
3.38	"	"	4428 Å	4750 Å to 4950 Å
3.39	"	"	4308 Å	4750 Å to 4950 Å
3.40	"	"	3665 Å	4550 Å to 4950 Å
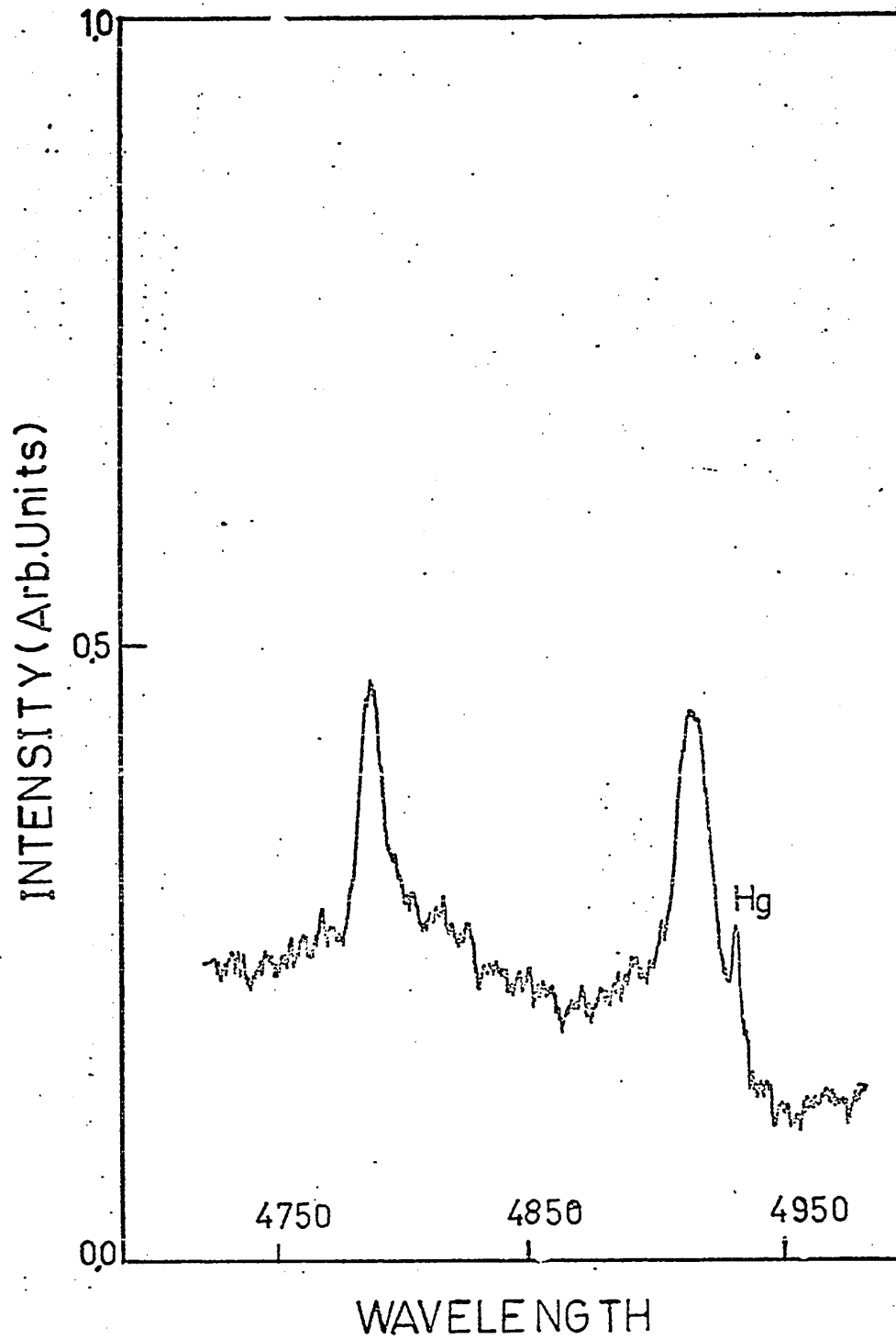
Fig. 3.35 Emission spectrum of CaF_2Pr^{+3} at RT from 4750 Å to 4950 Å excited with 4382 Å.
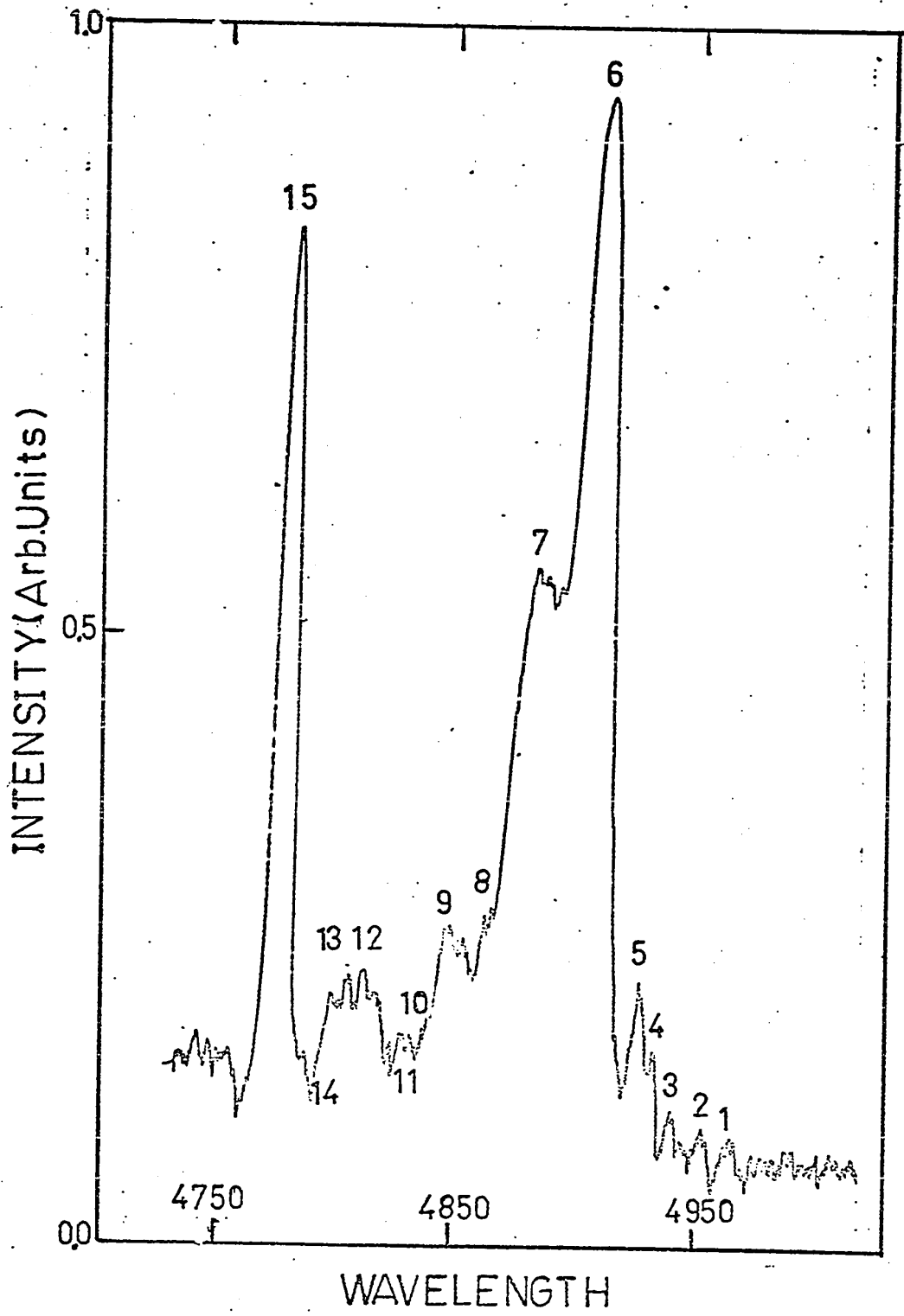
Fig. 3.36   Emission spectrum of CaF_2Pr^{+3} at LNT from 4750 Å
to 4950 Å excited with 4382 Å.
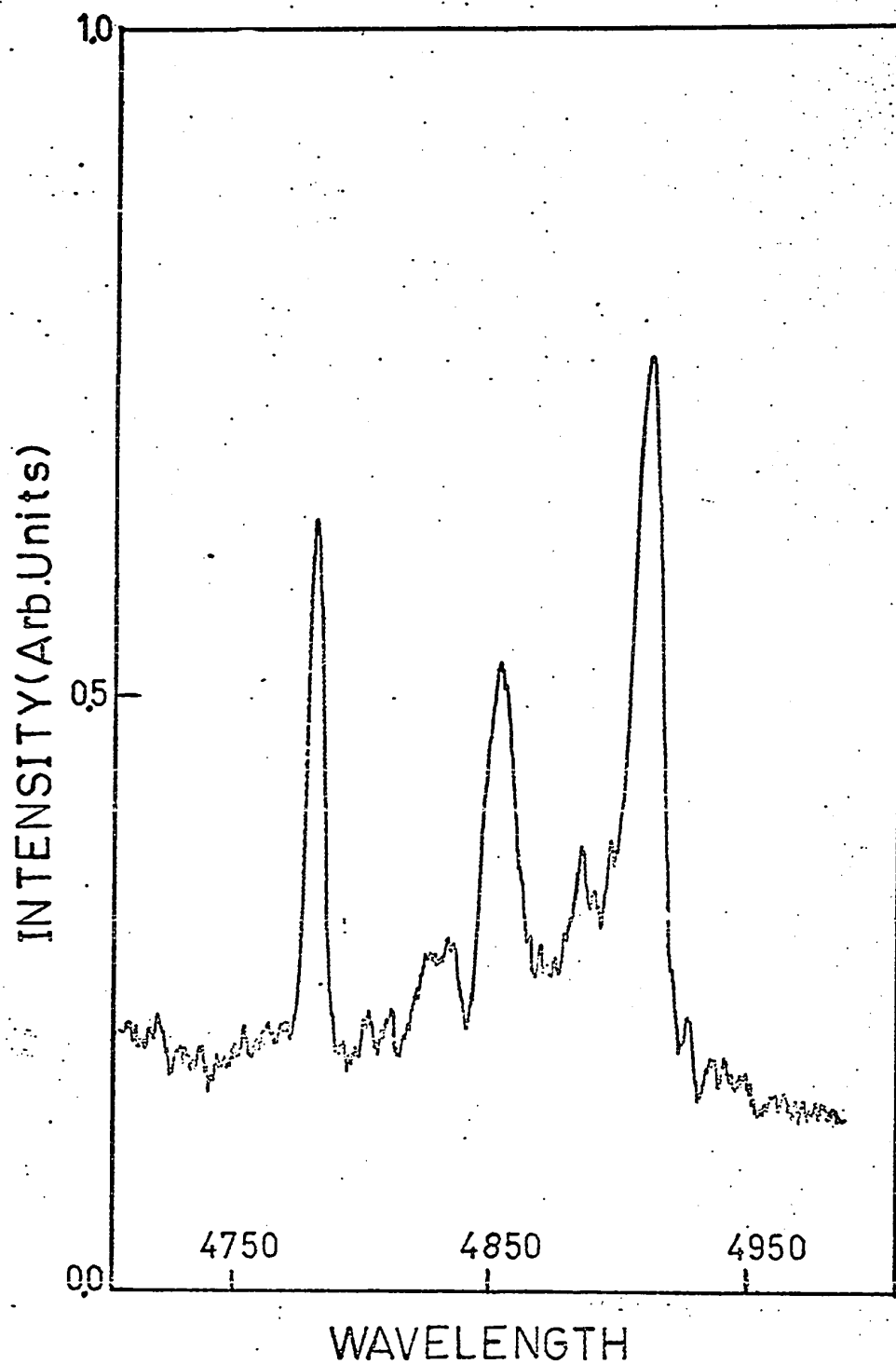
Fig. 3.37 Emission spectrum of CaF_2Pr^{+3} at LNT from 4750 Å
to 4950 Å excited with 4448 Å.
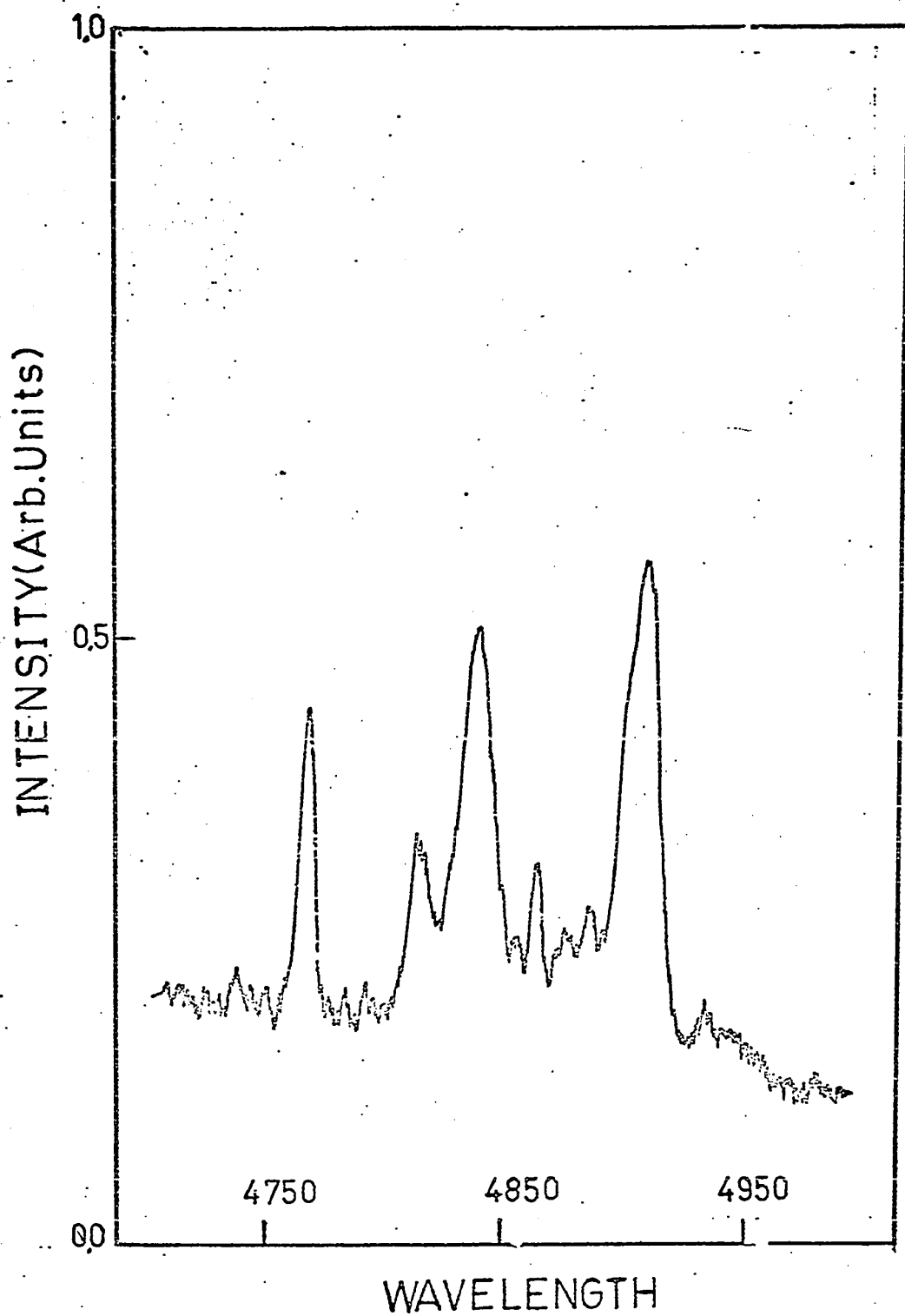
Fig. 3.38   Emission spectrum of CaF_2Pr^{+3} at LNT from 4750 Å
to 4950 Å excited with 4428 Å.
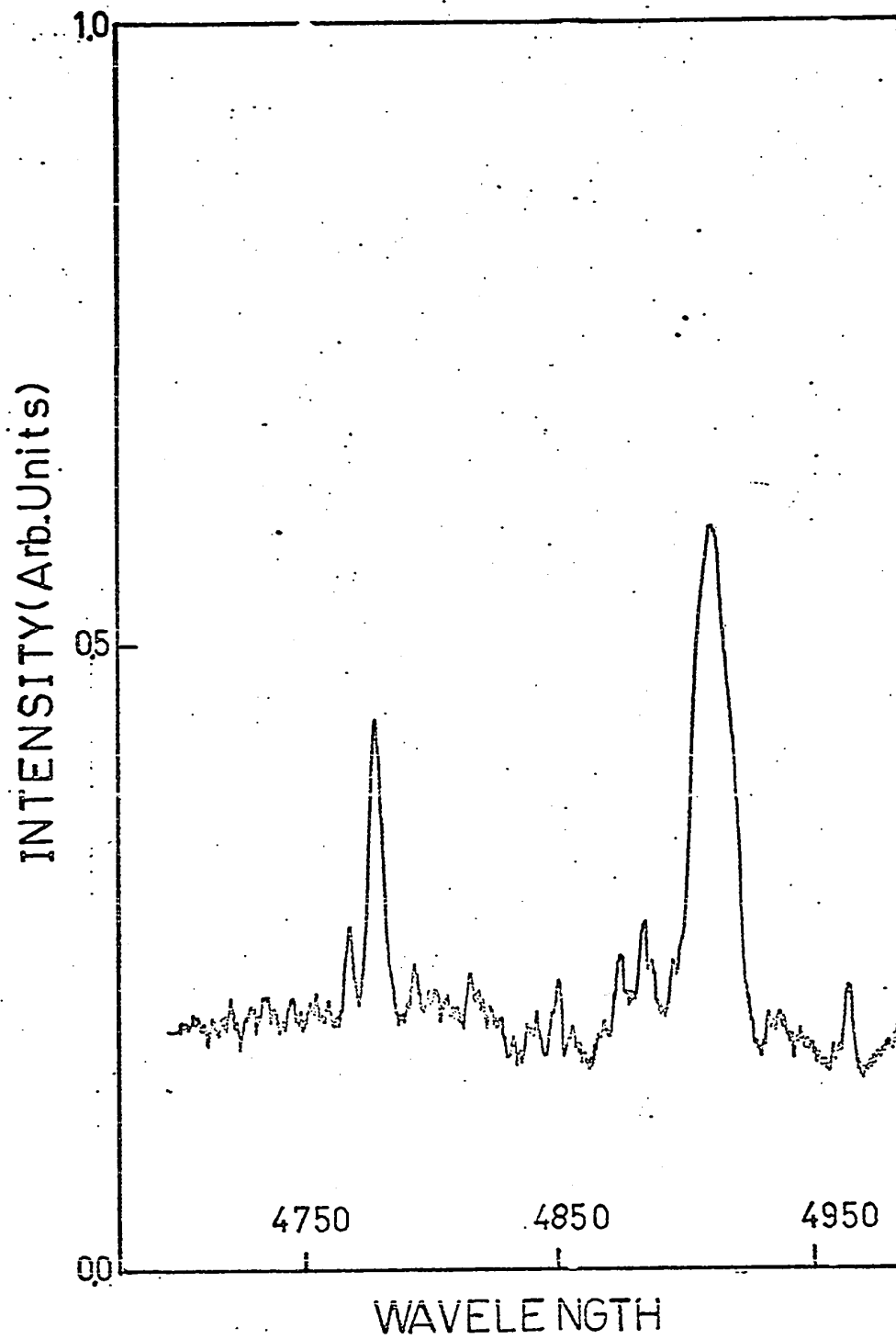
Fig. 3.39 Emission spectrum of CaF_2Pr^{+3} at LNT from 4750Å to 4950 Å excited with 4308 Å.
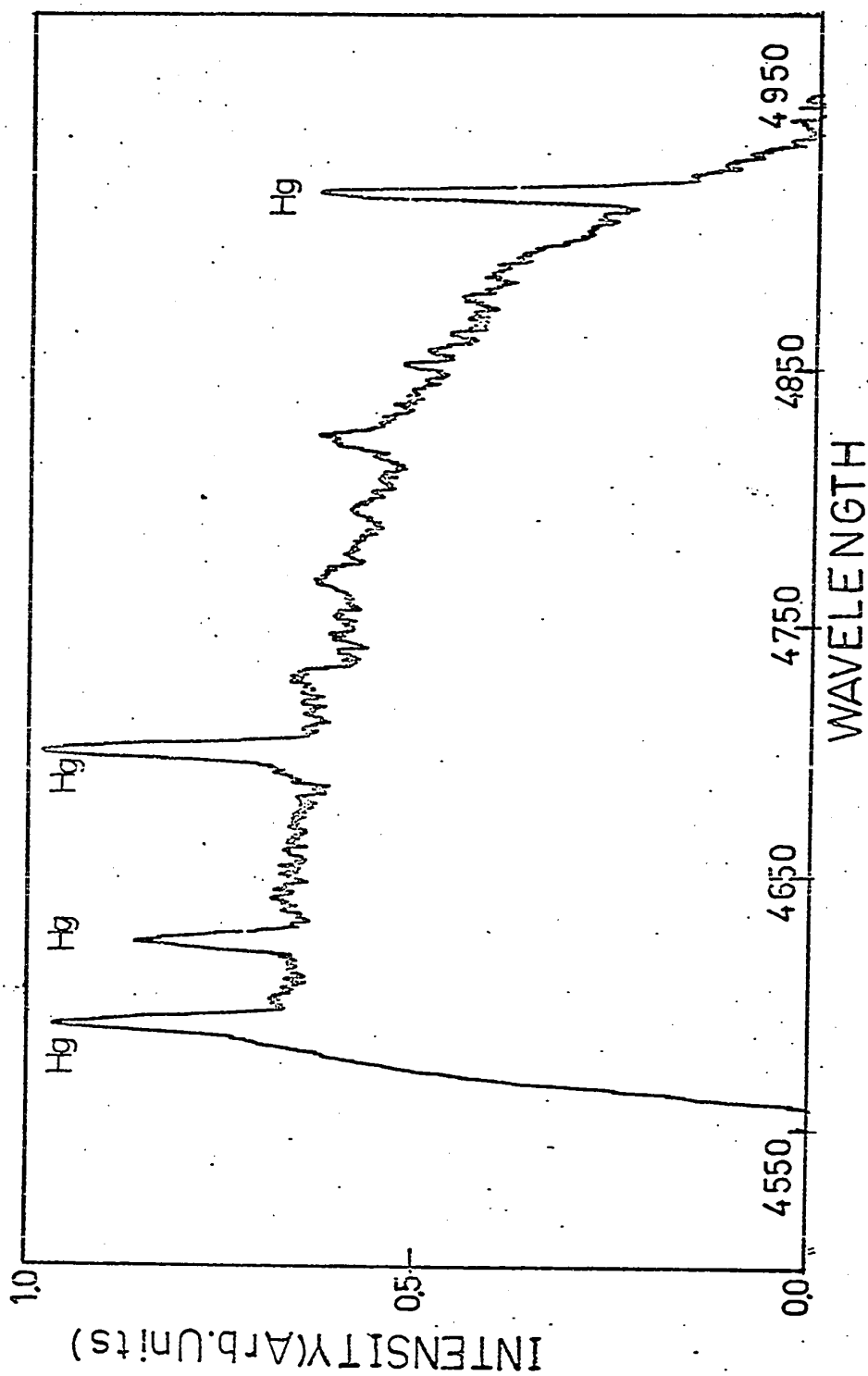
Fig. 3.40 Emission spectrum of $CaF_2 Pr^{+3}$ at LNT from 4550 Å to 4950 Å excited with 3665 Å.

TABLE 3.8

Emission Spectrum of $CaF_2:Pr^{+3}$ at $77^{\circ}K$

SLJ Assignment	Emission Peaks Energy (cm⁻¹)	Wavelength λ (Å)	Peak No.	Centroid (cm⁻¹)	Difference between Expt. and Calc. Values (cm⁻¹)
	20149	4963	1		
	20202	4950	2		
	20259	4936	3		
	20280	4931	4		
	20300	4926	5		
$3P_0$	20387	4905	6		
	20438	4881	7		
	20563	4863	8		
	20618	4850	9		
	20678	4836	10		
	20721	4826	11		
	20764	4816	12		
	20820	4803	13		
$3P_1$	20859	4794	14		
	20951	4773	15		

down to LNT and its temperature was recorded on a strip

chart recorder. Then the crystal was x-irradiated at LNT

for one hour to two hours, as indicated on the figures.

The x-ray tube had a copper target and it was operated at

40 kV and 14 ma.

The general glow curve and its spectral composition

were taken simultaneously in the following way: one of the

windows of the cryostat was held as close as possible against

the entrance slit of the home-made spectrograph, adjusted

to the desired spectral range. An EMI 6256B type photo-

multiplier was placed against the opposite window. A

specially designed camera   loaded with 3-x

Kodak film was fixed on the exit slit of the home-made

spectrograph. This was done in order to get the spectral

composition of emission at different glow peaks. The

temperature of the crystal was recorded continuously on

the strip chart recorder. The photocurrent from the photo-

multiplier was fed to a Keithley type 410 micro-microammeter,

the output of which was recorded by the Hewlett-Packard

strip chart recorder. The heating rate during the experi-

ment was kept constant at (dT/dt = 11 deg/min). For

CaF_2Er^{+3} Fig. 3.41 shows the variation in emission with

temperature. In the case of CaF_2Pr^{+3} (0.1 %), emission

was very weak and we could not record a satisfactory

spectrum above 140°K. We were unable to observe the thermo-

luminescence spectrum of CaF_2Pr^{+3} with concentration; i.e.,

the highest concentration that we could go was 0.5 % and 1%.

Film exposed between
temperatures as
indicated

80°K -- 300°K

80°K -- 140°K

140°K -- 170°K

5350   5450   5550   5650
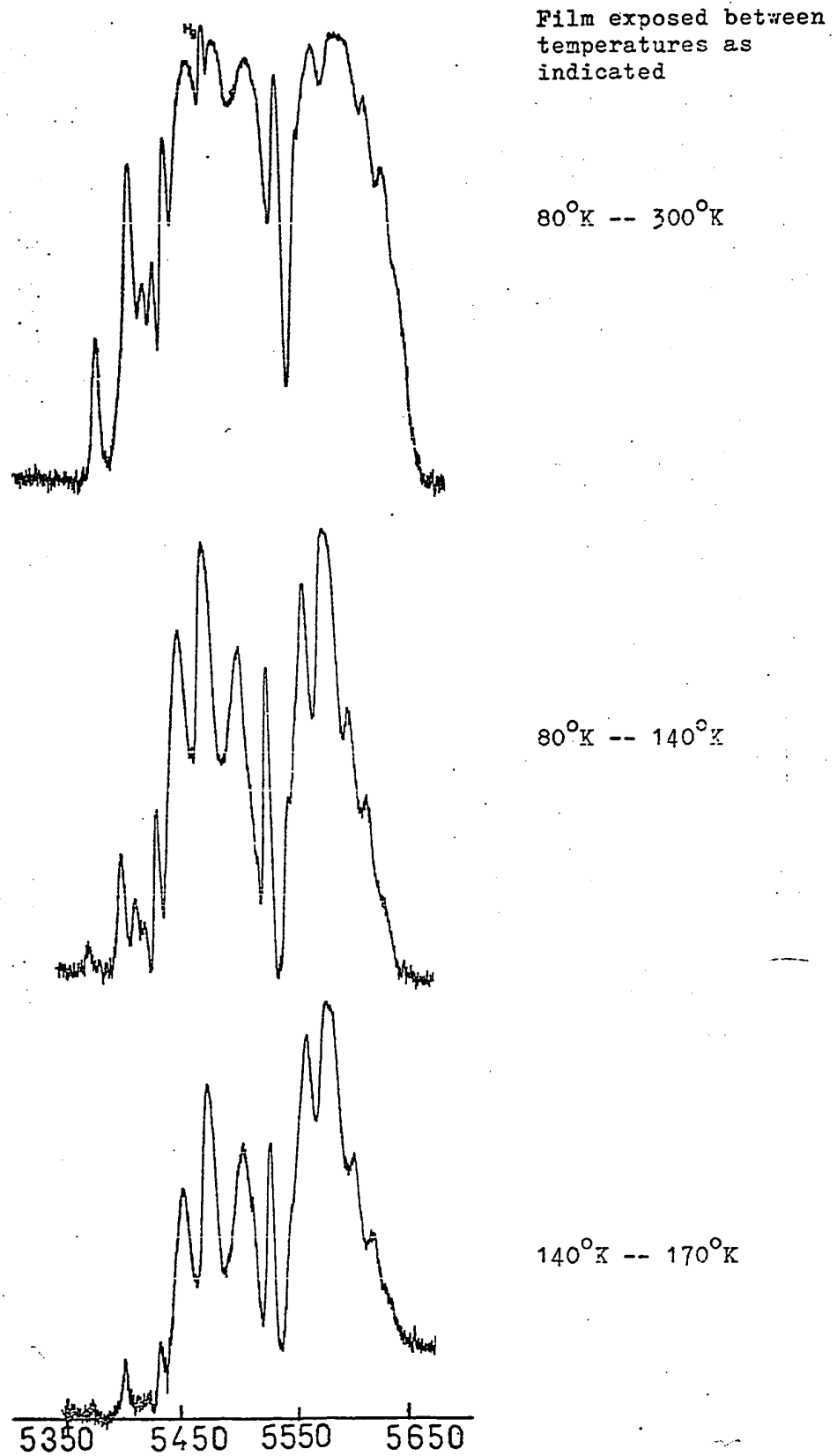
Fig. 3.41(a)   Variation of thermoluminescence emission spectrum
with temperature in CaF$_2$:Er^{+3}

170°K -- 213°K

213°K -- 259°K

259°K -- 282°K

282°K -- 300°K

Hg

5350 5450 5550 5650
WAVELENGTH
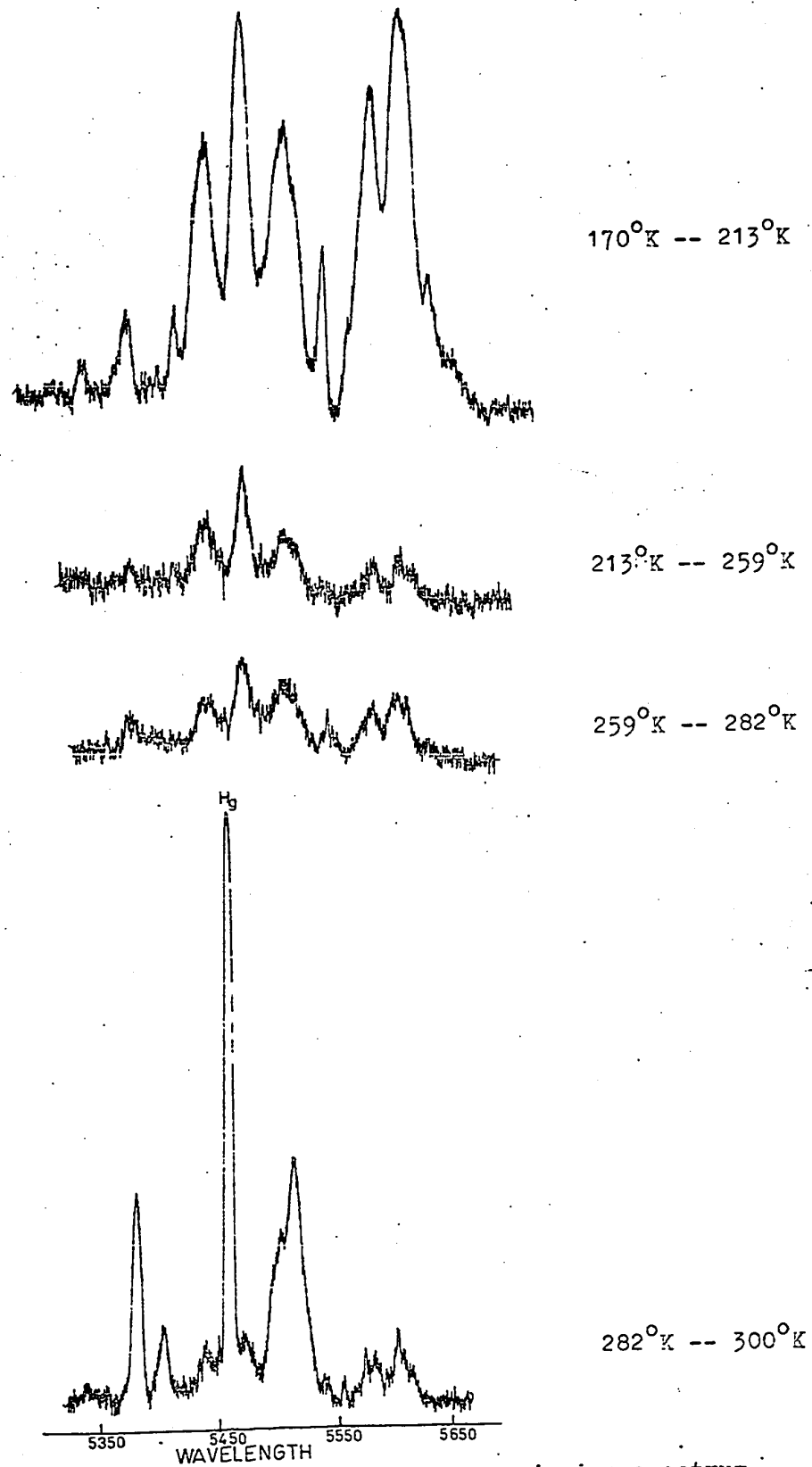
Fig. 3.41(b) Variation of thermoluminescence emission spectrum
with temperature in CaF$_2$:Er^{+3}.

Fig.3.42 is the glow curve of CaF_2Er^{+3} between 77^oK and 310^oK. There are six main glow peaks at 114^oK, 155^oK, 192^oK, 247^oK, 272^oK and 301^oK in the glow curve. Fig. 3.43 is the glow curve of CaF_2Pr^{+3} between 77^oK and 300^oK. There are three main peaks at 114^oK, 157^oK and 235^oK in the glow curve. The microdensitometer traces of thermoluminescence emission spectrum of CaF_2Er^{+3} and that of CaF_2Pr^{+3} are shown in Figs.3.44 and 3.45, respectively. Peaks have been numbered for future use and their energies are expressed in cm^{-1} in Tables 3.9 and 3.10.

The activation energies for the thermoluminescent peaks were calculated by using the formula (3)

$$E = k\, T_g^{2}/(T_2 - T_g) \quad ,$$

where E (ev) is the activation energy, k is Boltzmann's constant, T_g (k) is the temperature of the glow peak maximum and T_2 is the temperature at half intensity on the high temperature side of the peak. The value of activation energy for CaF_2Er^{+3} and CaF_2Pr^{+3} is presented in Tables 3.11 and 3.12, respectively. The varying activation energies corresponding to the different glow peaks show the presence of traps with different activation energies in the crystal.
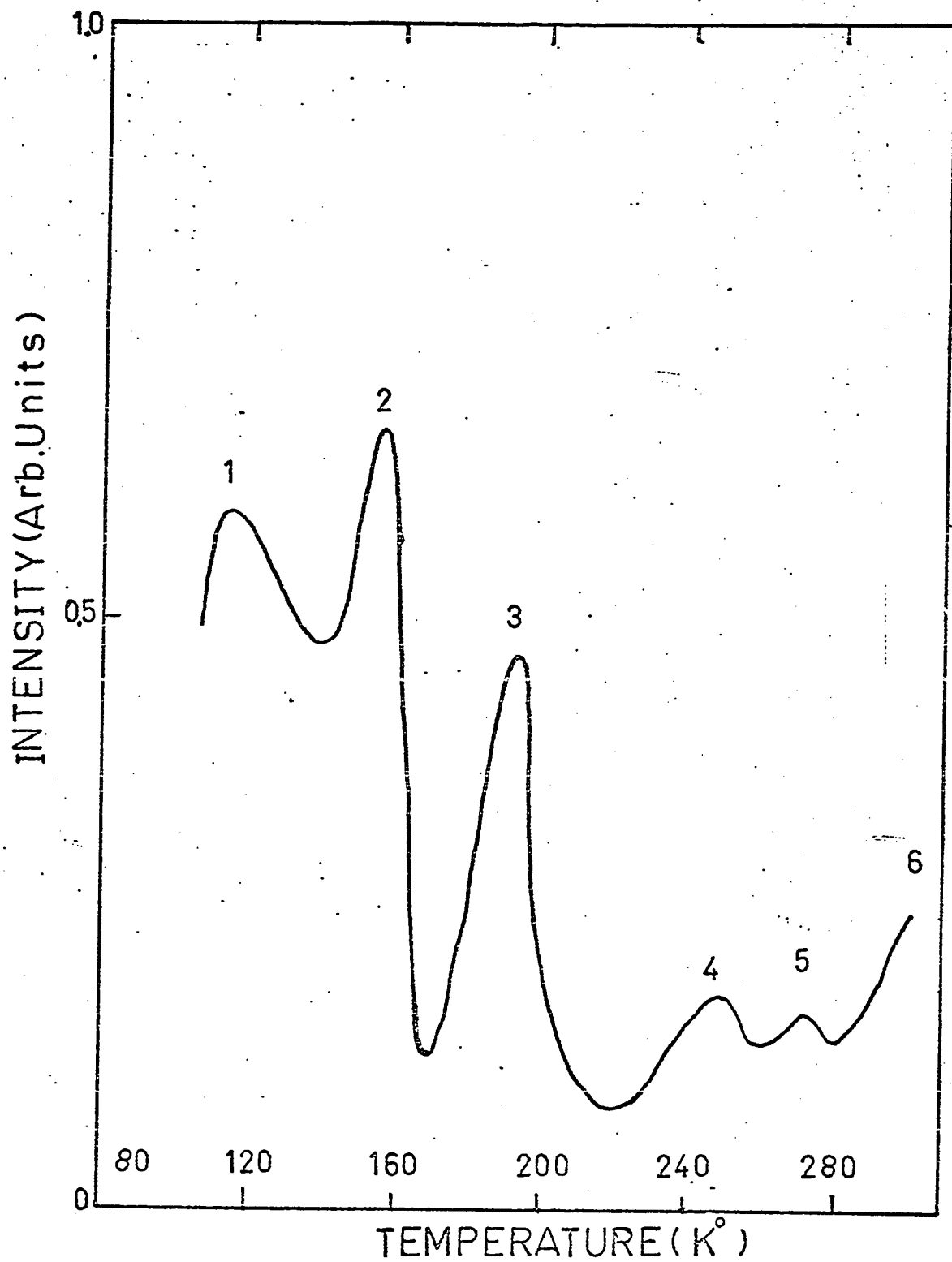
Fig. 3.42   Thermoluminescence glow curve of CaF_2Er^{+3}.
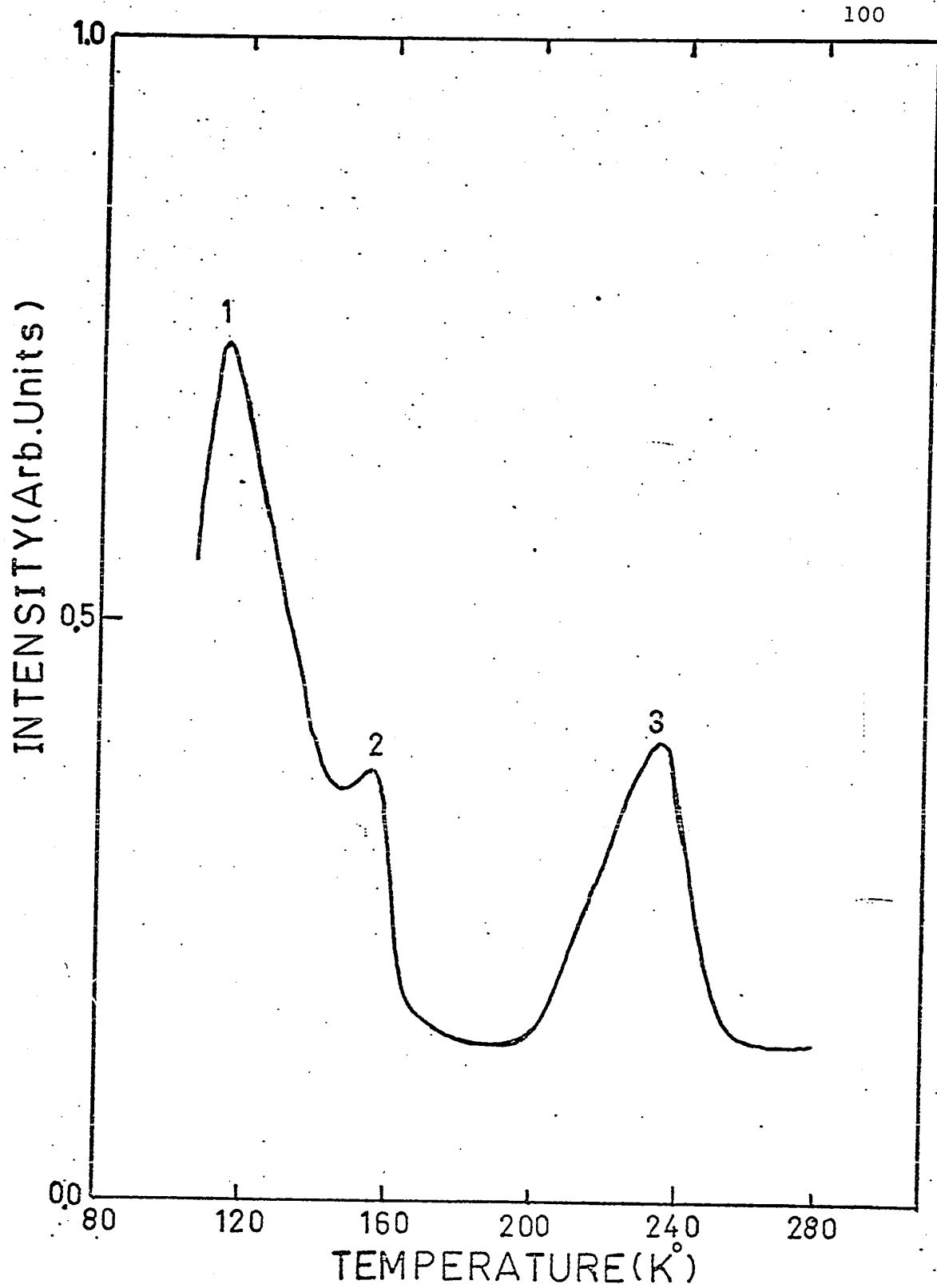
Fig. 3.43   Thermoluminescence glow curve of CaF_2Pr^{+3}.
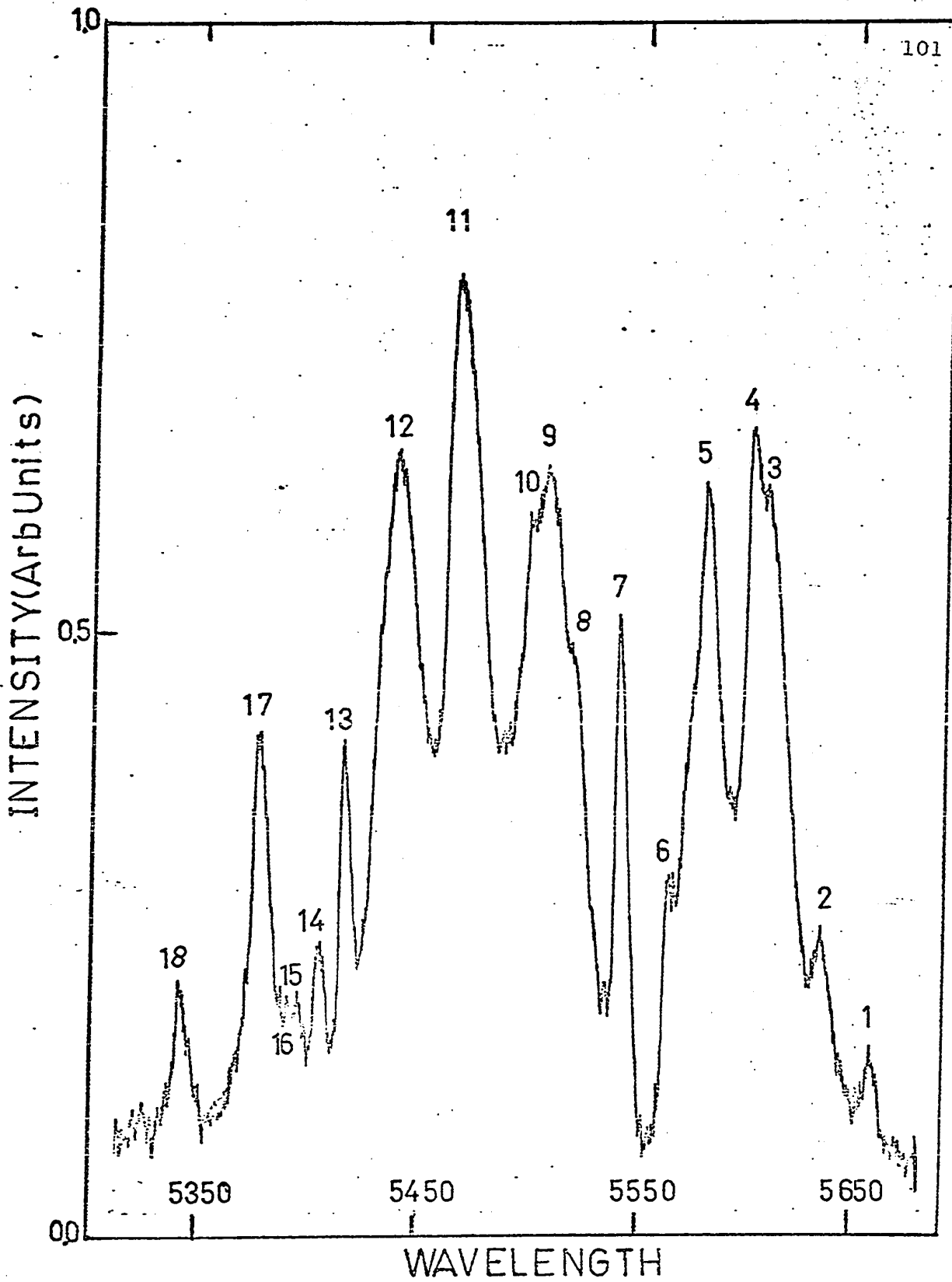
Fig. 3.44 Spectral composition of the thermoluminescence of CaF$_2$Er^{+3} in the green spectral region.

TABLE 3.9

Thermoluminescence Spectrum of CaF_2Er^{+3}

Transition	Thermoluminescence Peaks Energy (cm^{-1})	Wavelength λ (A)	Peak No.	Centroid (cm^{-1})	Differences between Expt. and Calc. Energy Values (cm^{-1})
	17670	5659	1		
	17736	5638	2		
	17793	5620	3		
	17812	5614	4		
	17901	5586	5		
	17943	5573	6		
	18034	5545	7		
$^4S_{3/2} \rightarrow {}^4I_{15/2}$	18109	5522	8		
	18135	5514	9		
	18152	5509	10		
	18272	5473	11		
	18372	5444	12		
	13450	5419	13		
	18508	5403	14		
	18542	5393	15		
	18552	5390	16		
	18608	5375	17		
	18733	5338	18		
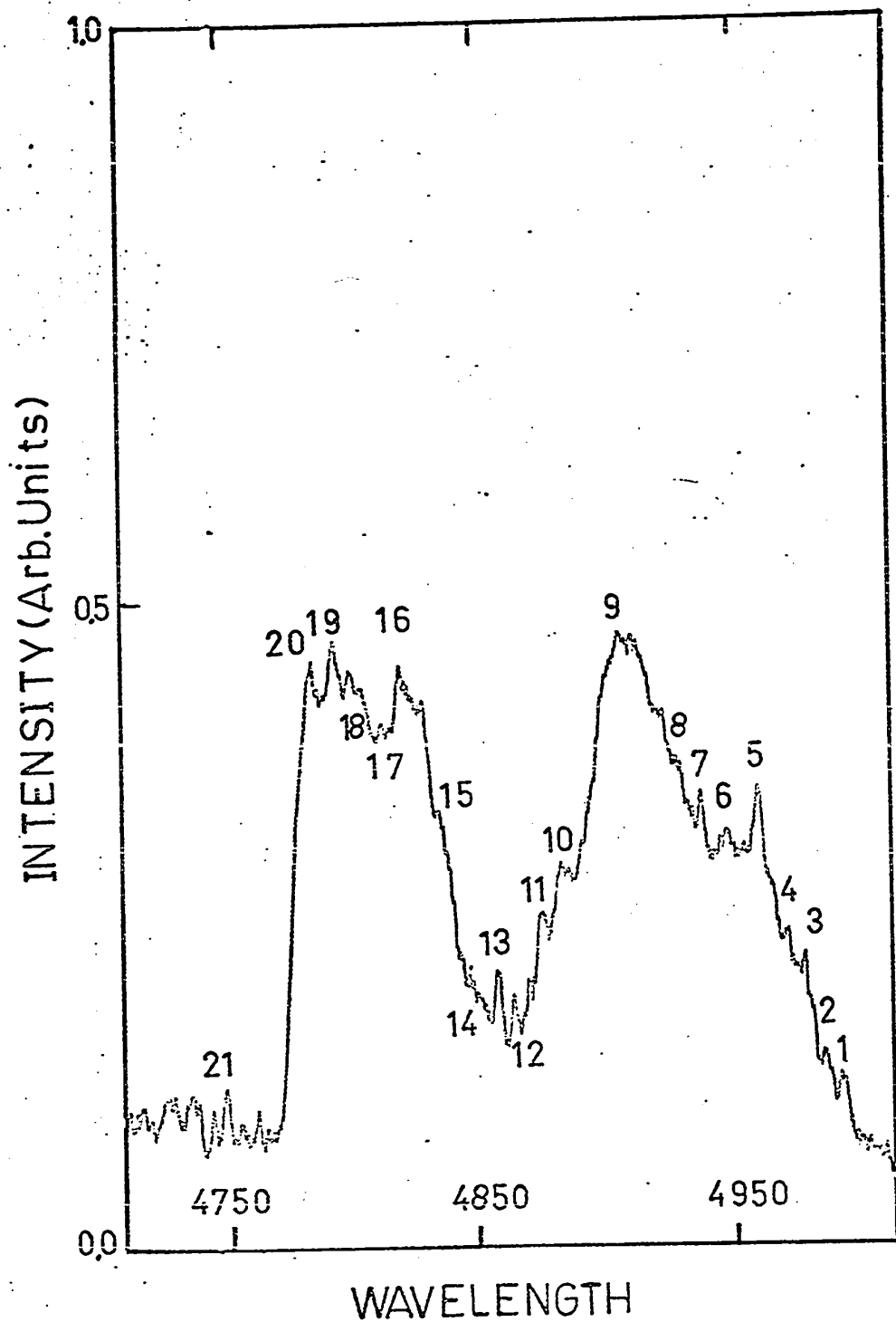
Fig. 3.45   Spectral composition of the thermoluminescence
of CaF_2Pr^{+3} in the blue-green spectral region.

TABLE 3.10

Thermoluminescence Spectrum of CaF$_2$Pr^{+3}

SLJ Assignment	Thermoluminescence Peaks Energy (cm^{-1})	Wavelength λ (Å)	Peak No.	Centroid (cm^{-1})	Difference between Expt. and Calc. Values (cm^{-1})
	20032	4992	1		
	20056	4986	2		
	20084	4979	3		
	20116	4971	4		
	20149	4963	5		
	20202	4950	6		
	20251	4938	7		
	20292	4928	8		
^{3}P$_0$	20387	4905	9		
	20488	4881	10		
	20512	4875	11		
	20563	4863	12		
	20584	4858	13		
	20618	4850	14		
	20678	4836	15		
	20721	4826	16		
	20764	4816	17		
	20820	4803	18		
	20859	4794	19		
^{3}P$_1$	20951	4773	20		
	21066	4747	21		

TABLE 3.11

Activation Energies of Thermoluminescent

Peaks in CaF_2Er^{+3} (0.1%)

Peak No. (see Fig.)	T_g (°K)	T_2 (°K)	Activation Energy (ev)
1	114	125	0.10
2	156	160	0.52
3	192	197	0.63
4	247	253	0.87
5	272	276	1.59
6	302		

TABLE 3.12

Activation Energies of Thermoluminescent

Peaks in CaF_2Pr^{+3} (0.1%)

Peak No. (see Fig.)	T_g (°K)	T_2 (°K)	Activation Energy (ev)
1	113	122	0.12
2	156	159	0.7
3	235	243	0.59

Chapter 4   ABSORPTION SPECTRA

4.1 Monochromator Model 225

The Model 225 spectrograph works on the principle
that the grating is constrained to move along the bisector
of the angle subtended by the slits, at the centre of the
grating, while simultaneously the grating is rotated about
a vertical axis tangent to its centre. The rotation of the
grating provides the monochromatic action, whereas the
linear motion of the grating determines the degree of
focussing.

The Model 225 consists of a stainless steel chamber
which can be pumped down to 3×10^{-7} torr by means of a high
speed diffusion pump and mechanical pump. The flap valves
with external controls are mounted in the entrance and
exit slit housings in order to isolate the slit chambers
from the main chamber while maintaining the vacuum in the
main chamber. The monochromator is also equipped with a
600 lines/mm, MgF_2 coated grating of focal length one meter
and an aperture ratio f/12. The wavelength can be read
directly in angstroms and this model can be used from 300 Å
to 6000 Å with an automatic focussing throughout the entire
wavelength range. The angle between the normal to the
grating and entrance slit or exit slit is $7^{\circ}-30'$.

106

4.2 (a) Vacuum U.V. Light Source

The light sources may be classified according to
the spectrum they emit, as continuous or discontinuous.
With the exception of synchroton radiation, there is no
single light source which will satisfy all the experimental
requirements for the vacuum ultraviolet region. The light
source in the ultraviolet region must be able to operate
either in the high vacuum or at the low pressure. The
choice of the source depends upon its application. The
light source which has been used in our experiment is a
high vacuum U.V. Hinteregger type discharge lamp, Model 630
supplied by McPherson Instrument Corporation. The discharge
lamp consists of a water cooled quartz capillary, a water
cooled anode and a forced air cooled cathode. This discharge
source is capable of handling 1000 watts of energy
continuously and up to 800 watts intermittently. The source
can be mounted directly on the entrance slit of the McPherson
225. There are also separate provisions for the gas and
water inlets and outlets, as shown in Fig. 4.1.

(b) Xe, Ar Continuum and the Operation

The light source was mounted on the entrance slit
and a home-made cryostat was fixed on the exit slit of the
monochromator. A photomultiplier, Model 650 supplied by
McPherson Instrument Corporation, was fixed on the other
side of the cryostat. The monochromator was evacuated with
the diffusion pump, No. 0162-2 provided by N.R.C., and a
mechanical pump, Model 500 supplied by Precision Scientific

Water cooled anode 1
Air cooled cathode 2
Gas inlet & outlet 3,4
Water inlet & outlet 5,6
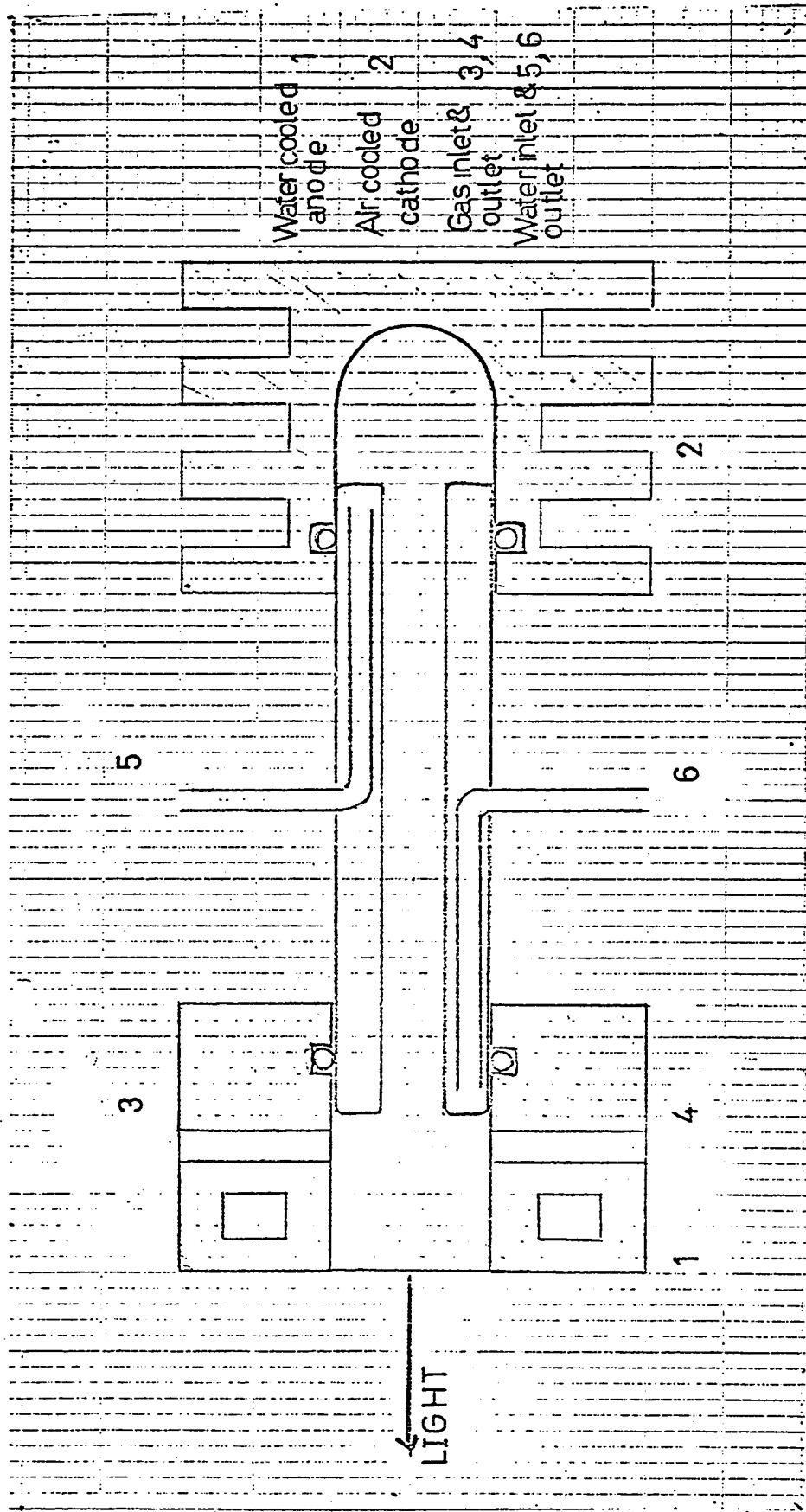
LIGHT

Fig. 4.1 U.V. light source.

Company. The pressure thus obtained was always better than
10^{-7} torr at all times.

The light source and the cryostat were also evacuated
by means of a diffusion pump and the mechanical pump, till
the pressure in this system was better than 10^{-4} torr. The
gas pressure in the light source was controlled by the
throttling valve. Xe gas was supplied by Union Carbide
Company while the argon gas was supplied by Liquid Carbonic
Canadian Corporation. The purity of the gas claimed by
each company was 99.9999%.

The cryostat was cut off from the vacuum line and
the gas pressure in the light source was adjusted to less
than 10 torr in order to start the source. The power
needed for the light source was supplied from a DCR300-.5
power supply. After starting the source, the gas pressure
was slowly increased to 200 torr, the voltage was adjusted
to 2 kV and the current to 200 ma. Five to ten minutes
later, the photocurrent from the photomultiplier Model 650
was fed to a Keithley type 410 micro-microammeter, the
output of which was recorded by a strip chart recorder
Model 7128A obtained from Hewlett-Packard. Fig. 4.2 shows
the continuum of xenon in the spectral region 1500 Å to
2000 Å and Fig. 4.3 shows the continuum of argon from 1800 Å
to 2600 Å. We did observe the continuum of argon from
1200 Å to 1500 Å by mounting the photomultiplier directly
on the exit slit of the monochromator. Fig. 4.4 shows the
continuum of argon from 1200 Å to 1500 Å.
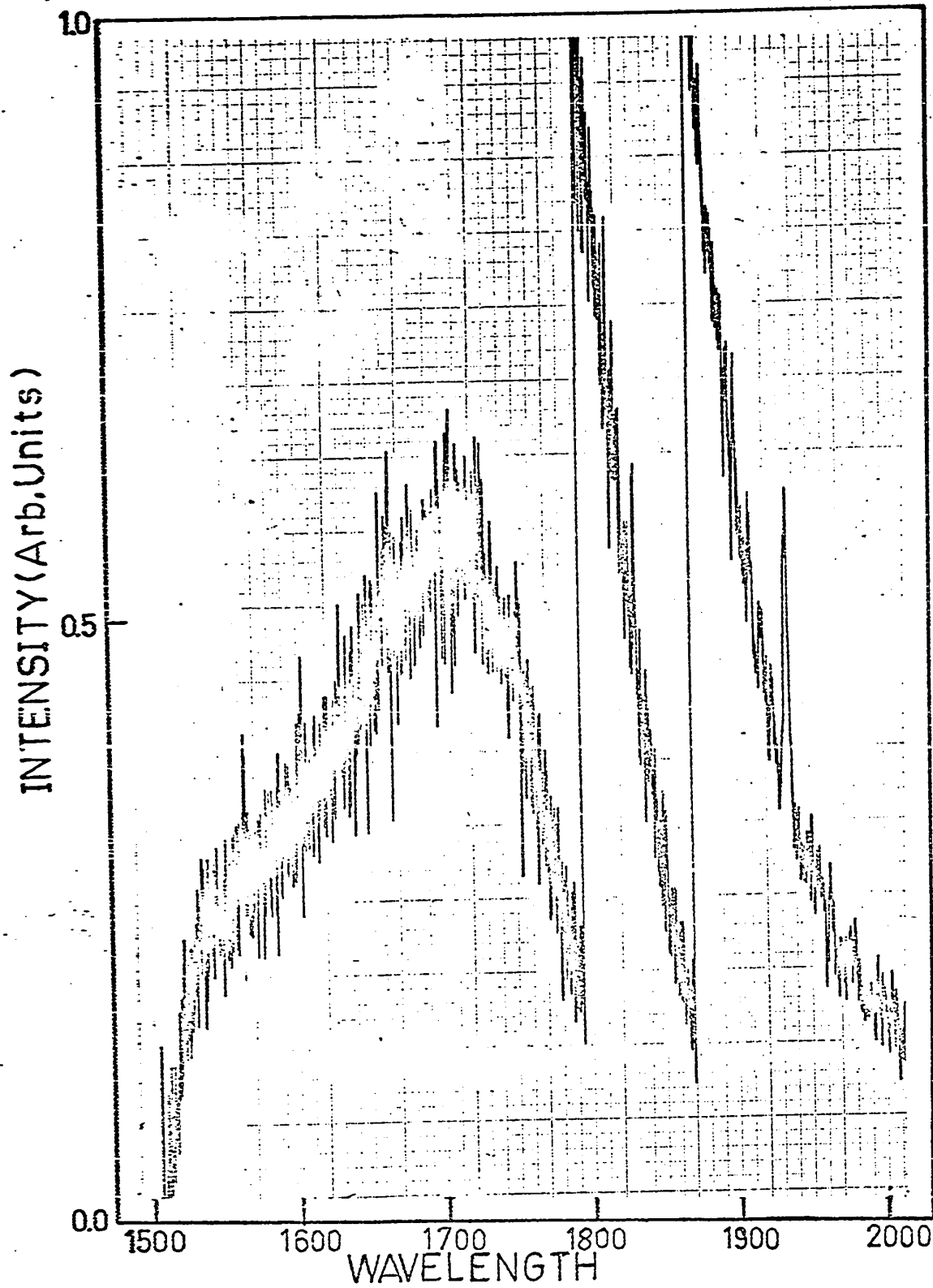
Fig. 4.2   Xenon continuum from 1500 Å to 2000 Å.
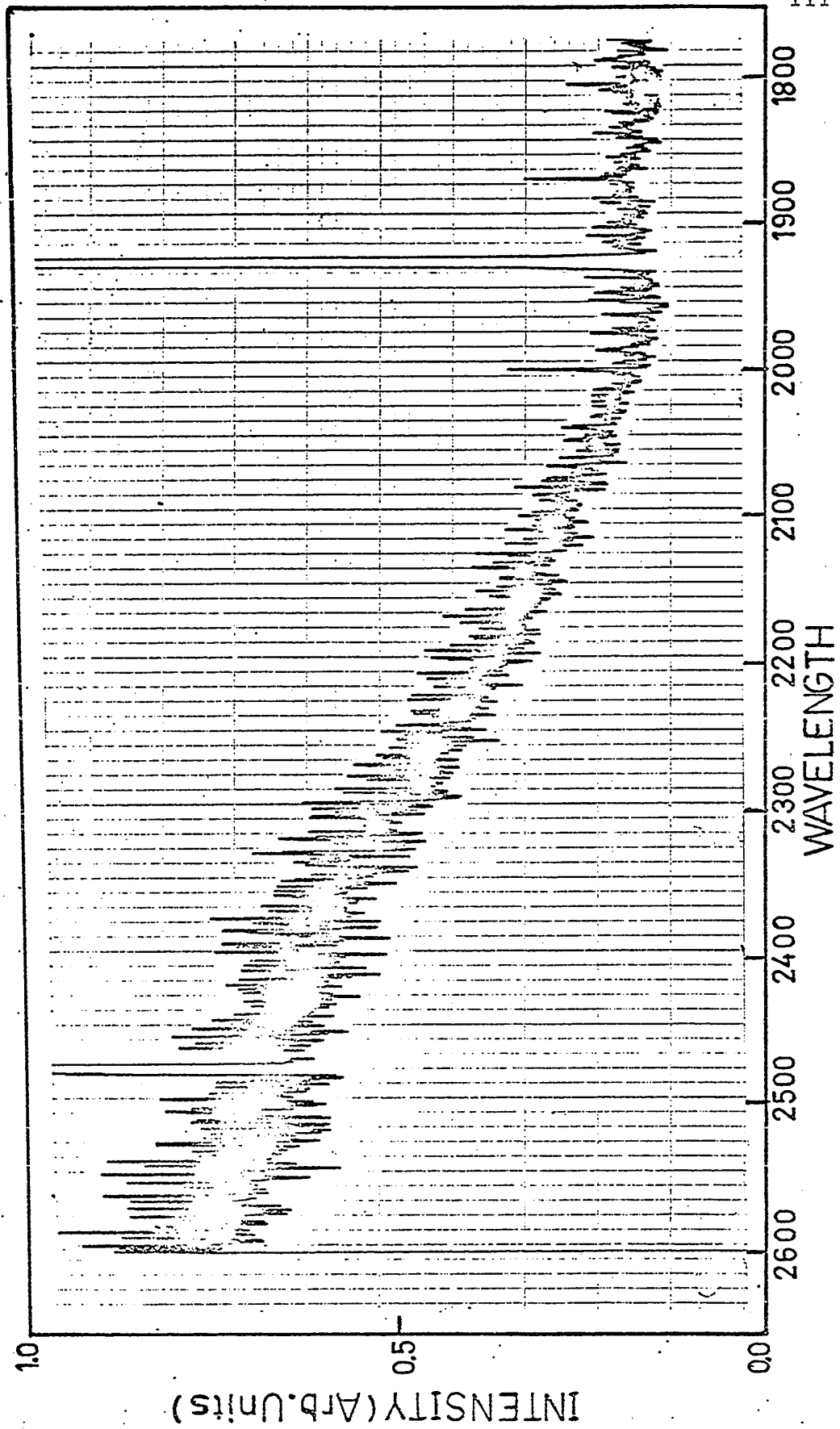
Fig. 4.3 Argon continuum from 1800 Å to 2600 Å.
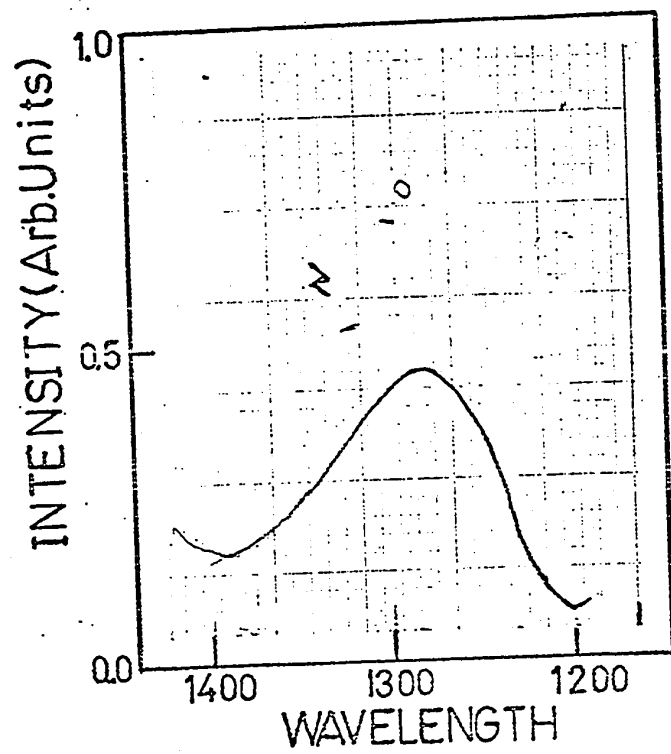
Fig. 4.4 Argon continuum from 1200 Å
to 1400 Å.

4.3 Absorption Spectra of CaF_2Er^{+3} and CaF_2Pr^{+3}

The experimental set-up for recording absorption spectrum is shown in Fig. 4.5. CaF_2 windows were used on the entrance and exit slits of the monochromator,

(a) In the U.V. Region

Crystals of CaF_2 doped with 1% Er^{+3} and 1% Pr^{+3} were obtained from Optov Incorporated. The crystal 10 x 4 mm was held in the crystal holder of the home-made vacuum cryostat. The absorption spectra of CaF_2Er^{+3} from 1500 to 1800 Å and from 1800 to 2600 Å were recorded at RT and LNT by using Xe gas and argon gas in the discharge lamp. The results are shown in Figs. 4.6 to 4.9. Peaks have been numbered and their energies are expressed in cm^{-1} in Table 4.2. A summary of these figures is given in Table 4.1.

The absorption measurements of CaF_2Pr^{+3} were also carried out at RT and LNT. The results were not satisfactory.

(b) In the Visible and Infrared Regions

The crystal 10 x 4 mm was held in the crystal holder of an Andonian custommade vacuum cryostat. The absorption spectra of CaF_2Er^{+3} and CaF_2Pr^{+3} were recorded at room temperature and at LNT with a Cary Model 14 spectrophotometer. The tail of the cryostat was adapted to fit the sample compartment of the spectrophotometer.

The absorption spectrum of CaF_2Er^{+3} from 2000 to 16000 Å at LNT is shown in Figs. 4.10 to 4.17. Peaks have been numbered and their values are expressed in cm^{-1} in Table 4.2. A summary of these figures is given in Table 4.1.

Power Supply — 1
UV Light Source — 2
Mechanical Pump — 3
Throttling Valve — 4
Gas Cylinder — 8
Cell — 10

For other parts see Fig. 3.2
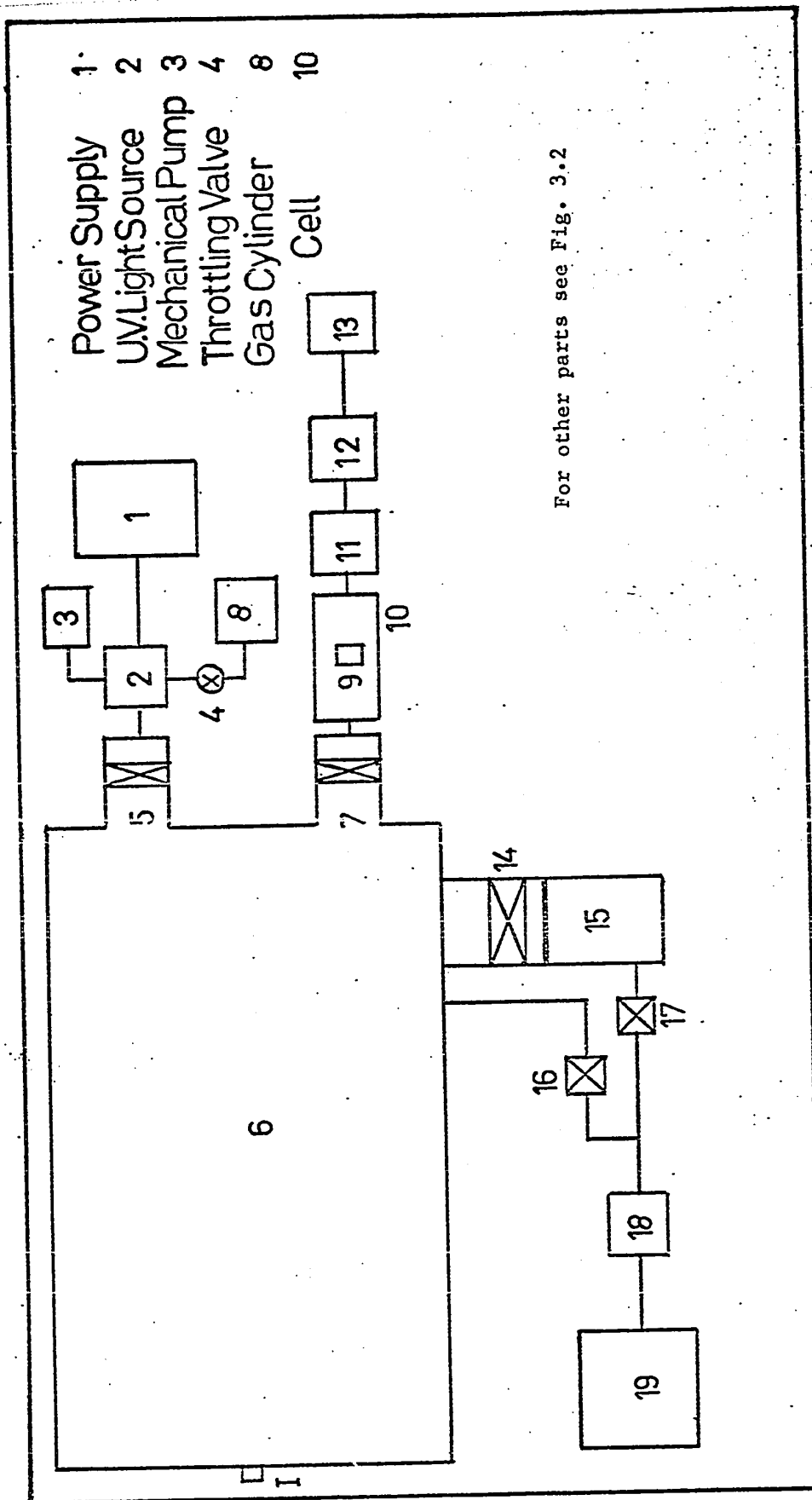
Fig. 4.5 Experimental set-up for recording absorption spectrum.

TABLE 4.1

Summary of the Figures Regarding the Absorption

Spectrum of CaF_2Er^{+3} (1%)

Fig. No.	Crystal	Temperature	Spectral Range
4.6	As-received	RT	1500 Å to 2000 Å
4.7	" "	"	1900 Å to 2800 Å
4.8	" "	LNT	1500 Å to 2000 Å
4.9	" "	"	1900 Å to 2800 Å
4.10	" "	"	14400 Å to 16000 Å
4.11	" "	"	7900 Å to 10300 Å
4.12	" "	"	6350 Å to 6650 Å
4.13	" "	"	5050 Å to 5450 Å
4.14	" "	"	4350 Å to 4950 Å
4.15	" "	"	3500 Å to 4100 Å
4.16	" "	"	2850 Å to 3150 Å
4.17	" "	"	2300 Å to 2750 Å
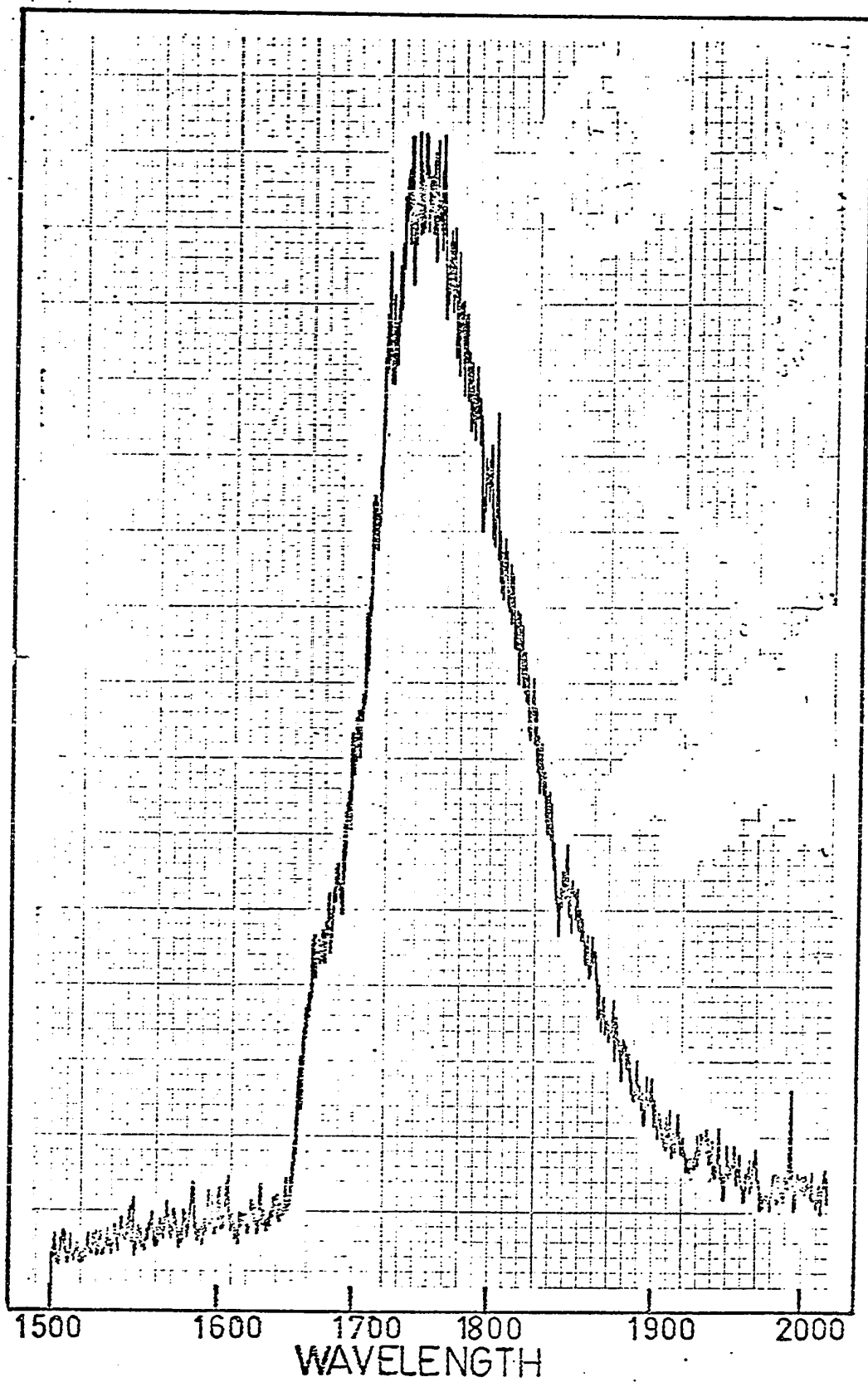
Fig. 4.6   Absorption spectrum of CaF_2Er^{+3} at RT from 1500 Å to 2000 Å.
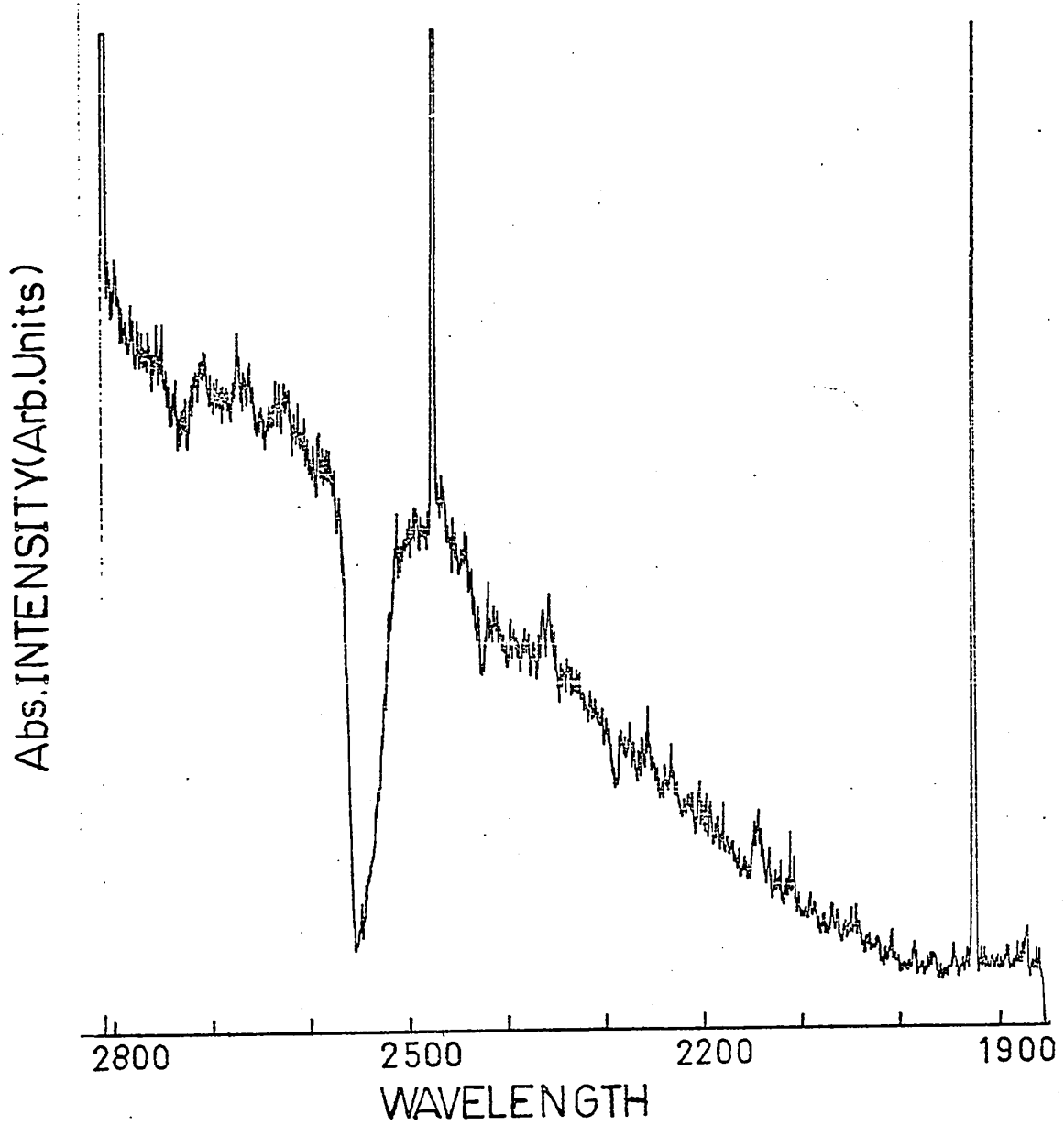
Fig. 4.7 Absorption spectrum of CaF_2Er^{+3} at RT from 1900 Å to 2800 Å.
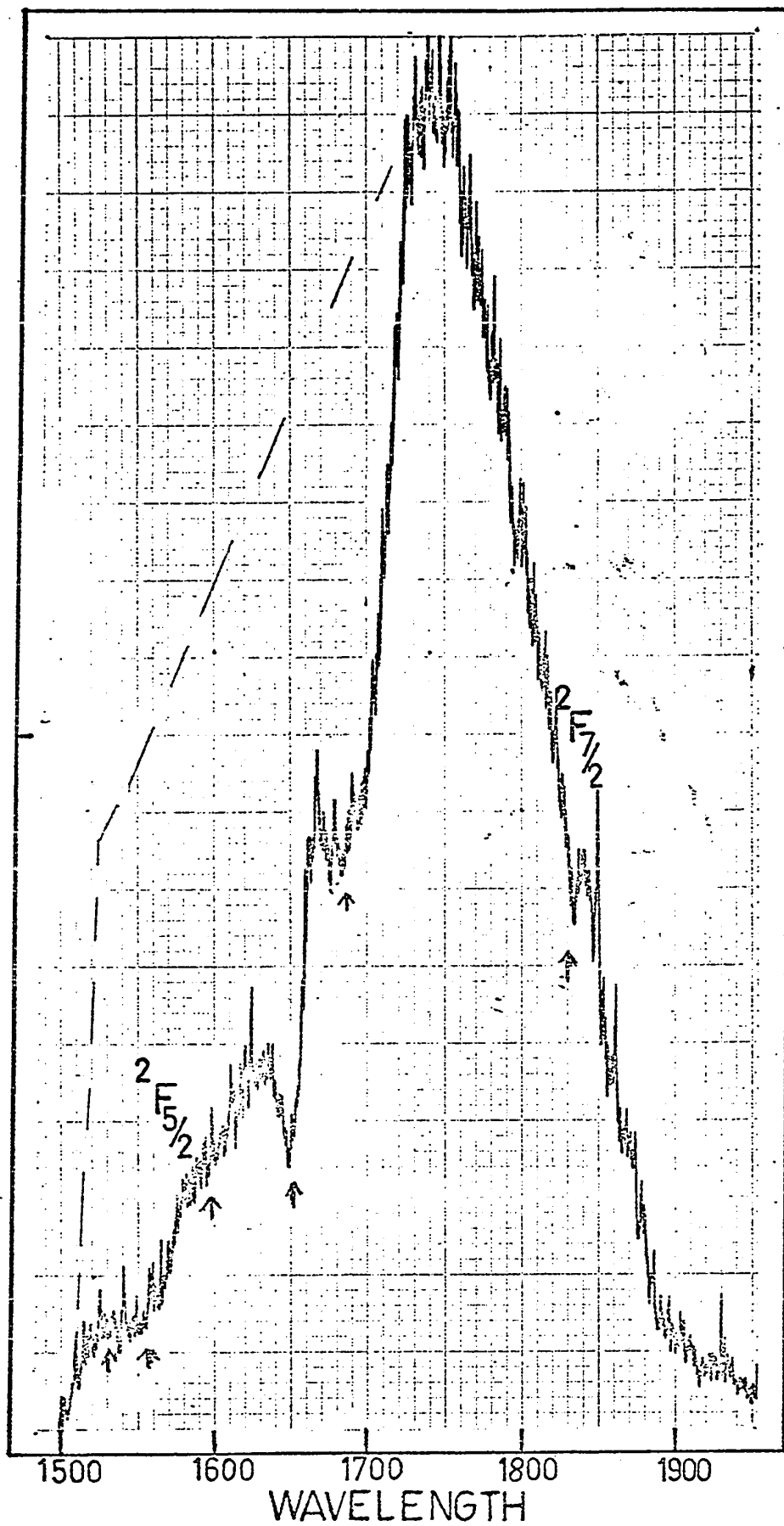
Fig. 4.8   Absorption spectrum of CaF_2Er^{+3} at LNT from 1500Å to 2000 Å.
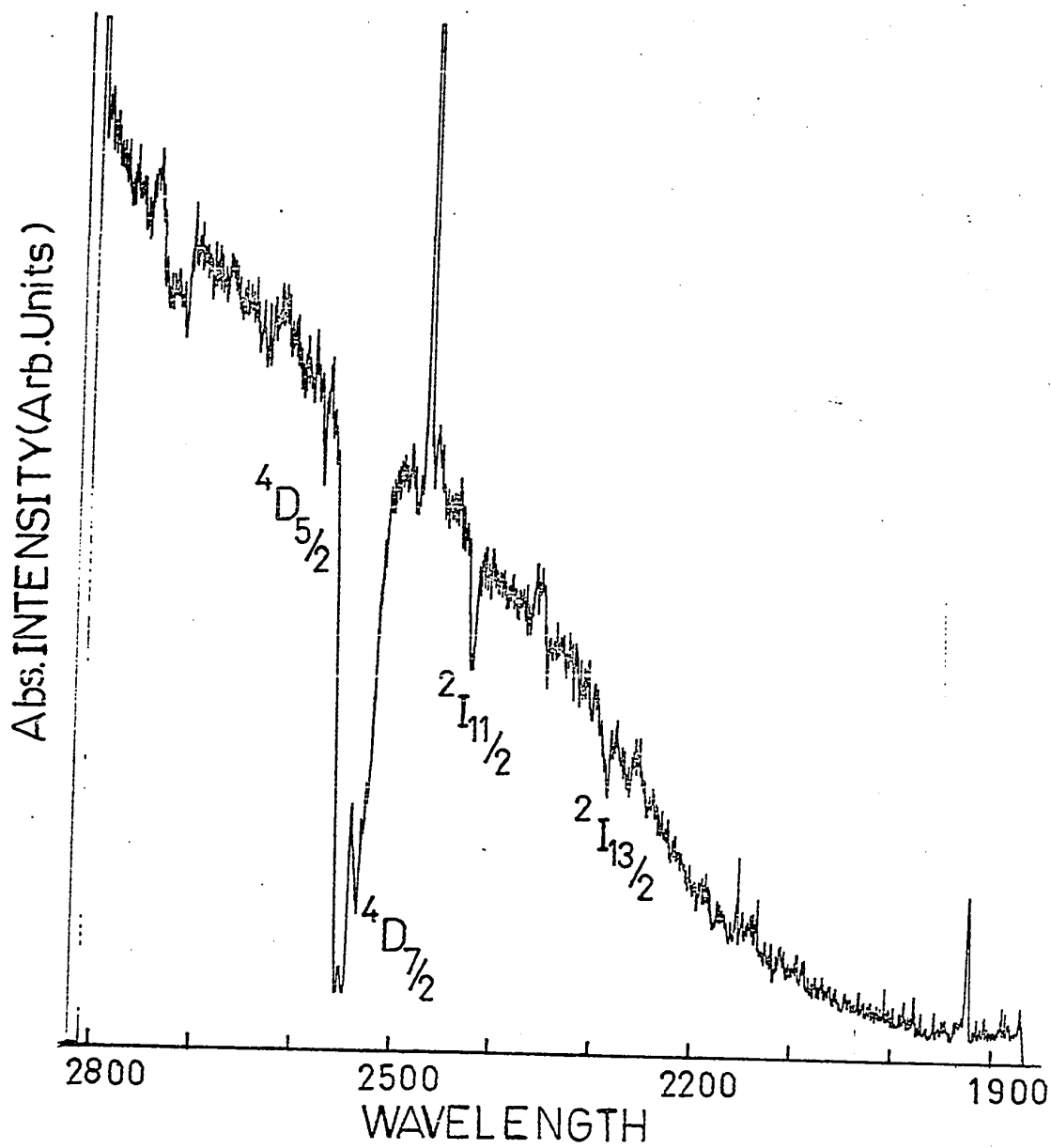
Fig. 4.9 Absorption spectrum of CaF_2Er^{+3} at LNT from 1900 Å to 2800 Å.
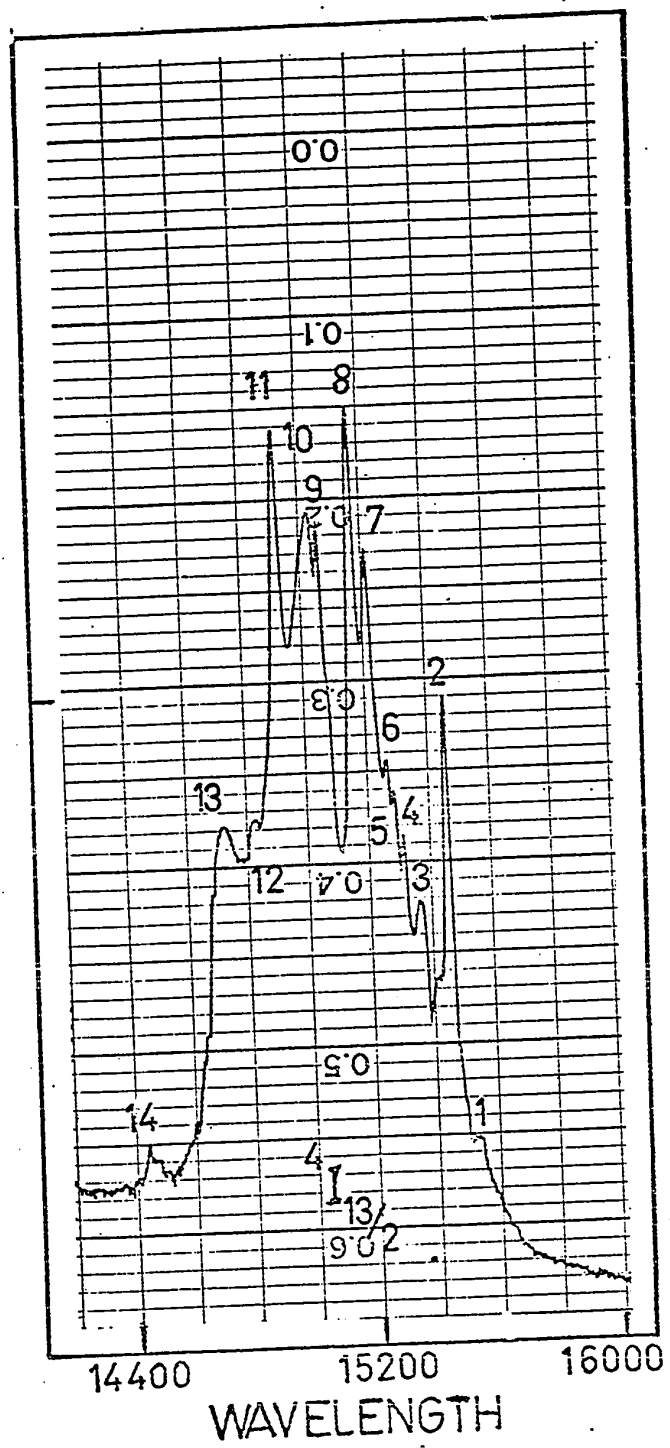
Fig. 4.10 Absorption spectrum of CaF_2Er^{+3} at LNT from 14400 Å to 16000 Å.
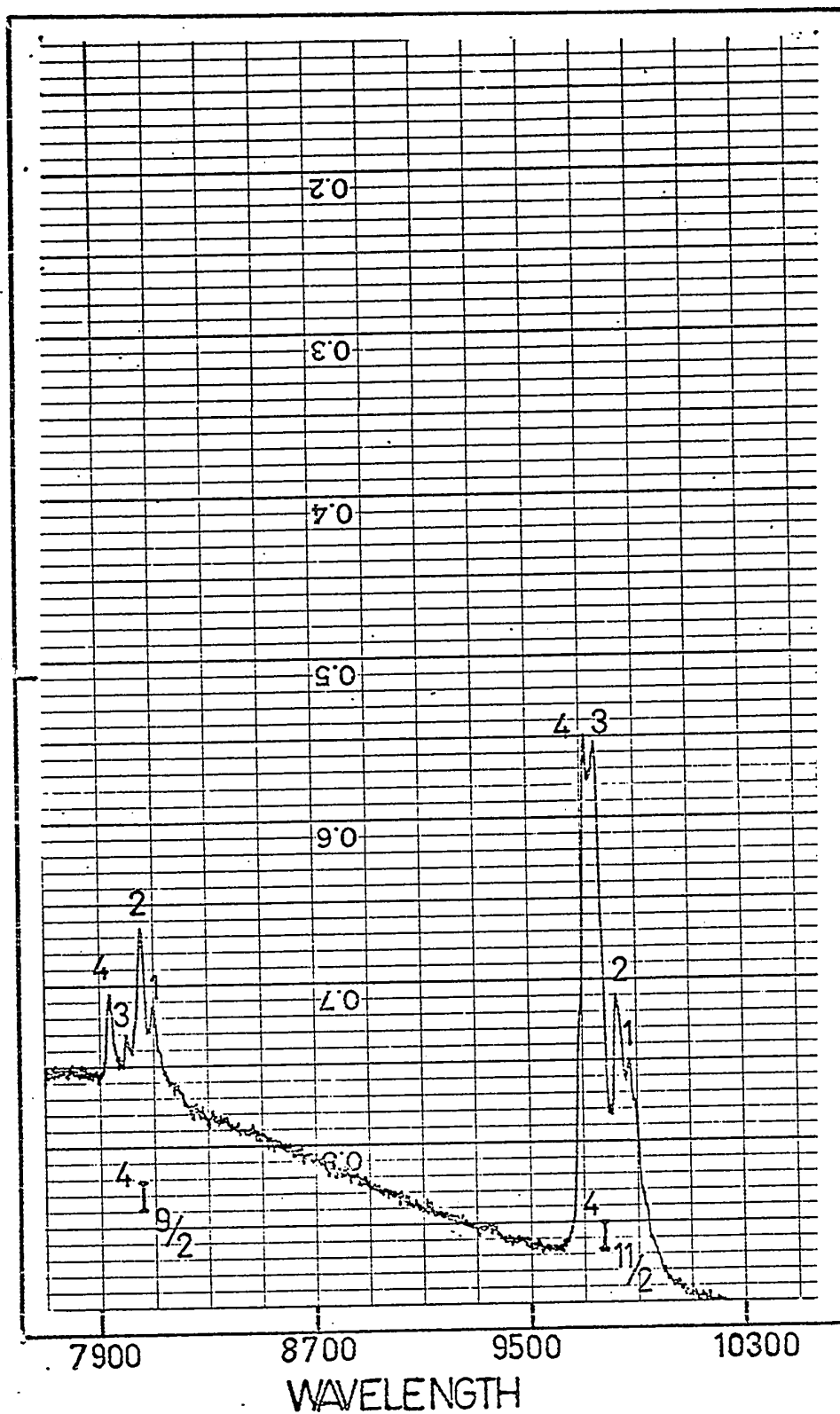
Fig. 4.11   Absorption spectrum of CaF_2Er^{+3} at LNT from 7900 Å to 10300 Å.
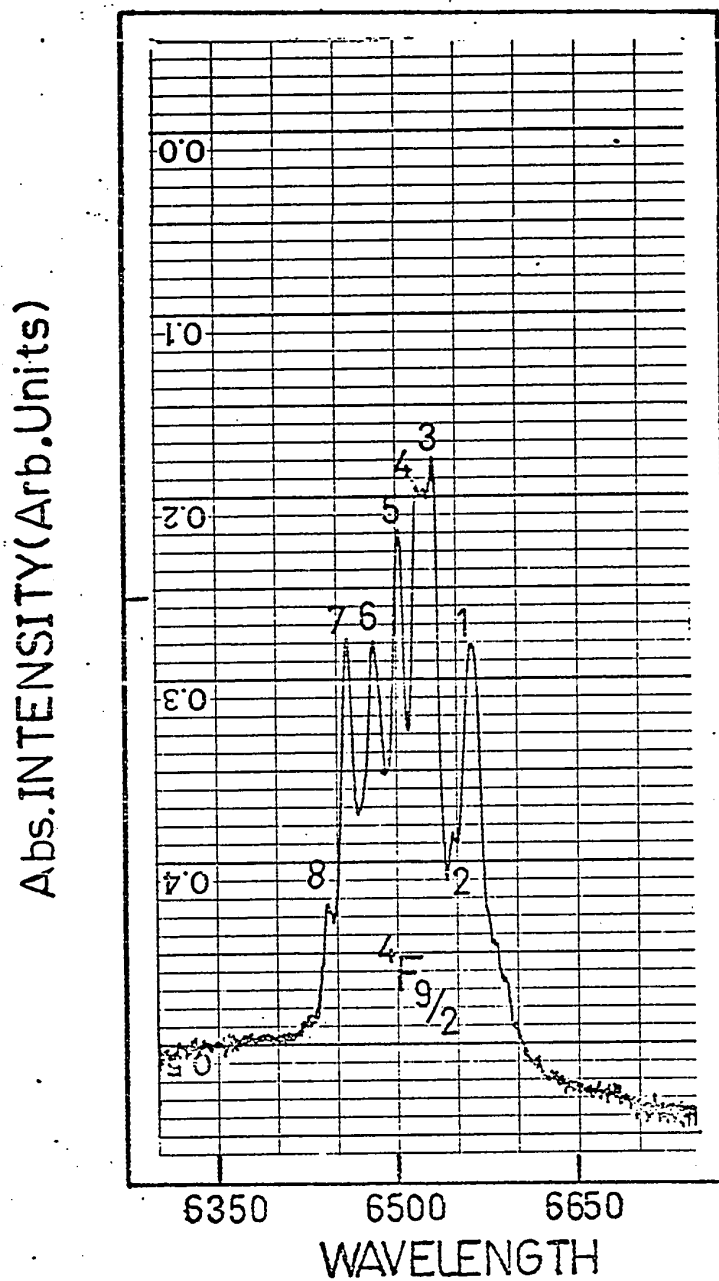
Fig. 4.12   Absorption spectrum of CaF_2Er^{+3} at LNT
from 6350 Å to 6650 Å.
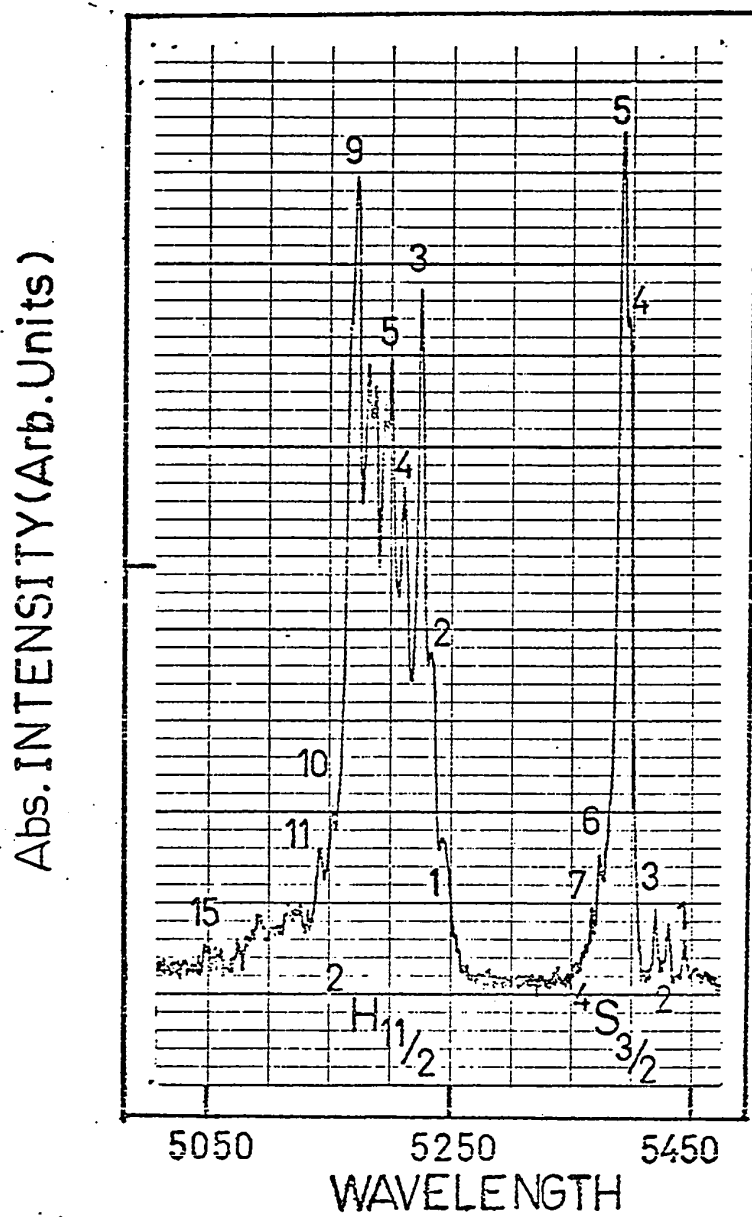
Fig. 4.13 Absorption spectrum of CaF_2Er^{+3} at LNT from 5050 Å to 5450 Å.
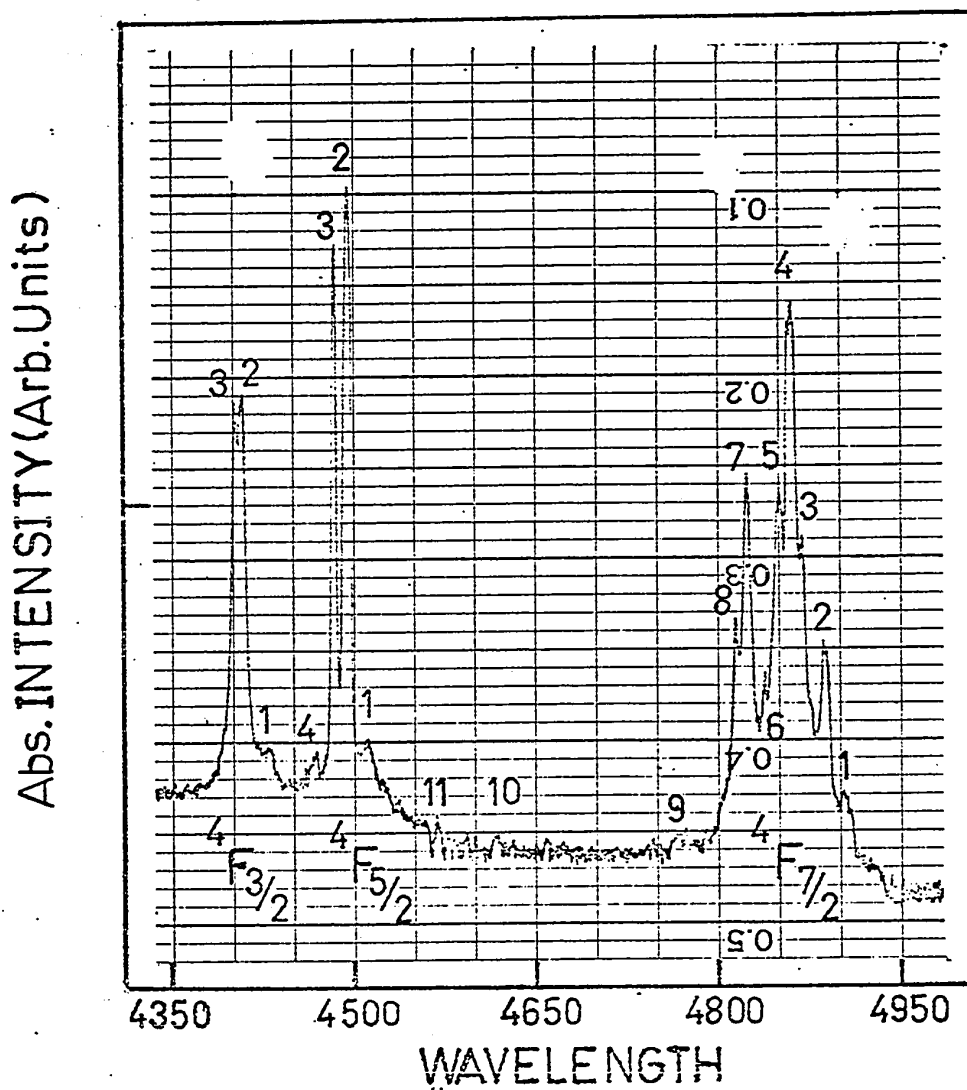
Fig. 4.14 Absorption spectrum of CaF_2Er^{+3} at LNT from 4350 Å to 4950 Å.
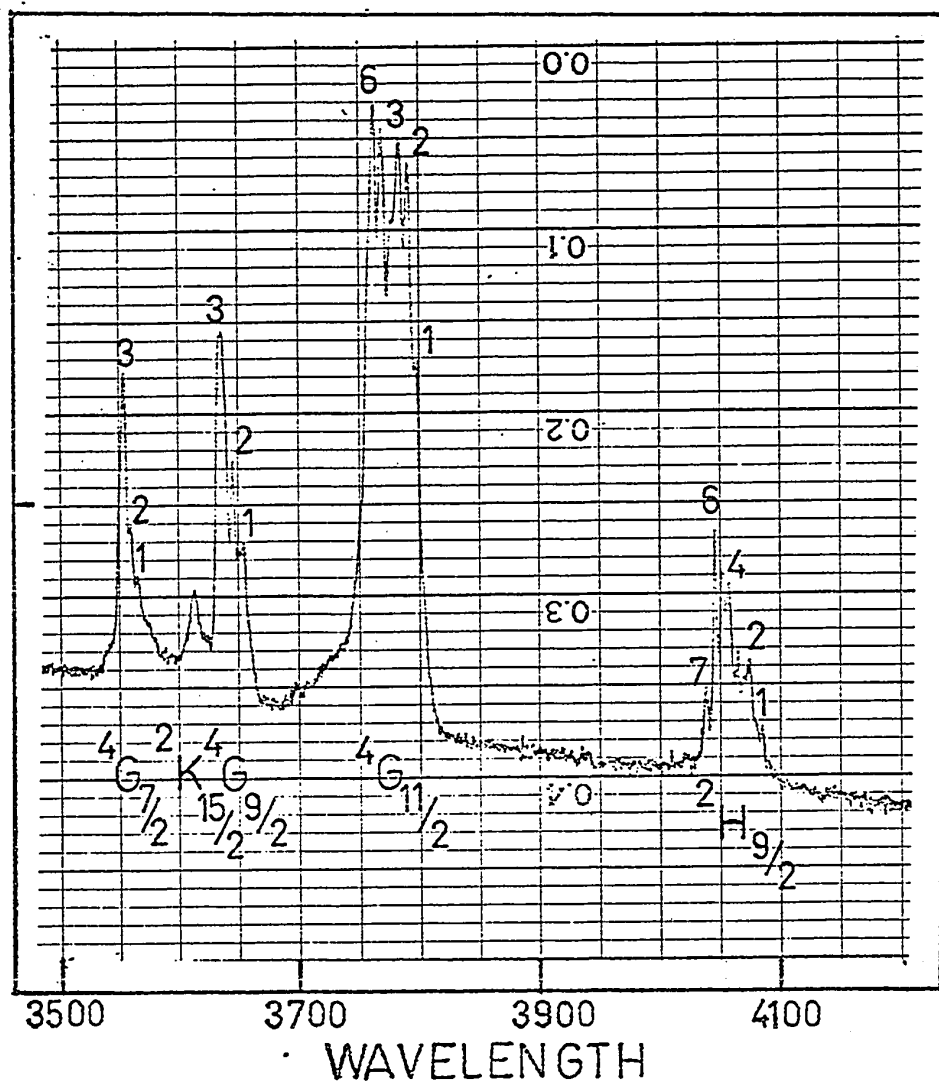
Fig. 4.15 Absorption spectrum of CaF_2Er^{+3} at LNT from 3500 Å to 4100 Å.
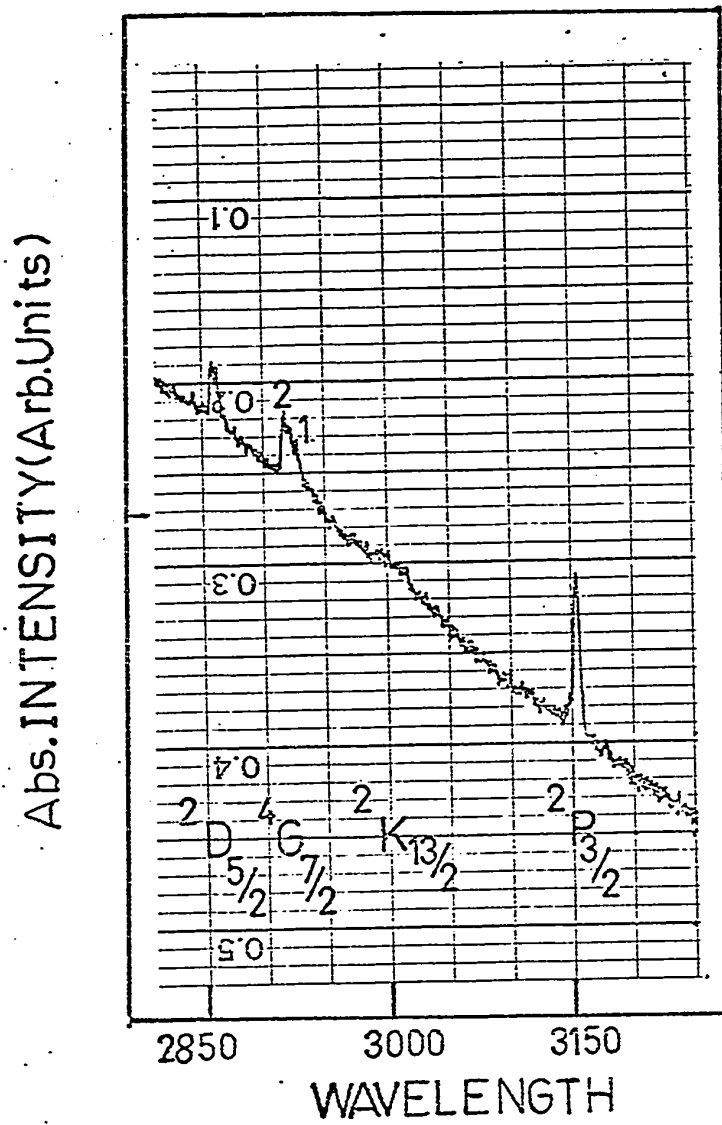
Fig. 4.16 Absorption spectrum of CaF_2Er^{+3} at LNT from 2850 Å to 3150 Å.
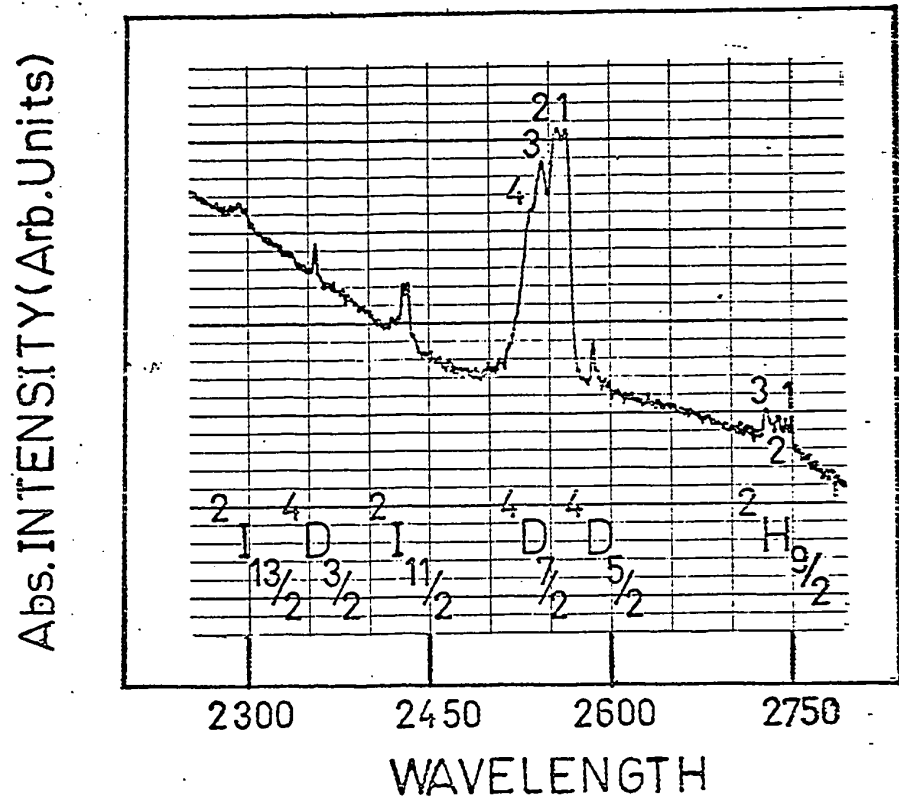
Fig. 4.17 Absorption spectrum of CaF_2Er^{+3} at LNT from 2300 Å to 2750 Å.

TABLE 4.2

Absorption Spectrum of CaF_2Er^{+3} at LNT

SLJ Assignment	Absorption Peaks Energy (cm^{-1})	Wavelength λ (Å)	Peak No.	Centroid (cm^{-1})	Differences between Expt. and Calc. Energy Values Δ (cm^{-1}) Ref. (1)
	6439	15530	1		
	6469	15459	2		
	6508	15365	3		
	6533	15306	4		
	6544	15282	5		
	6554	15259	6		
	6574	15212	7		
$^4I_{13/2}$	6594	15165	8	6617	11
	6641	15059	9		
	6656	15024	10		
	6703	14918	11		
	6746	14824	12		
	6785	14738	13		
	6928	14435	14		
	10167	9836	1		
$^4I_{11/2}$	10203	9801	2	10263	50
	10290	9718	3		
	10327	9683	4		
	12427	8047	1		
$^4I_{9/2}$	12500	8000	2	12546	95
	12574	7953	3		
	12687	7882	4		

Table 4.2 (continued)

SLJ Assignment	Absorption Peaks Energy (cm⁻¹)	Wavelength λ (Å)	Peak No.	Centroid (cm⁻¹)	Differences between Expt. and Calc. Energy Values Δ (cm⁻¹) Ref. (1)
$^4F_{9/2}$	15239	6562	1		
	15274	6547	2		
	15314	6530	3	15366	-16
	15340	6519	4		
	15378	6503	5		
	15427	6482	6		
	15482	6459	7		
	15518	6444	8		
$^4S_{3/2}$	18335	5454	1		
	18416	5430	2		
	18454	5419	3		
	18529	5397	4	18521	75
	18549	5391	5		
	18609	5374	6		
	18629	5368	7		
$^2H_{11/2}$	19069	5244	1		
	19113	5232	2		
	19135	5226	3		
	19186	5212	4		
	19231	5200	5		
	19264	5191	6		
	19286	5185	7	19273	21
	19305	5180	8		
	19339	5171	9		
	19406	5153	10		
	19451	5141	11		
	19539	5118	12		

Table 4.2 (continued)

Assignment	Absorption Peaks Energy (cm⁻¹)	Wavelength λ (Å)	Peak No.	Centroid (cm⁻¹)	Differences between Expt. and Calc. Energy Values Δ (cm⁻¹) Ref. (1)
$^2H_{11/2}$	19643	5091	13		
		5077	14		
		5050	15		
$^4F_{7/2}$	20396	4903	1		
	20470	4885	2		
	20517	4874	3		
	20580	4859	4	20605	9
	20618	4850	5		
	20683	4835	6		
	20730	4824	7		
	20768	4815	8		
	20973	4768	9		
	21654	4618	10		
	21891	4568	11		
$^4F_{5/2}$	22163	5412	1		
	22252	4494	2	22277	46
	22311	4482	3		
	22381	4468	4		
$^4F_{3/2}$	22573	4430	1		
	22696	4406	2	22683	166
	22727	4400	3		
$^2H_{9/2}$	24480	4085	1		
	24549	4074	2		
	24618	4062	3		
	24655	4056	4	24645	57
	24691	4050	5		

Table 4.2 (continued)

SLJ Assignment	Absorption Peaks Energy (cm⁻¹)	Wavelength λ (Å)	Peak No.	Centroid (cm⁻¹)	Differences between Expt. and Calc. Energy Values Δ (cm⁻¹) Ref.(1)
$^2H_{9/2}$	24710	4047	6		
	24765	4038	7		
$^4G_{11/2}$	26337	3797	1		
	26378	3791	2		
	26441	3782	3	26463	-16
	26483	3776	4		
	26521	3771	5		
	26581	3762	6		
$^4G_{9/2}$	27375	3653	1		
	27420	3647	2	27443	51
	27508	3635	3		
$^2K_{15/2}$	27685	3612		27685	-83
$^4G_{7/2}$	28050	3565	1		
	28098	3559	2	28104	43
	28145	3553	3		
$^2P_{3/2}$	31686	3156		31686	78
$^4G_{7/2}$	34211	2923	1	34242	271
	34270	2918	2		
$^2D_{5/2}$	34977	2859	1	35041	141
	35051	2853	2		

Table 4.2 (continued)

SLJ Assignment	Absorption Peaks Energy (cm⁻¹)	Wavelength λ (Å)	Peak No.	Centroid (cm⁻¹)	Differences between Expt. and Calc. Energy Values Δ (cm⁻¹) Ref. (1)
$^2H_{9/2}$	36483	2741	1		
	36603	2732	2	36609	62
	36738	2722	3		
$^4D_{5/2}$	38812	2577		38812	231
$^4D_{7/2}$	39170	2553	1		
	39262	2547	2	39368	91
	39490	2532	3		
	39580	2527	4		
$^2I_{11/2}$	41263	2424		41263	214
$^4D_{3/2}$	42608	2347		42608	320
$^2I_{13/2}$	43764	2285		43764	108
$^2F_{7/2}$	54795	1825		54795	179
	59453	1682		59453	193
	60606	1650		60606	
$^2F_{5/2}$	63091	1585		63091	
$4f^{11} \rightarrow 4f^{10}5d$ Transition	64516	1550	1		
	65359	1530	2		

The assignments of these peaks are made in accordance with reference (1).

The absorption spectrum of CaF_2Pr^{+3} from 2000 to 23500 $\overset{o}{A}$ at LNT is shown in Figs. 4.18 to 4.23. The peak values are expressed in cm^{-1} in Table 4.4 and they have been numbered for future use. The summary of all of these figures is given in Table 4.3. The peaks have been assigned in accordance with reference (2).

TABLE 4.3

Summary of the Figures Regarding the Absorption

Spectrum of CaF_2Pr^{+3} (1%)

Fig. No.	Crystal	Temperature	Spectral Range
4.18	As-received	LNT	21100 Å to 23500 Å
4.19	" "	"	17900 Å to 20300 Å
4.20	" "	"	13600 Å to 16000 Å
4.21	" "	"	9800 Å to 10400 Å
4.22	" "	"	5700 Å to 6100 Å
4.23	" "	"	4300 Å to 4900 Å
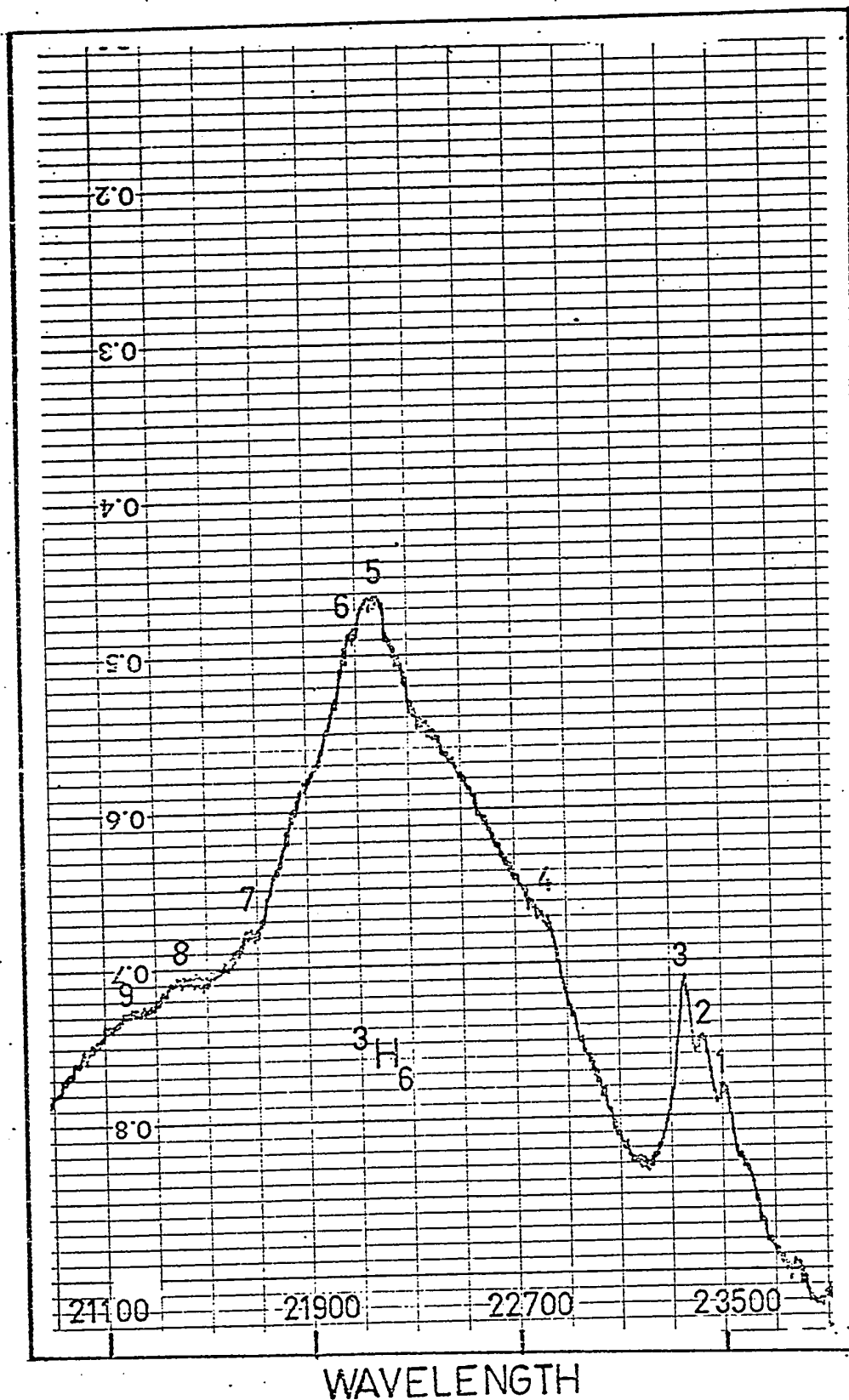
Fig. 4.18 Absorption spectrum of CaF_2Pr^{+3} at LNT from 23500 Å to 21100 Å.
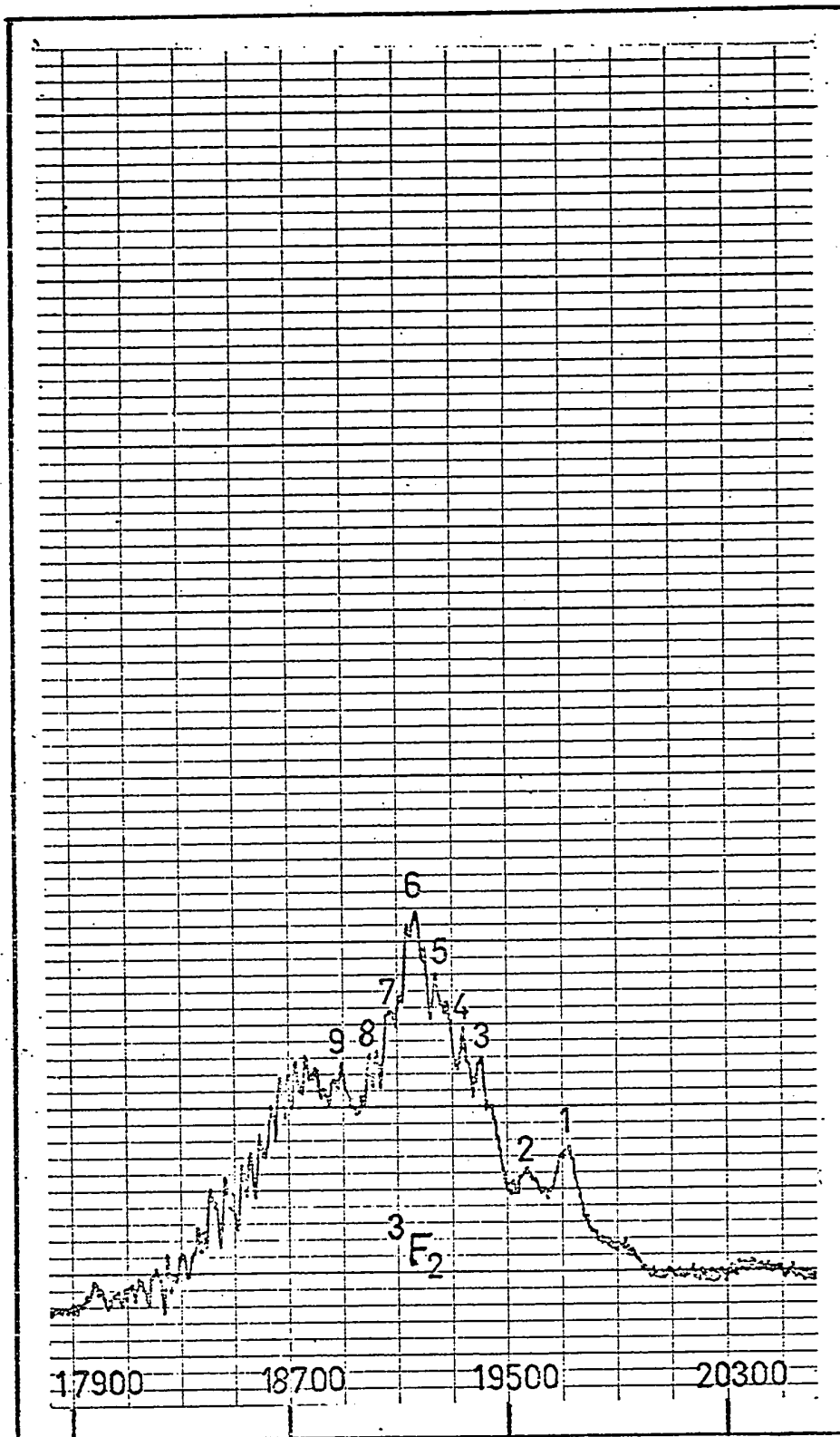
Fig. 4.19 Absorption spectrum of CaF_2Pr^{+3} at LNT from 17900 Å to 20300 Å.
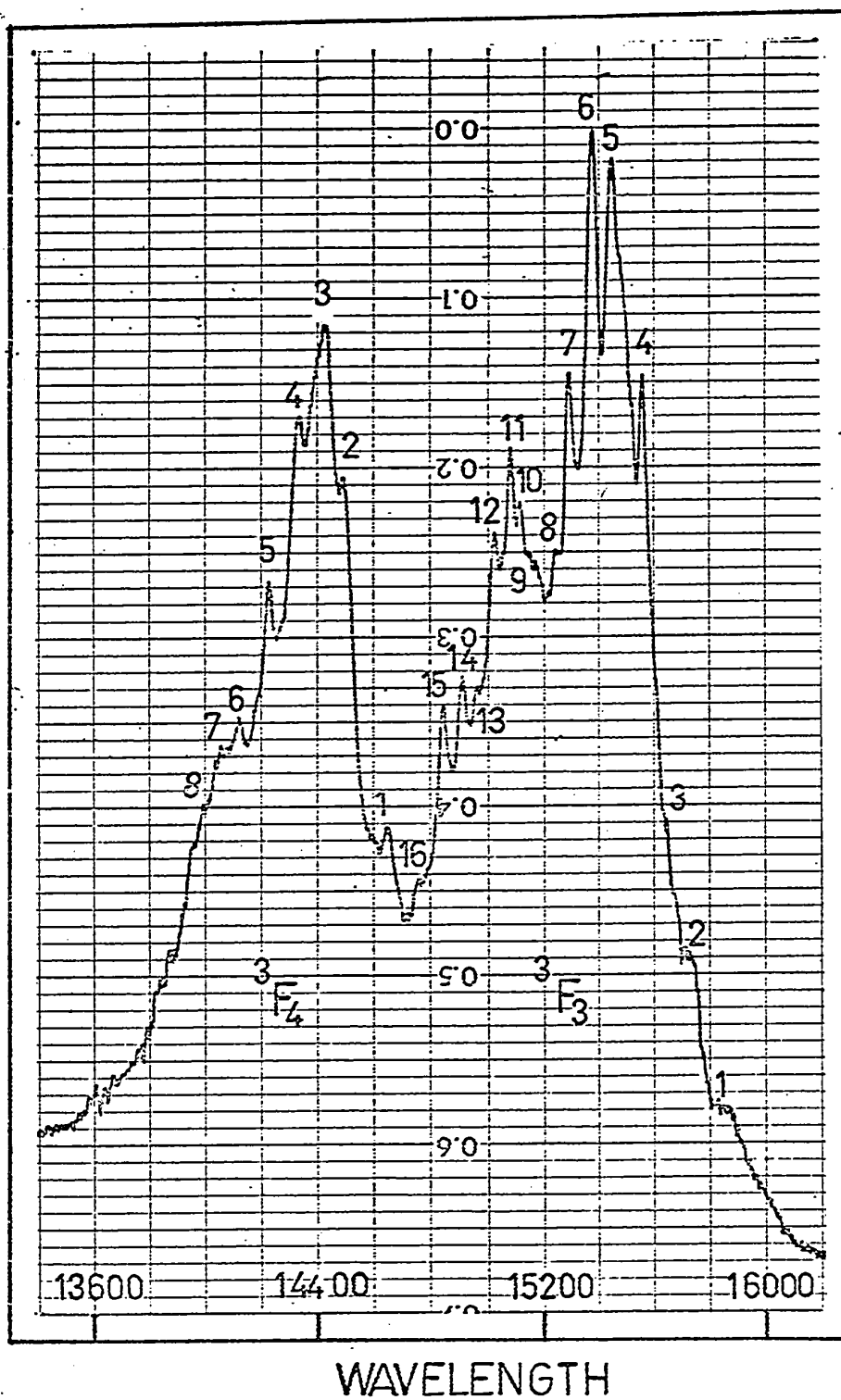
Fig. 4.20   Absorption spectrum of CaF_2Pr^{+3} at LNT from 13600 Å to 16000 Å.
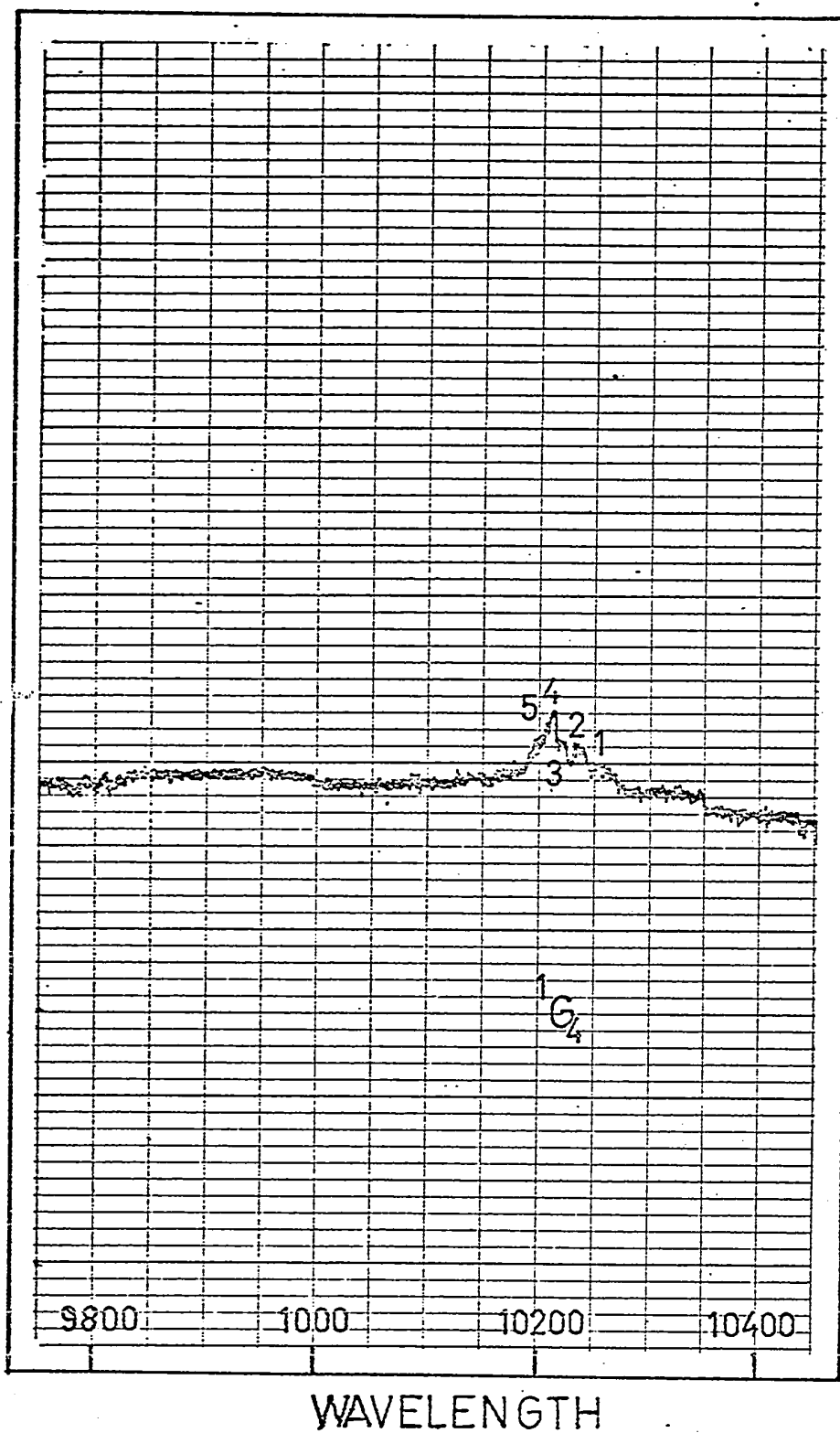
Fig. 4.21 Absorption spectrum of CaF_2Pr^{+3} at LNT from 9800 Å to 10400 Å.
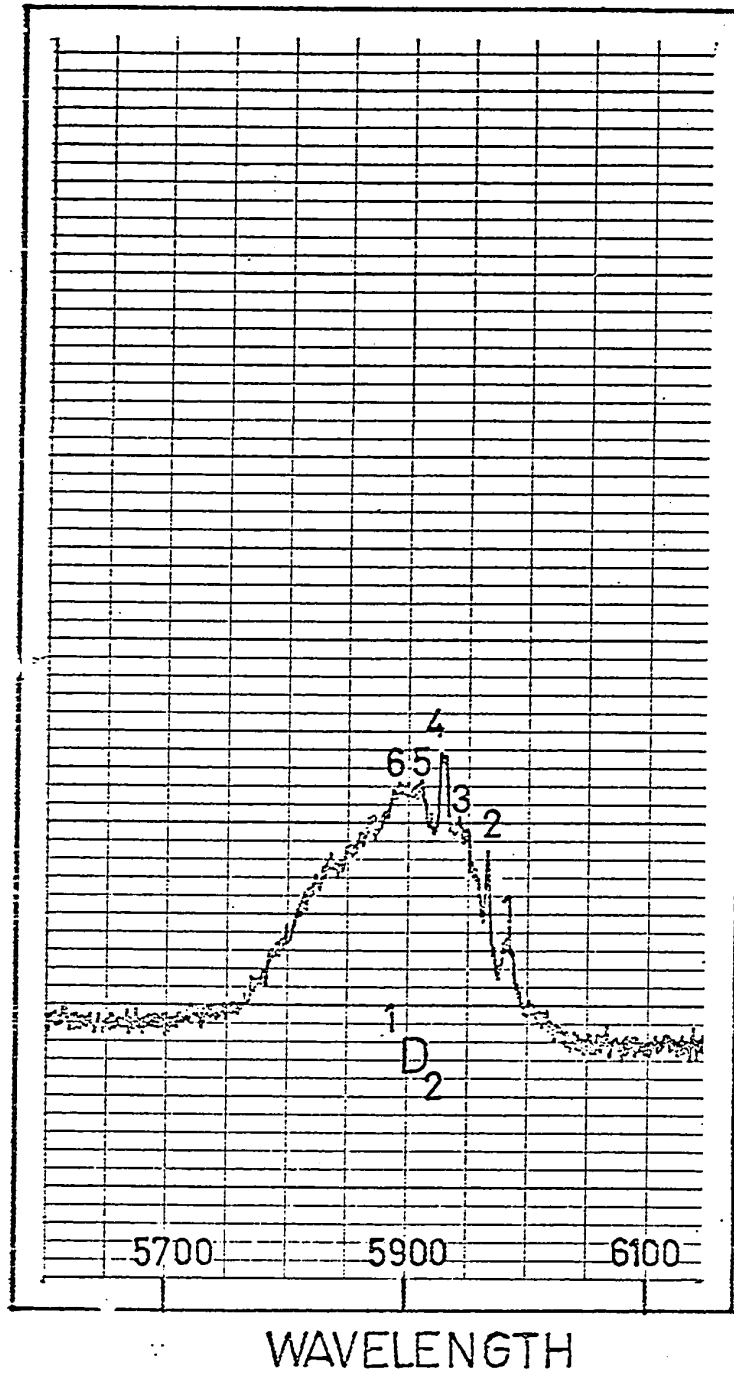
Fig. 4.22 Absorption spectrum of CaF_2Pr^{+3} at LNT from 5700 Å to 6100 Å.
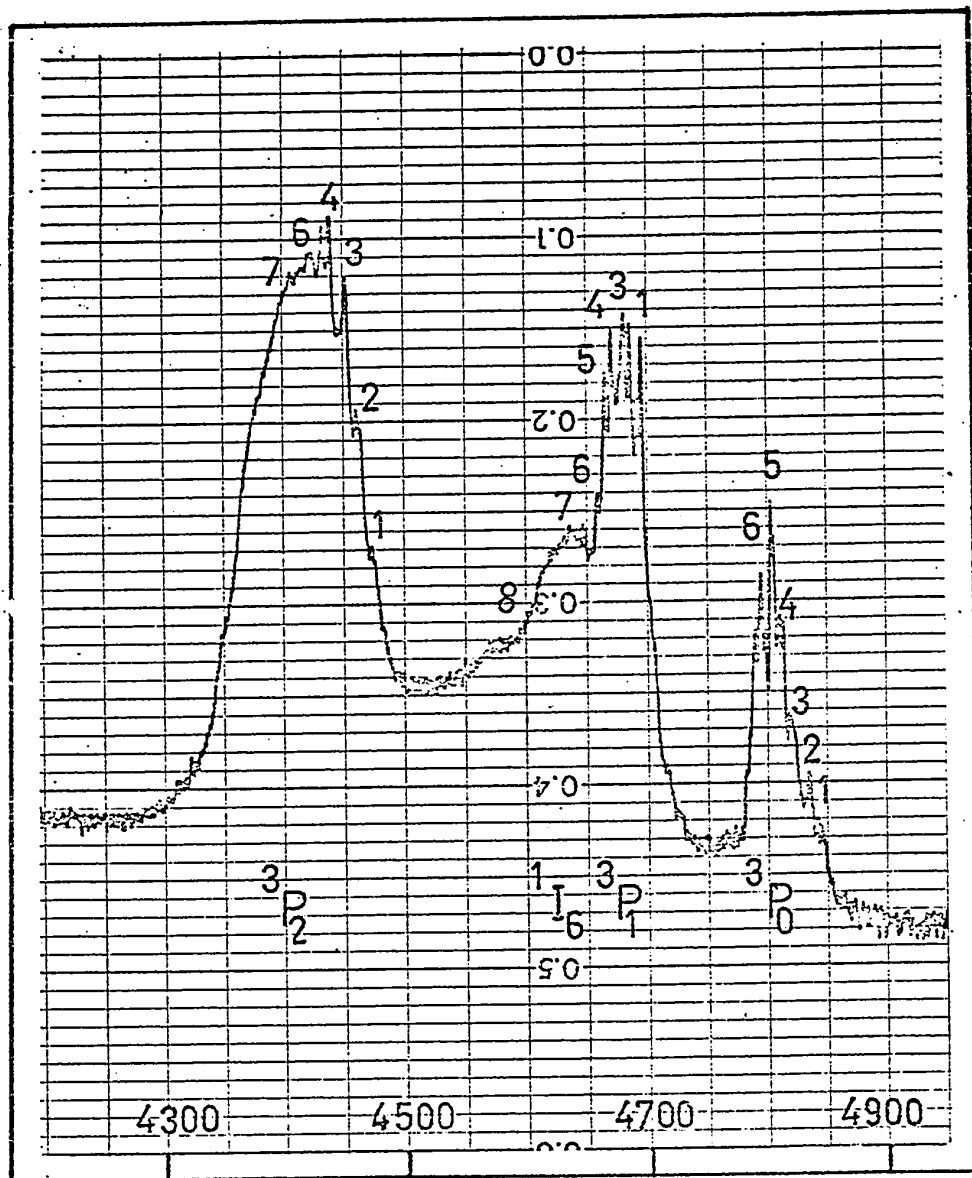
Fig. 4.23 Absorption spectrum of CaF_2Pr^{+3} at LNT from 4300 Å to 4900 Å.

TABLE 4.4

Absorption Spectrum of CaF_2Pr^{+3} at LNT

SLJ Assignment	Absorption Peaks Energy (cm^{-1})	Wavelength λ (Å)	Peak No.	Centroid (cm^{-1})	Differences between Expt. and Calc. Energy Values Δ (cm^{-1}) Ref. (2)
$^3H_6$	4253	23512	1		
	4268	23430	2		
	4281	23360	3		
	4387	22794	4	4484	-12
	4510	22170	5		
	4527	22088	6		
	4616	21665	7		
	4674	21394	8		
	4713	21218	9		
$^3F_2$	5070	19723	1		
	5110	19570	2		
	5153	19406	3		
	5175	19323	4		
	5197	19241	5	5204	55
	5216	19170	6		
	5242	19076	7		
	5261	19006	8		
	5291	18900	9		
$^3F_3$	6289	15900	1		
	6355	15735	2		
	6369	15700	3		
	6418	15582	4		
	6466	15465	5		
	6496	15394	6	6557	17
	6531	15312	7		

Table 4.4 (continued)

SLJ Assignment	Absorption Peaks Energy (cm^{-1})	Wavelength λ (Å)	Peak No.	Centroid (cm^{-1})	Differences between Expt. and Calc. Energy Values Δ (cm^{-1}) Ref. (2)
$^3F_3$	6546	15277	8		
	6586	15182	9		
	6607	15135	10		
	6623	15100	11		
	6648	15041	12		
	6669	14994	13		
	6701	14924	14		
	6733	14853	15		
	6771	14768	16		
$^3F_4$	6825	14653	1		
	6897	14500	2		
	6936	14418	3		
	6976	14335	4	7009	36
	7027	14230	5		
	7080	14124	6		
	7104	14077	7		
	7146	13994	8		
$^1G_4$	9748	10259	1		
	9770	10235	2		
	9784	10221	3	9780	-105
	9792	10212	4		
	9803	10200	5		
$^1D_2$	16717	5982	1		
	16764	5965	2		
	16832	5941	3	16856	16
	16863	5930	4		

Table 4.4 (continued)

SLJ Assignment	Absorption Peaks Energy (cm⁻¹)	Wavelength λ (Å)	Peak No.	Centroid (cm⁻¹)	Differences between Expt. and Calc. Energy Values Δ (cm⁻¹) Ref. (2)
$^1D_2$	16923	5909	5		
	16966	5894	6		
$^3P_0$	20657	4841	1		
	20700	4831	2		
	20756	4818	3	20777	71
	20781	4812	4		
	20820	4803	5		
	20859	4794	6		
$^3P_1$	21290	4697	1	21306	-24
	21322	4690	2		
	21358	4682	3		
	21409	4671	4		
	21436	4665	5		
$^1I_6$	21464	4659	6	21481	-19
	21547	4641	7		
	21810	4585	8		
$^3P_2$	22368	4471	1		
	22427	4459	2		
	22457	4453	3		
	22517	4441	4	22525	-10
	22542	4436	5		
	22607	4424	6		
	22696	4406	7		

Chapter 5 DISCUSSION AND ANALYSIS OF RESULTS

5.1 Discussion of Absorption Spectra

When an ion in a crystal is excited by a source
having a continuum in the desired spectral range, sharp
lines characteristic of the ion can be observed on the
continuous background. The transitions which give rise
to the groups start from the lowest levels of the ground
multiplet and terminate on various excited levels belong-
ing to the $4f^N$ configuration of the rare-earth ion split
by the crystal field. The absorption spectra of CaF_2Er^{+3}
and that of CaF_2Pr^{+3} will be discussed in the subsections
(a) and (b) of this section.

(a) $\underline{CaF_2Er^{+3}}$

Fig. 5.1 shows the energy levels of CaF_2Er^{+3} (1%)
at $77^\circ K$ in the spectral range 6600 cm^{-1} to 65400 cm^{-1}. In
this figure, a comparison has been made between the
calculated energy levels of $ErCl_3 \cdot 6H_2O$ and the mean energy
levels in CaF_2Er^{+3}. The SLJ assignments were made by
comparisons with energy levels of $ErCl_3 \cdot 6H_2O$ (1) . These
energy levels are more accurate for comparison than those
of free ion energy levels of Er^{+3} (2) , as Carnall et al
(1) have included the configuration interaction while
calculating the energy levels of $ErCl_3 \cdot 6H_2O$. The mean
energy levels in CaF_2Er^{+3} lie between the calculated energy
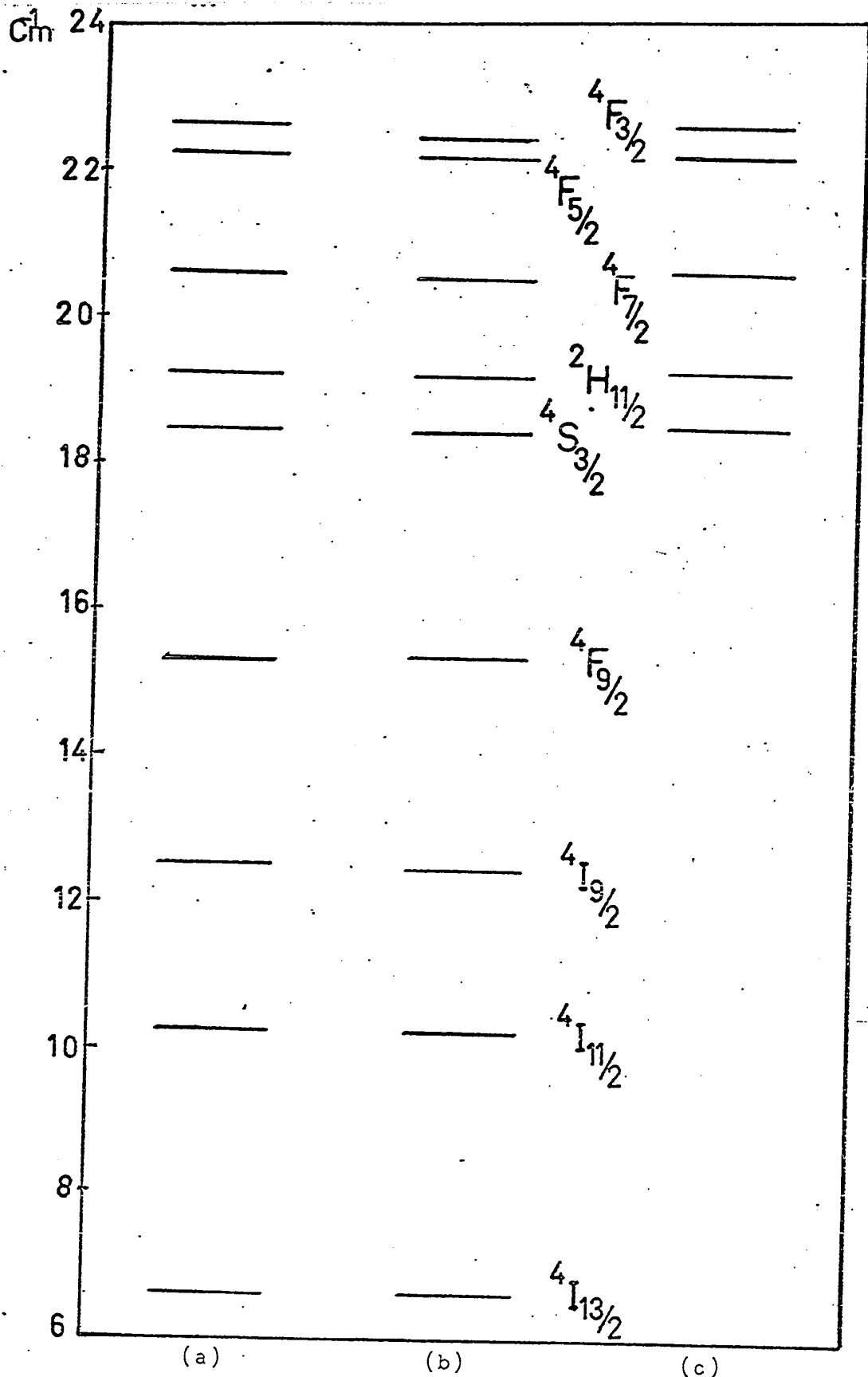
Fig. 5.1 Comparison of energy levels of CaF_2Er^{+3} with $ErCl_3.6H_2O$.
(a) Absorption (b) $ErCl_3.6H_2O$ (c) Excitation
(1%)   (0.1%)
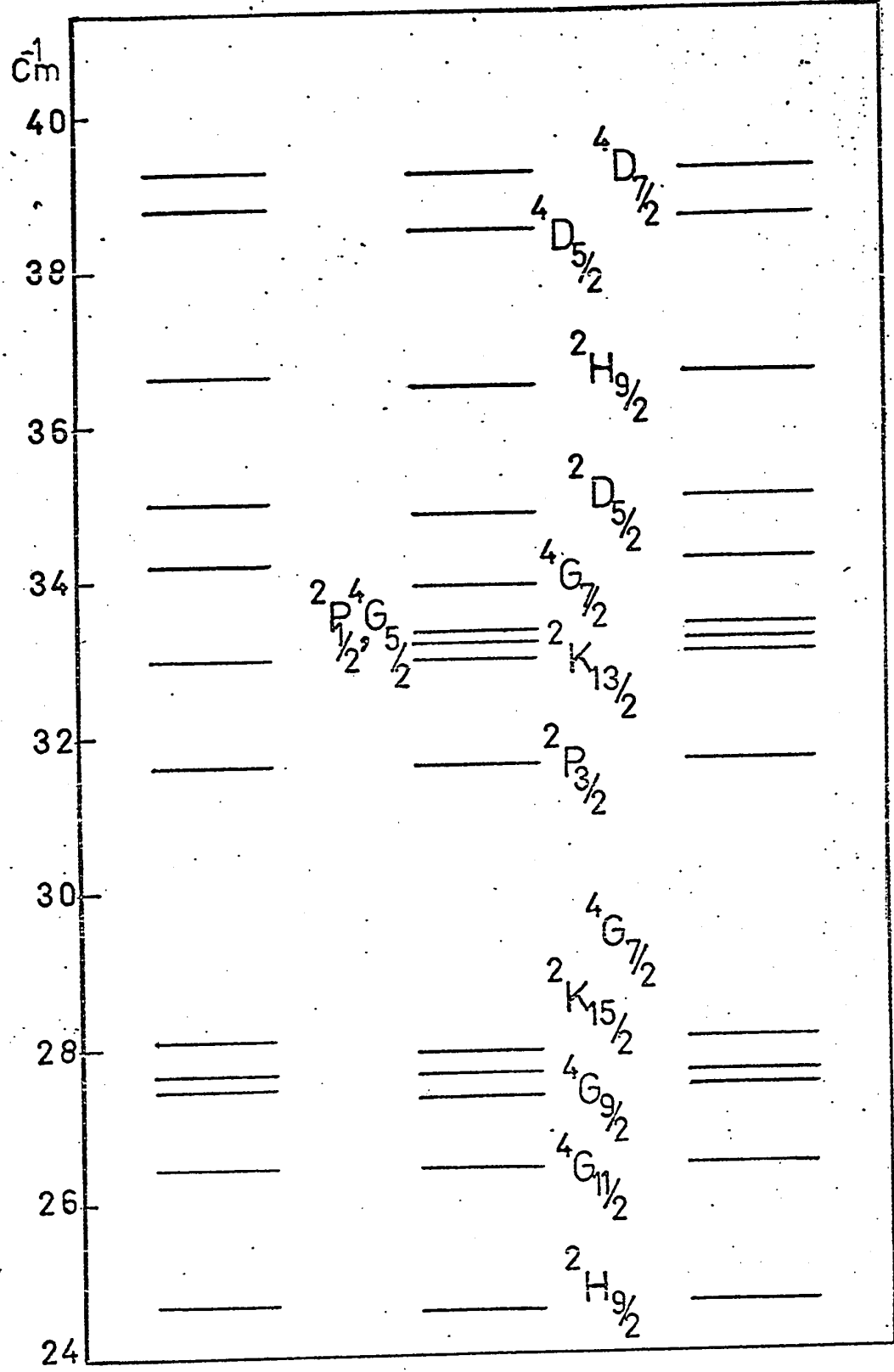
Fig. 5.1 Comparison of energy levels of CaF_2Er^{+3} with $ErCl_3 \cdot 6H_2O$.
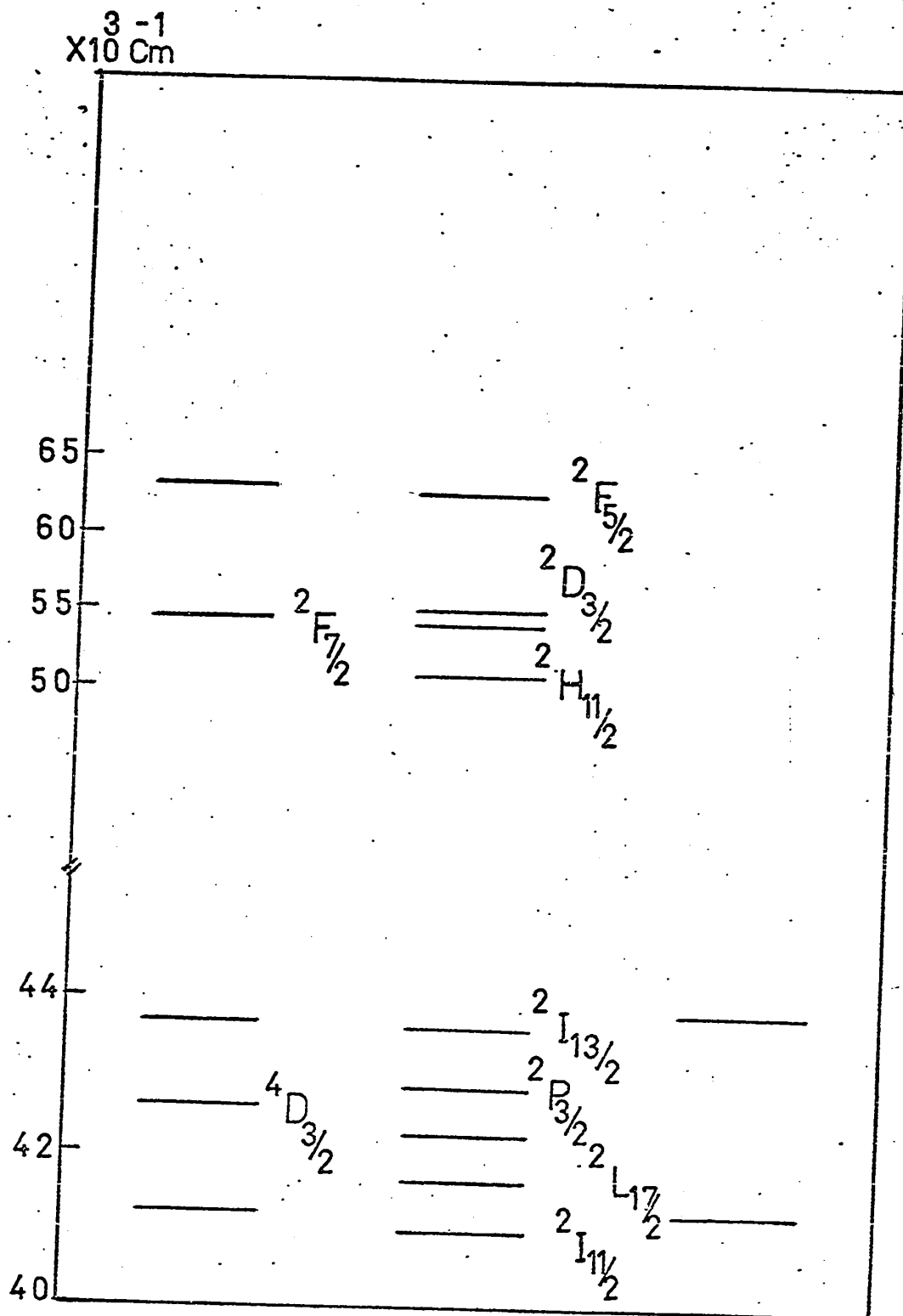
Fig. 5.1 Comparison of energy levels of CaF_2Er^{+3} with $ErCl_3 \cdot 6H_2O$.

levels of LaF_3Er^{+3} (1%) and $ErCl_3 \cdot 6H_2O$ (1%). We believe that this difference is due to the Er^{+3} ion being in a different host lattice, and possibly in a different site symmetry. This difference should be responsible for a different amount of "total down shift" as discussed in (3). Nevertheless, it is remarkable that essentially the characteristic spectra are seen.

In Figure 3 of reference (4), the energy level $^4G_{9/2}$ at 36500 cm^{-1} should be $^2H_{9/2}$ and, moreover, some of the energy levels in the spectral range 41000 cm^{-1} to 43600 cm^{-1} have not been assigned at all. In reference (5) no energy level above 31000 cm^{-1} has been observed. In our results, two new energy levels, $^2F_{7/2}$ and $^2F_{5/2}$ at 54795 cm^{-1} and 63091 cm^{-1}, respectively, are observed experimentally which have not been reported in the literature before. These values are comparable with the calculated values in (1). It should be noted that experimentally, Carnall et al (1) did not observe these levels either in LaF_3Er^{+3} or in $ErCl_3 \cdot 6H_2O$. The absorption around 33080 cm^{-1} is very weak and the exact position of the energy level $^2K_{13/2}$ could not be marked accurately.

In our results, some interconfiguration transitions $(4f^{11} \rightarrow 4f^{10}5d)$ have been observed at 64516 cm^{-1} and at 65359 cm^{-1}, and these are in good agreement with the result obtained by Loh (3). We have also observed a few more lines in the U.V. region around 59453 cm^{-1} and 60606 cm^{-1} and very weak absorption lines in the visible region

around 5050 Å, 5077 Å, 4768 Å, 4618 Å and 4568 Å. The origin of these lines is not yet known. Due to the very weak intensity of the xenon continuum in the region around 51182 cm^{-1}, we were unable to observe the expected energy level $^2H_{11/2}$. Below 1500 Å, xenon does not have a good continuum and we did not get satisfactory results. In the continuum of argon, there are too many impurity lines and to observe any meaningful absorption spectrum is difficult, unless double beam techniques are used. This is now under way in our laboratory.

The ground state of Er^{+3} is $^4I_{15/2}$ and the observed results indicate that all the transitions obey the selection rules $\Delta J \leq 6$ and $\Delta L \leq 6$. This might indicate that the observed transitions are mainly electric dipole in character. From Figs. 4.16, 4.17, 4.13, 4.14, we see that energy levels $^2P_{3/2}$ and $^4D_{3/2}$ have not split while the levels $^4S_{3/2}$ and $^4F_{3/2}$ have split up. This might be caused by the presence of a mixture of symmetries surrounding the Er^{+3} ions in the CaF$_2$ crystal, or the weaker transitions from $^4I_{15/2}$ to $^2P_{3/2}$ or $^4D_{3/2}$ have not been observed. However, further work is obviously needed in order to have a conclusive interpretation on this aspect.

(b) <u>CaF$_2$Pr^{+3}</u>

The energy level scheme of CaF$_2$Pr^{+3} (1%) at LNT in the spectral region 4000 cm^{-1} to 23000 cm^{-1} is shown in Fig. 5.2. The mean energy levels of CaF$_2$Pr^{+3} have been compared with those of the free ion and with those of
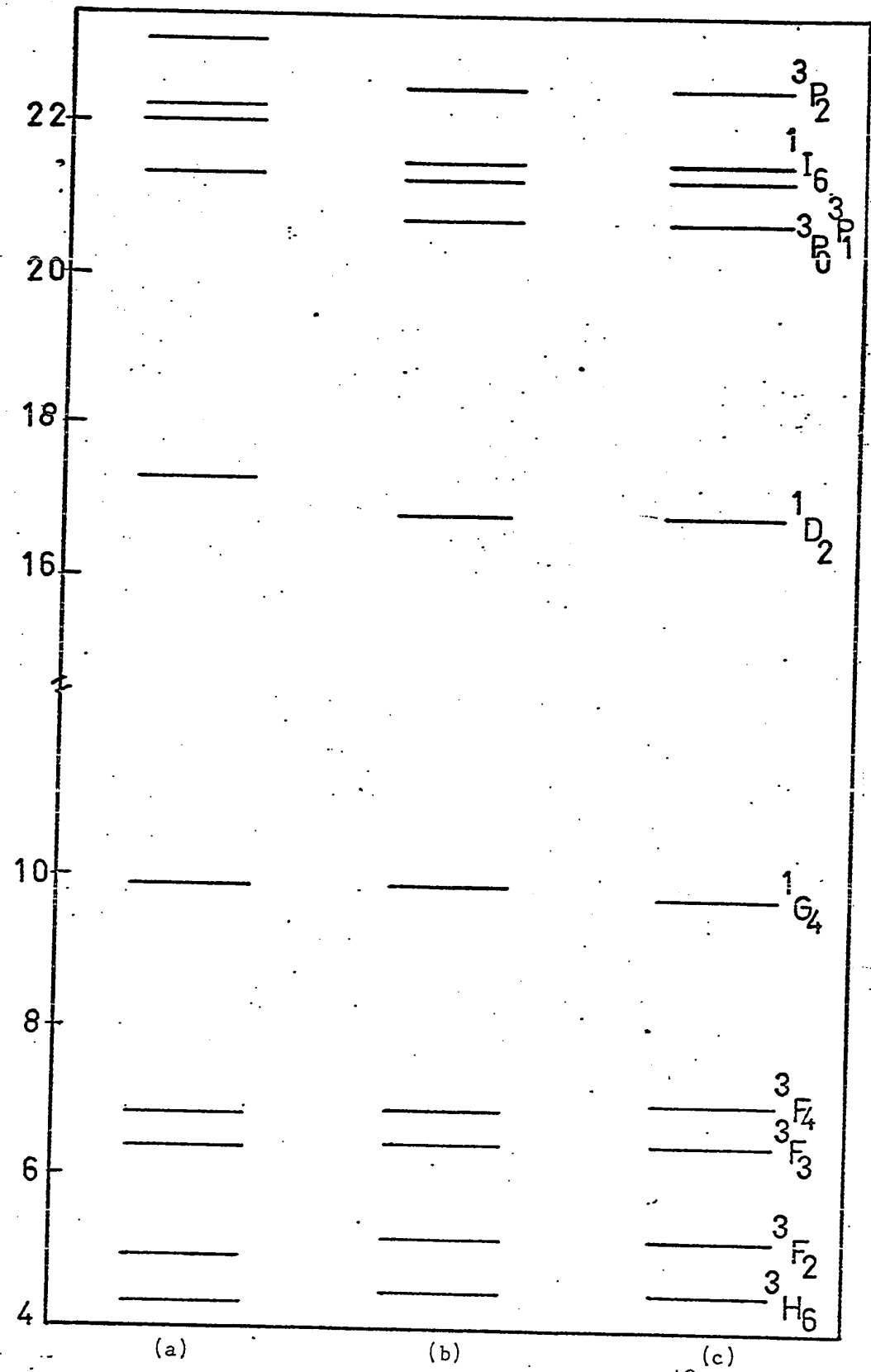
Fig. 5.2 Comparison of energy levels of CaF_2Pr^{+3} with (a) free ion (b) aqueous solution (c) CaF_2Pr^{+3}.

aqueous solution energy levels in the same figure. The
SLJ assignments of these levels are made in accordance with
reference (6) . Our results are in agreement with the
energy levels of Pr^{+3} in aqueous solution. The absorption
around 9900 cm^{-1} is very weak and the mean energy level of
$^1G_4$ could not be determined more accurately.

Recently, Hargreaves (7) has claimed that under
the tetragonal symmetry, the positions of $^3P_2$, $^1I_6$ and $^3P_1$
are 22640 cm^{-1}, 21470 cm^{-1} and 20830 cm^{-1}, respectively.
No $^3P_0$ level was observed in his results. Also, there was
a deviation of 300 cm^{-1} from the calculated value of $^3P_2$.

Comparing our results of the mean energy levels
with those of aqueous solution, we suggest that the positions
of energy levels $^3P_2$, $^1I_6$, $^3P_1$ and $^3P_0$ should be 22526 cm^{-1},
21481 cm^{-1}, 21306 cm^{-1} and 20777 cm^{-1}, respectively. We
have also noticed a disproportionate shift in the mean
energy levels for $^3P_2$, $^1I_6$, $^3P_1$ and $^3P_0$ by making a
comparison with the energy levels of free ions of Pr^{+3} (8,9)
This difference in the shift can be explained by consider-
ing the configuration interaction and mixing of energy
levels due to crystal field. We further suggest that the
energy levels from $^1D_2$ to $^3P_2$ should be treated separately
from the group of energy levels $^3H_4$ to $^1G_4$ as the two groups
are separated from one another by ≈ 7400 cm^{-1}. Detailed
discussion regarding this aspect has been given by Schlesinger
and Nara (10).

The ground state of Pr^{+3} is $^3H_4$ and all the

transitions except $^1S_0$ have been observed which follow the selection rules $\Delta J \leq 6$ and $\Delta L \leq 6$. This suggests that the observed transitions are also electric dipole in character.

The above did not exclude the presence of more than one symmetry but in absorption spectrum the transitions due to dominant symmetry are observed. Transitions due to weaker symmetry may be observed in thermoluminescence or luminescence spectrum which will be discussed later.

5.2 Discussion of Luminescence Excitation Spectrum

When a rare-earth ion in the CaF_2 matrix is irradiated with monochromatic radiation, the ion undergoes a transition from the ground state E_g to an excited state E_e. Subsequently, the ion will lose part of its energy in a radionless process or by cascade process, coming to an intermediate state E_I as shown in Figure 5.3. From the intermediate level E_I, it will decay to the ground state E_g emitting electromagnetic radiations, which can be observed experimentally with relative ease. By changing the wavelength of exciting light, one gets an excitation spectrum. The intensity of light in absorption spectrum depends upon the thickness of the sample, but in luminescence excitation spectrum, it is independent of thickness. This method has proven to be better than absorption due to its strong intensity and good resolution. The luminescence spectra of CaF_2 Er^{+3} (0.1%) in the green region and that
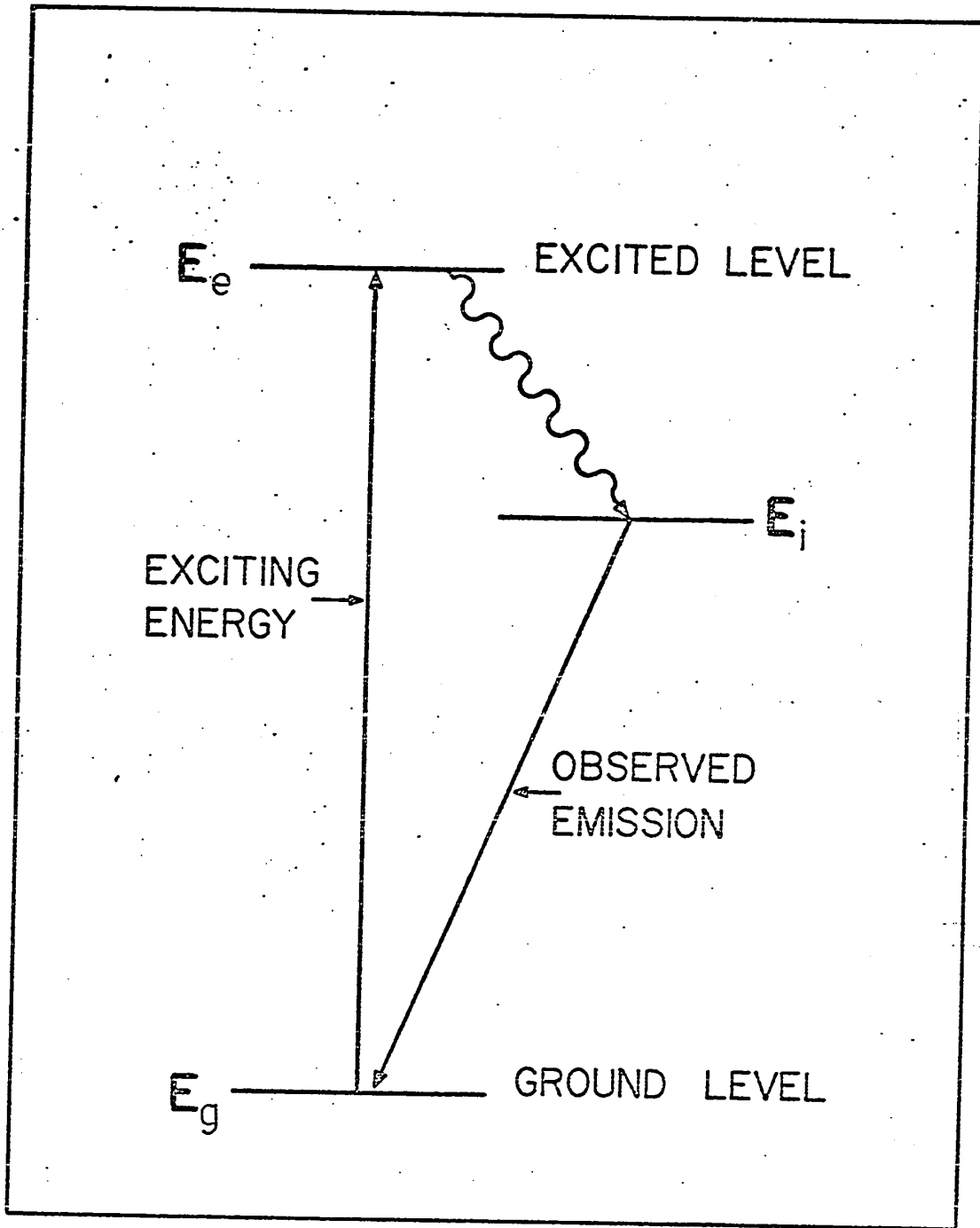
Fig. 5.3 Process for luminescence excitation.

of CaF_2Pr^{+3} (0.1%) in the blue-green region will be discussed

in the subsections (a) and (b) of this section.

(a) $\underline{CaF_2Er^{+3}}$

Fig.   shows the energy levels of CaF_2Er^{+3} (0.1%)

in the spectral range 18100 cm^{-1} to 50,000 cm^{-1}. In the same figure

the mean energy levels have been compared with those of

$ErCl_3 \cdot 6H_2O$ and that of CaF_2Er^{+3} (1%) obtained by the

absorption method. The maximum deviation observed is 365

cm^{-1} and the maximum splitting produced is 430 cm^{-1}.

It is evident from Fig. 5.1 that the results of absorption

and excitation spectra are in good agreement, which means

that both the spectra are of the same origin. In the

absorption spectra we could not observe the energy levels

$^2K_{13/2}$, $^4G_{5/2}$ and $^2P_{1/2}$. In the luminescence excitation

spectrum we believe that the energy levels around 3000 $\overset{o}{A}$

consist of $^2K_{13/2}$, $^4G_{5/2}$ and $^2P_{1/2}$ levels. They are very

close to each other and it is therefore difficult to draw

an exact boundary for these levels. The effect of tempera-

ture on the spectrum can be seen by making a comparison of

the spectrum obtained at room temperature with that

obtained at liquid nitrogen temperature.

Some differences in intensity as well as in the

number of components have been observed in the spectra

obtained from crystals furnished by Harshaw Chemical Co.

and Optovac Inc. There is a strong level at $\simeq$ 2600 $\overset{o}{A}$ in

the sample obtained from Harshaw Chemical Co. while a very

weak shoulder at 2580 $\overset{o}{A}$ was observed in the Optov sample.

Since the concentrations of the Er^{+3} ion are the same in both samples, we believe that this difference is due to the presence of a mixture of symmetries in different proportion in the two respective samples.

An attempt has been made to construct an energy level scheme for the observed excited states of Er^{+3} in the tetragonal and cubic fields respectively, as shown in Figs. 5.4 and 5.5 . The lowest stark split component of the ground state $^4I_{15/2}$ is Γ_7 in both the symmetries. The next excited state occurs at 21 cm^{-1} in the tetragonal field (5) and at 91 cm^{-1} in the cubic field (11). The observed transitions are marked by solid lines and the unobserved transitions are marked by broken lines. The allowed transitions under different symmetries were obtained from Tables 2.8 and 2.10. Experimentally observed transitions under C_{4v} and O_h symmetries, along with their calculated values, and the differences between the two, are given in Tables 5.1 and 5.2.

(b) $\underline{CaF_2 Pr^{+3}}$

The excitation spectrum of $CaF_2 Pr^{+3}$ (0.1%) in the spectral region 2000 $\overset{o}{A}$ to 4200 $\overset{o}{A}$ has been carried out. We have observed bands at 2620 $\overset{o}{A}$, 2740 $\overset{o}{A}$, 3530 $\overset{o}{A}$, 3660 $\overset{o}{A}$ and 3950 $\overset{o}{A}$. We also observed the energy level $^3P_2$ and its estimated mean energy is $\approx$ 22795 cm^{-1}. From Figs. 3.29 it was found that the intensity of the band at 3660 $\overset{o}{A}$ and that of the energy level $^3P_2$ decreases with increasing the concentration of the Pr^{+3} ion in the CaF_2 crystal. These
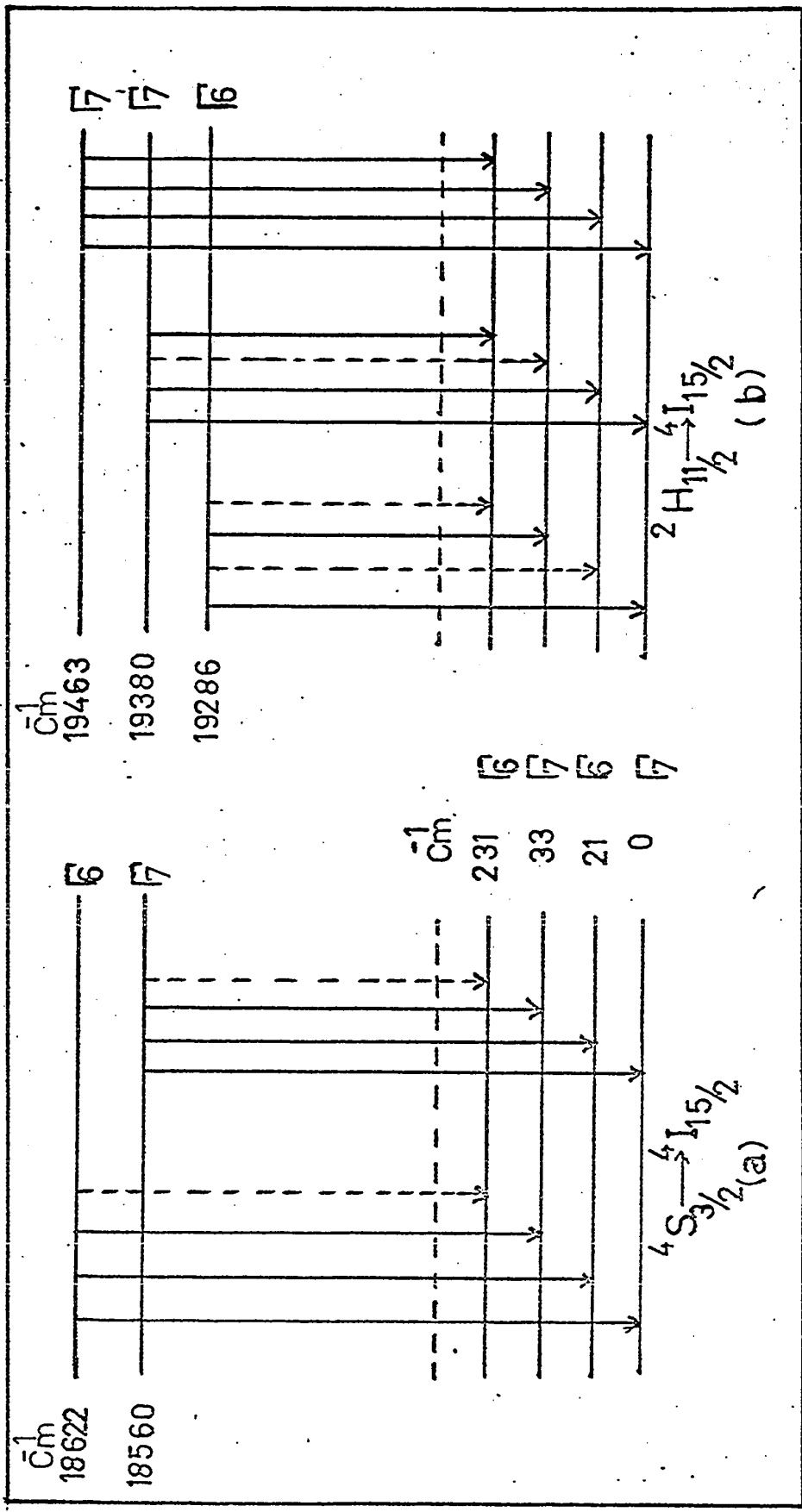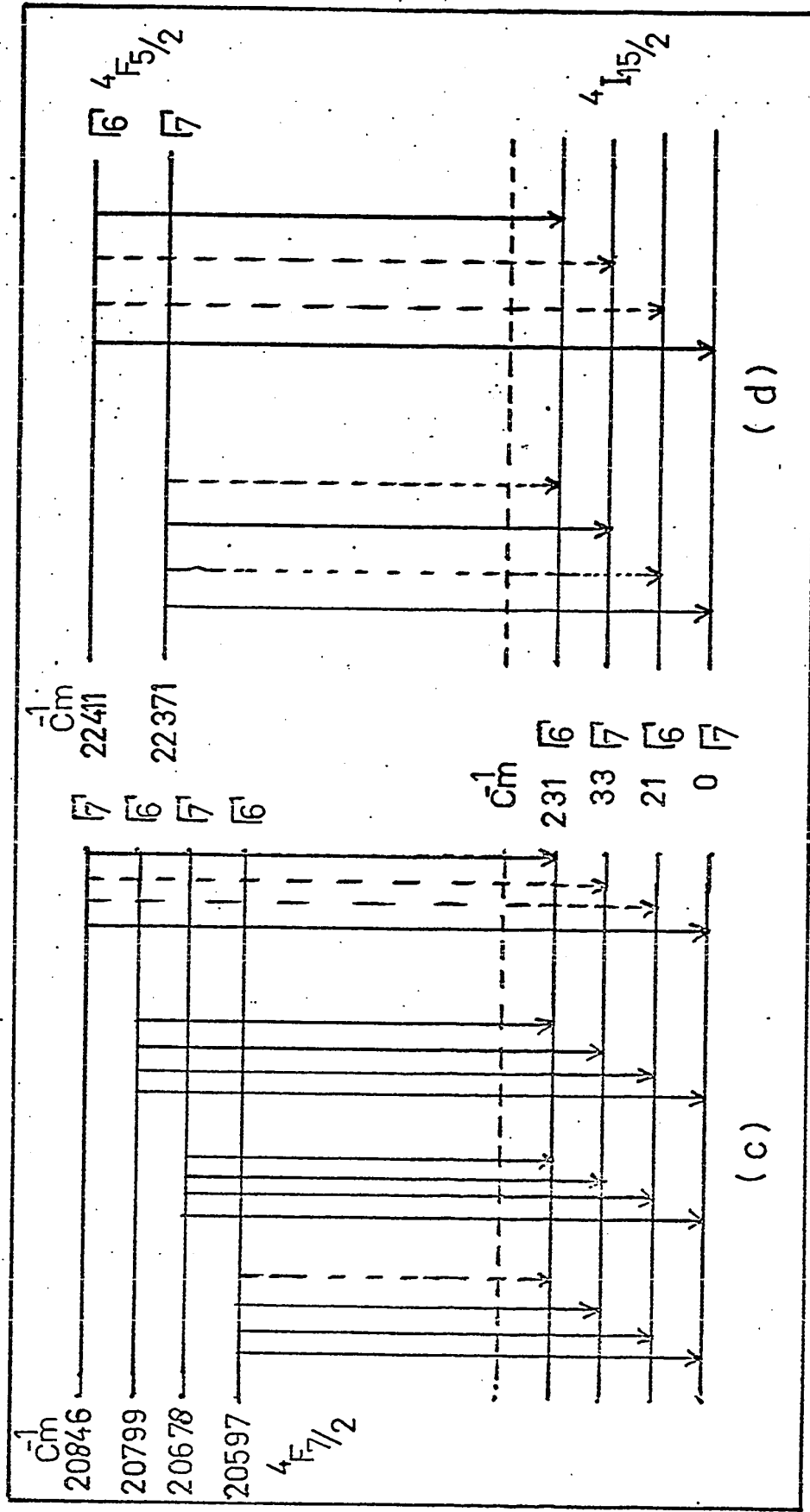
Fig. 5.4 Semi-empirical energy levels transitions for CaF_2Er^{+3} under tetragonal symmetry (excitation spectrum).

Fig. 5.4 Semi-empirical energy levels transitions for $CaF_2 Er^{+3}$ under tetragonal symmetry (excitation spectrum).

157

Fig. 5.4 Semi-empirical energy levels transitions for CaF_2Er^{+3} under tetragonal symmetry (excitation spectrum).

158
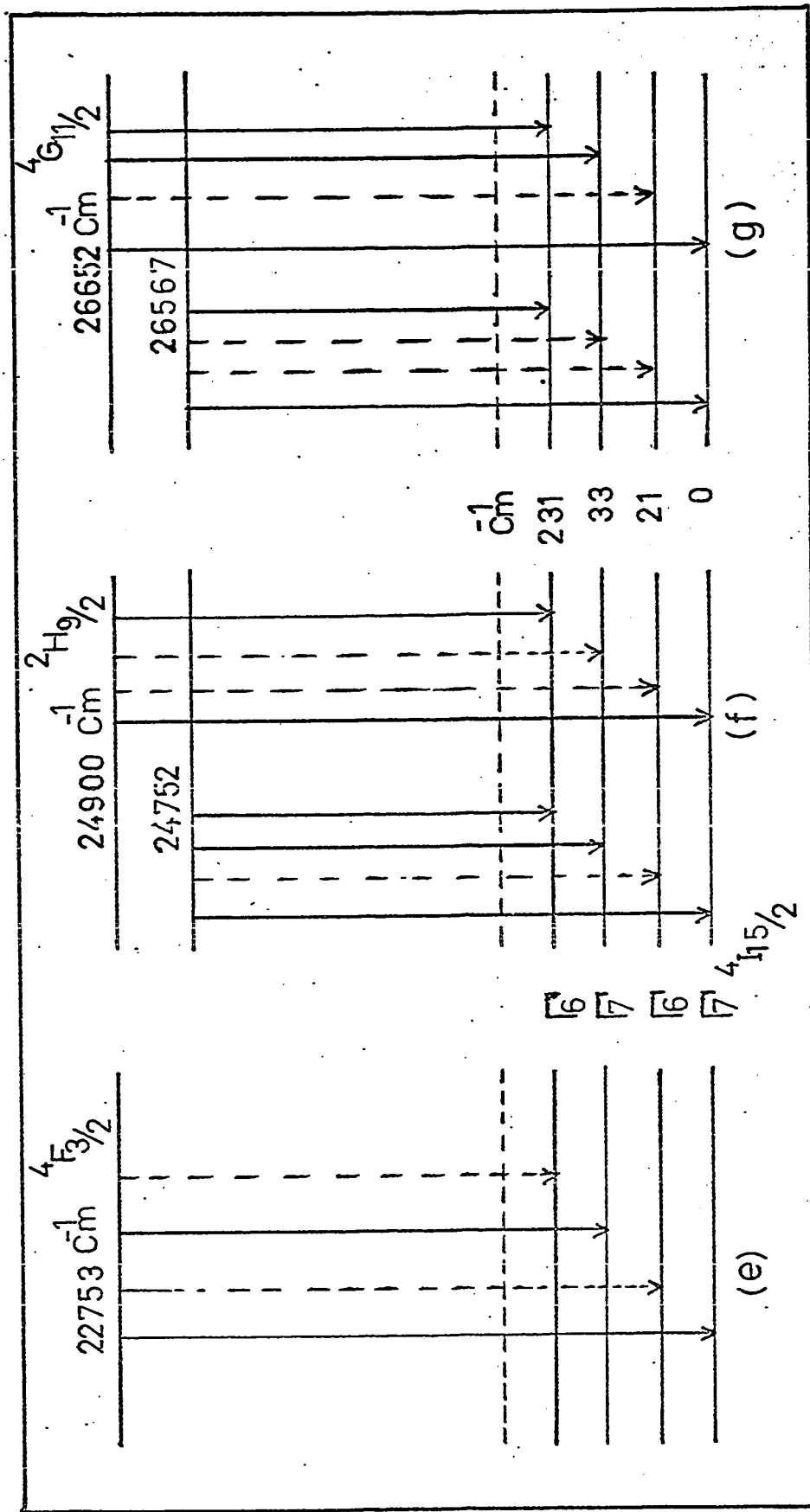
TABLE 5.1

From Luminescence Excitation Spectrum of CaF_2Er^{+3} at LNT C_{4v} Symmetry.

Splitting of Ground State $^4I_{15/2}$ is according to (5).

Transition	Electronic Line Energy Calculated (cm^{-1})	Expt. Observed (cm^{-1})	Δ = Difference Between Obs. and Cal.	Peak No. in Figs.	Figure No.
$^4S_{3/2} \rightarrow {}^4I_{15/2}$	18622-0 = 18622	18622	0	6	
	18622-21 = 18601	18601	0	5	3.12
	18622-33 = 18589	18587	-2	4	
	18622-231 = 18391				
$^4S_{3/2} \rightarrow {}^4I_{15/2}$	18560-0 = 18560	18560	0	3	
	18560-21 = 18539	18539	0	2	3.12
	18560-33 = 18527	18518	-9	1	
	18560-231 = 18329	18335 Abs.	-6		
$^2H_{11/2} \rightarrow {}^4I_{15/2}$	19286-0 = 19286	19286	0	5	
	19286-21 = 19265	19264 Abs.	-1		3.13
	19286-33 = 19253	19257	4		
	19286-231 = 19055	19069 Abs.	-14	4	
$^2H_{11/2} \rightarrow {}^4I_{15/2}$	19380-0 = 19380	19380	0	8	
	19380-21 = 19359	19350	-9	7	3.13
	19380-33 = 19347	19324	-23		
	19380-231 = 19149	19164	15	2	
$^2H_{11/2} \rightarrow {}^4I_{15/2}$	19463-0 = 19463	19463	0	11	
	19463-21 = 19442	19425	-17	10	3.13
	19463-33 = 19430	19410	-20	9	
	19463-231 = 19332	19324	-8	6	

Table 5.1 (continued)

Transition	Electronic Line Energy Calculated (cm⁻¹)		Expt. Observed (cm⁻¹)	Δ = Difference Between Obs. and Cal.	Peak No. in Figs.	Figure No.
$^4F_{7/2} \to {}^4I_{15/2}$	20678-0	= 20678	20678	0	8	
	20678-21	= 20657	20653	-4	7	3.14
	20678-33	= 20645	20640	-5	6	
	20678-231	= 20447	20462	15	1	
$^4F_{7/2} \to {}^4I_{15/2}$	20597-0	= 20597	20597	0	5	
	20597-21	= 20576	20572	-4	3	3.14
	20597-33	= 20564	20551	-13	2	
	20597-231	= 20366				
$^4F_{7/2} \to {}^4I_{15/2}$	20799-0	= 20799	20799	0	13	
	20799-21	= 20778	20773	-5	12	3.14
	20799-33	= 20766	20764	-2	11	
	20799-231	= 20568	20585	17	2	
$^4F_{7/2} \to {}^4I_{15/2}$	20846-0	= 20846	20846	0	14	
	20846-21	= 20825				3.14
	20846-33	= 20813				
	20846-231	= 20615	20618 Abs.	3		
$^4F_{5/2} \to {}^4I_{15/2}$	22371-0	= 22371	22371	0	5	
	22371-21	= 22350				3.15
	22371-33	= 22338	22336	-2	4	
	22371-231	= 22140				
$^4F_{5/2} \to {}^4I_{15/2}$	22411-0	= 22411	22411	0	6	
	22411-21	= 22390	22381 Abs.	-9		3.15
	22411-33	= 22378				
	22411-231	= 22180	22173	-7	1	

Table 5.1 (continued)

Transition	Electronic Line Energy Calculated (cm⁻¹)	Expt. Observed (cm⁻¹)	Δ = Difference Between Obs. and Cal.	Peak No. in Figs.	Figure No.
$^4F_{3/2} \to {}^4I_{15/2}$	22753-0 = 22753	22753	0	1	3.15
	22753-21 = 22732	22727	-5	Abs.	
	22753-33 = 22720	22717	-3	2	
	22753-231 = 22522				
$^2H_{9/2} \to {}^4I_{15/2}$	24900-0 = 24900	24900	0	5	3.16
	24900-21 = 24879				
	24900-33 = 24867				
	24900-231 = 24669	24667	-2	3	3.16
	24752-0 = 24752	24752	0	4	
	24752-21 = 24731				
	24752-33 = 24719	24710	-9	Abs.	
	24752-231 = 24521	24510	-11	1	
$^4G_{11/2} \to {}^4I_{15/2}$	26652-0 = 26652	26652	0	8	
	26652-21 = 26631				
	26652-33 = 26619	26617	-2	7	3.17
	26652-231 = 26421	26420	-1	3	
$^4G_{11/2} \to {}^4I_{15/2}$	26567-0 = 26567	26567	0	6	
	26567-21 = 26546				
	26567-33 = 26534	26521	-13	Abs.	3.17
	26567-231 = 26336	26316	-20	1	
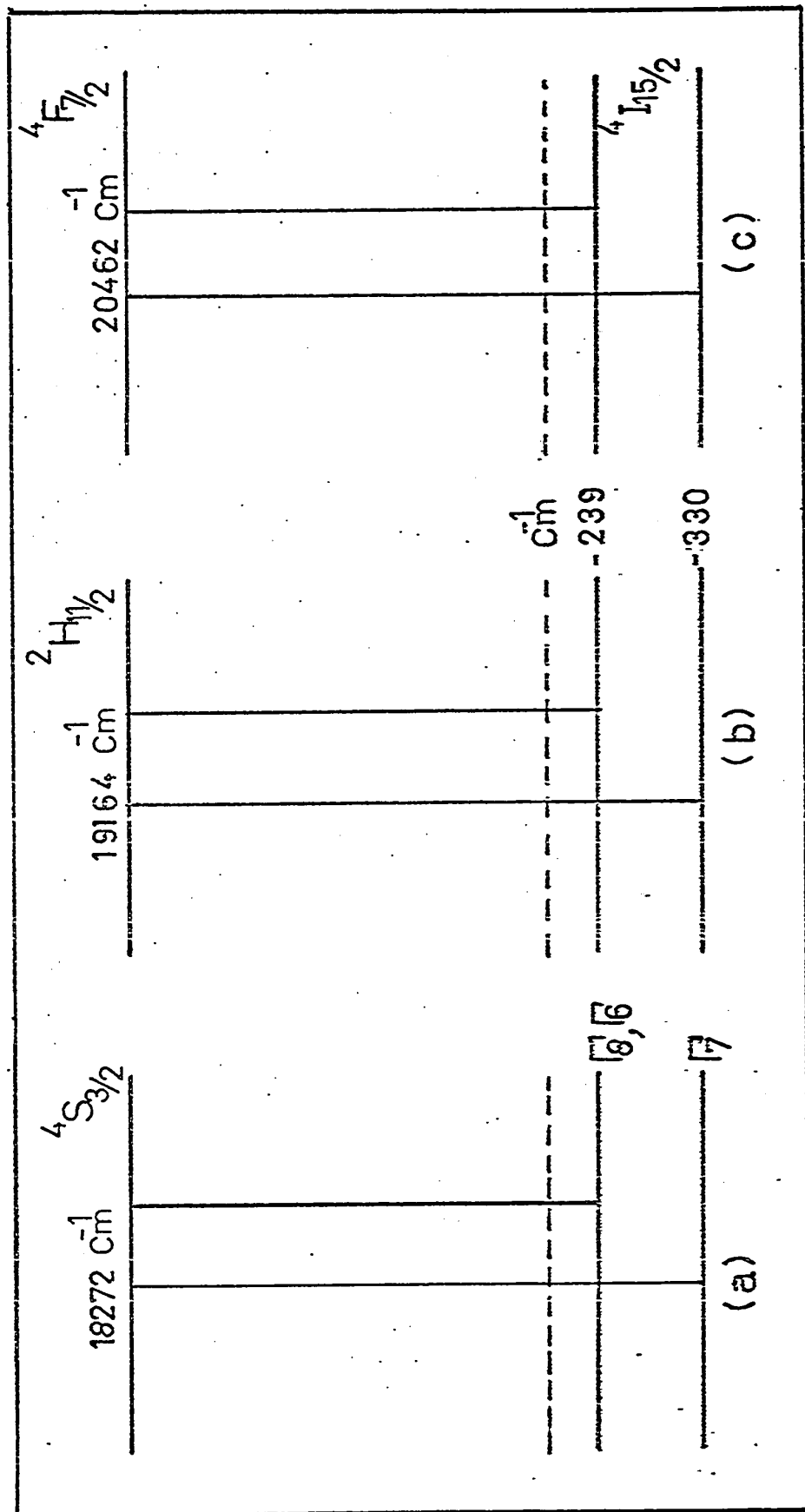
Fig. 5.5 Semi-empirical energy levels transitions for CaF_2Er^{+3} under cubic symmetry (excitation spectrum).
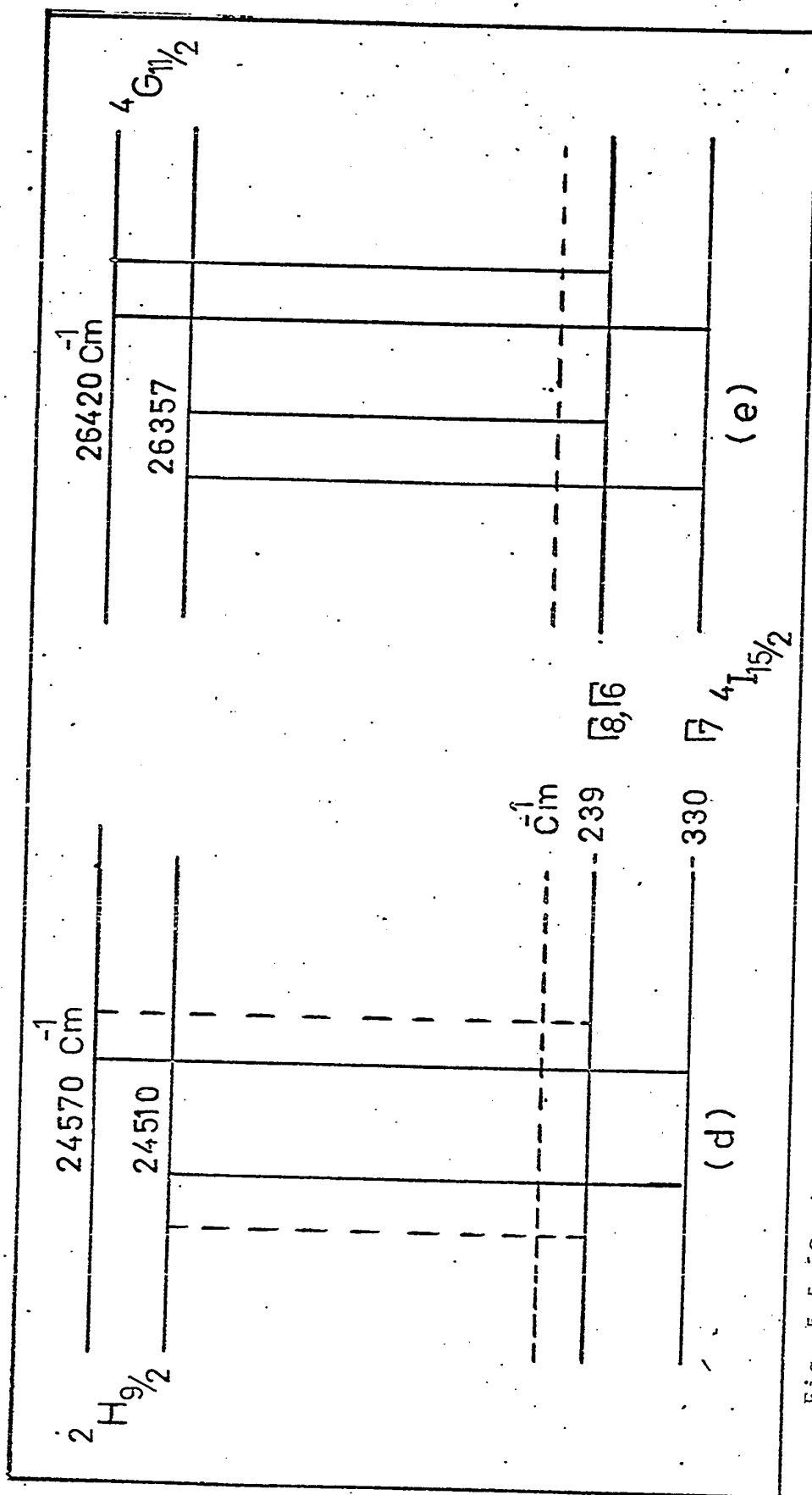
Fig. 5.5 Semi-empirical energy levels transitions for CaF$_2$Er^{+3} under cubic symmetry (excitation spectrum).

TABLE 5.2

Under O_h Symmetry from Luminescence Excitation Spectrum of CaF_2Er^{+3} at LNT.

Splitting of Ground State is according to (11). */

Transition	Electronic Line Cal. (cm⁻¹)	Obs. (cm⁻¹)	Δ (cm⁻¹)	Peak No. see Fig.	Fig. No.
$^4S_{3/2} \rightarrow {}^4I_{15/2}$	18272-(-330) = 18602	18601	-1	5	3.12
	18272-(-239) = 18511	18518	7	1	
$^2H_{11/2} \rightarrow {}^4I_{15/2}$	19164-(-330) = 19494	19485	-9	12	3.13
	19164-(-239) = 19403	19410	7	9	
$^4F_{7/2} \rightarrow {}^4I_{15/2}$	20462-(-330) = 20792	20799	7	13	3.14
	20462-(-239) = 20701	20708	7	9	
$^2H_{9/2} \rightarrow {}^4I_{15/2}$	24570-(-330) = 24900	24900	0	5	3.16
	24570-(-239) = 24809				
	24510-(-330) = 24840				
	24510-(-239) = 24749	24752	3	4	3.16
$^4G_{11/2} \rightarrow {}^4I_{15/2}$	26357-(-330) = 26687	26688	1	9	3.17
	26357-(-239) = 26596	26567	-29	7	
	26420-(-330) = 26750	26745	-5	10	3.17
	26420-(-239) = 26659	26652	-7	8	

bands were not seen in the absorption spectrum of CaF_2Pr^{+3}. The strongest band was observed in emission spectrum (Fig. 3.40). We believe that these bands are either due to the interconfiguration transition $4f^2 \rightarrow 4f5d$ or due to the presence of divalent prosedymium.

Hargreaves (7) has claimed the position of $^3P_2$ at 22696 cm^{-1} but there is a difference of 300 cm^{-1} between his experimentally observed level and the theoretical calculated value. The difference between our observed $^3P_2$ level and that of Hargreaves could well be caused by the presence of relatively higher symmetry in our crystal. We have found a difference of approximately 270 cm^{-1} in the positions of energy level $^3P_2$ as observed from the lumines- cence excitation and absorption measurements. As pointed out by Schlesinger (12), in the presence of higher symmetry the mean energy levels move towards the higher energy side and vice versa. From the same crystal we have seen four more components in the higher energy side as compared with that of the absorption spectrum and, among those four, two components are very strong. We believe that efficiency of excitation of a certain type of symmetry depends upon the exciting light used. Support of this has been given by Schlesinger and Kwan (13).

An attempt has been made to construct an energy level scheme under the cubic symmetry by assuming that vibronic lines are also present. The results are shown in Fig. 5.6 . The lowest stark split component of the

TABLE 5.3

Cubic Symmetry from Luminescence Excitation Spectrum of CaF_2Pr^{+3}.

$^3P_2$ will split into two components $^2\Gamma_3$ and $^3\Gamma_5$.

Transition		Electronic Line Cal. (cm^{-1})	Expt. (cm^{-1})	Δ (cm^{-1})
$^3P_2 \rightarrow {}^3H_4$	$^2\Gamma_3$	$23212-144 = 23068$	23084	16
		$23212-234 = 22978$	22988	10
	$^3\Gamma_5$	$22831-144 = 22687$	22696	9
		$22831-227 = 22604$		
		$22831-234 = 22597$	22599	2
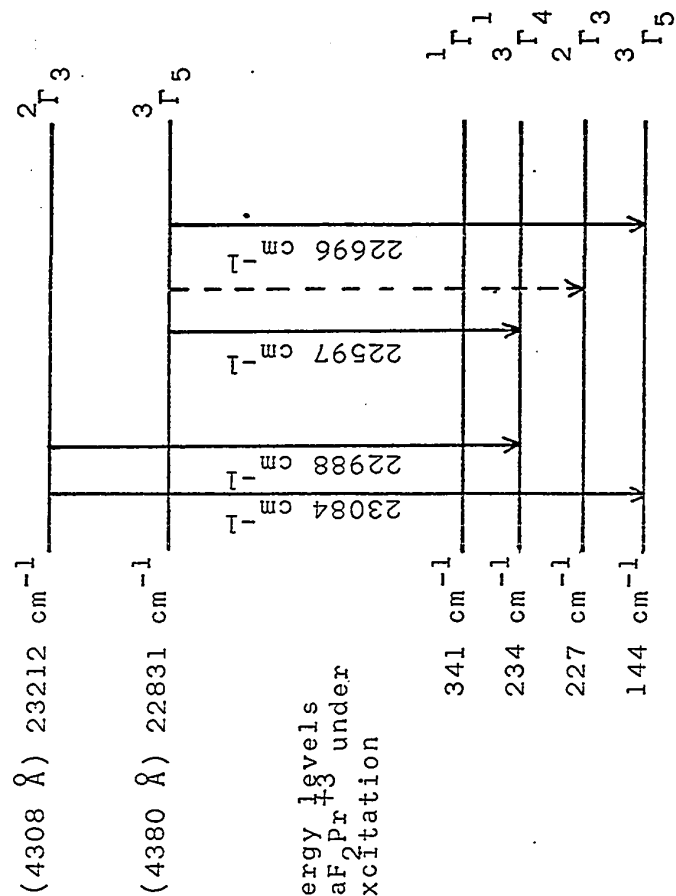
Fig. 5.6 Semi-empirical energy levels transitions for CaF_2Pr^{+3} under cubic symmetry (excitation spectrum).

ground state of Pr^{+3} under the cubic symmetry is Γ_5 and

the other excited states are Γ_3, Γ_4 and Γ_1. The

allowed transitions under different symmetries were

obtained from Table 2.11. Experimentally observed transi-

tions under O_h symmetry, along with their calculated

values, and the differences between the two are given in

Table 5.3.

5.3 Discussion of Emission Spectra

(a) CaF_2Er^{+3}

The electron configuration of Er^{+3} is $4f^{11}$ with a ground state $^4I_{15/2}$. There exists an excited state $^4S_{3/2}$ approximately at 18300 cm^{-1} in the free ion. The observed green emission corresponds to the $^4S_{3/2} \rightarrow {}^4I_{15/2}$ stark split transitions. Working in the spectral region 17970 cm^{-1} to 18610 cm^{-1}, our crystals were excited with different exciting energies. Figs. 3.31 to 3.34 show that the intensities of some of the emission lines change and some new lines have appeared in the emission. We suggest that this is due to the presence of a mixture of site symmetries of the Er^{+3} ion in the crystal. Specifically by exciting the crystal with different wavelengths, components belonging to a particular symmetry which happens to absorb in that wavelength will be excited more readily than in the other. Such was shown to be the case in $CaF_2:Dy^{+3}$ by Schlesinger and Kwan (13).

An attempt has been made to construct the transition scheme of energy levels for CaF_2Er^{+3} assuming tetragonal symmetry (see Fig. 5.7 and Table 5.4). The emission lines due to sites of cubic symmetry seem to be very weak. It should be noted that the splitting of the ground state $^4I_{15/2}$ is in accordance with Reference (5).

TABLE 5.4

Under C_{4v} Symmetry from the Luminescence Spectrum of $CaF_2:Er^{+3}$ at LNT.

Splitting of the ground state is according to reference (5).

Transition	Electronic Line Energy Calculated (cm^{-1})		Expt. observed line (cm^{-1})	Δ (cm^{-1})	Peak No. see Fig.	Fig. No.
$4S_{3/2} \rightarrow 4I_{15/2}$	18543-0 =	18543	18543	0	12	3.31
	18543-21 =	18522	18516	-6	11	
	18543-33 =	18510	18508	-2	Thermo.	
	18543-231 =	18312	18308	-4	4	
	18543-403 =	18140	18135	-5	Thermo.	
	18543-436 =	18107	18109	2	3	
	18543-452 =	18091	18084	-7		
	18608-0 =	18608	18608	-2	13	
	18608-21 =	18587	18587	0	Lum. Excit.	
	18608-33 =	18575	18552	-23	Thermo.	
	18608-231 =	18377	18372	-5	9	
	18608-403 =	18205	18212	7	6	
	18608-436 =	18172	18181	9	5	
	18608-452 =	18156	18152	-4	Thermo.	

18608 cm^{-1}
18543 cm^{-1}

452 cm^{-1} Γ_6
436 cm^{-1} Γ_7
403 cm^{-1} Γ_7
231 cm^{-1} Γ_6
33 cm^{-1}
21 cm^{-1} Γ_7
0 cm^{-1}
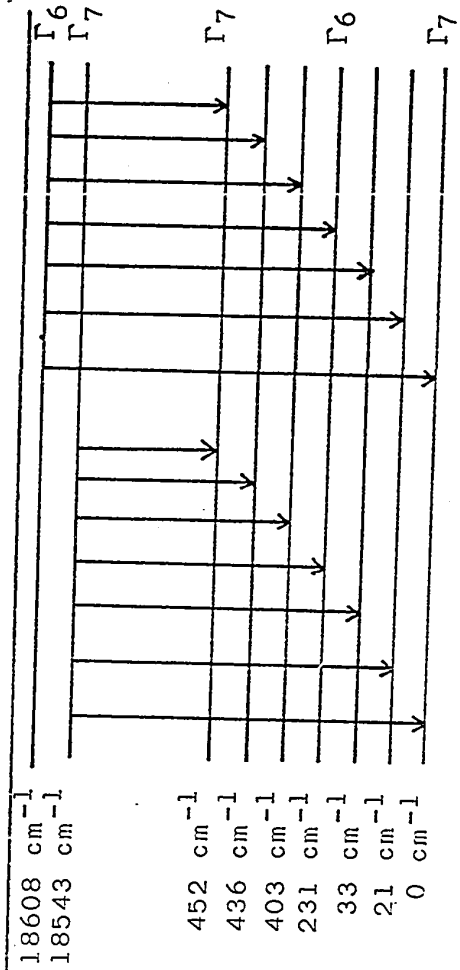
Fig. 5.7   Semi-empirical energy levels transitions for $CaF_2:Pr^{+3}$ under tetragonal symmetry (luminescence spectrum).

We claim that at LNT the emission in the luminescence spectrum is mainly due to sites of tetragonal symmetry surrounding the Er^{+3} ion in the CaF_2 crystal. A comparison between luminescence and thermoluminescence spectra will be given in the next section, where it will be evident that in the thermoluminescence emission more than one symmetry can be observed.

(b) $\underline{CaF_2 Pr^{+3}}$

The electron configuration of Pr^{+3} is $4f^2$ with a ground state $^3H_4$. There exists an excited state $^3P_1$ approximately at 22000 cm^{-1} in the free ion. The observed blue-green emission corresponds to the $^3P_1 \rightarrow {}^3H_4$ transitions. Working in the spectral region 20400 cm^{-1} to 22000 cm^{-1}, the crystal was excited with different wavelengths as shown in Figs. 3.35 to 3.39 . Our results are, once again, parallel to the conclusions drawn by Schlesinger and Kwan (13), who worked with Dy^{+3} doped CaF_2.

An attempt has been made to construct energy level schemes for cubic and tetragonal site symmetries as shown in Figs. 5.8ab, Tables 5.5, 5.6. Under the influence of a crystal field of cubic symmetry, the ground state $^3H_4$ of Pr^{+3} splits into four components Γ_1, Γ_3, Γ_4 and Γ_5 among which Γ_5 is the lowest and Γ_1 is the highest. All the electric dipole transitions from $^3P_1$ to $^3H_4$ are allowed (see Table 2.11). We suggest that under the influence of the cubic crystal field, the ground state will split to

TABLE 5.5

Under O_h Symmetry from the Luminescence Spectrum

of CaF_2Pr^{+3} at LNT

Transition	Electronic Line Calc. (cm⁻¹)	Experimentally Observed (cm⁻¹)	$\overset{\Delta}{(cm^{-1})}$	Peak No.	Fig. No.
$^3P_1 \rightarrow {}^3H_4$	$20951 - 144 = 20807$	20820	13	13	
	$20951 - 227 = 20724$	20721	-3	11	3.36
	$20951 - 234 = 20717$				
	$20951 - 341 = 20610$	20618	-8	9	
$^3P_0 \rightarrow {}^3H_4$	$20387 - 234 = 20153$	20149	-4	1	
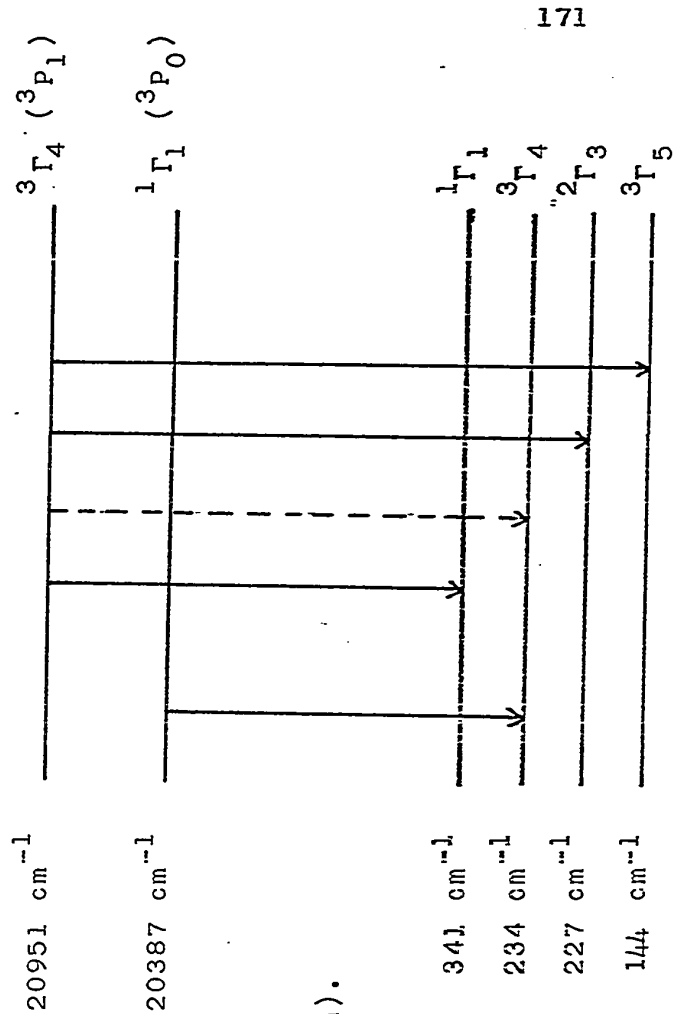
Fig. 5.8(a) Semi-empirical energy levels transitions for CaF_2Pr^{+3} under tetragonal and cubic symmetries (from luminescence spectrum).

$3\Gamma_4$ $(^3P_1)$ 20951 cm⁻¹

$1\Gamma_1$ $(^3P_0)$ 20387 cm⁻¹

$1\Gamma_1$ 341 cm⁻¹

$3\Gamma_4$ 234 cm⁻¹

$2\Gamma_3$ 227 cm⁻¹

$3\Gamma_5$ 144 cm⁻¹

TABLE 5.6

Under C_{4v} Symmetry from the Luminescence Spectrum of CaF_2Pr^{+3} at LNT.

Splitting of the ground state is according to reference (7).

Transition	Electronic Line Energy Calculated (cm⁻¹)	Experimentally Observed (cm⁻¹)	Δ (cm⁻¹)	Peak No.	Fig. No.
$^3P_1 \rightarrow {}^3H_4$	20764 - 0 = 20764	20764	0	12	
	20764 - 35 = 20729	20721	-8	11	
	20764 - 83 = 20681	20678	-3	10	3.36
	20764 - 99 = 20665				
	20764 - 134 = 20630	20618	-12	9	
$^3P_0 \rightarrow {}^3H_4$	20387 - 99 = 20288	20280	-8	4	
	20387 - 134 = 20253	20259	6	3	
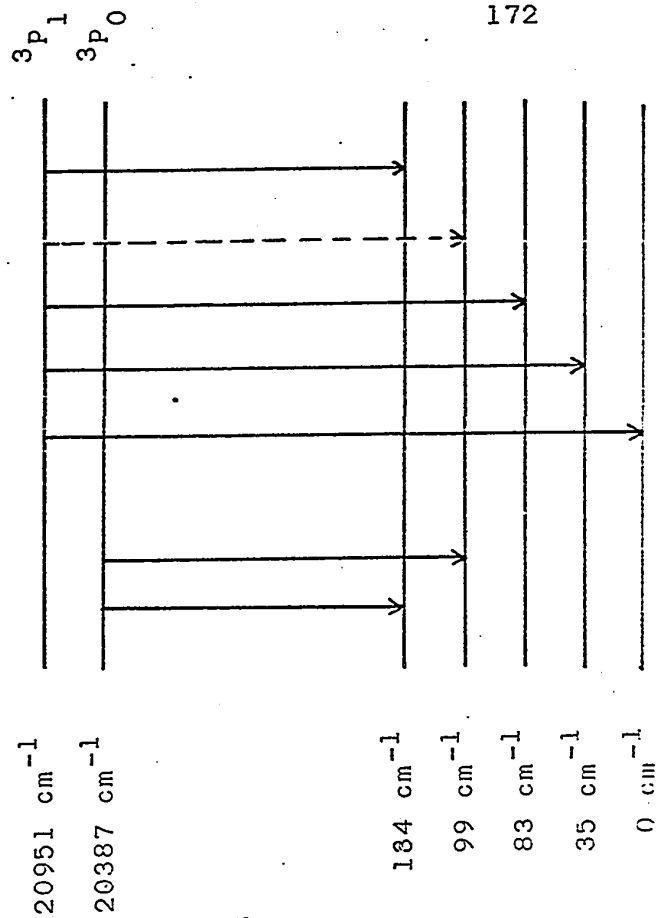
Fig. 5.8(b) Semi-empirical energy levels transitions for CaF_2Pr^{+3} under tetragonal and cubic symmetries (from luminescence spectrum).

$^3P_1$ 20951 cm⁻¹

$^3P_0$ 20387 cm⁻¹

184 cm⁻¹

99 cm⁻¹

83 cm⁻¹

35 cm⁻¹

0 cm⁻¹

approximately 200 cm^{-1}. We did observe a strong line at
20387 cm^{-1} and we believe that this is due to a $^3P_0 \rightarrow {}^3H_4$
transition as under the cubic symmetry there is only one
allowed electric dipole transition from Γ_1 to Γ_4 (see
Table 2.11).

Results indicate that at LNT in the as-received
crystals, the emission observed in luminescence spectrum
is due mainly to tetragonal sites for the Pr^{+3} ion in the
CaF_2 crystal. Indeed, while the main lines are due to
tetragonal symmetry, lines due to cubic symmetry are also
present but are very weak in intensity. Comparison between
luminescence and thermoluminescence spectra will be given
in the next section, where it will be evident that the
"tetragonal" to "cubic" line intensity ratio is different.

5.4 Discussion of Thermoluminescent Spectra

In general, upon x-irradiation, some of the tri-
positive rare-earth ions are reduced to the divalent state,
while the generated hole is trapped in a nearby site. Upon
heating, the trapped hole is released and recombines with
the extra electron on the rare-earth ion, thus reoxidizing
it to an excited state of tripositive ion. The excited
ion returns to its ground state, emitting its characteristic
radiation. The thermoluminescent spectra of CaF_2Er^{+3} and
CaF_2Pr^{+3} will be discussed in the subsections (a) and (b),
respectively.

(a) <u>CaF$_2$Er^{+3}</u>

      The observed green emission in the thermoluminescent spectrum of CaF$_2$Er^{+3} corresponds to the $^4S_{3/2} \rightarrow {}^4I_{15/2}$ stark split transition. The thermoluminescent spectrum of CaF$_2$Er^{+3} was studied by Merz and Pershan (15). They have proposed that all the thermoluminescent emission in rare-earth doped CaF$_2$ below room temperature comes from ions in cubic lattice sites. A careful comparison between our Fig. 3.41 with Fig. 7 of reference (15) reveals that we have an almost identical profile except with the difference that at RT we have less number of lines and also the general intensity decreases as the temperature increases. Based on the observed results and the comparison with luminescence emission, we propose that in the as-received crystal, even at LNT, there exists a mixture of site symmetries (O$_h$, C$_{4v}$) for the Er^{+3} ions in the CaF$_2$ crystal. As the temperature is increased, the effect on different symmetries will be different and above room temperature, the lines observed in thermoluminescence spectrum are due to sites of cubic symmetry only. Some vibronic lines are also present.

      Figs. 5.7 and 5.9 show the transition scheme due to cubic and tetragonal symmetries surrounding the Er^{+3} ion in CaF$_2$ crystal. Table 5.7 gives the comparison between the calculated and observed values. A careful comparison between the Figs. 3.44 and 3.31 reveals that the emission in the luminescence spectrum is mainly due to tetragonal

TABLE 5.7

From the Thermoluminescence Spectrum of CaF_2Er^{+3} under O_h Symmetry.

Splitting of the ground state is according to reference (11).

Transition	Electronic Line Energy Calculated (cm^{-1})		Expt. Observed Line (cm^{-1})	Δ (cm^{-1})	Peak No. see Fig.	Fig. No.
$^4S_{3/2} \to {}^4I_{15/2}$	18272 + 330 =	18602	18608	6	17	
	18272 + 239 =	18511	18508	-3	14	
	18272 - 228 =	18044	18034	-10	7	
	18272 - 296 =	17976	17943	-33	6	3.44

Vibronic Lines Cal. (cm^{-1})		Obs. (cm^{-1})	(cm^{-1})	Peak No.
18508 - 135 =	18373	18372	-1	12
18034 - 135 =	17899	17901	2	5
17943 - 135 =	17808	17812	4	4
17943 - 270 =	17673	17670	-3	1

$^4\Gamma_8$

$^4\Gamma_8{}^3$
$^4\Gamma_8{}^3$
$^2\Gamma_6, \, ^4\Gamma_8{}^1$
$^2\Gamma_7$

18272 cm^{-1}

296 cm^{-1}

228 cm^{-1}

-239 cm^{-1}

-330 cm^{-1}
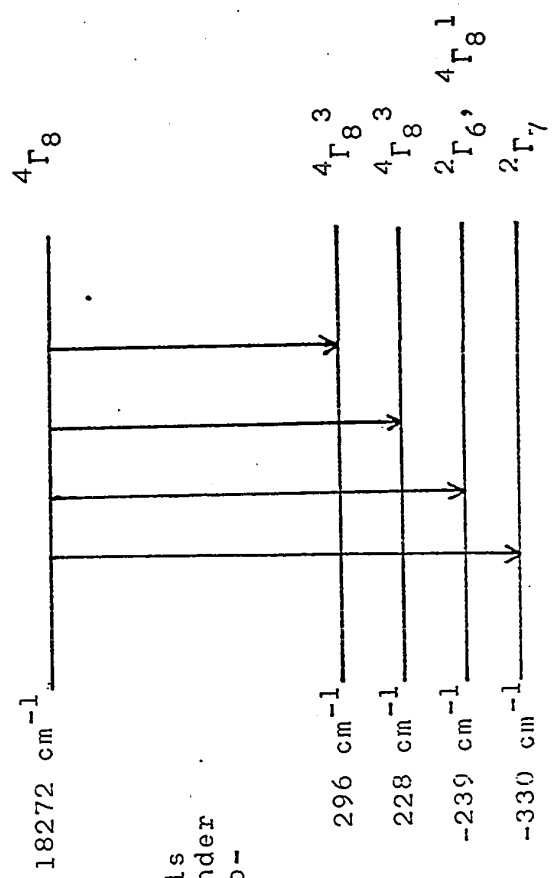
Fig. 5.9 Semi-empirical energy levels transitions for CaF_2Er^{+3} under cubic symmetry (from thermo-luminescence spectrum).

site symmetry while the emission in the thermoluminescence spectrum is due to cubic and tetragonal sites. Table 5.8 gives the comparison between the two. As noted earlier, Schlesinger and Kwan (13) have observed parallel results in the case of CaF_2Dy^{+3}.

(b) $\underline{CaF_2Pr^{+3}}$

We have observed two groups in the thermoluminescent spectrum of CaF_2Pr^{+3}, one group belongs to the $^3P_1 \rightarrow {}^3H_4$ transition and the other belongs to the $^3P_0 \rightarrow {}^3H_4$ transition. We observed a larger number of components in the lower energy side as compared with the luminescence spectrum. We believe that this is due to excitation of ions in symmetry sites lower than cubic. Once again our results are consistent with the conclusion drawn by Schlesinger and Kwan (13).

Table 5.9 gives the comparison between luminescence and thermoluminescence spectra. Figs. 5.8 (a) and (b) show the transition schemes for cubic and tetragonal site symmetries. A careful comparison between Fig. 3.45 and 3.36 reveals that emission in luminescence spectrum is a true subset of that of thermoluminescence spectrum, which again means that in the luminescence we observe possibly one and in the thermoluminescence possibly two (or more) site symmetries.

TABLE 5.8

Assignments of Peaks in Luminescence and

Thermoluminescence Spectra Exhibited by Er^{+3} in CaF_2.

Peak Values are Expressed in cm^{-1}.

SLJ Assignment	Luminescence	Thermoluminescence	Assignment	
		17670	Vib	
		17736		
		17793		
		17812	Vib	
		17901	Vib	
		17943		
	17976		O_h	
		18034		
	18059		O_h	
	18084			C_{4v}
		18109		C_{4v}
	18135	18135		C_{4v}
		18152		
	18181			C_{4v}
	18212			C_{4v}
	18272	18272	O_h	
	18308			C_{4v}
	18342		Vib	
	18372	18372		C_{4v}
	18423			
	18450	18450		C_{4v}
		18508		
	18516		O_h	
	18543	18543		C_{4v}
		18552		
	18608	18608	O_h	C_{4v}
		18733		

TABLE 5.9

Assignments of Peaks in Luminescence and Thermoluminescence Spectra

Exhibited by Pr^{+3} in CaF_2.

Peak Values are expressed in cm^{-1}.

SLJ Assignment	Luminescence	Thermoluminescence	Assignment
		20032	
		20056	
		20084	
		20116	
	20149	20149	O_h
	20202	20202	
		20251	Vibronic line to 20387 cm^{-1} (-135 cm^{-1})
	20259		C_{4v}
	20280	20292	C_{4v}
	20300		
	20387	20387	O_h
			Vibronic line to 20618 cm^{-1} (-135 cm^{-1})
	20488	20488	C_{4v}
		20512	Vibronic line to 20387 cm^{-1} (135 cm^{-1})
	20563	20563	Vibronic line to 20721 cm^{-1} (-135 cm^{-1})
		20584	
	20618	20618	O_h
			C_{4v}
	20678	20678	C_{4v}
	20721	20721	O_h
			C_{4v}
	20764	20764	C_{4v}
	20820	20820	O_h
			C_{4v}
	20859	20859	O_h
	20951	20951	O_h
		21066	

5.5 A Possible Model for Thermoluminescence

$$
\begin{array}{ll}
\overset{+2}{\text{Ca}} & \circ \\
\overset{+3}{\text{RE}} & \odot \\
\bar{\text{F}} & \text{X}
\end{array}
$$
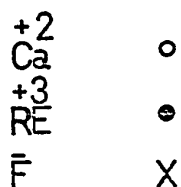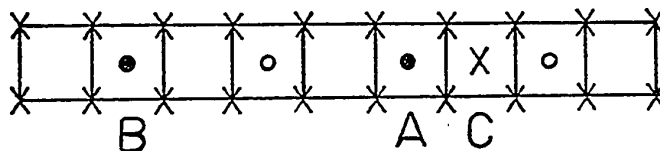
Fig. 5.10 Suggested model for thermoluminescent spectrum.

As shown in Fig. 5.10, the rare-earth ion at site A will be under the influence of C_{4v} symmetry. The rare-earth ion at site B, which is well separated from the charge compensator, will experience a cubic field. Thus, in this type of model, there exists a mixture of symmetries surrounding the rare-earth ions.

Upon x-irradiation, the rare-earth ion at site A is reduced to the divalent state, while the hole is trapped in a nearby site. After the reduction of the RE^{+3} ion to the RE^{+2} state, the compensator is no longer required. At RT the charge compensator at site C becomes mobile and RE^{+2} at site A may be left in the cubic site symmetry. On further heating, the hole is released from its trap and reoxidizes RE^{+2} at site A to an excited state $(RE^{+3})^*$. The excited ion $(RE^{+3})^*$ returns to its ground state, emitting

its characteristic radiation. Thus the emission above RT is characteristic of the RE^{+3} ion in the cubic sites, while the emission at lower temperatures are believed to originate from sites of mixed symmetries. A similar model was proposed by Schlesinger and Whippey (12).

Chapter 6 CONCLUSIONS

6.1 $CaF_2 Er^{+3}$

The optical spectrum of $CaF_2 Er^{+3}$ (1%) at LNT has been studied in the spectral region 6600 cm^{-1} to 65400 cm^{-1} and 4f → 4f and interconfiguration transitions $4f^{11}$ → $4f^{10} 5d$ have been observed. In the case of $CaF_2 Er^{+3}$ two new energy levels $^2F_{7/2}$ and $^2F_{5/2}$ at 54795 cm^{-1} and 63091 cm^{-1} have been identified, which have not been observed previously in any host lattice. New lines at 59453 cm^{-1} and 60606 cm^{-1} have been observed but their origins are not well understood.

Employing luminescence excitation techniques, the excitation spectrum has been studied in the spectral region 18200 cm^{-1} to 50000 cm^{-1}. From the excitation spectrum, it is concluded that at LNT the emission is due to a mixture of symmetries (O_h, C_{4v}) surrounding the Er^{+3} ion in the matrix of CaF_2. An attempt was made to construct an energy level scheme for an ion under the influence of cubic and tetragonal field symmetries. The excitation spectra obtained from the two samples obtained from Harshaw Chemical Company and Optovac Inc. are not identical. We suggest that this difference is due to the presence of mixed symmetries in different proportion in the two samples.

From luminescence experiments at LNT, it is concluded that the emission is predominantly due to tetragonal symmetry surrounding the Er^{+3} ion in the CaF_2 crystal while

the emission due to cubic symmetry is very weak. From the
thermoluminescent spectrum exhibited by CaF_2Er^{+3}, it is
inferred that at LNT the emission is due to cubic and
tetragonal symmetries, while the emission at RT is
predominantly due to the Er^{+3} ion in cubic sites.

By comparing luminescence and thermoluminescence
spectra of CaF_2Er^{+3}, we claim that the lines observed in
luminescence spectrum constitute a true subset of the lines
observed in thermoluminescence spectrum. This is taken to
be an indication that while the former is due to one
symmetry, the latter might be attributed to more than one
site symmetry.

6.2 CaF_2Pr^{+3}

The optical spectrum of CaF_2Pr^{+3} (1%) has been studied in
the spectral region 4250 cm^{-1} to 50000 cm^{-1}. The mean
energy levels obtained from absorption experiments are in
agreement with those of the Pr^{+3} ion in aqueous solution.
By comparing the mean energy levels of CaF_2Pr^{+3} with those
of a free ion, we have noticed a disproportionate shift
in the energy levels. This is claimed to be due to the
presence of a strong field around the Pr^{+3} ion in the CaF_2
crystal, and also due to the configuration interaction.
The positions of the energy levels $^3P_2$, $^1I_6$, $^3P_1$ and $^3P_0$
have been established to be 22526 cm^{-1}, 21481 cm^{-1}, 21306
cm^{-1} and 20777 cm^{-1}, respectively. It is suggested that
energy levels $^3P_1$ and $^1I_6$ are brought into close proximity

in the matrix of CaF_2.

Excitation spectrum of CaF_2Pr^{+3} (0.1%) has been studied in the spectral region 23800 cm^{-1} to 50000 cm^{-1}. Impurity concentration dependent bands at 3950 Å, 3660 Å, 3530 Å, 2740 Å and 2620 Å have been observed and are tentatively identified. The intensities of these bands decrease by increasing the concentration of the Pr^{+3} ion. An attempt has been made to construct an energy level scheme for ions in sites of cubic symmetry. The splitting of the ground state has been found to be approximately 200 cm^{-1}. The position of $^3P_2$ has been established to be at 22800 cm^{-1} which does not agree with the value inferred from absorption spectrum.

Emission in the luminescence spectrum at LNT is mainly due to tetragonal symmetry around the Pr^{+3} ion in the CaF_2 crystal, while the emission in thermoluminescence spectrum is due to both cubic and tetragonal site symmetries.

BIBLIOGRAPHY

<u>Chapter 1</u>

0. M. G. Mayer, Phys. Rev., <u>60</u>, 184 (1941).

1. M. J. Weber and R. W. Bierig, Phys. Rev., <u>134</u>, A1492
    (1964).

2. W. Low, J. Phys. Soc. Japan, <u>17</u>, Suppl. B-I, 440 (1962).

3. B. Bleaney, P. M. Llewellyn and D. A. Jones, Proc. Phys.
    Soc. (London), <u>B69</u>, 858 (1956).

4. J. M. Baker, W. Hayes and M. C. M. O'Brien, Proc. Roy.
    Soc. (London), <u>A254</u>, 273 (1960).

5. W. Low, Phys. Rev., <u>134</u>, A1479 (1964).

6. B. G. Berulava et al, Sov. Phys. JETP, <u>21</u>, 228 (1965).

7. I. V. Stepanov and P. P. Feofilov, Sov. Phys. Doklady,
    <u>1</u>, 350 (1956).

8. P. A. Forrester and C. F. Hempstead, Phys. Rev., <u>126</u>,
    923 (1962).

9. W. Low and V. Rosenberger, Compt. Rend., <u>254</u>, 1771 (1962).

10. V. M. Vinokurov et al, Sov. Phys. Solid State, <u>4</u>, 1637
    (1963).
    ibid., <u>5</u>, 436 (1963).
    ibid., <u>5</u>, 2126 (1964).

11. J. Makovsky, Phys. Quantum Electronics Conf., (McGraw-
    Hill Co. Inc., New York, 1966).

12. J. Sierro, Helv. Phys. Acta, <u>36</u>, 505 (1963).
    ibid., J. Chem. Phys., <u>34</u>, 2183 (1961).
    ibid., Phys. Letters, <u>4</u>, 178 (1963).

13. S. D. McLaughlan and R. C. Newman, Phys. Letters, <u>19</u>,
    552 (1965).

14. Z. J. Kiss, J. Chem. Phys., <u>38</u>, 1476 (1963).

15. W. Low, Phys. Rev., <u>109</u>, 265 (1958).

16. C. Ryter, Helv. Phys. Acta, 30, 353 (1957).

17. M. Dvir and W. Low, Proc. Phys. Soc. (London), 75, 136 (1960).

18. W. Low, Phys. Rev., 134, A1479 (1964).

19. W. Low, Proc. Phys. Soc. (London), 76, 307 (1960).

20. W. Low, Phys. Rev., 118, 1608 (1960).

21. W. Hayes and J. W. Twidell, J. Chem. Phys., 35, 1521 (1961).

22. S. T. Pai, Ph.D. Thesis, University of Windsor, Windsor, Ontario (1970).

23. E. Friedman and W. Low, J. Chem. Phys., 33, 1275 (1960).

24. M. Schlesinger and P. W. Whippey, Phys. Rev., 177, 563 (1969).

25. S. Kh. Batygov and V. V. Osiko, Sov. Phys. Solid State, 13, 1886 (1972).

26. W. Low and U. Ranon, Paramagnetic Resonance (Academic Press Inc., New York, 1963), p. 167.

27. W. Hayes and J. W. Twidell, J. Chem. Phys., 35, 1521 (1961).

28. W. Hayes, G. D. Jones and J. W. Twidell, Proc. Phys. Soc. (London), 81, 371 (1963).

29. W. Hayes and J. W. Twidell, Proc. Phys. Soc. (London), 82, 330 (1963).

30. F. R. Merritt, H. Guggenheim and C. G. B. Garrett, Phys. Rev., 145, 188 (1966).

31. B. Bleaney, J. Appl. Phys., 33, Suppl. I, 358 (1962).

32. J. M. Baker, W. Hayes and D. A. Jones, Proc. Phys. Soc. (London), 73, 942 (1959).

33. J. M. Baker, B. Bleaney and W. Hayes, Proc. Roy. Soc. (London), A247, 141 (1958).

34. T. F. Ewanizky and P. J. Kaplan and J. R. Pastore, J. Chem. Phys., 43, 4351 (1965).

35. R. W. Bierig and M. J. Weber, Phys. Rev., 132, 164 (1963).

36. M. Schlesinger and H. Nara, Phys. Rev., $\underline{3}$, 58 (1971).

37. M. Schlesinger and H. Nara, J. Phys. C. Solid State Phys., $\underline{5}$, 606 (1972).

38. M. Schlesinger and C. T. Kwan, Phys. Rev., $\underline{3}$, 2852 (1971).

39. M. Schlesinger and P. W. Whippey, Phys. Rev., $\underline{162}$, 286 (1967).

40. M. Schlesinger and M. Nerenberg, Phys. Letters, $\underline{26A}$, 109 (1968).

41. D. Marsh, J. Phys. C., $\underline{5}$, 863 (1972).

42. M. Schlesinger and H. Nara, Solid State Communication, $\underline{9}$, 1247 (1971).

43. M. A. El'Yashevich, Spectra of the Rare-Earths (State Publishing House of Technical-Theoretical Literature, Moscow, 1953).

44. G. H. Dieke et al, Spectra of Rare Earth Ions in Crystals (John Wiley and Sons, New York, 1968).

45. W. T. Carnall et al, J. Chem. Phys., $\underline{49}$, 4424 (1968).

46. I. V. Stepanov and P. P. Feofilov, Doklady Abad. Nauk., $\underline{1}$, 350 (1957).

47. S. D. McClure and Z. Kiss, J. Chem. Phys., $\underline{38}$, 1037 (1963).

48. Y. K. Voron'ko et al, Sov. Phys. Solid State, $\underline{13}$, 1842 (1972).

49. W. Low, J. Makovsky and S. Yatsiv, Quantum Electronics, Vol. I, p. 655 (Columbia University Press, New York, 1964).

50. W. Low, J. Makovsky and S. Yatsiv, Phys. Letters, $\underline{2}$, 186 (1962).

51. E. Loh, Phys. Rev., $\underline{140}$, A1463 (1965).

52. J. L. Merz and P. S. Pershan, Phys. Rev., $\underline{162}$, 217 (1967).

53. U. Ranon, J. Phys. Chem. Solids, $\underline{25}$, 1205 (1964).

54. K. R. Lea, M. J. Leask and W. P. Wolf, J. Phys. Chem. Solids, $\underline{23}$, 1381 (1962).

55. S. D. McLaughlan, Phys. Rev., 150, 118 (1966).

56. H. Masui, J. Phys. Soc. Japan, 22, 1387 (1967).

57. J. Noonan and L. Esterowitz, Optical Properties of Ions in Crystals (John Wiley and Sons, New York, 1967).

58. E. Loh, Phys. Rev., 147, 332 (1966).

59. E. Loh, Phys. Rev., 158, 273 (1967).

60. E. Loh, Phys. Rev., 175, 533 (1968).

61. W. A. Hargreaves, Phys. Rev., B6, 3417 (1972).

62. H. W. Morse, Astrophysics J., 21, 410 (1905).

63. G. Urbain, Ann. Chim. Phys., 18, 222 (1909).

64. N. Chatterjee, Z. Physik, 113, 96 (1939).

65. S. A. Pollack, J. Chem. Phys., 40, 2751 (1964).

66. C. W. Rector et al, J. Chem. Phys., 45, 171 (1966).

67. U. Ranon and W. Low, Phys. Rev., 132, 1609 (1963).

68. A. I. Smirnov et al, Sov. Phys. Solid State, 8, 1750 (1967).

69. G. M. Zverev, Sov. Phys. Solid State, 6, 2225 (1965).

70. I. B. Aizenberg et al, Sov. Phys. Solid State, 13, 2155 (1972).

71. K. V. Narasimham, Indian J. Pure Appl. Phys., 7, 653 (1969).

72. A. I. Smirnov et al, Sov. Phys. Solid State, 9, 1586 (1968).

73. A. I. Smirnov et al, Sov. Phys. Solid State, 12, 590 (1970).

74. Y. K. Voron'ko et al, Sov. Phys. JETP, 23, 10 (1966).

75. A. L. Stolov et al, Sov. Phys. Solid State, 10, 1595 (1969).

76. B. R. Judd and R. Loudon, Proc. Roy. Soc. (London), A251, 127 (1959).

77. B. G. Wybourne, J. Chem. Phys., 32, 639 (1960).

Chapter 2

1. J. C. Slater, Phys. Rev., $\underline{34}$, 1293 (1929).

2. E. U. Condon and G. H. Shortley, The Theory of Atomic Spectra (University Press, Cambridge, 1963).

3. G. Racah, Phys. Rev., $\underline{61}$, 186 (1942).

4. G. Racah, Phys. Rev., $\underline{62}$, 438 (1942).

5. G. Racah, Phys. Rev., $\underline{63}$, 367 (1943).

6. G. Racah, Phys. Rev., $\underline{76}$, 1352 (1949).

7. R. J. Elliot, Proc. Roy. Soc. (London), $\underline{A240}$, 509 (1957).

8. M. Tinkham, Group Theory and Quantum Mechanics (McGraw-Hill Book Company Inc., New York, 1964).

9. V. Heine, Group Theory and Quantum Mechanics (Pergamon Press, London, 1960).

10. B. R. Judd, Operator Technique in Atomic Spectroscopy (McGraw-Hill Book Company Inc., New York, 1963).

11. B. R. Judd, Phys. Rev., $\underline{141}$, 4 (1966).

12. B. R. Judd, Physica, $\underline{33}$, 174 (1967).

13. B. R. Judd, Phys. Rev., $\underline{162}$, 28 (1967).

14. B. R. Judd, Advan. Chem. Phys., $\underline{14}$, 91 (1968).

15. B. G. Wybourne, Spectroscopic Properties of Rare-Earths (John Wiley and Sons, New York, 1965).

16. D. S. McClure, Solid State Physics, edited by F. Seitz and D. Turnbull (Academic Press Inc., New York, 1959), Vol. 9.

17. C. J. Ballhausen, Introduction to Ligand Field Theory (McGraw-Hill Book Company Inc., New York, 1962).

18. T. I. Ishidogu and Shin-Ya, Phys. Soc. Japan, $\underline{5}$, 142 (1950).

19. C. W. Nielson and G. F. Koster, Spectroscopic Coefficients for p^n, d^n and f^n Coefficients (M.I.T. Press, Cambridge, Mass., 1964).

20. M. Rotenberg, R. Bireins, N. Metropolis and J. K. Wooten, The 3-j and 6-j Symbols (M.I.T. Press, Cambridge, Mass., 1959).

21. B. R. Judd and R. Loudon, Proc. Roy. Soc. (London), A251, 127 (1959).

22. M. H. Crozier and W. A. Runciman, J. Chem. Phys., 35, 1392 (1961). ibid., 36, 1088 (1962).

23. A. J. Freeman and R. E. Watson, Phys. Rev., 127, 2058 (1962).

24. B. R. Judd, Proc. Phys. Soc. (London), 74, 330 (1959).

25. B. R. Judd, Proc. Roy. Soc. (London), A250, 562 (1959).

26. R. Sarup and M. H. Crozier, J. Chem. Phys., 42, 371 (1965).

27. J. C. Slater, The Quantum Theory of Atomic Structure Vol. II, (McGraw-Hill Book Company Inc., New York, 1960).

28. M. Schlesinger and H. Nara, Phys. Rev., 3, 58 (1971).

29. J. S. Margolis, J. Chem. Phys., 35, 1367 (1961).

30. W. T. Carnall et al, J. Chem. Phys., 57, 43 (1972).

31. J. H. Van Vleck, J. Phys. Chem., 41, 67 (1937).

32. L. Broer, C. Gorter and J. Hoogschagen, Physica, 11, 231 (1945).

33. G. S. Ofelt, J. Chem. Phys., 37, 511 (1962).

34. W. T. Carnall et al, J. Chem. Phys., 42, 3797 (1965).

35. H. U. Rahman, J. Phys. C., 5, 306 (1972).

36. W. A. Runciman and B. G. Wybourne, J. Chem. Phys., 32, 1149 (1959).

37. W. A. Runciman, J. Chem. Phys., 36, 1481 (1962).

38. G. S. Ofelt, J. Chem. Phys., 38, 2171 (1963).

39. B. G. Wybourne, J. Chem. Phys., 32, 639 (1960).

40. B. G. Wybourne, J. Chem. Phys., 36, 2301 (1962).

41. K. Rajnak and B. G. Wybourne, Phys. Rev., $\underline{132}$, 280 (1963).

42. J. C. Eisentein, J. Chem. Phys., $\underline{39}$, 2128 (1963).

43. J. C. Eisentein, J. Chem. Phys., $\underline{39}$, 2134 (1963).

44. J. C. Eisentein, Symposium on Paramagnetic Resonance, W. Low, Ed., (Academic Press, New York, 1963), Vol. I, p. 253.

45. W. T. Carnall et al, Phys. Rev., $\underline{B2}$, 3526 (1970).

46. K. Rajnak and B. G. Wybourne, J. Chem. Phys., $\underline{41}$, 565 (1964).

Chapter 3

1. W. T. Carnall et al, J. Chem. Phys., $\underline{57}$, 43 (1972).

2. W. T. Carnall et al, J. Chem. Phys., $\underline{49}$, 4424 (1968).

3. A. Halperin and A. A. Braner, Phys. Rev., $\underline{117}$, 408 (1960).

Chapter 4

1. W. T. Carnall et al, J. Chem. Phys., $\underline{57}$, 43 (1972).

2. W. T. Carnall et al, J. Chem. Phys., $\underline{49}$, 4424 (1968).

Chapter 5

1. W. T. Carnall et al, J. Chem. Phys., $\underline{57}$, 43 (1972).

2. G. H. Dieke, Spectra and Energy Levels of Rare-Earth Ions in Crystals (Interscience-Wiley, New York, 1968).

3. E. Loh, Phys. Rev., $\underline{147}$, 332 (1966).

4. S. A. Pollack, J. Chem. Phys., $\underline{40}$, 2751 (1964).

5. C. W. Rector et al, J. Chem. Phys., $\underline{45}$, 171 (1966).

6. W. T. Carnall et al, J. Chem. Phys., $\underline{49}$, 4424 (1968).

7. W. A. Hargreaves, Phys. Rev., $\underline{B6}$, 3417 (1972).

8. J. Sugar, Phys. Rev. Letters, $\underline{14}$, 731 (1965b).

9. J. Sugar, J. Opt. Soc. Am., $\underline{55}$, 1058 (1965c).

10. M. Schlesinger and H. Nara, Phys. Rev., $\underline{3}$, 58 (1971).

11. I. B. Aizenberg, B. Z. Malkin and A. L. Stolov, Sov.
    Phys. Solid State, $\underline{13}$, 2155 (1972).

12. M. Schlesinger and P. W. Whippey, Phys. Rev., $\underline{177}$, 563
    (1969).

13. M. Schlesinger and C. T. Kwan, Phys. Rev., $\underline{3}$, 2852
    (1971).

14. M. Schlesinger and P. W. Whippey, Phys. Rev., $\underline{162}$,
    286 (1967).

15. J. L. Merz and P. S. Pershan, Phys. Rev., $\underline{162}$, 235
    (1967).

VITA AUCTORIS

November 4, 1938   Born in Talagung (Pakistan)

1959   Graduated from Punjab University with
B.Sc. degree.

1959-1962   Taught in D. N. College HISSAR
HARYANA (India)

1964   Graduated from Vikram University,
UJJAIN with M.Sc. degree.

1964-1967   Taught in D. N. College Hissar,
HARYANA (India).

1967-1969   Enrolled at St. Francis Xavier University,
Antigonish, Nova Scotia for M.Sc.
degree.

1969-1973   Enrolled at the University of Windsor
for further studies.